

Daily streamflow estimation using remote sensing data

Meepegalkatiya Gamage Sisiri Danaka Nilantha

B. Sc. (Peradeniya), Postgrad-Dip. (Dehradun), M. Tech. (Visakpattnam)

Thesis submitted in fulfillment of the requirement for
the degree of Doctor of Philosophy

College of Engineering and Science

Victoria University

Australia

2015

*Dedicated to
my beloved wife - Ancy,
who is my inspiration.*

ABSTRACT

Streamflow data are critical for water resource investigations, and their development projects. However, the scarcity of such data, particularly measured streamflow through streamflow gauges, constitutes a serious impediment to the successful implementation of development projects. In the absence of such measured streamflow data, streamflow estimation using measured meteorological data represents a viable alternative. Nevertheless, this alternative is not always possible due to the unavailability of required meteorological data. In the face of such data limitations, many have advocated the use of remote sensing (RS) data to estimate streamflow. The aim of this study was to generate daily streamflow time series data using remote sensing data through catchment process modelling and statistical modelling.

This study was conducted in two contrasting case study areas. The first case study area was the Macalister catchment in Australia, which is a data rich catchment. The second case study area was the Ribb catchment in Ethiopia, which is a data scarce catchment. The Soil and Water Assessment tool (SWAT) was used as the catchment process modelling tool, and Artificial Neural Networks (ANN) were used as the statistical modelling technique. Remote sensing data were used to estimate rainfall and potential evapotranspiration (PET), and to classify landuse/landcover (LULC), which in turn were used as inputs to catchment process modelling. Various vegetation and thermal indices, and brightness temperature were considered as surrogates to meteorological variables. They were used as inputs to statistical modelling to estimate daily streamflow.

The SWAT models of the two study catchments were initially calibrated with ground measured meteorological data (base models). For the Macalister catchment, the calibrated model parameters were used to run the SWAT model with estimated rainfall and estimated PET (both estimated from remote sensing data), replacing ground measured data one at a time, and then together with both estimated rainfall and estimated PET replacing ground measured data. Performance indices were calculated using the estimated streamflow of each model and the measured streamflow. Ground measured PET data (i.e. lysimeter data) were not available for both catchments. Therefore the SWAT model generated the PET data using ground measured data (or data in publicly available databases) on temperature, wind speed, solar radiation and relative humidity. These SWAT derived PET data were

used as ground measured PET data. The results showed that the daily streamflow estimation with ground measured data was the best, while the daily streamflow estimation with estimated rainfall and estimated PET was the poorest. No significant difference to the daily streamflow estimates was noted when SWAT model derived PET was substituted with estimated PET.

For the Ribb catchment, the calibrated model parameters were used to estimate daily streamflow by replacing ground measured rainfall and SWAT model derived PET with estimated rainfall and estimated PET (both estimated from remote sensing data). Note that similar to the Macalister catchment ground measured data were not available for the Ribb catchment and therefore the SWAT derived PET data were used as ground measured PET data. Intermediate models as used in the Macalister catchment were not considered in the Ribb catchment. This was because the model with ground measured rainfall data and estimated PET data produced similar results to the base model, and the model with estimated rainfall and SWAT model derived PET produced similar results to the model with estimated rainfall and estimated PET, in the Macalister catchment. The results of the base model were the best, and the results of model run with estimated rainfall and estimated PET is reasonable. This showed that estimated variables using remote sensing data can successfully be employed in catchment process modelling to estimate daily streamflow in both data rich and data scarce catchments at the same level of accuracy.

The vegetation indices (i.e. *NDVI*, *NDWI* and *EVI*) of current day, seven lag days and 8-day average, and the thermal indices of brightness temperature difference and gradient, as well as the brightness temperature of current day and three lag days were considered as potential input variables for ANN modelling. The Partial Mutual Information method was used to select the influential inputs for these ANN models. The ANN models of total period and seasons, which were developed for the Macalister catchment, revealed that the seasonal models outperformed the total period model. In light of this finding, seasonal ANN models with influential input variables were developed for the Ribb catchment. It was shown that the ANN models developed with vegetation indices, thermal indices and brightness temperature in estimating daily streamflows showed similar performance in terms of accuracy of results for both data rich and data scarce catchments.

Results also showed that the performance of ANN models with vegetation indices, thermal indices and brightness temperature in both case studies was better than the performance of the catchment process models with estimated rainfall and estimated PET (both estimated from remote sensing data). Furthermore, the results indicated that the performance of ANN models (i.e. seasonal) in both case studies were as good as the performance of the catchment process models (i.e. base models) developed with ground measured data.

In summary, this study concluded that the ANN modelling approach provided better predictions of daily streamflow than the catchment process modelling approach when remote sensing data were entirely used to estimate daily streamflow for both data rich and scarce catchments.

DECLARATION

I, *Meepegalkatiya Gamage Sisiri Danaka Nilantha* declare that the PhD thesis entitled '*Daily streamflow estimation using remote sensing data*' is no more than 100,000 words in length including quotes and exclusive of tables, figures, appendices, bibliography, references and footnotes.

This thesis contains no material that has been submitted previously, in whole or in part, for the award of any other academic degree or diploma. Except where otherwise indicated, this thesis is my own work.

.....
Meepegalkatiya Gamage Sisiri Danaka Nilantha
September 2015

ACKNOWLEDGEMENTS

This PhD could not have been undertaken without the support of various people. Although it is not possible to give particular mention to all of them here, I gratefully acknowledge all their contributions.

Above all, I would like to express my heartfelt gratitude to my principal supervisor, Professor Chris Perera for his support, guidance and encouragements whilst giving me freedom to pursue independent work. I am very fortunate to have Professor Perera as my mentor. He not only dedicated significant time and efforts to review my work, but also introduced me to the right networks and kept me focused throughout this journey. I could not have asked for a better role model – knowledgeable, patient, compassionate and inspirational – and I hope I can make him proud in the future.

I am also deeply indebted to Dr. Vladimir Smakhtin, my associate supervisor, for his valuable comments and for encouraging me to undertake a PhD in the first place. His help in tackling administrative tasks at the International Water Management Institute (IWMI) and in introducing me to IWMI's Ethiopian office staff ensured the smooth progression of my studies.

To the individuals and organisations who supported me during field work, I owe a huge debt of thanks. Particularly, I would like to thank the IWMI team at Colombo including Dr. Colin Charters, Dr. David Molden, Mr. David van Eyck, and Mr. Lal Muthuwatte; the IWMI Ethiopian office including Dr. Matthew McCartney; and the Ethiopian Ministry of Water Resources and the Ethiopian National Meteorological Organisation.

Last but not least, this thesis would not have been possible without the love and support of my family and friends: my parents, who raised and supported me in all my pursuits; my wife and daughter, who drove me to push myself even further when I was feeling discouraged and tired; my mother-in-law and Radha who travelled from overseas to take care of my daughter; my siblings, nephews and nieces whose love encouraged me to complete my studies; and my friends who made my time at Victoria University enjoyable.

LIST OF PUBLICATIONS AND AWARDS

Journal Articles:

Gamage, N., Perera, C., 2014 Estimate streamflow data using Artificial Neural Network models with remote sensing based vegetation and thermal indices. Journal of Hydrology
(*In submission*)

Gamage, N., Smakhtin, V., Perera, C., 2014. Estimation of Potential Evapotranspiration using Remote Sensing Data for data scarce catchments. Remote Sensing of Environment.
(*Under review*)

Conference Articles:

Gamage, N., Smakhtin, V., Perera, C., 2011. Estimation of Actual Evapotranspiration using Remote Sensing Data. In: Chan, F., Marinova, D., Anderssen, R.S. (Eds.), 19th International Congress on Modelling and Simulation. Modelling and Simulation Society of Australia and New Zealand, Perth Conventional and Exhibition Centre, pp. 3356-3362.

Gamage, N., Smakhtin, V., Perera, C., 2011. Simulating streamflow using remote sensing data: Artificial neural network approach, XXV IUGG General Assembly - Earth on the Edge: Science for a Sustainable Planet, Melbourne Convention and Exhibition Centre, Melbourne, Australia.

Gamage, N., Agrawal, R., Smakhtin, V., and Perera, B. J. C. (2011). An Artificial Neural Network Model for Simulating Streamflow Using Remote Sensing Data. In: 34th IAHR World Congress - Balance and Uncertainty, 26 June - 1 July (2011), Brisbane. Australia: IAHR & Engineers Australia, pp 1371 - 1378.

Awards:

- Finalist to Outstanding Student Award by Victoria University Alumni -2013.
- Awarded travelling scholarships to attend international conferences.
- Received Secomb scholarship, Office of Postgraduate Research –Victoria University.

TABLE OF CONTENTS

ABSTRACT	I
DECLARATION	IV
ACKNOWLEDGEMENTS	V
LIST OF PUBLICATIONS AND AWARDS.....	VI
TABLE OF CONTENTS	VII
LIST OF FIGURES	XIII
LIST OF TABLES.....	XVII
LIST OF ABBREVIATIONS AND UNITS.....	XIX

Chapter 1: Introduction..... 1-1

1.1 Stress on water resources	1-2
1.2 Importance of this investigation	1-4
1.3 Applications of remote sensing	1-7
1.4 Objectives of the study.....	1-9
1.5 Research methodology.....	1-10
1.6 Research significance	1-13
1.7 Outline of the thesis	1-13

Chapter 2: Streamflow estimation using remote sensing – A critical review 2-1

2.1 Introduction	2-1
2.2 Streamflow estimation	2-2
2.2.1 Classification of streamflow estimation models	2-4
2.3 Remote sensing.....	2-5
2.3.1 History of remote sensing	2-6
2.3.2 The remote sensing system	2-6
2.3.3 Satellites and sensors on board.....	2-7
2.4 Streamflow estimation using remote sensing data	2-12
2.4.1 Use of catchment process models.....	2-12
2.4.1.1 Estimation of input variables using remote sensing data.....	2-16

2.4.1.2	Rainfall estimation using remote sensing data.....	2-17
(a)	Use of visible and thermal remote sensing data for rainfall estimation ...	2-17
(b)	Use of microwave data for rainfall estimation.....	2-20
(c)	Use of combined data for rainfall estimation.....	2-22
2.4.1.3	Evapotranspiration estimation using remote sensing data.....	2-22
2.4.1.4	Landuse/landcover classification	2-26
2.4.2	Use of statistical models	2-30
2.4.2.1	Artificial Neural Networks applications on streamflow estimation.....	2-33
2.4.2.2	Remote sensing based indices for streamflow estimation	2-35
2.5	Summary	2-38

Chapter 3: Study Area, data and methodology..... 3-1

3.1	Introduction	3-1
3.2	Rationale for the selection of study areas	3-1
3.2.1	The first case study area.....	3-1
3.2.2	The second case study area	3-2
3.3	The Macalister catchment	3-5
3.3.1	Data.....	3-11
3.3.1.1	Remote sensing data (satellite-based data)	3-12
3.3.1.2	Ground-based data.....	3-14
3.4	The Ribb catchment.....	3-15
3.4.1	Data.....	3-22
3.4.1.1	Remote sensing data (satellite-based data)	3-22
3.4.1.2	Ground-based data.....	3-22
3.5	Estimation of input variables using remote sensing data for catchment process modelling.....	3-23
3.5.1	Rainfall estimation.....	3-24
3.5.1.1	Rain no-rain cloud separation	3-26
3.5.1.2	Brightness temperature threshold.....	3-28
3.5.1.3	Rainfall estimation using gamma function	3-30
3.5.2	Estimation of potential evapotranspiration	3-34
3.5.2.1	Estimation of R_{n24} for non-cloudy days.....	3-35

3.5.2.2	Estimation of R_{n24} for cloudy days	3-38
3.5.3	Classification of landuse/landcover.....	3-39
3.5.3.1	Ground-truth data collection.....	3-42
3.5.3.2	Training of satellite image	3-42
3.5.3.3	Classification stage.....	3-44
3.5.3.4	Accuracy assessment	3-44
3.6	Catchment process modelling	3-48
3.6.1	Brief description of SWAT	3-48
3.6.2	Model set up and calibration	3-50
3.7	Estimation of remote sensing based indices for statistical modelling.....	3-52
3.7.1	Selection of remote sensing based indices.....	3-52
3.7.2	Equations used to generate remote sensing based inputs for statistical modelling.....	3-53
3.8	Statistical modelling	3-55
3.8.1	Influential inputs.....	3-57
3.8.2	Artificial neural networks modelling.....	3-58
3.9	Performance assessment	3-63
3.10	Summary	3-64

Chapter 4: The Macalister catchment..... 4-1

4.1	Introduction	4-1
4.2	Estimation of remote sensing based variables for catchment process modelling ...	4-2
4.2.1	Rainfall estimation.....	4-2
4.2.1.1	Brightness temperature threshold.....	4-3
4.2.1.2	Rainfall estimation function and results	4-6
4.2.1.3	Performances of rainfall estimation.....	4-12
4.2.2	Potential evapotranspiration estimation.....	4-14
4.2.2.1	PET of non-cloudy days	4-16
4.2.2.2	PET of cloudy days	4-19
4.2.2.3	Mean annual PET	4-21
4.2.2.4	Comparison of PET estimates for total period and seasons.....	4-21
4.2.3	Landuse/landcover classification.....	4-24

4.2.3.1	Principal Component Analysis.....	4-25
4.2.3.2	Results of landuse/landcover classification	4-26
4.2.3.3	Accuracy assessment of the landuse/landcover classification	4-29
(a)	Descriptive techniques.....	4-29
(b)	Analytical techniques	4-33
4.3	Catchment process modelling	4-34
4.3.1	Model calibration and validation with ground measured data	4-36
4.3.2	Streamflow estimation with remote sensing based input variables.....	4-43
4.3.2.1	Model with estimated PET and ground measured rainfall	4-44
4.3.2.2	Model with estimated rainfall and SWAT derived PET.....	4-46
4.3.2.3	Model with estimated rainfall and estimated PET	4-50
4.3.2.4	Flow duration curves for all models.....	4-53
4.4	Streamflow estimation using statistical modelling.....	4-54
4.4.1	Remote sensing based input variables and streamflow	4-55
4.4.2	Determination of influential variables	4-61
4.4.3	Artificial Neural Networks modelling	4-64
4.4.3.1	Streamflow estimation - total period model.....	4-65
4.4.3.2	Streamflow estimation with seasonal ANN models.....	4-67
4.4.3.3	Performance assessment of ANN models.....	4-72
4.5	Comparison of catchment process modelling and statistical modelling.....	4-73
4.6	Summary	4-76

Chapter 5: The Ribb catchment 5-1

5.1	Introduction.....	5-1
5.2	Estimation of remote sensing based variables for catchment process modelling ...	5-2
5.2.1	Rainfall estimation.....	5-2
5.2.1.1	Separation of rain and no-rain clouds.....	5-2
5.2.1.2	Brightness temperature threshold.....	5-2
5.2.1.3	Rainfall estimation function and results	5-4
5.2.1.4	Performance of rainfall estimation	5-7
5.2.2	Potential evapotranspiration estimation.....	5-8
5.2.2.1	PET of non-cloudy days	5-10

5.2.2.2	PET of cloudy days	5-12
5.2.2.3	Mean annual PET	5-14
5.2.2.4	Performance of PET estimates for total period and seasons.....	5-14
5.2.3	Landuse/landcover classification.....	5-15
5.2.3.1	Principal Component Analysis.....	5-16
5.2.3.2	Results of landuse/landcover classification	5-17
5.2.3.3	Accuracy assessment of the landuse/landcover classification.....	5-19
(a)	Descriptive technique	5-19
(b)	Analytical technique	5-22
5.3	Catchment process modelling	5-23
5.3.1	Model calibration and validation using ground measured data.....	5-24
5.3.2	Model with estimated rainfall and estimated PET	5-28
5.3.3	Comparison of results of base model and model with estimated rainfall and estimated PET.....	5-31
5.4	Streamflow estimation using statistical modelling.....	5-32
5.4.1	RS based input variables and streamflow	5-33
5.4.2	Determination of influential input variables	5-38
5.4.3	Artificial Neural Networks modelling.....	5-39
5.4.3.1	Streamflow estimation with seasonal ANN models.....	5-39
5.4.3.2	Performances of ANN based streamflow estimation	5-43
5.5	Comparison of results from catchment process modelling and statistical modelling.....	5-44
5.6	Summary	5-45

Chapter 6: Summary, conclusions and recommendations.... 6-1

6.1	Summary	6-1
6.1.1	Catchment process modelling using remote sensing data.....	6-2
6.1.1.1	Rainfall estimation using remote sensing data.....	6-2
6.1.1.2	Estimation of potential evapotranspiration using remote sensing data	6-4
6.1.1.3	Landuse/landcover classification using remote sensing data.....	6-5
6.1.1.4	Catchment process modelling	6-6
6.1.2	Statistical modelling using remote sensing data.....	6-8
6.1.2.1	Calculation of vegetation and thermal indices	6-9

6.1.2.2	Determination of influential input variables	6-9
6.1.2.3	Artificial Neural Networks modelling	6-10
6.1.3	Comparison of catchment process modelling and statistical modelling.....	6-10
6.2	Conclusions	6-11
6.3	Limitations and directions for future research	6-12
	References.....	7-1
	Appendices.....	8-1

LIST OF FIGURES

Figure 1.1 Schematic diagram of the proposed methodology.....	1-11
Figure 3.1 Macalister catchment showing relevant meteorological stations	3-5
Figure 3.2 Elevation map of the Macalister catchment	3-7
Figure 3.3 Spatial distribution of mean annual potential evapotranspiration over the Macalister catchment	3-9
Figure 3.4 Mean monthly rainfall over the Macalister catchment	3-10
Figure 3.5 Mean monthly streamflow - Macalister River at Stringybark Creek.....	3-10
Figure 3.6 Ribb catchment showing meteorological stations in and around the catchment area.....	3-16
Figure 3.7 Elevation map of the Ribb catchment.....	3-17
Figure 3.8 Annual potential evapotranspiration over the Ribb catchment.....	3-19
Figure 3.9 Mean monthly rainfall over the Ribb catchment	3-20
Figure 3.10 Mean monthly streamflow in the Ribb River near Lake Tana	3-20
Figure 3.11 Major soil types in the Ribb catchment.....	3-21
Figure 3.12 Rainfall estimation procedure used in this study	3-33
Figure 3.13 Error matrix of classified image in terms of number of pixels.....	3-46
Figure 3.14 Three layer feed-forward ANN used in this study.....	3-59
Figure 3.15 MSE of training and testing phases in each iteration.....	3-62
Figure 4.1 Ground measured rainfall and BT of MODIS band 31 at Mount Tamboritha.	4-5
Figure 4.2 Rainfall estimation procedure using BT difference and TRMM rainfall.....	4-7
Figure 4.3 BT of band 31 (BT31) on 13 June 2004.....	4-8
Figure 4.4 TRMM rainfall on 13 June 2004	4-9
Figure 4.5 Estimated rainfall on 13 June 2004.....	4-10
Figure 4.6 Estimated annual rainfall and TRMM annual rainfall – Macalister catchment	4-10
Figure 4.7 Estimated seasonal rainfall and TRMM seasonal rainfall - Macalister catchment	4-11
Figure 4.8 Scatter plot of estimated daily rainfall and TRMM daily rainfall	4-12
Figure 4.9 Cumulative distribution of mismatching days of rain/no-rain under TRMM and estimated rainfall	4-14
Figure 4.10 Test locations within the Macalister catchment.....	4-16

Figure 4.11 A comparison of estimated PET and PM-based PET for non-cloudy days - Macalister catchment	4-18
Figure 4.12 PM based PET and estimated PET for cloudy days - Macalister catchment	4-20
Figure 4.13 PCA components and their cumulative variance	4-26
Figure 4.14 Landuse/landcover classes of the Macalister catchment (after image classification).....	4-28
Figure 4.15 Measured and estimated streamflow of the Macalister catchment – base model	4-40
Figure 4.16 Scatter plots of the measured and estimated streamflow of the Macalister catchment – base model	4-40
Figure 4.17 Scatter plots of the measured and estimated streamflow for different seasons of the Macalister catchment – base model	4-42
Figure 4.18 Measured and estimated streamflow of the Macalister catchment – model with estimated PET and ground measured rainfall.....	4-45
Figure 4.19 Scatter plots of the measured and estimated streamflow of the Macalister catchment with estimated PET and ground measured rainfall	4-45
Figure 4.20 Estimated and measured streamflow of the Macalister catchment – model with estimated rainfall and SWAT derived PET.....	4-48
Figure 4.21 Scatter plots of the estimated and measured streamflow of the Macalister catchment - model with estimated rainfall and SWAT derived PET	4-48
Figure 4.22 Seasonal scatter plots of measured and estimated streamflow of the Macalister catchment – model with estimated rainfall and SWAT derived PET.....	4-49
Figure 4.23 Measured and estimated streamflow of the Macalister catchment - model with estimated rainfall and estimated PET	4-51
Figure 4.24 Scatter plots of the measured and estimated streamflow – model with estimated rainfall and estimated PET	4-51
Figure 4.25 Seasonal scatter plots of the measured streamflow and estimated streamflow using estimated rainfall and estimated PET	4-52
Figure 4.26 Flow duration curves – Macalister catchment	4-54
Figure 4.27 Streamflow and 8-day average <i>NDVI</i> - Macalister catchment	4-56
Figure 4.28 Streamflow and 8-day average <i>NDWI</i> - Macalister catchment	4-56
Figure 4.29 Streamflow and 8-day average <i>EVI</i> - Macalister catchment	4-58
Figure 4.30 Streamflow and brightness temperature of band 31 (<i>BT31</i>) - Macalister catchment	4-58

Figure 4.31 Brightness temperature of band 31 and band 32.....	4-59
Figure 4.32 Streamflow and BT difference (BT31-BT32) - Macalister catchment	4-60
Figure 4.33 Streamflow and BT gradient - Macalister catchment	4-60
Figure 4.34 Measured streamflow and estimated streamflow using ANN model for total period – Macalister catchment.....	4-66
Figure 4.35 Scatter plots of measured, and estimated streamflow using ANN model for the total period – Macalister catchment.....	4-66
Figure 4.36 Flow duration curve of the measured and estimated streamflow – Macalister catchment	4-67
Figure 4.37 Scatter plots of measured and estimated streamflow for calibration and validation periods during each season – Macalister catchment.....	4-69
Figure 4.38 Measured streamflow and estimated streamflow (based on seasonal-combined results) - Macalister catchment.....	4-71
Figure 4.39 Scatter plot of the measured streamflow and estimated streamflow (based on seasonal-combined results) – Macalister catchment.....	4-71
Figure 4.40 Flow duration curve of observed and estimated (with the seasonal ANN model) streamflow – Macalister catchment	4-72
Figure 4.41 Comparison of flow duration curves of measured and estimated streamflow from catchment process and statistical models	4-74
Figure 5.1 Ground measured rainfall and brightness temperature of the Ribb catchment	5-3
Figure 5.2 TRMM rainfall data over catchment area and its surrounding areas.....	5-5
Figure 5.3 Estimated rainfall over the Ribb catchment and its surrounding areas.....	5-5
Figure 5.4 Annual rainfall of the Ribb catchment – TRMM and estimated rainfall	5-6
Figure 5.5 Seasonal rainfall (estimated and TRMM) over the Ribb catchment.....	5-7
Figure 5.6 Cumulative distribution of mismatching days of rain/no-rain under TRMM and estimated.....	5-8
Figure 5.7 Meteorological stations and test locations over the Ribb catchment.....	5-9
Figure 5.8 PM based PET and estimated PET for non-cloudy days at selected test locations in the Ribb catchment	5-12
Figure 5.9 PM based PET and estimated PET for cloudy days at selected test locations in the Ribb catchment	5-13
Figure 5.10 Principal components of the selected six bands of Landsat 7 ETM+ and their cumulative variability	5-17
Figure 5.11 Landuse/landcover types of the Ribb catchment	5-18

Figure 5.12 Measured and estimated streamflow of the Ribb catchment – base model..	5-26
Figure 5.13 Scatter plots of the measured and estimated streamflow of the Ribb catchment – base model	5-26
Figure 5.14 Scatter plots of the measured and estimated streamflow of wet and dry seasons in the Ribb catchment – base model	5-27
Figure 5.15 Measured streamflow, and estimated streamflow with both estimated rainfall and PET – Ribb catchment.....	5-29
Figure 5.16 Scatter plots of the measured and estimated streamflow of the Ribb catchment with both estimated rainfall and PET.....	5-29
Figure 5.17 Scatter plots (seasonal) measured and estimated streamflow of the Ribb catchment – model with both estimated rainfall and PET	5-30
Figure 5.18 Flow duration curves of measured and estimated streamflows – Ribb catchment	5-32
Figure 5.19 Streamflow and 8-day average of <i>EVI</i> , <i>NDWI</i> and <i>NDVI</i> in the Ribb catchment	5-34
Figure 5.20 Streamflow and <i>BT31</i> of MODIS in the Ribb catchment	5-36
Figure 5.21 <i>BT_{diff}</i> and streamflow in the Ribb catchment	5-36
Figure 5.22 <i>BT_{grad}</i> and streamflow in the Ribb catchment.....	5-37
Figure 5.23 Scatter plots of the measured and estimated streamflows – Ribb catchment	5-40
Figure 5.24 Estimated (combined) and measured streamflows with their calibration and validation periods – the Ribb catchment.....	5-42
Figure 5.25 Scatter plots of the measured streamflow and estimated streamflow – Ribb catchment	5-42
Figure 5.26 Flow duration curve of the seasonal ANN models	5-43
Figure 5.27 FDCs of catchment process models and statistical model	5-44

LIST OF TABLES

Table 2.1 Band widths and spatial resolution of the MODIS sensor.....	2-10
Table 3.1 Mean monthly maximum and minimum temperatures at Licola and Mt. Tamboritha	3-8
Table 3.2 Mean monthly maximum and minimum temperatures at two different meteorological stations over the Ribb catchment.....	3-18
Table 3.3 Contingency matrix of the rain/no-rain combinations of MODIS BT and TRMM	3-29
Table 3.4 Landuse/landcover classes.....	3-41
Table 4.1 Mean seasonal BT and mean monthly BT over the Macalister catchment	4-5
Table 4.2 <i>HSS</i> , <i>POD</i> , <i>FAR</i> and bias values for the different thresholds – Macalister catchment	4-6
Table 4.3 Rain/no-rain days under TRMM and estimated rainfalls during the study period	4-13
Table 4.4 Comparison of surface albedo of the Macalister catchment.....	4-15
Table 4.5 Estimated and PM based mean annual PET-Macalister catchment.....	4-21
Table 4.6 Performance indices of estimated PET and PM based PET - Macalister catchment	4-23
Table 4.7 Band information of the Landsat 5 TM sensor	4-25
Table 4.8 Areas of the catchment covered by different LULC classes (after image classification).....	4-29
Table 4.9 Contingency matrix of the landuse/landcover classification – the Macalister catchment	4-31
Table 4.10 Kappa statistics and user’s accuracy of the landuse/landcover classification.....	4-34
Table 4.11 SWAT model parameters used for calibration purposes	4-38
Table 4.12 <i>RMSE</i> (in MI/day) and E_f values of the streamflow estimation using measured data - base model	4-43
Table 4.13 Performance indices of the streamflow estimation – model with estimated PET and ground measured rainfall data.....	4-46
Table 4.14 Performance indices of estimated streamflow using a model with estimated rainfall, and a model with both estimated rainfall and PET.....	4-53
Table 4.15 RS-based input variable, PMI and their 99 th percentile.....	4-63

Table 4.16 Performance indices of the estimated streamflow from various ANN models – Macalister catchment	4-73
Table 4.17 Performance indices of estimated streamflow-model with ground measured data, model with both estimated rainfall and PET, and seasonal-combined ANN	4-75
Table 5.1 Mean seasonal brightness temperature over the Ribb catchment	5-4
Table 5.2 Rain/no-rain days under TRMM and estimated rainfall during the study period	5-7
Table 5.3 Comparison of estimated surface albedo values for different LULC of the Ribb catchment with literature values	5-10
Table 5.4 Mean annual PET over selected test locations.....	5-14
Table 5.5 Performance of PM-based PET and estimated PET for non-cloudy days at selected test locations in Ribb catchment.....	5-15
Table 5.6 Extent and percentage of each LULC class obtained through classification...	5-19
Table 5.7 Contingency matrix of the landuse/landcover classification of the Ribb catchment	5-21
Table 5.8 Kappa statistics of the landuse/landcover classification	5-23
Table 5.9 SWAT model parameters used for calibration purposes – Ribb catchment....	5-25
Table 5.10 Performance indices of the estimated streamflow with catchment process modelling.....	5-31
Table 5.11 PMI results of input variables	5-38
Table 5.12 Performance indices of the estimated streamflow using ANN models – Ribb catchments	5-43
Table 5.13 Performance indices of all the models.....	5-45

LIST OF ABBREVIATIONS AND UNITS

List of abbreviations:

The following list of abbreviations has been used in this thesis. They are the most frequent ones. However, some of the abbreviations are not listed here, and they are defined at their first use.

ANN	Artificial Neural Networks
BT	Brightness Temperature
BT27	Brightness Temperature of MODIS band 27
BT31	Brightness Temperature of MODIS band 31
BT32	Brightness Temperature of MODIS band 32
BT_{diff}	Brightness Temperature difference of band 31 and 32
BT_{grad}	Brightness Temperature gradient
DEM	Digital Elevation Model
E_f	Nash-Sutcliffe efficiency
EVI	Enhanced Vegetation Index
FAR	False Alarm Ratio
FDC	Flow Duration Curve
HRU	Hydrological Response Units
HSS	Heidke skill score
IGGC	Infrared Global Geostationary Composite
LULC	Landuse/landcover
MI	Mutual Information
MODIS	Moderate Resolution Imaging Spectroradiometer
NDVI	Normalized Different Vegetation Index
NDWI	Normalized Difference Water Index
PCA	Principal Component Analysis
PET	Potential evapotranspiration
PM	Penman and Monteith
PMI	Partial Mutual Information
POD	Probability of Detection
RMSE	Root Mean Square Error
RS	Remote Sensing

SWAT	Soil and Water Assessment Tool
TRMM	Tropical Rainfall Measuring Mission

List of Units:

m	Meters
mm	Millimeters
μm	Micrometers
$^{\circ}\text{C}$	Centigrade
km^2	Square kilometers
ha	Hectare
MI	Megalitres
MI/day	Megalitres per day
GI/month	Gigalitres per month
Wm^{-2}	Watts per square meter
m^3s^{-1}	Cubic meters per second
K	Kelvin

CHAPTER 1: INTRODUCTION

Scarcity and misuse of fresh water pose a serious and growing threat to sustainable development and protection of the environment. Human health and welfare, food security, industrial development and the ecosystem on which they depend, are all at risk unless water and land resources are managed more effectively in the present decade and beyond than they have been in the past (ICEW, 1992).

The above quote summarizes the findings of the Dublin Statement¹ on ‘Water and Sustainable Development’ (ICEW, 1992). This statement was accepted by 114 countries and by a large number of international, intergovernmental and non-governmental organizations, at the Rio de Janeiro “Earth Summit” in 1992 (Abbott and Refsgaard, 1996). Although this conference was held 20 years ago, the situation described above remains the same in some parts of the world, and has even worsened in some other parts.

More recently, it was revealed by the UN World Water Development Report (World Water Assessment Programme, 2006) that over 800 million people still do not have enough water and food necessary for a healthy and productive life. This report further noted that the implications of lack of water for food and sanitation go far beyond the question of simple access to the resource. In fact, water scarcity represents a complex social and economic issue which is central to poverty in the community. Water shortage has become even more pronounced due to rapid population growth and increasing industrial and environmental demands.

Although water is a renewable resource and a large amount of water exists on the surface of the earth, only a minute fraction of this amount can be used to meet human requirements. Of the total volume of surface water, 96.5% is salt water which is found primarily in the oceans. This salt water is unsuitable for agriculture, domestic human needs

¹ Scarcity and misuse of fresh water poses a serious and growing threat to sustainable development and protection of the environment. This was acknowledged by experts as an emerging global water crisis at the International Conference on Water and the Environment (ICWE) in Dublin, Ireland, on 26-31 January 1992. At its closing session, the Conference agreed to certain principles which they believed should be implemented by political hierarchy to address the aforementioned issues. These principles form the Dublin Statement.

and for most industrial processes. Whilst the remaining 3.5% is fresh water, almost all of it is stored in the ice caps of the Antarctica and the Arctic (1.7%), or in sub-surface aquifers and groundwater (1.7%). The remaining 0.1% is on the surface and in the atmosphere. In sum, only 0.006% of the total water content can be found in the rivers (Chow et al., 1988) and this is the main water source for global populations.

At this juncture, it is important to highlight that this small portion of potable water is shared amongst all living organisms including humans, flora and wildlife. Furthermore, it should also be noted that the maintenance of the waterway ecology implies that a healthy water flow needs to be upheld. Consequently, a massive demand has been created on the available supplies of fresh water, emphasizing the critical need for better water management for sustainability reasons. In this respect, whilst it is recognized that the knowledge of the spatio-temporal variation and quantification of fresh water is essential on a local scale for better management practices, this knowledge is not currently available in many parts of the world (Sivapalan, 2003; Sivapalan et al., 2003).

1.1 Stress on water resources

Water is the one of the basic constituents of all living organisms, and its importance is reflected in the fact that living bodies currently hold an amount of water which is nearly half of what is available in all the rivers (Chow et al., 1988). However, what is more relevant is that, in addition to this structural requirement (i.e. water that is used as building blocks of living organisms), living organisms continually need an input of additional water to meet their biological activities. Furthermore, the required volume of this potable water (for their biological purposes), which is necessary for daily consumption, is increasing daily as a result of population growth, adding additional pressure on the remaining water sources and ultimately on the environment.

To better understand the reasons behind population growth, it should be noted that since the late 19th century and early 20th century, the global death rate has declined, but the birth rate, at least until the mid-1960s, has been maintained, causing a peak in population growth in the mid-1960s. During this peak time, the population growth rate was above 2%, but later, with improved literacy, the population growth rate was gradually reduced as a result of low birth rate, and has now stagnated at 1.1% (USCB, 2011). Notwithstanding

this reduction in growth rate, according to the United States Census Bureau (USCB) statistics, the world population will reach 8 billion in year 2027, which means that, on average, 71 million people (calculations based on USCB statistics - 2011) will be added to the total population each year. The implication of this population increase is that, at the current rate of water use, an additional amount of 56.8 billion m³ of water per year will be needed to fulfill the demands of the additional population.

The most pressing needs relate to the provision of reliable clean drinking water, and adequate supplies of non-saline water for agricultural purposes and ensuring healthy food production and sanitation. In addition, there must be sufficient water for a wide range of industrial, recreation and community uses. An adequate amount of water should also be available for flora and fauna, and river flows must meet or exceed minimum levels, which are of long-term importance for environmental sustainability. In the light of these concerns, it is clear that the existing water resources must be carefully managed to cater for these varied requirements (World Water Assessment Programme, 2009).

Vast amounts of water are also needed for many industries. Whilst the economic return per unit of water is very high in the industrial sector, the growing energy and manufacturing industries pose increasing pressure on available water resources. According to recent statistics, industries consume around 10% of total water used in the world per annum (World Water Assessment Programme, 2009). These industries make a significant contribution to the standard of living of communities. Nevertheless, there are several challenges with the industrialized use of water such as the increase in water pollution.

The environmental demand for water is of utmost importance for ensuring the sustainability of the ecosystem, since in a closed system even small changes in the shared environment can adversely affect all contributing sectors. The continued presence and availability of volumes of fresh water and other related systems that depend on water, provide a range of benefits to human communities and a variety of wild life (Revenga et al., 2000). A reduction of the ready availability of water supplies can have major adverse effects on these fragile ecosystems. In fact, there are examples where some of these systems are already in a state of total collapse. One obvious example is the Aral Sea in Uzbekistan, which once was a massive body of fresh water that supported the shipping trade, fishing industry and many thriving communities, has now turned into a desert.

Over the last decade, unexpected variations in water availability (changes in precipitation patterns and disastrous events such as droughts and floods) and demand (e.g. agricultural demand) have increased alarmingly, placing augmented pressures on existing water supplies. These unexpected variations in water availability and demand strongly emphasise the urgent necessity of better management and control of available limited water to ensure the wellbeing of all living creatures and the maintenance of a healthy environment.

1.2 Importance of this investigation

To achieve a fair water allocation for sustainable development, water availability and water flow must be accurately quantified, because this knowledge is the most fundamental and critical piece of information for the development of any water-related project. Therefore, of considerable importance to this investigation is the observation that the collection of this information at a local level throughout the world is declining. There are a number of reasons for this, some of which have been identified by the recent UN World Water Development Report (World Water Assessment Programme, 2006):

There has been a severe decrease in the data collected, especially in developing countries, owing to political and institutional instability, economic problems, budget constraints, emphasis on new infrastructure, and lack of professional education. Increased investment in the basic hydrological data collection network is needed to provide information to prevent gross errors in water resources decision-making in an unanticipated future. Investments in ground-based monitoring networks are particularly needed to complement recent advances made in remote sensing and geographic information systems (World Water Assessment Programme, 2006).

By far the largest consumer of available fresh water resources is the massive demand of water for food production. Out of the total world water usage, almost 90% is consumed by agricultural operations in all countries (World Water Assessment Programme, 2006). Consequently, agricultural water management is a crucial factor in global water accounting, and usage must be carefully balanced against an accurate knowledge of water availability. Poor decisions, which may occur because of faulty resource information, can

ultimately affect the quality of agricultural management, with a resulting decrease in food yield and a possible threat to global food security. As an example, Sarvestani et al. (2008) highlighted that the agricultural yield of rice, one of the world's most important food resources, can be reduced by 20 – 51% as a result of water stress during the vegetative, flowering and grain filling stages. Compounding this issue is that the loss of the crops, which can be quite disastrous in itself, can also adversely affect animal husbandry. This begins an exponential propagation of effects down the food chain, with ultimate negative ramifications for global food security. It is argued here that these potential situations can be avoided with precise knowledge of water availability within any given spatial and temporal context.

In this respect, the quantification of river flows and the assessment of water resources are of immense importance in order to scientifically plan better water allocation for users, for timely management of river operations, and to alert authorities of extreme events which can allow users to be warned and which can, in the long run, lead to the introduction of mitigating strategies (Grimes and Diop, 2003).

Traditionally, the use of flow gauges (or ground networks) represents the mechanism for measuring river flows. Flow gauges were introduced some 3000 years ago, with the use of the 'Nilometer' (Sivapalan, 2003) to measure the flows in the Nile River. Since this time, many rivers have had gauges installed, but there is still an unacceptably large number of rivers which are ungauged (Sivapalan, 2003). Also, exacerbating this problem is that ground networks of hydrological measuring stations are declining and are often very sparsely distributed across the world (Adeaga et al., 2005). This is a reality in many countries, and even in developed countries like the United Kingdom (UK), where many small catchments remain ungauged despite the fact that 1,400 gauging stations are currently in operation (Sefton and Howarth, 1998). In Australia, a country which has a much larger surface area than the UK, a large number of catchments still remain ungauged, and this poses a significant problem in water resources management.

For some of the regions across the world, water-related data are available; however, these data related to very short time periods with many missing records. In addition, the limited access to available data is also a problem. This is common in Asia and Africa, where streamflow data are urgently needed to manage water resources in order to alleviate

increasing poverty levels. Often flow gauges are not calibrated in both these regions, and there have been serious issues raised with the quality of available data. These problems have been further aggravated with unhelpful institutional and political barriers (World Water Assessment Programme, 2006) not only in the above mentioned regions but more generally across the world.

The existing gauge network in the world is shrinking due to high maintenance costs, administrative difficulties and collateral issues such as war related damages, civil unrest and animals. This is a common problem, and not restricted to developing countries. In the USA, for example, approximately 2,200 flow stations, which were maintained by various organizations, closed down between 1980 and 2005 (Smakhtin, 2012). In Canada, only 2,837 flow stations are active at present, while 5,584 were made inactive in the last decade (Environment Canada, 2011). In Australia, streamflow monitoring with gauges has started as early as 1865, and has expanded continuously till 1965. Since then, the gauge network severely declined in 3 states of Australia, while there has been modest expansion in the other four states (Cordery, 2007). According to Smakhtin and Wichelns (2010), in Thailand there are 305 streamflow gauging stations which are regularly maintained by the Royal Irrigation Department at 2002, but maintenance of 535 stations has stopped. In Nepal during the last five years, the stream gauge network shrank from 174 to 120 stations. In Bosnia-Herzegovina, where the entire streamflow gauge network totally collapsed during the war (1992-1995), recovery of the network is very slow and yet to reach its full capacity (Kupusovic, 2007).

In the absence of available measurements of streamflow through ground networks, one alternative is to use simulation models that utilize meteorological variables such as precipitation, temperature, evapotranspiration and landuse/landcover. Unfortunately, the collection of data for these variables is laborious, and the realities of managing meteorological stations are not much different to the maintenance of streamflow gauging stations. As such, the use of simulation models using the above mentioned meteorological variables and landuse/landcover has become extremely difficult and indeed nearly impossible with the lack of data on such variables. Likewise, simulating the hydrological regime and/or estimating hydrologic parameters to quantify streamflow is extremely difficult because the complex nature of the hydrological regime implies strenuous work. Often this is costly, especially over large areas with multiple variables, or across several

countries. Furthermore, the costs are multiplied when dealing with different agencies that handle these data within a country. Simulations become even more complex and costly when handling data that deal with catchments that involve several countries. Additionally, long record of meteorological data is a basic requirement for streamflow simulation, and such long records are not available.

In order to address the issue of the lack of hydrological and meteorological variables for streamflow simulation, Lakshmi (2004) suggested that remote sensing data can be used to generate these variables and capture surface information such as surface temperature and landuse/landcover. Due to its ready availability, cost effectiveness and the ability of this data collection method to overcome the natural heterogeneity of the landscape, remote sensing is becoming an attractive and common tool among the research community for various applications such as agriculture, surface hydrology, forestry and urban development.

1.3 Applications of remote sensing

The applications of remote sensing (RS) for civilian purposes started as early as the 1960s. Now the applications span over a wide range of sciences including meteorology, volcanology, geology, oceanography, agriculture and hydrology (Lillesand and Kiefer, 1999). Initially, these applications were limited to the identification of surface objects and mapping, based on the limited capabilities of satellite sensors at that time. However, there have been recent advances in sensor technology, thereby producing advanced sensors. These new advanced sensors stretch from visible to microwave regions of the electromagnetic spectrum. Based on these developments, the early RS based applications (i.e. mapping and object identification) were expanded to more quantitative applications such as rainfall estimation and landuse/landcover assessments. As examples, in meteorology, the initial application of cloud identifications was expanded to precipitation estimates (Arkin, 1979; Huffman et al., 1995; Huffman et al., 1997; Sorooshian et al., 2000), and in volcanology, the identification of volcanos was expanded to mapping/measuring the surface heat of the volcanos' surrounding areas as well as volcanic ash clouds (Schneider et al., 1999). In hydrology, early applications were limited to mapping water bodies, but later applications were expanded to quantifying reservoir sedimentation and pollution, monitoring glaciers, monitoring and estimating flood damage,

and modelling groundwater (Joseph, 2005). RS data were also widely used in agriculture and forestry to monitor crop extent and crop stress, and estimate crop yield (Joseph, 2005), and more generally in forest inventory making, species identification and anthropogenic damages detection (Roy et al., 1991).

There exist several examples of studies which used RS data to generate climatic and landuse/landcover variables. RS data have been directly used to classify and acquire landuse/landcover (Wegmuller, 1993; Anys and Dong-Chen, 1995; Gamage et al., 2007) and such landuse/landcover information have been used as inputs to many agricultural and hydrological applications. Bastiaanssen et al.(1998a), Su (2002) and Senay (2007a) used RS data, plus ancillary data, to calculate evapotranspiration, while Grimes and Diop (2003) and Artan et al. (2007) applied RS data to estimate rainfall amount. The RS data have also been used to quantify soil moisture (Rüdiger et al., 2003; Scott et al., 2003; Mallick et al., 2009). The estimates of the above variables can be used in hydrologic models to generate streamflow.

The direct estimation of streamflow is possible with RS data by measuring water level heights using radar/lidar data (Birkett, 1994; Birkett, 1995; Velpuri et al., 2012). Even though this is a robust method, there are numerous difficulties associated to its implementation. Among them, high costs and the unavailability of high spatial resolution radar/lidar data represent the major setbacks. These difficulties have been overcome with catchment models which have been used to estimate streamflow by applying hydrological and meteorological variables estimated from RS data. As an example, the surface temperature obtained from RS data has been used to estimate evapotranspiration and soil moisture, which were then used in a hydrological model to generate streamflow data (Ottlé et al., 1989). Schultz (1996) used three different models with different inputs computed from RS data to generate interception, evapotranspiration and soil water storage data, which were then used to estimate streamflows. Andersen et al. (2002) used the precipitation and leaf area index that were estimated using RS data to generate streamflow through a streamflow simulation model over the Senegal River catchment in West Africa. However, since some ground based data were equally used in the above applications, the applicability of those models has been restricted by the quality and quantity of such ground measured data.

1.4 Objectives of the study

As noted above, there are significant difficulties associated with the collection of both streamflow data, and meteorological data required for traditional catchment modelling to estimate streamflows. Therefore, the need is felt for a new mechanism that generates streamflow data with no or minimum reliance on ground gauging networks and their data. With this in mind, the main objective of this research project was set as the generation of daily streamflow time series data using (daily) RS data with minimum reliance on ground-collected data. This was achieved through the estimation of rainfall, potential evapotranspiration, and landuse/landcover using RS data, which were used as input to generation of daily streamflow data.

The scope of the study was limited to estimate streamflow data using both catchment process modelling and statistical modelling approaches. These two approaches were developed and tested in estimating streamflow data with RS data. Rainfall and potential evapotranspiration were estimated, and required landuse/landcover was classified using RS data. They were used as inputs in the catchment process modelling approach. Various remote sensing based indices were estimated and their suitability was assessed to estimate streamflow under the statistical approach. Streamflow data estimated using RS data were tested against ground measured streamflow data. In addition, the rainfall data estimated using RS data were tested against ground measured rainfall. However, the potential evapotranspiration (PET) estimated using RS data could not be tested against ground measured PET, since lysimeter data were not available to compute PET as ground measured data at both study areas; instead the PET estimated from RS data were tested against PET computed from the Penman-Monteith (PM) method using ground measured data (or data in publicly available databases) on temperature, wind speed, solar radiation and relative humidity. The PM estimation method for PET is acknowledged to produce similar results to ground measured PET data (Allen et al., 1998; Utset et al., 2004; Allen et al., 2011).

The objective of the study was achieved using two phases. The first phase of the research was dealt with a data-rich catchment - the Macalister catchment (a sub catchment of the Thomson catchment) in Victoria, Australia. This catchment has temperate climate condition. The second phase of the research dealt with a data-poor catchment - the Ribb

catchment (a sub catchment of the Blue Nile catchment) in Ethiopia. This catchment represents tropical climatic conditions, and its meteorological data with regard to some climatic variables were not available as in the Macalister catchment. Also the quality of data for the Ribb catchment was not as good as in the Macalister catchment. However, it had some streamflow data which were used to develop and test both catchment process models and statistical models. A brief description of the methodology is given in Section 1.5.

1.5 Research methodology

A research design was built around the two approaches (i.e. catchment process modelling and statistical modelling) as mentioned in the previous section to achieve the study objectives. First, the methods and techniques were developed to generate selected meteorological variables such as rainfall and potential evapotranspiration as well as landuse/landcover that have an impact on streamflow using the RS data. These variables were then used in the Soil and Water Assessment Tool (SWAT) (Arnold et al., 1998) to generate the required daily streamflow data. Second, vegetation and thermal indices were calculated using RS data. These indices and brightness temperature were used as input variables to estimate daily streamflow with statistical modelling. These input variables were considered as surrogates for meteorological variables that influence streamflow. The schematic diagram for these two approaches is shown in Figure 1.1. These two approaches were carried out using the following four tasks:

- Task 1:** All relevant data were collected. These data included relevant RS data, ground measured meteorological data and streamflow data for the study period.
- Task 2:** Algorithms were built to estimate rainfall, potential evapotranspiration, and classify landuse/landcover from RS data.
- Task 3:** Estimated rainfall, potential evapotranspiration and landuse/landcover were used as inputs to estimate daily streamflow using the SWAT hydrological model.
- Task 4:** Relevant vegetation and thermal indices were calculated using RS data. The relationships between streamflow and these indices (together with other variables such as brightness temperature) were built using statistical

modelling. These relationships were then used to estimate daily streamflow data.

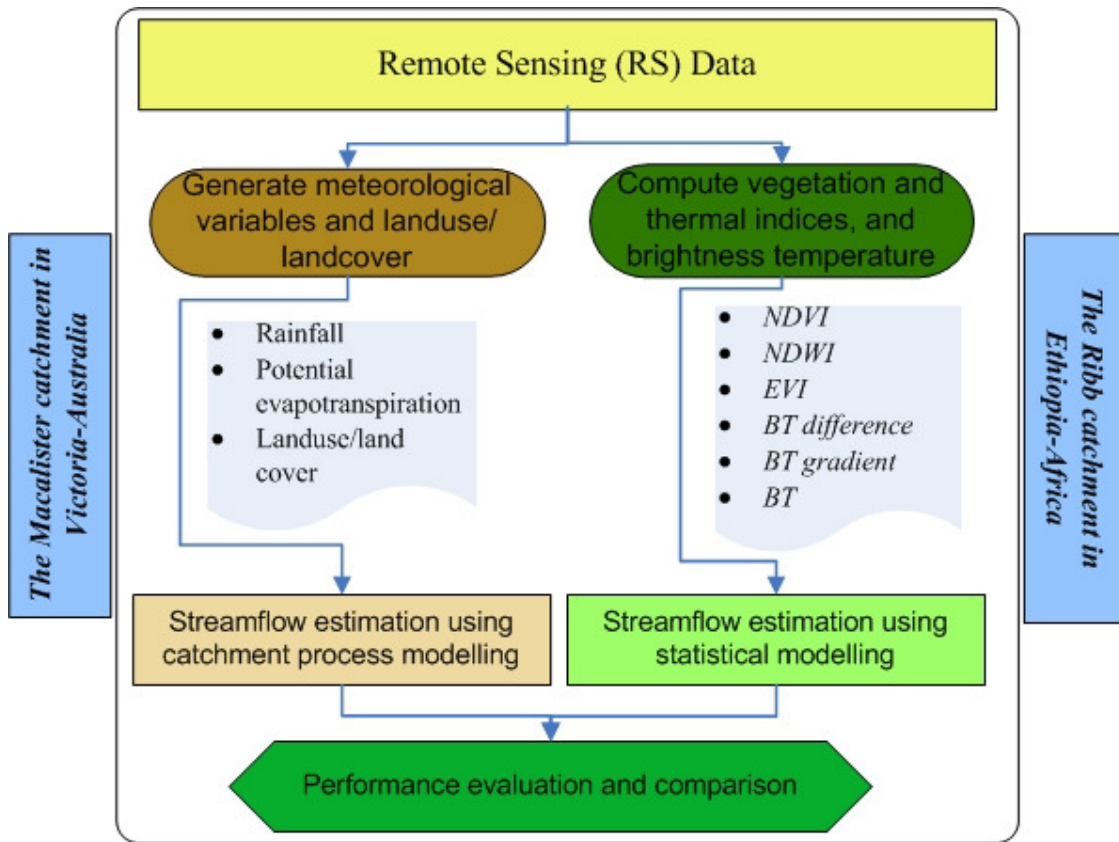


Figure 1.1 Schematic diagram of the proposed methodology

A brief description of above mentioned four tasks are as below.

Task 1: RS data, streamflow data as well as the required meteorological data were collected during this task. RS data are available since the 1970s from several satellite programs which are operated by diverse nations. Much of these data are available free of charge. The recently introduced Moderate Resolution Imaging Spectroradiometer (MODIS) data were collected under this task. MODIS bands are characterised by very high signal-to-noise ratio (SNR) with moderate spatial resolution (1 km), which is suitable for use in small and medium scale catchments (Thenkabail et al., 2004).

Streamflow data and meteorological data of the selected study areas were available from the Bureau of Meteorology in Australia (for the Macalister catchment), and the National

Meteorological Agency and Ministry of Power and Water Resources in Ethiopia (for the Ribb catchment). These data were collected from the above mentioned organizations.

Task 2: High temporal resolution (3 hourly) but low spatial resolution Tropical Rainfall Measuring Mission (TRMM) data and low temporal resolution (daily) but high spatial resolution MODIS brightness temperate data were used to estimate daily rainfall. Daily potential evapotranspiration data were estimated using RS data by employing the surface energy balance method (Su, 2002; Glenn et al., 2007; Gamage et al., 2011b). Surface emissivity, surface albedo and surface temperature obtained through RS data were used in this process. The performance of these estimates were assessed through Root Mean Square Error (*RMSE*) and Nash-Sutcliffe efficiency (E_f). The supervised classification approach with the maximum likelihood classifier was used to classify landuse/landcover for both catchments using reflectance data and vegetation index data. Ground-truth data were used in the supervised image classification process to train the images and hence acquire a higher level of classification accuracy (Gamage et al., 2007).

Task 3: SWAT (Arnold et al., 1998) is a physical-based semi-distributed model that was developed to assess the impact that changing land management practices has on streamflow, nutrients and soil erosion of the catchments. This model can use variables which are estimated from RS data as an input variables. Thus, in this project, variables estimated under Task 2 were used as inputs to the SWAT model of the catchments to estimate daily streamflow. The performance of these estimates were assessed through Root Mean Square Error (*RMSE*) and Nash-Sutcliffe efficiency (E_f).

Task 4: The appropriate surrogates for climate variables that influence streamflow were constructed based on the vegetation and thermal properties of RS data. Specifically the vegetation indices such as Normalized Different Vegetation Index (*NDVI*), Enhanced Vegetation Index (*EVI*) and Normalized Difference Water Index (*NDWI*) (Tucker, 1979; Gao, 1996; Bastiaanssen, 1998; Huete et al., 2002; Jackson et al., 2004; Thenkabail et al., 2004), the thermal indices such as the brightness temperature difference (brightness temperature difference at band 31 and 32), and the brightness temperature gradient, and the brightness temperature (Adler and Negri, 1988; Kuligowski, 2002) were constructed. These indices (and the brightness temperature) were used in statistical modelling to

estimate daily streamflow. Artificial neural networks models were developed as statistical models in this study. The performance of the models was assessed through *RMSE* and *E_f*.

1.6 Research significance

Continuous streamflow data records are essential for the assessment of water resources and environmental flows, for the quantification of available water for agriculture, and for various other water resources and hydrological analyses. Whilst the use of *in-situ* stream gauges is the traditional way of collecting these data, such gauging stations are often sparse and declining in numbers, especially in developing countries. It is also appreciated that managing stream gauge networks is laborious and costly, and institutional and political barriers in some countries limit the accessibility of such data to various users. These reasons are the motivation for hydrologists to develop innovative and alternative methodologies to obtain essential streamflow data which have no or less dependency on stream gauge networks.

This project used RS data with minimum ground data as an alternative way of obtaining daily streamflow data for reasonably long records and at less costs. These RS data have the added advantage of better representation of the ground coverage over large areas. Most of the RS data are now freely available and well maintained according to international best practice standards.

1.7 Outline of the thesis

Chapter 2 discusses the past work relevant to the topic. This includes reviews of streamflow modelling using catchment process and statistical modelling approaches, the estimation of meteorological and landuse variables (precipitation, potential evapotranspiration and landuse/landcover) using RS data, and the estimation of vegetation and thermal indices using RS data.

In Chapter 3, a description of the two study areas is given, in terms of specific climatic, topographic and environmental conditions. Both ground measured and RS data are also discussed with regards to their availability, quality and sources. The chapter then outlines the methodologies that were used in relation to the estimation of daily rainfall and potential evapotranspiration, the classification of landuse/landcover variables, and the

calculation of vegetation and thermal indices. Finally, the chapter closes with a discussion of the catchment process modelling and statistical modelling approaches used in this thesis.

Chapter 4 presents the application of the methodology (detailed in Chapter 3) to the Macalister catchment. This chapter first discusses the results obtained with regards to the estimation of input variables (rainfall, potential evapotranspiration and landuse/landcover) using RS data. These data were used as inputs to the SWAT model of the catchment and the results of the SWAT model were thereafter compared with ground measured data. The performance of the estimated streamflow is also discussed in this chapter. A similar description is given for statistical modelling in this chapter with respect to input variables and the statistical models. The input variables for statistical modelling were made up of vegetation and thermal indices and brightness temperature. The artificial neural networks was the modelling technique that was used for statistical modelling. Chapter 5, which pertains to the Ribb catchment, follows the same structure as that of Chapter 4.

Chapter 6 presents a summary of the findings, and concludes thesis. It further provides suggestions and recommendations for future research.

CHAPTER 2: STREAMFLOW ESTIMATION USING REMOTE SENSING – A CRITICAL REVIEW

2.1 Introduction

Streamflow in a given catchment is the aggregated result of all geological and climatological factors that operate in that catchment (Hersch, 1995). Knowledge of the availability of streamflow (i.e. both temporal and quantity) forms the basic foundation of any water management project. Therefore, measuring streamflow is important to good water management practices. According to Hersch (1995), Sivapalan (2003) and Sutcliffe (2004), streamflow is the only component of the hydrological cycle that is confined in well-defined channels, as the rest of the components such as rainfall, evapotranspiration and soil moisture are spatially distributed. Therefore the measurement of streamflow provides higher confidence than measurement of other components (Sivapalan, 2003).

The amount of water that flows in well-defined channels (whether a stream or a river) in a given time period defines streamflow data or streamflow record. Streamflow data are important for planning, designing and operating water resource projects that deal with irrigation water supply, hydroelectric power generation, and urban and industrial water supply (Grimes and Diop, 2003). They are also important in monitoring the efficiency and sustainability of such projects. This was highlighted by Sutcliffe (2004) who claimed that streamflow is the most important and directly applicable variable for monitoring and evaluating water resources projects.

Traditionally, stream gauges have been used to measure the amount of streamflow at a particular location (called a gauging station) of a river or a stream at regular time intervals (Hersch, 1995; Sivapalan, 2003). Despite the importance of streamflow data, the total number of stream gauges across many parts of the world is declining (Sivapalan, 2003). A few examples of this decline were outlined in Chapter 1. To complicate matters further, existing gauges are at the outset sparse and poor management practices in developing countries mean that either streamflow data are not recorded at all or false information is recorded (Stisen et al., 2008). The false recording of streamflow data in some countries has more adverse effects than the non-availability of data and has serious effects on the

planning, designing and evaluation of water resource projects. This situation is exacerbated due to increased negligence in maintaining the streamflow gauges properly especially since the benefits of such gauging network are invisible and difficult to account for accurately (Herschy, 1995).

The above mentioned issues can be handled to a certain degree by estimating streamflow using meteorological variables. For such purposes, various models can be used and many of these existing models were briefly described by Singh and Woolhiser (2002). For the successful estimation of streamflow, these models require data of meteorological variables, as well as the appropriate values of catchment and model parameters. However, the availability of data of meteorological variables is poor in most parts of the world, especially in developing countries. As a consequence, many studies have attempted to estimate these meteorological variables with RS data. These were briefly described in Chapter 1. Several attempts have also been made to estimate streamflow directly with RS data.

This chapter will review the literature on RS applications aimed at estimating meteorological variables such as rainfall and potential evapotranspiration. In addition, landuse/landcover classification with RS data will also be reviewed. It will further review the applications of RS based meteorological variables in catchment process modelling. Finally, the use of RS data for estimating indices and their use in streamflow estimation with statistical models will be elaborated.

2.2 Streamflow estimation

This section will address the emergence, classification and background of streamflow estimation modelling. In the absence of ground measured streamflow data, many attempts have been made to estimate streamflows, and a streamflow estimation model (variously known as the streamflow simulation model (SSM) or hydrological model) has been particularly used in this regard. By definition, the streamflow estimation model is a simplified representation of the natural system which consists of rainfall, evapotranspiration and ground water. This representation is built by combining a set of mathematical expressions and logical statements in order to simulate the natural system (Refsgaard, 1996).

The streamflow estimation model was initially introduced to the hydrological world by Mulvarny (1850), as a modelling approach based on a 'rational' method. Four decades later, Imbeau (1892) introduced a different dimension to hydrology, presenting an 'event-based' model. This model particularly focused on storm peak runoff and rainfall intensity. Subsequently, in the first half of the 20th century, important scientific innovations were developed to understand the hydrological cycle. These innovations were related to physical and biological processes within the catchment, and opened the way to the emergence of many streamflow estimation models. Additionally, this era of hydrological applications was strengthened by Sherman (1932) who introduced the 'unit hydrograph' concept. The latter concept was a breakthrough in the calculation of runoff with excess rainfall in a given rain event. Concurrently, Horton (1933) introduced the 'infiltration theory' and 'hydrograph separation' techniques, while Lowdermilk (1934) and Hursh and Brater (1944) introduced the subsurface water movement component into hydrology. Later, Thornthwaite (1948) and Penman (1948) contributed significantly to hydrology with their understanding and quantification of evapotranspiration, as an abstraction of the hydrological cycle.

The second half of the last century marked the golden era of streamflow estimation modelling as a result of the creation of a wealth of knowledge on physical and biological processes of the hydrologic water cycle. It led to the development of streamflow estimation models, and this was facilitated by the availability of advanced computing facilities and other infrastructure. The Stanford Watershed Model-SWM (Crawford and Linsley, 1966) was the first model which considered the physical processes related to the hydrologic water cycle at the catchment scale. During the late 60s and early 70s, the spatial analysis techniques were introduced on a Geographic Information System (GIS) platform. This innovation allowed streamflow estimation models to be developed on a GIS platform, thereby enabling spatial variability of hydrometeorological variables into hydrological processes. Following the development of better infrastructure (such as relevant institutions, upgraded hardware to measure input variables of the models, and advanced computing hardware and enhanced human capacity), hydrological modelling reached a new level, with the emergence of a variety of different models. Amongst them, Storm Water Management Model (SWMM) (Metcalf and Eddy Inc. et al., 1971), TOPMODEL (Beven and Kirkby, 1979), SHE (Abbott et al., 1986a; Abbott et al., 1986b) and SWAT (Arnold and Allen, 1996) are dominant. Singh and Woolhiser (2002) listed more than 60 such

models. These models vary based on their internal processes, and requires a variety of meteorological variables and catchment and model parameters to enable them to estimate streamflow. Given the limited data availability, selecting a particular model for an application can prove to be a challenging task. However, the classification of streamflow estimation models provides guidance on the suitability of models for different context.

2.2.1 Classification of streamflow estimation models

The classification of streamflow estimation models has started as early as 1970s (Woolhiser, 1973; Fleming, 1975). Later, Singh (1995) proposed a classification scheme for the existing streamflow estimation models based on their building process. Based on this idea, all streamflow estimation models were classified into six categories, namely; process description, time scale, space scale, land-use, model use and technique of solution. Since this classification is derived from the model building process, it has only one hierarchical level, with all six categories being equally important. The American Society of Civil Engineers (ASCE) (1996) proposed an alternative classification mechanism for flood analysis models under the headings of (i) event-based rainfall runoff models, (ii) continuous precipitation runoff models, (iii) steady flow routing models, (iv) unsteady flow routing models, (v) reservoir regulation models, and (v) flood frequency models (ASCE, 1996). Since this classification is based on the objective of flood condition simulation (Singh and Woolhiser, 2002), it neglected other existing streamflow estimation models which are used for planning and operating water resources systems.

Refsgaard (1996) proposed a different classification method for all streamflow estimation models based on the mathematical structure of the model. The use of the particular mathematical structure of the model as classifier led to the introduction of various hierarchical levels in contrast to Singh's (1995) single level classification scheme. In the first level of Refsgaard's classification scheme, all streamflow estimation models are classified as deterministic or stochastic, as shown in Figure 2.1. In general terms, the deterministic model branch of Refsgaard's (1996) classification was considered as catchment process modelling, and the stochastic branch was considered as statistical modelling. The empirical models under the stochastic branch are further explained under Section 2.4.2.

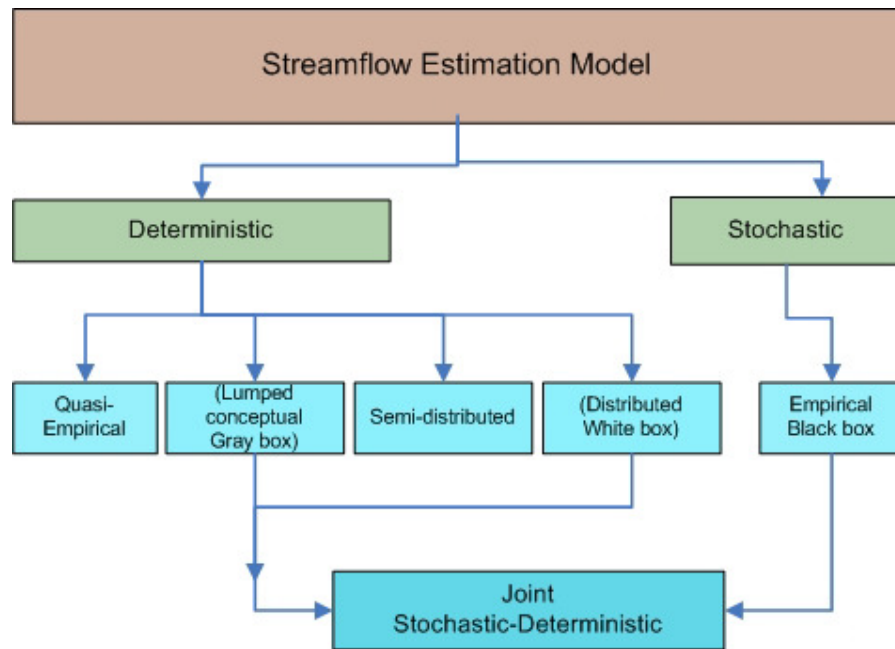


Figure 2.1 Schematic diagram of the classification of streamflow estimation models (adopted from Refsgaard – 1996)

2.3 Remote sensing

The emergence of remote sensing (RS) stemmed from the development of conventional, multispectral and infrared photography, non-photographic sensors and scanners, platforms for RS such as aircraft and satellites, launching vehicles, communication and data transmission, data processing and computer technology and other relevant infrastructure (Lillesand and Kiefer, 1999). Importantly, with the advent of RS, the observation regions of the electromagnetic spectrum have expanded far beyond the range of human. This has significant implications for data collection and subsequent predictive analysis.

The term ‘remote sensing’ was initially used by Evelyn L. Pruitt of the USA Office of Naval Research in the early 1960s to denote satellite images which were markedly different from conventional cameras. These images used both visible light and other parts of the electromagnetic spectrum, and as such represented a clear difference from the conventional photography which relies on visible light only. This led to the development of RS as a separate field in the science of data application. Lillesand and Kiefer (1999) defined RS as *‘the technique of obtaining information about an object without physical contact, as opposed to in-situ sensing in which the measuring device is in touch with the*

object'. According to this definition, the emitted or reflected electromagnetic energy of an object is measured by a sensor as part of the RS process. However, this definition was narrowed down by Joseph (2005) following the UN general assembly resolution A/RS/41/65, at the 95th plenary meeting in 1986. According to this later definition, remote sensing is the '*sensing of the earth's surface from space by making use of the properties of electromagnetic wave emitted, reflected or diffracted by the sensed objects, for the purpose of improving natural resources management, landuse and the protection of environment*'. This second definition successfully captures the aims of RS unlike the broader definition set forward by Lillesand and Kiefer (1999).

2.3.1 History of remote sensing

The history of RS is intricately linked to World Wars I and II. The rapid development of RS technology took place during World War I. After this war, the technology and corresponding experts were adapted and used for civilian applications. (Lillesand and Kiefer, 1999; Joseph, 2005). The launch of Earth Resources Technology Satellite-1 (ERTS 1) by NASA in 1972 which was the parts of work started in the 1960s, was the landmark in the history of RS, and is arguably the beginning of modern RS (Estes, 2005; Irons, 2011) with respect to the civilian applications. This series was later named 'Landsat', and was the first of several earth-orbiting satellites designed specifically for land observation for civil applications. The Landsat program provides systematic and repetitive observation of the oceans, atmosphere and land areas (Taylor, 2014). In the recent past, various stakeholders such as the Indian Space Research Organization (ISRO), European Space Agency (ESA), Centre national d'études spatiales – the French space agency (CNES) and Japan Aerospace Exploration Agency (JAXA) have developed numerous sensors with various capabilities and have launched satellites to provide better data for the user community.

2.3.2 The remote sensing system

The entire RS system (up to the image acquisition level) consists of several steps. The initial step is the emission of source electromagnetic radiation (either from the sun or from the collection apparatus), and the transmission of that energy from the source to the object of interest location in the ocean, on earth or in the atmosphere. RS can be broadly divided into two categories based on the energy used by the sensors to capture RS data: *active* and

passive. Sensors which carry electromagnetic radiation of specific wavelength or band of wavelengths to illuminate the earth's surface are called active sensors, while sensors that capture natural radiation, which is emitted or reflected from the earth are called passive sensors (Joseph, 2005).

The next step involved in the RS system pertains to the fact that the energy either contained in or impinging on the object of interest is subsequently reflected, absorbed, scattered or emitted. Once this energy leaves the object, it is picked up by the remote sensor (collector). The remote sensor will then transform the data and finally transmits signals to the receiving center. These remote sensors are embedded with four different resolutions (Joseph, 2005; Lillesand and Kiefer, 1999), namely they are:

- Spatial resolution – the ability of the sensor to separately identify two different objects. Therefore, the higher the spatial resolution, the smaller the object that can be identified.
- Spectral resolution – the spectral bandwidth within which data are collected.
- Temporal resolution (revisit time) – the ability to view the same target under similar conditions at regular intervals.
- Radiometric resolution – the ability to differentiate between two targets based on their reflectance/remittance difference.

The vehicle upon which the remote sensor is mounted is called the platform (i.e. satellite, air plane balloon).

The final step of the RS system is the acquisition of transmitted data by ground station/s. This data are recorded on hardware, and are released to data analysts for processing and interpretation. The level of processing and interpretation of RS data are directly linked with the applications.

2.3.3 Satellites and sensors on board

There are numbers of satellites and sensors which have been launched for various purposes. Amongst them the Landsat, the Indian Remote Sensing (IRS) satellites, ASTER and SPOT satellites which are sun-synchronized satellites that acquire detailed ground information with higher spatial resolution. In contrast, meteorological satellites such as

MTSAT and KALAPANA are geo-stationary satellites which acquire data on higher temporal resolution. Thus, they are more sensitive to the temporal changes, but have low spatial resolutions. MODIS and AVHRR are sun-synchronized, but have medium spatial and temporal resolution. Spatiotemporal characteristics and the applications of Landsat, MODIS and Tropical Rainfall Measuring Mission (TRMM) satellites are briefly discussed here, since they are important in this study.

Landsat

The Landsat series of satellites have the longest historical records in RS data collection, with these records starting in the early 1970s. The National Aeronautics and Space Administration (NASA) has successfully operated the Landsat series (Landsat 1, 2, 3, 4, 5, 6, 7 and 8) throughout the last 40 years, and has continually improved the sensor features from Landsat 1 to Landsat 8.

A variety of applications is possible with Landsat because of the diversity of sensors with different bands operating on board. The blue band has been used in the applications of water body penetration (Benny and Dawson, 1983; Harrington Jr et al., 1992), coastal water mapping (Gamage and Smakhtin, 2009), soil/vegetation discrimination (Gamage et al., 2009b) and forest feature identification (Oguro et al., 1999; Pax-Lenney et al., 2001). However, the blue band has its own limitations in terms of scattering due to the range of electromagnetic spectrum. Therefore incoming radiance to the sensor is often insufficient in intensity. To address this problem, the green band is used as an alternative for vegetation discrimination and vigor assessment. The red band has been used to measure chlorophyll absorption (Tucker, 1979) of vegetation. The Near Infrared (NIR) band is the most important band among all visible range bands, as it enables the determination of vegetation types, vigor and biomass (Tucker, 1979), and delineates water bodies (Islam et al., 2008). These bands have been prominent in the mapping of landuse/landcover in many studies (Pax-Lenney et al., 2001; Shupe and Marsh, 2004; Jackson et al., 2004; Gamage et al., 2007).

The Mid Infrared (MIR) band of the Landsat TM/ETM+ sensors is important in segregating snow cover from clouds. The Thermal Infrared (TIR) band is intensively used to measure vegetation stress via skin temperature and other thermal mapping applications such as the estimation of actual evapotranspiration (Bastiaanssen et al., 1998b; Su, 2002;

Sánchez et al., 2008; Oguro et al., 2011). Among all the applications mentioned earlier, those related to landuse/landcover and evapotranspiration can directly be used for streamflow estimation, and are consequently of interest in this study.

Terra and Aqua satellites

The Moderate Resolution Imaging Spectroradiometer (MODIS) is the primary sensor on board of the Terra and Aqua satellites. This sensor is used for monitoring the terrestrial ecosystem in the NASA's Earth Observing System (EOS) program (Justice et al., 2002). The MODIS sensor is the predecessor of the Advanced Very High Resolution Radiometer (AVHRR). MODIS is very sensitive to the changes in vegetation dynamics (Huete et al., 2002), and was found to be a more accurate and versatile instrument to monitor global vegetation conditions than the AVHRR (Justice et al., 2002). The narrow bands that represent vegetation qualities facilitate this accuracy, and because of this ability, MODIS based vegetation indices give a better representation of landuse/landcover parameters.

The MODIS sensor consists of 36 bands with spatial resolution varying from 250 m to 1 km (Table 2.1). This table shows band width, spatial resolution and broader applications of each band. Furthermore, this table shows that MODIS band widths are narrower than Landsat sensors' band width, and represent visible, near, mid and thermal infrared regions of the electromagnetic spectrum. Therefore, MODIS obviously provides unprecedented volumes of data for a wider range of research and applications (Justice et al., 2002).

Table 2.1 Band widths and spatial resolution of the MODIS sensor

Band Number	Band width (µm)	Spatial Resolution (m)	Bandwidth use*
1	0.620-0.670	250	L
2	0.841-0.876	250	A, L
3	0.459-0.479	500	L
4	0.545-0.565	500	L
5	1.230-1.250	500	L
6	1.628-1.652	500	A, L
7	2.105-2.155	500	A, L
8	0.405-0.420	1000	O
9	0.438-0.448	1000	O
10	0.483-0.493	1000	O
11	0.526-0.536	1000	O
12	0.546-0.556	1000	O
13	0.662-0.672	1000	O
14	0.673-0.683	1000	O
15	0.743-0.753	1000	O
16	0.862-0.877	1000	O
17	0.890-0.920	1000	A
18	0.931-0.941	1000	A
19	0.915-0.965	1000	A
20	3.660-3.840	1000	O, L
21	3.929-3.989	1000	Fire, Volcano
22	3.929-3.989	1000	A, L
23	4.020-4.080	1000	A, L
24	4.433-4.498	1000	A
25	4.482-4.549	1000	A
26	1.360-1.390	1000	Cirrus cloud
27	6.535-6.895	1000	A
28	7.175-7.475	1000	L
29	8.400-8.700	1000	Ozone
30	9.580-9.880	1000	A, L
31	10.780-11.280	1000	A, L
32	11.770-12.270	1000	A, L
33	13.185-13.485	1000	A
34	13.485-13.785	1000	A
35	13.785-14.085	1000	A
36	14.085-14.385	1000	

*Broader applications of band use L for land, O for ocean and A for atmosphere.

The most common applications of MODIS relate to vegetation and seasonal dynamic assessments (Huete et al., 2002; Justice et al., 2002; Thenkabail et al., 2005; Huete et al., 2006; Colditz et al., 2007; de Silveira et al., 2007). MODIS data have also been widely used in evapotranspiration (ET) estimation on various scales from catchment to global level (Kuo et al., 2005; Mu et al., 2007; Guerschman et al., 2009; Zhang et al., 2009b). Such ET information have further been used in water productivity measurements (Gamage et al., 2009b), and have improved rainfall runoff modelling (Zhang et al., 2009b). Furthermore, calculated ET has widely been used in root zone soil moisture assessments (Schnur et al., 2010). More than this, MODIS has been widely used in oceanic, atmospheric and forestry applications.

The Landsat onboard sensors and the MODIS sensor are restricted to the visible, infrared and thermal regions of the electromagnetic spectrum. Therefore, acquiring information related to the internal structure of clouds is difficult, since they are unable to penetrate the cloud cover. This can be avoided by using microwave sensors, which have cloud penetration capabilities. Thus, Tropical Rainfall Measuring Mission (TRMM) Microwave Imager (TMI) and Precipitation Radar (PR) sensors onboard of the TRMM satellite can be used to acquire information of internal structure of clouds.

Tropical Rainfall Measuring Mission satellite

The Tropical Rainfall Measuring Mission satellite is a platform for a collection of sensors to acquire data from many aspects of the atmosphere and clouds in order to estimate precipitation in tropical regions. The group of sensors on board of this satellite includes the Precipitation Radar (PR), TRMM Microwave Imager (TMI), Visible and Infrared Scanner (VIRS), Cloud and Earth Radiant Energy Sensor (CERES) and Lightning Imaging Sensor (LIS) (Kummerow et al., 1988).

The data acquired from these sensors on board of TRMM (i.e. TRMM data) are available as raw data (such as PR data, TMI data), and as various products (such as TRMM precipitation estimates). These data and products are available in various spatiotemporal resolutions (Pierce, 2008). They have been used in various rainfall-related applications such as streamflow estimation (Giglio, 2007; Collischonn et al., 2008; Su et al., 2008) and flood estimation. Additionally, TRMM data have also been used in the identification of

fire circles in tropical regions (Giglio, 2007) and in the retrieval of latent heating profiles of the atmosphere (Shoichi et al., 2009).

2.4 Streamflow estimation using remote sensing data

RS data are used in various forms in different modelling approaches to estimate streamflow. Indeed, both catchment process modelling and statistical modelling approaches have been used with RS data to estimate streamflows in various spatiotemporal scales (Ottlé et al., 1989; Hardy et al., 1989; Giacomelli et al., 1995; Minnas and Hall, 1996; Andersen et al., 2002; Boegh et al., 2004; Chen et al., 2005; Wesseling and Feddes, 2006; Campo et al., 2006; Asante et al., 2008; Stisen et al., 2008; Milzow et al., 2009; Yong et al., 2012).

2.4.1 Use of catchment process models

Catchment process models with various RS based inputs have been used to estimate streamflow in the past (Andersen et al., 2002; Boegh et al., 2004; Campo et al., 2006; McMichael et al., 2006). These inputs estimated from RS data are rainfall (Stisen et al., 2008; Yong et al., 2012), evapotranspiration (Droogers and Kite, 2002; Chen et al., 2005) landuse/landcover (LULC) and Leaf Area Index (LAI) (Andersen et al., 2002; Gamage et al., 2007), and soil moisture (Giacomelli et al., 1995). The application of rainfall, evapotranspiration and LULC to estimate streamflow in catchment process modelling is discussed in the remaining part of this section.

Early meteorological satellite data have been used to estimate rainfall data based on cold cloud duration (CCD) or GOES Precipitation Index (GPI) (Arkin and Meisner, 1987), and they were then used as an input variable to estimate streamflow with the catchment process models. Hardy et al. (1989) used daily rainfall estimates for streamflow estimation. They derived rainfall using the CCD technique with MTSAT data as inputs. The Pitman model (a conceptual rainfall runoff model which was widely used in Africa) (Pitman, 1976) used daily rainfall and monthly evapotranspiration as inputs to estimate daily streamflow, in the Senegal River basin in West Africa. It was found that the model with estimated rainfall performed as accurately as the model with ground measured rainfall. However, it was also noted that streamflow estimation was weak with estimated rainfall during large rain events (Hardy et al., 1989). Pietroniro et al. (1989) used a simple monthly rainfall runoff model to

estimate streamflow, and found a minor improvement in runoff statistics when rainfall estimated from RS data was used as an input in a catchment in West Africa.

Andersen et al. (2002) used the MIKE SHE model (a fully distributed hydrological model) to estimate streamflow in West Africa with estimated rainfall based on GPI. They concluded that the introduction of estimated rainfall, and estimated rainfall complimented with ground measured rainfall did not improve the model's results. They also concluded that the improvement of rainfall estimates from RS data could improve the accuracy of streamflow estimates.

The introduction of the TRMM satellite took place in late 90's and the sensors onboard this satellite are dedicated to measuring rainfall from space. The data of these sensors not only cover the majority of the globe but they also give more information on clouds and hence to improve the accuracy of rainfall estimation compared to previous rainfall estimates that were based on visible and thermal infrared data. Especially, TRMM microwave sensor data empowered existing rainfall estimation procedures by adding structural information on clouds (Huffman et al., 1995; Huffman et al., 2007). Since then, TRMM data have been used to produce various precipitation products such as 3B42 (Huffman et al., 2007), and have been extensively applied in hydrology.

TRMM rainfall products have been widely applied in various parts of the world to estimate streamflow and results with different levels of performance have been obtained (Collischonn et al., 2008; Mc Cabe et al., 2008; Su et al., 2008; Bitew and Gebremichael, 2011; Yong et al., 2012). For example, while using TRMM rainfall data to estimate the streamflow of a large catchment at high latitude, Yong et al. (2012) found several issues such as the overestimation of rainfall in higher elevations (snow covered areas), especially during winter. The latter concluded that TRMM data do not accurately represent the magnitude and spatiotemporal variability of the precipitation in higher latitudes. Wagner et al. (2009) used TRMM 3B42 rainfall data, climatological model based rainfall, and ground measured rainfall to estimate streamflow in a water balance model. They applied this methodology to estimate streamflow in the White Volta basin, and obtained no improvement in estimating streamflow with TRMM 3B42.

Collischonn et al. (2008) used ground measured and TRMM 3B42 rainfall data to simulate streamflow separately in a very large catchment ($>460,000 \text{ km}^2$). They compared the simulation results of both models with observed streamflow data, and concluded that the performance of the model based on TRMM 3B42 rainfall data is as good as that with the model with ground measured data at the most downstream gauge point of the catchment. In the same study, they tested several upstream gauge points in which case they found that the performance of estimated streamflow with TRMM 3B42 rainfall data was reduced towards the upstream of the catchment, i.e. with decreasing catchment area. Nikolopoulos et al. (2010) used TRMM 3B42, KIDD (a rainfall product that was estimated on the algorithm proposed by Kidd et al. (2003)), radar and ground measured rainfall data in streamflow estimation to investigate the relationship between the error of satellite based rainfall data and the size of the catchment. In this study, they concluded that the error in streamflow estimation increased while catchment size decreased. They highlighted that the use of rainfall products of higher spatial resolution could alleviate the error propagation in small catchments. In sum, above studies showed that the spatial representation of TRMM rainfall data is not sufficient enough to estimate streamflow accurately in medium and small size catchments.

Several attempts have been made to use evapotranspiration estimated from RS data in streamflow estimation (Kite and Droogers, 2000; Boegh et al., 2004; Oudin et al., 2005a; Oudin et al., 2005b; Zhou et al., 2006; Immerzeel and Droogers, 2008). Boegh et al. (2004) highlighted that the evapotranspiration estimates using RS data during the dry season were overestimated in the study area, where cultivation fields of Denmark. This overestimation has underrated the contribution of groundwater to streamflow. Immerzeel and Droogers (2008) used evapotranspiration estimates using RS data (based on Surface Energy Balance Algorithm for Land method) for streamflow estimation in the Krishna basin of India, and obtained promising results for ungauged catchments. Oudin et al. (2005a) used 27 potential evapotranspiration (PET) estimation methods to investigate the efficiency of PET in runoff estimation using a lumped model. Interestingly they found that PET estimation methods using temperature and radiation provided the best PET estimates, while the Penman method responded weakly. They showed that the PET estimations based on temperature and radiation are sufficient to estimate streamflow. Given those studies, RS data will be used in this study to estimate PET, which will be then used to estimate streamflow.

Landuse/landcover classified using RS has also been widely used in streamflow estimation. These landuse/landcover maps have been extensively used in defining crops area, and the hydrological model has mainly been used to define the cropping pattern and the rest of the parameters (Boegh et al., 2004). The LULC information computed from RS data has been used as early as 1977 (Pluhowski, 1977) to improve estimates of streamflow characteristics. It was concluded that landuse/landcover information of RS provides an effective means of significantly improving estimates of streamflow. Even though landuse/landcover has widely been used in streamflow estimation as an input, landuse/landcover has been considered as a time constant variable in most of the applications.

Landuse/landcover has not only been used as input to streamflow estimation, but it has also been utilized to investigate the impact on hydrology due to LULC changes (Githui et al., 2009; Dadhwal et al., 2010; Gumindoga, 2010). Gumindoga (2010) used RS data to classify landuse/landcover over the Gilgal Abay catchment in Blue Nile in Ethiopia, and thereafter used it in the TOPMODEL hydrological model to investigate the impact of landuse/landcover changes on the hydrology of the catchment. Gumindoga (2010) concluded that RS data not only helped to achieve the objectives of the study, but also facilitated the derivation of vital information for planning and implementation of development projects, especially in ground measured data scarce areas like Ethiopia. Moreover, Vaze et al. (2011) used landuse/landcover information obtained from RS data to estimate regional model parameters of Sacramento and SIMHYD models. They then used these parameters to estimate streamflows in ungauged catchments in Australia.

The above mentioned literature clearly shows the depth of the applications of estimated rainfall, evapotranspiration, and landuse/landcover using RS data in streamflow estimation. However, the use of these RS based estimates is challenging in that applications vary according to the catchment's size and required fine time scale such as daily.

2.4.1.1 Estimation of input variables using remote sensing data

The primary driver of streamflow is rainfall (Tang et al., 2009), and is a highly important meteorological variable, which intimately affects terrestrial living conditions (Huffman et al., 2010). This importance is mainly attributed to the amount and rate of rainfall, which can lead to the potentially disastrous situations like droughts and floods. Streamflow amount at a given time is determined by the spatiotemporal variation of rainfall. Therefore, it is important to know the magnitude and spatiotemporal variation of rainfall to quantify streamflow. Whilst rainfall can be measured using a physical gauge, the existing rain gauge network is not sufficient to address the spatial variability of rainfall in many areas (Huffman et al., 2007; Tang et al., 2009; Huffman et al., 2010).

Other than rainfall, evapotranspiration and landuse/landcover also play important roles in determining streamflow. Evapotranspiration, as the second largest component of the water cycle (Chow et al., 1988), removes significant amounts of water from a catchment. Therefore, the consideration of evapotranspiration in streamflow estimation is essential for the accuracy of such estimation. Because direct measurements of evapotranspiration are not available for streamflow estimation, water lost by evapotranspiration has been estimated using a number of indirect methods. These methods use several meteorological variables, and data for those variables are often not readily available. Therefore, similar to the case of precipitation estimation using RS data, attempts have also been made to estimate evapotranspiration using RS data.

Landuse/landcover in a catchment influences evapotranspiration directly, and soil moisture indirectly. Therefore, the use of accurate landuse/landcover information in streamflow estimation is very important, and RS data have become particularly advantageous in gathering landuse/landcover when traditional mapping techniques such as topo sheets are not available or are not convenient.

In summary, the rapid development of the field of RS has empowered the estimation of precipitation, evapotranspiration and landuse/landcover through the use of both active and passive RS data. In that regard, the relevant literature for estimating precipitation, evapotranspiration and landuse/landcover with RS will be investigated in Sections 2.4.1.2, 2.4.1.3 and 2.4.1.4 respectively.

2.4.1.2 Rainfall estimation using remote sensing data

Since the first dataset was received from the Television and Infrared Observation Satellite (TIROS-1) soon after its launch on 1 April 1960, RS data have been used to understand cloud properties and to measure the cloud fraction (Arking and Childs, 1985) which are both important in the rainfall process. During the last three decades, satellite sensors have become more advanced when compared to the rudimentary sensors of TIROS-1. These advanced sensors are used to collect an enormous amount of data on the land, in the atmosphere and over the sea. Most of these sensors are specially designed to acquire reflectance and radiance data in the visible, infrared, thermal and passive microwave regions of the electromagnetic spectrum. Due to the variety of sensors, these data can represent different features of the atmosphere and clouds in various temporal, spatial, spectral and radiometric resolutions. The use of these data to estimate rainfall is one of the oldest applications, and still represents a leading research area in RS (Michaelides et al., 2009).

(a) Use of visible and thermal remote sensing data for rainfall estimation

Initial geostationary satellite sensors were only capable of acquiring data through the visible and thermal windows of the electromagnetic spectrum. As such, algorithms which were used to estimate rainfall before the 1980s were mostly based on these data (Barrett, 1970; Barrett, 1973; Scofield and Oliver, 1977; Arkin, 1979). Many of these algorithms were based on the cloud indexing method, and were written as:

$$R = \sum_{i=0}^i (r_i \times f_i) \quad (2.1)$$

where, r_i is the rain rate assigned to the cloud type, f_i is the fraction of time of a given point covered with cloud and R is the total rain at a given point.

Cloud fraction was estimated using geostationary satellite images and rain rate was decided based on the possible maximum rainfall per hour. Whilst the assumption that all clouds over a given area contribute equally to rainfall weakens this estimation, these algorithms are still in use even though they need to be calibrated locally. Later, Arking and Childs (1985) used visible and thermal data available from the National Oceanic and

Atmospheric Administration (NOAA) Advanced Very High Resolution Radiometer (AVHRR) sensor (i.e. NOAA AVHRR) to extract cloud parameters. They extracted cloud fraction, optical thickness of the clouds, cloud top temperature and microphysical parameters (i.e. size and shape of cloud particles) from the NOAA AVHRR data. These parameters were used to understand basic elements of cloud climatology, and could be used as inputs to rainfall estimation models. In the recent past, Levizzani et al. (2007) have explained in detail the use of such parameters in rainfall estimation using RS data.

Arkin and Meisner (1987) used thermal data from the GOES satellite over the northern hemisphere to investigate the relationship between large scale convective rains and cold clouds. They introduced a different scale to Equation (2.1) by replacing cloud fraction with cloud-top temperature threshold. They found that the cloud-top temperature threshold depends on the latitude of the location, since a slightly different relation between convective rains and cold clouds was noted with the latitudinal change of location. A year later, Adler and Negri (1988) used the same satellite sensor data to estimate tropical convective and stratiform rainfall. They highlighted a number of rainfall estimation methods, and proposed the Convective Stratiform Technique (CST) to estimate rainfall using visible and thermal RS data. In this technique, the amount of rainfall in a given cloud is quantified as a function of the minimum brightness temperature of the cloud. They found that their method of estimating rainfall had the highest accuracy when compared to contemporary methods.

Ba and Gruber (2001b) used a different approach to estimate rainfall using the visible and thermal data of the GOES satellite. Initially, they used thermal data to identify rainy clouds from non-rainy clouds based on the temperature gradient method introduced by Adler and Negri (1988). Second, they introduced a rain probability function for rainy clouds, based on the cloud top temperature to estimate amount of rainfall. They concluded that the probability function based algorithm of rainfall estimation showed a higher accuracy in daily and monthly rain estimation. Moreover they emphasised that although this method is capable of estimating daily and monthly rainfall accurately, the accuracy of extreme rainfall events in small areas are poor.

An artificial neural networks (ANN) model has been used by Grimes et al. (2003) to estimate rainfall over Africa with the Cold Cloud Duration (CCD) technique. They used

METEOSAT thermal data to estimate CCD, and then used estimated CCD and numerical weather model analysis data as inputs to the ANN model. In their study, they observed that the ANN model approach gave a slightly better rainfall estimate than the standard CCD technique (i.e. assigning a constant rain rate for cloud duration). Furthermore, Grimes et al. (2003) highlighted that the accuracy improved significantly for higher rainfalls, thereby benefitting to hydrological modelling applications.

All of the above mentioned methods of estimating rainfall are based on visible and thermal data of polar orbital and geostationary satellites, and these data have certain advantages. They are easy to handle and are freely available most of the time. These data are usually available in sub-daily intervals, and as such continuous information on cloud systems can be collected (Adler and Negri, 1988). However, there are some disadvantages involved with using visible and thermal RS data to estimate rainfall. The main disadvantage is the lack of accuracy of rainfall, thereby limiting further applications. Furthermore, most of these data are based on geostationary satellites. Therefore the spatial resolution of these data is significantly lower than polar orbital satellite data, thereby causing problems in capturing localized rain events using geostationary satellites. These geostationary satellites cover most of the area in tropical regions but are less useful in Polar Regions. Despite these weaknesses, visible and thermal data are still used to estimate rainfall, mainly because of the better spatiotemporal coverage.

Some of the disadvantages of visible and thermal data have been addressed through the bispectral technique of rainfall estimation introduced by Dittberner and Vonder Haar (1973). Clouds which are brighter in visible images were combined with clouds which are colder for better accuracy since they have a greater tendency to rain than dark and warm clouds. However, rain estimates with methods that only used cloud-top variables poorly represent the underlying rain amount, so that research has predominantly focused on the use of different frequencies of the electromagnetic spectrum which have cloud penetration abilities.

(b) Use of microwave data for rainfall estimation

Both passive microwave (most commonly known as microwave) and active microwave (most commonly known as radar) data have been used in estimation of rainfall. These data can be used to address some of above mentioned disadvantages of visible and thermal data. Microwave frequencies are capable of penetrating clouds, therefore, they are able to give information on the internal structure of the cloud. Since clouds' internal processes have direct influence on the rainfall process and its magnitude, the use of microwave data provides a significant advancement in rainfall estimation compared to the use of visible and thermal data (Michaelides et al., 2009). Additionally, microwave data can penetrate through haze and smoke which visible and thermal waves are incapable of doing (Lillesand and Kiefer, 1999).

Nonetheless, the estimation of rainfall using microwave is a complicated process. At first, microwave based temperature is used to separate water bodies and land surfaces from cloud cover. Then, the known rain rate is assigned to a cloud temperature which is based on the microwave data (Pierce, 2008). Moreover, microwave scatters and absorbs in the presence of rain/ice drops. Both the scattering and absorption rates increase with the frequency of microwave data and rain rate. These features are employed to estimate precise rainfall amounts.

Lovejoy and Austin (1980) introduced a rainfall estimation algorithm with microwave data using both absorption and scattering, and explained the advantages and disadvantages of this approach in details. In their study, they stressed the fact that the separation of cloud water from rainwater was difficult, and that the use of only one emissivity factor over such a large area weakened the results.

Recently more efficient algorithms for estimating rainfall using microwave data were introduced by Kummerow et al. (2001), Weng et al. (2003), and Kummerow et al. (2007). These algorithms have been drawn from the initial work of Mugnai et al. (1993) who introduced statistical physical algorithms to estimate rainfall with microwave data. This was the foundation of an algorithm used to estimate rain with TRMM Microwave Imager (TMI). The basic function of this algorithm was written as (Kummerow et al., 2001):

$$P(R|BT) = P(R) \times P(BT|R) \quad (2.2)$$

where, $P(R|BT)$ is the probability of a particular rain profile in a given BT (brightness temperature), $P(R)$ is the probability of observing R rain profile, $P(BT|R)$ is the probability of observing the BT vector. The accuracy of this model to estimate rainfall was found to be quite high. However, it was also argued that the model should be optimized separately for different satellite sensors (Kummerow et al., 2001).

As mentioned in the earlier part of this section, high frequency microwave data yield higher accuracy in rainfall estimation than low frequency microwave data (Michaelides et al., 2009). TRMM TMI sensor is sensible for high frequency microwave data, and provides fundamental information to estimate rainfall globally. Even though they are good in providing necessary information to estimate rainfall, they still cause issues in some areas of application. The main issue relates to the noise of data created with emissivity uncertainties over mixed areas (land and water bodies) such as coastal regions. These disadvantages paved the way to explore radar as an alternative method for rainfall estimation.

The use of radar data for rainfall estimation has a long history. Initially, ground based radar was used to forecast, monitor and estimate rainfall. However, ground radar has limited coverage due to terrain undulations. Other than that, installing, managing and maintaining a ground radar system (i.e. hardware, software and skilled labor) is very expensive. These disadvantages are significantly hampered on its applicability and usefulness. Some of these disadvantages were overcome by satellite based radar sensor which is attached to TRMM satellite (Kummerow et al., 1988).

TRMM satellite is a platform to a precipitation radar sensor (Pierce, 2008). This sensor opened a new avenue in rainfall estimation using satellite data. According to Michaelides et al. (2009) different algorithms were quickly developed to serve rainfall estimation with radar data, and a platform was made available to evaluate all other rainfall satellite products. However, this data only covered a narrow swath, and data were limited to 35°N and 35°S latitudes.

(c) Use of combined data for rainfall estimation

The availability of wide varieties of RS data which represent different features of the rainfall process suggests that a combination of different varieties of data could give a better result in the estimation process. Early foundations were laid in this regard by Arkin (1979), who combined visible data and radar data to estimate rainfall. Later, many studies, were introduced using multispectral RS data to estimate rainfall (Arking and Childs, 1985; Huffman et al., 1995; Huffman et al., 1997; Sorooshian et al., 2000; Ba and Gruber, 2001b; Huffman et al., 2001; Weng et al., 2003).

Amongst the products that use combined data to estimate rainfall, the Climate Prediction Center's morphing technique (CMORPH) product (Joyce et al., 2004), the Tropical Rainfall Measuring Mission (TRMM) Multisatellite Precipitation Analysis (TMPA) near real time products (Huffman et al., 2007), and the Precipitation Estimation from Remotely Sensed Information using Artificial Neural Networks (PERSIANN) (Sorooshian et al., 2000) are the dominant ones. These products are almost identical to the spatiotemporal resolution and are used as input data to generate rain rates with different algorithms. The ability of these products to predict streamflow has been investigated by Bitew et al. (2011) who applied them to the MIKE SHE model. The latter researchers concluded that TMPA data outperformed PERSIANN and CMORPH data in this application.

The availability of TRMM data made a breakthrough by combining precipitation estimation, with visible, thermal, microwave as well as radar sensors. Since then, numerous studies have used TRMM data to estimate streamflow (Collischonn et al., 2008; Su et al., 2010; Bitew et al., 2011; Chen et al., 2011; Li et al., 2012; Wang et al., 2014), and hence obtained various levels of accuracy. Better results have been obtained in yearly and monthly time scales than in daily streamflow estimation. In these studies, it was concluded that TRMM data are not comparable to ground measured rainfall in small to medium catchments on a daily basis.

2.4.1.3 Evapotranspiration estimation using remote sensing data

Evapotranspiration is a combined term for evaporation which is the direct removal of water from open water bodies, soil and vegetation surfaces in the form of vapour, and transpiration through vegetation. The above processes are very difficult to quantify

separately, and as such they are collectively called evapotranspiration (ET). Energy supply, vapour transport and water availability (open water source or soil moisture) affect the rate of ET (Chow et al., 1988). The energy available, the carrying capacity of air (Bastiaanssen et al., 1998a; Su, 2002) and the amount of soil moisture control transpiration, and as such control ET (Biggs et al., 2008).

ET is the second largest component of the terrestrial water balance. Water that is removed in the process of ET contributes to atmospheric water vapour and cloud formation. These clouds precipitate on the same or different areas. In this way, ET plays an important role in the water balance and in the energy cycle for the maintenance of maintain the atmospheric temperature. Knowledge of ET is essential for policy makers and managers to make out decisions, and conduct technical and management tasks such as watershed management and hydrological modelling, irrigation scheduling, and weather forecasting. Moreover, this knowledge is important to understand the long term effect of landuse/landcover changes and the effect of climate change on catchment water budget (Glenn et al., 2007). In brief, the quantification of ET is essential for better management of water resources.

The quantification of ET has been undertaken in two ways. First, ET has been derived from a range of measurement systems including lysimeter, eddy covariance, Bowen ratio, water balance (gravimetric, neutron meter, other soil water sensing), sap flow and scintillometer. Second, ET has been estimated through the use of modelling techniques with hydrometeorological variables as inputs (Allen et al., 2011). The Lysimeter method is the oldest and the most direct method of deriving ET from measurement systems. In this method, ET is calculated as a residual of the water balance equation. However, the available number of lysimeters is not sufficient for the water management decision making process. Moreover, many of these lysimeters are located within cropping areas, and thus do not represent other LULCs within a catchment. In general, this situation is common to all methods that derive ET through measurement systems. The second is the modelling techniques, and this included catchment water balance, hydrometeorological equations and the energy balance method.

Several modelling techniques have been developed in the absence of derived ET from measurement systems (Thornthwaite, 1948; Penman, 1948; Monteith, 1965; Priestley and Taylor, 1972). Thornthwaite (1948) explained a way to estimate potential

evapotranspiration (i.e. the maximum amount of water removed as a result of ET, when there is no limitation to water availability) using surface temperature as input data. Potential evapotranspiration (PET) was computed as a function of monthly average temperature. Later various correction factors were introduced to Thornthwaite's method to improve the accuracy of estimates (Willmott et al., 1985; Camargo et al., 1999; Pereira and Pruitt, 2004). However, the Thornthwaite's method does not account for the thermodynamic effect. As such, the accuracy of PET remains low when compared to other methods such as the Penman-Monteith and the Priestley-Taylor methods (PT) (Malek, 1987). Moreover, the Thornthwaite's method estimates PET on a monthly basis. Thus, this information is insufficient to make decisions in certain applications like irrigation scheduling.

The above mentioned disadvantages are partially addressed by the Penman ET estimation method (Penman, 1948). The Penman ET estimation method which is essentially based on the energy used to evaporate water, was further enhanced by introducing the 'advection effect' into the process (Monteith, 1965). The Penman-Monteith (PM) formula is a combination of both the energy term and this advection term, and is widely used in PET estimation (Allen et al., 1998). In addition, Priestley and Taylor (1972) introduced a simplified ET estimation procedure over uniform wet surfaces. Considering that dry air moving over a uniform wet surface comes to a level of equilibrium, they simplified the energy balance by inserting a constant.

The above discussed methods are based on several meteorological variables. However, many catchments do not have sufficient ground measured data to estimate PET. Whilst heterogeneity of the surface vegetation makes estimation of ET difficult, partial canopies create further problems. Su (2002) highlighted that PET estimation procedures such as PM and PT estimate PET accurately over homogenous small areas. Nevertheless, the accuracy of estimates are reduced as the area becomes larger, in which case PET estimation procedures become insensitive due to the lack of representative hydrometeorological variables.

Over large areas, RS based ET estimation has numerous advantages (Bastiaanssen and Chandrapala, 2003; Bandara, 2003; Bos, 2004; Ahmad et al., 2005). RS gives a better representation of the ground heterogeneity, and its temporal changes. The accessibility and

the quality of RS data are superior compared with ground measured data, and data are available to the research community on a near-real time basis. Additionally, RS data are available at zero or minimum costs. In the light of all these advantages, Bastiaanssen et al. (1998a) and Su (2002) advocated the use of surface energy balance based ET estimation method with RS data as inputs as an alternative to the above mentioned estimation methods.

The Surface Energy Balance Algorithm for Land (SEBAL) method which was proposed by Bastiaanssen et al. (1998a), uses the surface energy balance equation to estimate ET. In this method, ET is calculated as the residual of the difference between the net radiation to the surface and losses due to the ground heat flux (energy stored in the soil and vegetation) and the sensible heat flux (energy used to heat the air) (Senay et al., 2007b).

The net radiation of the above method is the difference between incoming and outgoing radiation, and RS based surface albedo and emissivity are used as inputs to calculate it. The ground heat flux is estimated using surface temperature, albedo, and *NDVI*. The sensible heat flux is estimated as a function of the temperature gradient above the surface. Surface roughness and wind speed are required for this, and surface roughness is calculated as a function of the *NDVI* in SEBAL (Bastiaanssen et al., 2002; Bastiaanssen and Chandrapala, 2003; Ahmad et al., 2005; Ahmad et al., 2009; Gamage et al., 2009a). The Surface Energy Balance Systems (SEBS) method (Su, 2002) also used the surface energy balance equation to estimate ET. This method uses the same inputs computed from RS data as the SEBAL. However, SEBS uses a numerical simulation model to estimate ET, instead of SEBAL's *hot* and *cold* pixel approach.

The Surface energy balance method used in SEBAL and SEBS was further simplified by Senay et al. (2007b) with their proposed methodology of Simplified Surface Energy Balance (SSEB). They introduced the *fraction of surface temperature* instead of the *hot* and *cold* pixel approach of SEBAL and the numerical simulation approach of SEBS.

Initially, evapotranspiration computed from the surface energy balance method was used to calculate water efficiency, agricultural water requirement (Ahmad et al., 2009), and water resources assessment (Muthuwatta et al., 2010). These calculations require computing daily, monthly and annual ET values. However, non-cloudy RS images are

essential to estimate ET using the above described methods. Therefore, calculating ET continually on a daily basis is virtually impossible. This has slightly been overcome to a certain extent in monthly and annual estimation of ET by introducing a temporal integration mechanism (Ahmad et al., 2009). Temporally integrated ET can be used in water resources assessments and planning, but not for daily streamflow estimation purposes.

The above mentioned RS based ET estimation methods require a few ground measured meteorological data, with wind speed being the most important input. Unfortunately, obtaining wind speed data in data scarce catchments represent a challenging if not impossible task. Therefore, a method is proposed in this study to estimate PET, and then use it for streamflow estimation. The surface energy balance method has been modified under the proposed method, so that minimum ground measured data and maximum RS data are used.

2.4.1.4 Landuse/landcover classification

Since the early stages of remote sensing, RS data have been used to categorize landuse/landcover (LULC) classes (i.e. LULC classification or thematic mapping). Later, the digitally acquired data from space borne RS (satellites) opened a new era of LULC classification. The ability to acquire data more frequently, high spatial resolution, easy access and low costs collectively make the use of RS data for LULC classification purpose a popular option. Currently, LULC classification is the most common application of RS data (Foody, 2002).

Basically, classification is done by grouping pixels that have the same spectral signature (or *pattern*) in a single or multiple bands (Bastiaanssen, 1998; Lillesand and Kiefer, 1999). This pixel grouping has been done through two main approaches; unsupervised classification and supervised classification. Unsupervised classification is defined as a categorization of pixels in RS data solely based on the statistics of that RS data without considering training samples or a priori knowledge of the area. In this classification approach, a statistical algorithm (i.e. unsupervised classification algorithm) is used to make clusters of pixels that have the same spectral signature. Implementing an unsupervised classification on an image is a fairly simple task which is handled by a

computer with less user intervention. However, this can lead to a reduction in the accuracy of the classification. Moreover, some of the classes under this approach may not be equivalent to the actual classes (Hasmadi et al., 2009), thereby lowering the accuracy of LULC results (Kiptala et al., 2013).

The supervised classification is defined as the procedure of identifying spectrally similar areas on an RS data by identifying 'training' sites of known targets (i.e. LULCs) and then extrapolating those spectral signatures to other areas of unknown targets (Lillesand and Kiefer, 1999). The supervised classification approach has been more widely used compared with the unsupervised classification approach (Bastiaanssen, 1998), mainly because of the better level of control of the LULC classification process by the user. Indeed, the number of classes is controlled in supervised classification, and is based on a meaningful representation of ground based LULC classes.

According to Lillesand and Kiefer (1999) the process of supervised classification can be summarized into three stages namely the:

1. Training stage: The main objective of this stage is to identify the signatures of RS data relevant to existing LULC classes within the interested area (i.e. the study area in this study). This can be achieved in two ways. One way is to use prior knowledge of the LULC classes of the study area. The other way is to carry out a *ground-truth* data survey to identify existing or existed LULC classes in the study area (Foody and Mathur, 2004). Ground-truth data is a representative sample (homogeneous) of a particular LULC class in the study area. A portion of this ground-truth data is used to *train* the images for appropriate LULC classes. Compared to the total image, training samples cover a small portion of the image, but they are chosen well to represent all LULC classes. These small portions of the image are called training sets (Gamage et al., 2007).
2. Classification stage: Categorizing all the pixels in the image into relevant LULC classes using the signatures that were identified during the training stage is the main task of the classification stage. In order to achieve this task, training sets, and a parametric rule/classifier are used. A number of parametric rules have been introduced to serve this purpose such as the maximum likelihood classifier, the

minimum distance to mean classifier and the parallelepiped classifier. Each pixel of the RS image is assigned an LULC class at the end of this stage (Joseph, 2005).

3. Output stage: The classified image is presented as a map, graph or table at this stage. In addition to that, some of the ground truth-data that were not used to train the image are instead used to calculate classification accuracy. Both descriptive and analytical techniques (Congalton, 1991; Thomlinson et al., 1999; Smits et al., 1999; Foody, 2002) are used in this stage to verify the accuracy of image classification. Once the accuracy assessment is satisfactory, the classified, data are ready to be used for other applications such as urban, agricultural, hydrological and forestry.

Compared with the unsupervised classification approach, supervised classification is advantageous in that it yields more accurate results. Nonetheless, the finalization of the LULC map is a costly process because of heavy user involvement.

Other than the above mentioned two approaches, Lillesand and Kiefer (1999) further reported that a hybrid classification approach is also available. This is a combination of supervised and unsupervised approaches. Initially, the unsupervised classification approach is used to understand the image signature, and later supervised classification is used to improve the accuracy of the classified map. Gamage et al. (2007) used a similar approach to acquire LULC information over small heterogeneous farmlands in Pakistan, and have obtained a high level of accuracy in the classification.

Various satellite sensor data have been used with the previous approaches (i.e. supervised and unsupervised) to classify LULC on various scales ranging from field to global levels. The scale of the application is determined by the sensor's characteristics in terms of spatial resolution, which in turn determines the LULC level of classification. Amongst available sensor data, feature the NOAA AVHRR sensor data, which are characterized by 1 km spatial resolution and which have been widely used at the global scale for LULC classification purposes (De Fries et al., 1998; Loveland et al., 2000). Thenkabail et al. (2008) used various AVHRR products and some other sensor data such as Landsat and IRS data. However, these classifications are undertaken at the global scale and the complexity involved with such a scale always reduces the accuracy of the maps irrespective of the quality of RS data. Furthermore, since collecting ground truth data to

represent all LULC classes is not practical, Thenkabail et al. (2008) used unsupervised classification, which in turn reduced the accuracy of such maps.

Thenkabail et al. (2005) used MODIS sensor data to develop an irrigated area map for the Ganges and Indus River catchments. They used a time series of MOD09 (i.e. a product of MODIS data which has a spatial resolution of 500 m) from 2001 to 2002 to classify LULC. In a separate study, Gamage et al. (2007) used Landsat ETM+ data at a field scale (in irrigated command areas) to make an LULC map. These maps have been used to detect seasonal changes of crops and cropping areas on a field scale.

An output map of such classifications has often been used as input variable for streamflow estimation models. Boegh et al. (2004) used Landsat TM data to classify LULC information, and used the resulting LULC information as an input to the MIKE SHE model. They used this information to investigate the relationship of vegetation with soil moisture availability and ET. Campo et al. (2006) used Landsat ETM+ data to create an LULC map over the Arno River catchment in Italy. They used the supervised classification approach to make the LULC map and obtained 49% of overall accuracy in their classification, which is less than the accepted level of accuracy. Indeed, the generally accepted accuracy is 70% for an individual class and 85% for the overall classification (Thomlinson et al., 1999). This LULC information was used in the BOBIDEC model (Campo et al., 2006), which is a distributed raster based model to estimate streamflows. In a separate study, Tibebe and Bewket (2011) used Landsat TM data to classify LULC information with the supervised classification approach. This study took place in the Awash catchment in Ethiopia, and RS based LULC information was used as input to a SWAT model to simulate surface runoff and to estimate soil erosion. He et al. (2008) used RS data to identify the dynamic change of LULC for the period of 1986 to 2000. They introduced this information to a SWAT model to examine the effect of LULC changes on surface runoff generation.

In most of the streamflow estimation applications, the RS based LULC has been used as a “one time” input variable since the change of LULC is much slower than the change in other meteorological variables such as rainfall and evapotranspiration. In some cases, LULC has been used as a dynamic variable in streamflow estimation, especially when

determining the effect of LULC changes in surface runoff generation, soil erosion estimation (Tibebe and Bewket, 2011) and groundwater recharge.

Various other satellite data such as SPOT, IRS, IKANOS and Quickbird have been also used for LULC classification purposes in various applications. The lack of LULC information has an adverse impact on any hydrological modelling, and the literature shows that RS data can be used in different scales to acquire LULC information. The LULC classifications in other studies have been derived for special purposes and have yielded different levels of accuracies. Considering prior studies, an attempt is made in this study to acquire LULC information for medium size catchments that have homogeneous and heterogeneous LULC classes.

2.4.2 Use of statistical models

Statistical models are categorized as empirical models under the model classification hierarchy proposed by Refsgaard (1996). They are developed without consideration to the physical processes that are associated with catchment streamflow generation. Therefore, model building, calibration and validation are less complex in statistical modelling than in catchment process modelling. However, these models do not consist of logical relationships between model inputs (meteorological and catchment variables/parameters) and output (streamflow) (Refsgaard, 1996).

Refsgaard (1996) further categorized empirical models into three types, namely the empirical-hydrological methods, the statistically based methods and the hydroinformatics based methods. A best known empirical-hydrological method is the unit hydrograph which is widely used for streamflow routing. Statistically based methods rely on traditional statistical methods, and according to Refsgaard (1996) these statistical methods are more advanced than the empirical-hydrological methods. It is highlighted that a time series analysis of the Autoregressive Integrated Moving Average (ARIMA), and Constrained Linear Systems (CLS), the gauge to gauge correlation, the Antecedent Precipitation Index (API) are all examples of methods that have been used in streamflow estimation under this category. According to Refsgaard (1996), hydroinformatics based methods are based on transfer function models, and are generally new and emerging. Artificial Neural Networks (ANN) represents one such type of modelling. It should, however, be noted that ANN have

travelled a long way since Refsgaard's comment, and are now well established in numerous hydrological applications (Maier et al., 2010). Most of the above mentioned techniques are based on regression (linear/nonlinear), and as such some of them will be discussed in this chapter considering the regression function of the models.

A review of the literature reveals that many studies have used regression analysis to estimate streamflow. For example, Bonne (1971) used a multiple regression model (multiple inputs) to estimate monthly streamflow using different independent variables such as the previous month's streamflow, the present month's precipitation, antecedent monthly precipitation and accumulated precipitation over several previous months. In this study, Bonne found that a multiple regression model performed better than several simple regression models (single input) in streamflow simulation with improvements being noted in the coefficient of determination. This early study clearly highlighted the complex relationship between variables and streamflow even within a monthly timescale, and consequently, this early work has been followed by many researchers as a base while estimating streamflow with regression modelling.

Zhu and Day (2009) used regression modelling to estimate total streamflow, base flow and storm runoff for water resources planning and management purposes. They used meteorological data as well as basin geomorphological, geological, soil and climatic characteristics that were estimated using geographic information systems as inputs to this modelling. They obtained a coefficient of determination of more than 0.94 in all models that were tested. It was concluded that such simple models are vitally important in water resources planning and management process since policy makers are not specialized in water related disciplines.

Many others used regression modelling to estimate streamflow (Brandes et al., 2005; Liang and Song, 2009; Lima and Lall, 2010). Of these studies, Lima and Lall (2010) used a periodic autoregression model to forecast monthly streamflow for the use of reservoir operations. They applied large scale climatic information such as sea surface temperature to forecast streamflows up to three months in the future, and have consistently obtained better results than simple linear regression models. However, they observed that the model's performance improved as they moved to large scale catchments, but applications to medium and small catchments were not promising as for the large catchments.

In addition to estimating streamflow, regression modelling has widely been used to investigate the effects of LULC changes on streamflow (Krishnaswamy et al., 2012; Wine and Zou, 2012; Yan et al., 2013a; Tran and O'Neill, 2013), and the impact of climate change on streamflow (Jiang et al., 2011; Yan et al., 2013b; Ahn and Merwade, 2014). However, all of the aforementioned studies have used ground measured meteorological data as inputs for regression models. Instead of the traditional input variables such as rainfall and surface temperature, which are scarce in some parts of the world, some academics have used RS based inputs with regression models to estimate streamflows.

Weissling and Xie (2009) used RS based indices (i.e. land surface temperature, vegetation indices, water stress index) and Next Generation Weather Radar system (NEXRAD) precipitation data to estimate the 8-day mean streamflow of a catchment in south central Texas in USA. They used a stepwise multiple linear regression model to estimate streamflow for the period running from 2001 to 2007. MODIS satellite data were used to calculate RS based indices on every 8-day, and such indices were then used in regression modelling. They observed the non-linearity of streamflow and RS based indices, and therefore used data transformations to transform input data to a suitable format for use in regression modelling. The ability of RS indices to detect soil moisture has been highlighted by the authors while claiming that more accurate NEXRAD precipitation could have improved the performance of streamflow estimation.

Fitch et al. (2010) used vegetation data computed using MODIS reflectance data to estimate hydrological response variables such as streamflow and ET. They used *NDVI*, the Leaf Area Index (*LAI*), the fraction of Photosynthetically Active Radiation (*fPAR*) and the Net Primary Production (*NPP*) as vegetation indices (independent variables) to estimate hydrological response variables using linear regression models. They tested a number of catchments in California (USA) for the period of 2001 to 2005, and found weaker to moderate performance in streamflow estimation. They concluded that the relationship between vegetation and streamflow, which is dependent on the ability of the ecosystem to transfer water from the soil to the atmosphere, can be represented by vegetation indices in the hydrological modelling process. However, they have not used any representative index of the water content of the vegetation. Furthermore, they concluded that the above method can be used to identify hydrologically similar catchments.

Most of the above examples are based on regression modelling. More recently Artificial Neural Networks (ANN) have gained popularity in hydrological applications (Maier et al., 2010), because of their ability to treat complex and non-linear problems. These ANN models have been used for streamflow estimation in gauged and ungauged catchments, streamflow forecasting, and regionalization (Lima and Lall, 2010; Rizzo et al., 2010; Samuel et al., 2011; Gamage et al., 2011a).

2.4.2.1 Artificial Neural Networks applications on streamflow estimation

The Artificial Neural Networks is an information processing system which resembles the structure and operation of the brain (Samarasinghe, 2006; Maier et al., 2010). The ANN modelling approach was initially developed by McCulloch and Pitts (1943), and later used in a variety of applications due to its power of addressing the relationships between a number of input variables to a single or multiple output (Morid et al., 2007). The ASCE Task Committee on Application of Artificial Neural Networks in Hydrology (2000) highlighted that with the availability of sufficient data, ANN can be used to model any relationship between a series of independent and dependent variables.

The ASCE Task Committee on Application of Artificial Neural Networks in Hydrology (2000) and many other studies have highlighted some of the following important advantages of ANN in water-related applications:

- ANN is suitable for dynamic flow forecasting because the weights associated with the input data can be updated when fresh observations are made available.
- ANN does not require any exogenous input other than a set of input–output vectors for training purposes (Thirumalaiah and Deo, 1998) since, like a human brain it is able to recognize the relationship between the input and output variables without explicit physical consideration (Haykin, 1999; ASCE Task Committee on Application of Artificial Neural Networks in Hydrology, 2000).
- ANN works well even when the training data sets are of poor quality and/or in the presence of missing data in limited number of inputs (Lee et al., 2003; Sudheer et al., 2003). In addition to the all above, ANN is easy to handle once it is trained (ASCE Task Committee on Application of Artificial Neural Networks in Hydrology, 2000).

- The ANN model can fully define its intermediate relationships without the operator's interference (Tran et al., 2009).

The ANN modelling technique has been designed by examining the way the human brain processes information through a network of neurons that connect together (Samarasinghe, 2006). The basic structure of ANN modelling has been explained by Minnas and Hall (1996), Samarasinghe (2006), Sahoo and Ray (2006), and Barua (2010). Additionally, the ANN modelling mechanism, the model architecture, model selection, input selection and model development is well documented in Maier et al. (2010).

A comprehensive description of ANN modelling applications in water resources have been given by many academics (Maier and Dandy, 2000; Bowden et al., 2005a; Bowden et al., 2005b; Maier et al., 2010). According to the latter, ANN has been used for streamflow estimation, streamflow forecasting, water quality modelling, drought and flood analysis and many more. A list of ANN applications to surface water for the period of 1999 to 2007 is tabled by Maier et al. (2010). In this paper, it was stressed that 90% of ANN applications on surface water pertain to the quantification of streamflows.

Sahoo and Ray (2006) discussed in detail the application of ANN models in streamflow forecasting, and highlighted that streamflow forecasting has been done with different architectures of ANN models and different input variables. They successfully used an ANN model to forecast streamflow in the Waiakeakua and Manoa Streams in Hawaii. Yilmaz et al. (2011) used an ANN model to estimate streamflow in the Karasu Basin located in eastern Turkey, and obtained high accuracy in estimating streamflow. They also mentioned that seasonal models performed better than a single model across all seasons.

In an earlier study, Minnas and Hall (1996) found that a single ANN model did not properly represent the estimation process because streamflow is a combination of extreme and normal events. This was further investigated by Wang et al. (2006) by applying a Divide and Conquer (DAC) based ANN model to estimate daily streamflow. They introduced DAC to the ANN model by categorizing streamflow into high and low flows, and, then described different ANN models to estimate high and low flows separately. The results from these different ANN models were then combined to produce a time series of streamflow for the total period. They found that this approach gave substantially better

results in streamflows compared to a single model dealing with extreme and normal events.

Sharma and Tiwari (2009) used various catchment variables, which are based on topographical, meteorological, soil, geomorphological and vegetation, to estimate runoff in the Upper Demodar Valley catchment – India, by employing an ANN model. They considered 39 variables, and used Principal Component Analysis (PCA) method to reduce data redundancy, and finally selected 10 variables from the initial set of variables. From this list, they found that monthly rainfall, slope, coarse sand, bifurcation ratio and *NDVI* gave the best results in estimating monthly runoff. They also found that increasing the number of variables did not improve the accuracy of the estimates.

At this juncture, it should be highlighted that, at the time of this study, no literature was available on the use of RS based input variables such as vegetation and thermal indices to estimate streamflow. This research gap will be subsequently investigated in this thesis.

2.4.2.2 Remote sensing based indices for streamflow estimation

Derivatives of RS data have been used as indicators of vegetation, water, soil, atmosphere and clouds. The use of RS based indices as indicators of biophysical properties of vegetation stemmed from the application of satellite data to civilian purposes (Jensen, 2000). Jackson (1983) emphasized several qualities that the vegetation index should have :“the index should be particularly sensitive to vegetative covers, insensitive to soil brightness, insensitive to soil color, little affected by atmospheric effects, environmental effects and solar illumination geometry and sensor viewing conditions”. Based on that, the reflectance value of visible, near infrared and mid infrared bands have been used as inputs to vegetation indices (Jensen, 2000).

Pearson and Miller (1972) developed the first two vegetation indices, which are the ‘Ratio Vegetation Index’ (RVI) and the ‘Vegetation Index Number’ (VIN). They are the band ratios of red and near infrared bands. They can be written as;

$$RVI = \frac{R}{NIR} \quad (2.3)$$

$$VIN = \frac{NIR}{R} \quad (2.4)$$

where R is the mean reflectance of the red band and NIR is the mean reflectance of the near infrared band. These indices were used to enhance contrast between land and vegetation, but they are very sensitive to the atmospheric effects.

Later, the Normalized Difference Vegetation Index ($NDVI$) was introduced by Tucker (1979), and quickly become the most commonly used vegetation index within the RS community (Kite and Pietroniro, 1996). It represents vegetation density, vigor, vegetation stage and seasonality (Jackson et al., 2004; Thenkabail et al., 2004). Furthermore, it has been used to estimate the Leaf Area Index (LAI). LAI is identified as the single most important variable for quantifying energy and mass exchange by plant canopies over landscapes (Running et al., 1986). Therefore, LAI has become a vital variable in hydrological process modelling. LAI has been widely used to generate ET information that are few into the catchment process models (Kite and Pietroniro, 1996; Andersen et al., 2002) for streamflow estimation. Since, the traditional method for calculating LAI is laborious (Kite and Pietroniro, 1996), many authors used $NDVI$ to calculate this vital information. As a representative index of vegetation, $NDVI$ has been used in various other applications such as LULC classification (Gamage et al., 2007), drought monitoring (Thenkabail et al., 2004), spatial downscaling of TRMM data (Immerzeel et al., 2009), soil moisture estimation (Wang et al., 2007; Schnur et al., 2010) and for understanding the seasonal dynamics of the canopy cover (de Silveira et al., 2007).

The inherent nonlinearity of ratio based indices (i.e. the index is not directly proportionate to the input) is the main disadvantage of the $NDVI$. In addition, this index is sensitive to additive noise effects such as atmospheric path radiances, and it exhibits scaling problems and saturated signals over high biomass conditions. Furthermore, it is very sensitive to canopy background variations with $NDVI$ degradation being particularly strong in case of high canopy background brightness (Huete, 1988). To address these disadvantages, Huete et al. (2002) introduced the Enhanced Vegetation Index (EVI) which has improved sensitivity in high biomass regions and improved vegetation monitoring through decoupling of the canopy background signal and a reduction in atmosphere influences.

EVI has been widely used in vegetation applications. Huete et al. (2006) used *EVI* to examine the vegetation growth of the Amazon forest during its dry season. *EVI* has also been used in *LAI* calculations as a substitute to *NDVI* in ET estimations (Ahmad et al., 2005). Guerschman et al. (2009) used monthly *EVI* and interpolated climate data as input variables to derive monthly actual ET estimates. The main advantage of this methodology which was facilitated by *EVI*, is that it required a single set of parameters. The *EVI* has been widely applied in many disciplines including in the calculation of Net Primary Production (Wu et al., 2011).

Both *EVI* and *NDVI* are good indices that represent vegetation greenness well, but they perform poorly in respect to vegetation water content (Jackson et al., 2004), which is a surrogate of soil moisture content. Therefore, Jackson et al. (2004) used the Normalized Difference Water Index (*NDWI*) (Gao, 1996) to map the vegetation water content over agricultural crops. They were able to successfully map the vegetation water content using *NDWI* over the period of 1 month which was their study period. This index was further examined by Weissling and Xie (2009) who used *NDWI* and other indices to estimate the 8-day mean streamflow in a Texas (USA) catchment. They tested 32 variables which are based on visible and thermal bands. Out of those 32 variables, they found that the deseasoned land surface moisture stress index, NEXRAD precipitation and the MODIS daytime land surface temperature are significantly related to streamflow. In this study, they also found a fair level of agreement between observed and estimated streamflow, and concluded that the estimation performances could have been improved by improving NEXRAD precipitation.

Other than vegetation indices, indices based on thermal bands were also used in vegetation and hydroclimatological applications. Visible, near infrared and mid infrared bands' reflectance values were directly used as inputs for the calculation of vegetation indices. However, the radiance values of thermal bands were converted into brightness temperature before they were used as inputs to thermal indices.

Brightness temperature (BT) has been directly used to estimate rainfall given its direct relationship with rainfall (Arkin, 1979; Arking and Childs, 1985; Arkin and Meisner, 1987). Furthermore, BT has been used to separate no-rain clouds from rain clouds (Ba and Gruber, 2001a; Kuligowski, 2002). For example, Kuligowski (2002) used brightness

temperature difference and brightness temperature gradient to conduct such separation. These indices indicate the presence of water vapor and textural information of the cloud top. These properties provide vital information needed to separate rain clouds from no-rain clouds. In addition to its cloud-related applications, BT has been widely used in ET estimation (Bastiaanssen et al., 1998b; Bastiaanssen et al., 2002), which were then used in water productivity investigations over large command areas (Gamage et al., 2009a).

The above mentioned thermal indices and BT based applications were initially restricted to the data acquired from meteorological satellites. However, such applications were made possible with sun synchronized satellites like NOAA AVHRR. Since NOAA AVHRR holds two thermal bands (band 4 and 5), it was possible to use BT difference as an index for rain/no rain cloud separation. This situation was further improved with the emergence of the MODIS satellite. MODIS introduces several other thermal bands in addition to the bands of NOAA AVHRR. Indeed, MODIS adds 14 new thermal bands in the range of 3.660 μm to 12.270 μm , which can be used in various applications such as surface and atmospheric temperature mapping, cirrus cloud identification and cloud top temperature estimation.

The literature described above has important implications for the hypothesis of this study: that remotely sensed indices (both vegetation and thermal) sufficiently represent the variation of hydrometeorological variables such as rainfall, evapotranspiration and soil moisture. However, sparse literature is available for using RS indices to estimate streamflow. This will be explored later in this study.

2.5 Summary

This chapter started by explaining the process of streamflow estimation, its history and classification of streamflow estimation models. It then proceeded to exploring the history of RS and discussing RS systems that are used to acquire data. Some satellites and sensors are also discussed. These satellites and their sensors were especially selected as they have been widely used in hydrological applications. Next, the chapter reviewed streamflow estimation with RS data. Under this section, both catchment process modelling and statistical modelling approaches were discussed in two separate sub sections. First the estimation of rainfall, evapotranspiration, and classification of LULC using RS data, which

are the most important inputs for catchment process modelling, were discussed under the sub section labelled catchment process modelling. Second the RS based vegetation and thermal indices that are surrogates of hydrometeorological variables were reviewed under the sub section labelled statistical modelling.

Different catchment process models that aim at estimating streamflow using RS based input variables as inputs were discussed in Section 2.4.1. The review showed that RS estimated inputs have been used in different spatiotemporal scales ranging from sub-daily to annual and micro catchments to mega catchments. The literature also showed that the accuracy of the estimation is higher in lower temporal resolution such as monthly and annually in large catchments. In contrast, the literature showed that results are not satisfactory when the same data were applied to medium or small catchments on finer temporal resolution (i.e. daily).

Rainfall estimation is the oldest application of RS data which is used in meteorological satellite data. Initial rainfall estimation was based on the cloud indexing technique using thermal infrared bands data. Later, this technique was modified by introducing a brightness temperature threshold for rainy clouds. However, the accuracy of the estimates were poor since brightness temperature only gave information relating to cloud-top. More accurate rainfall estimation processes were developed with microwave and radar RS data, which have the ability to penetrate clouds. However, rainfall estimates, which used microwave and radar, are low in spatial resolution, thus failing to address the variability of rainfall in medium and small catchments.

The estimation of potential evapotranspiration (PET) is another important variable, both in streamflow estimation as well as in agricultural applications. PET data can be derived using direct measurements such as the lysimeter or can be estimated using a modelling approach, which use meteorological variables as inputs. In the absence of direct measurements and meteorological variables, RS data have been used partially used as inputs to estimate PET. SEBAL and SEBS are examples of models that utilize RS data to estimate PET. However these estimations are limited to non-cloudy days.

RS data have been widely used in classifying LULC. The unsupervised and the supervised are the two main LULC classification approaches. The unsupervised classification is

simple but less accurate. In contrast, supervised classification is complex, but accurate and meaningful. It has three stages, and uses knowledge on the ground to classify LULC. LULC information has been applied in various hydrological models to assess the effect of LULC changes on streamflow generation, ground water discharge and climate change.

Various statistical models have also been used to estimate streamflow with meteorological variables. Recently, the Artificial Neural Networks models have gained popularity among various statistical models. They have also used meteorological variables as inputs to estimate streamflows. At the time of this writing, no literature was available on the use of RS based indices as inputs to estimate streamflow by employing ANN models.

The literature examined in this chapter shows some of the gaps in estimating rainfall, ET and LULC for streamflow estimation. In addition, it is clear that sparse literature is available on the application of RS based indices for streamflow estimation. Therefore, methodologies are proposed to overcome some of the gaps mentioned in this chapter. These methodologies will be discussed in Chapter 3.

CHAPTER 3: STUDY AREA, DATA AND METHODOLOGY

3.1 Introduction

This chapter presents the rationale for the selection and the consequent description of the two study areas, and the data that were used for these study areas. The chapter also includes a description of the methodologies that were used in this study.

3.2 Rationale for the selection of study areas

This study was made up of two case studies. First, suitable study area, which is rich with all required ground measured meteorological and streamflow data, was selected to enable the later investigation of streamflow estimation with RS data. In particular, the study was designed to test the accuracy and suitability of relevant RS data and to test the methodology used in estimating streamflow using RS data. The methodologies of the first case study were then used in the second case study, which deals with a study area where data availability is poor.

3.2.1 The first case study area

A data rich catchment site in Victoria (Australia) was selected as the first case study area. This catchment was selected on basis of several factors. It was considered that the selected catchment should be large enough to work with RS data, should have least or no streamflow regulation, should have least anthropogenic changes, and should have least agricultural use. These information was sought using the available water information from Water Resources Overview - Victoria (2009).

Agricultural areas in Victorian catchments are mostly irrigated and regulated with strict management practices. This is considered as a significant anthropogenic effect within the catchment, and therefore such catchments were not considered in the selection process. Information regarding all Victorian catchments, their areas, agricultural and non-agricultural areas as well as the percentage of non-agricultural areas are presented in Table A.1 of Appendix A.

Least streamflow regulation, least irrigated agriculture and minimum anthropogenic changes were the key selection criteria in the selection process. Based on these criteria, the East Gippsland catchment ranked as the most suitable one for the study. This catchment spans both New South Wales and Victoria, and consists of several smaller catchments, which are in Victoria. In some of these smaller subcatchments, ground measured meteorological and streamflow data are scarce (Water Resources Overview - Victoria, 2009). For this reason, the East Gippsland catchment was eliminated as a study area. As a consequence, the next ranked catchment, which is the Thomson catchment, was considered as being appropriate to carry out the first case study. At a finer detailed level, because the Macalister River of the Thomson catchment is not regulated before Glenmaggie Lake, the catchment area upstream of Glenmaggie Lake was selected as the first case study area.

3.2.2 The second case study area

In order to test the effectiveness of the use of RS data for streamflow estimation, a catchment area of considerable economic and human importance as the first case study area and with little or no ground monitoring stations, was selected as the second case study site. Although this catchment has some ground measured data, it was considered as a catchment with no ground measured data.

A sub catchment area located in the important Blue Nile catchment of northeast Africa (also known as Abbay in Ethiopia) was selected as the second case study area. In general, most catchments in Ethiopia are data scarce, but this selected catchment is one of the catchments which had some ground measured data. Still this catchment is data scarce compared to the Macalister catchment (Section 3.2.1), but had sufficient data to test the accuracy of modelling techniques used in this study. The reasons for selecting the Blue Nile catchment are explained below.

- The Blue Nile catchment is a very large catchment encompassing 311,548 km² of surface area (Hydrosult Inc et al., 2006). Referring to the Eastern Nile Technical Regional Office (ENTRO, 2006), Haileslassie et al. (2008) reported that the catchment has a population of at least 22.9 million. Of the total catchment area, approximately 199,000 km² is laid within Ethiopia. It is the largest and most important catchment which has direct impact on the Ethiopian economy. It covers

approximately 17% of the Ethiopian territory and 50% of surface water supply. This shows how important the Blue Nile catchment is to Ethiopia and its economy which mostly depends on agriculture. This is the major reason for selecting this catchment for the second case study.

- The Blue Nile catchment is not only important to Ethiopia but also to downstream countries as it provides 84% of the Nile River flow during high flows (Setegn, 2010). Sudan which is a neighbor country, where livelihood is not different to Ethiopia also fully depends on the Blue Nile. Likewise, the flow of the Blue Nile is a vital water source for Egypt for agriculture and hydropower generation purposes.
- Over 80% of the total population of the Blue Nile catchment lives in the rural areas, and are directly dependent on agriculture (Hailelassie et al., 2008). Agricultural practices put immense pressure on the water resources in the catchment which is characterised by low productivity and high soil erosion. In turn, this questions the sustainability of existing agricultural practices. Poverty and malnutrition are also major issues in the Blue Nile catchment (Setegn, 2010). The alleviation of poverty and malnutrition in the catchment population is only possible by shifting current primitive agricultural practices into modern practices. However, such changing in practices needs precise information on available water resource (such as streamflow), which is not sufficiently collected over the catchment.
- In this region, much of the required ground measured data for water management are not collected, and indeed many of the critical sites are not physically accessible, even to install gauges and collect data. The non-availability of the ground measured data can be estimated through RS data, which is the purpose of the case study.
- The researcher was employed by the International Water Management Institute (IWMI) which worked on water resources management issues in the Blue Nile catchment in Ethiopia to improve the living conditions of the catchment population while achieving sustainability of water resources. Findings of this research will enhance the effort made by IWMI to improve the living conditions in the Blue Nile catchment.

Access to water resource information in Ethiopia is not easy for the research community and the public, since these data are considered as ‘classified’, meaning not to the public. Therefore, a literature survey of publicly available information (Hailelassie et al., 2008; Awulachew et al., 2008) was done to build the initial knowledge on the catchment. The Blue Nile catchment within Ethiopia is sub-divided into 16 subcatchments (Yilma and Awulachew, 2009), based on its major tributaries. At the outset of the investigation, a comprehensive assessment was carried out to collect the available data from existing stream gauges, meteorological stations and water regulation facilities together with available LULC information and physical features of subcatchments such as area and elevation. The collected information for these 16 subcatchments are given in Tables A.2 and A.3 of Appendix A.

The collected information of these subcatchments was carefully investigated to select a suitable subcatchment for this study. Least or no streamflow regulation, appropriate catchment size ($> 1000 \text{ km}^2$) and the availability of key ground measured data were considered in this selection process. These key data are streamflow (to be used for accuracy assessment) and air temperature (which is needed to estimate potential evapotranspiration). After considering the information mentioned above, both the Jemma and the Lake Tana subcatchments were selected as potential catchments for the investigation. According to the field officers of the Ministry of Water Resources (Ethiopia), the Jemma subcatchment is subject to flash floods during the rainy season and often many of the installed gauges have been washed away during those flash floods. It also appears that the available data are not accurate due to serious issues (absence of periodic maintenance and calibration) with the calibration of the streamflow gauges (Personal Communication, MoWR, 2011). Furthermore, the ground condition of the Jemma subcatchment is extremely rough, and accessibility is difficult because of its terrain conditions and poor infrastructure, which means that it would be difficult to collect ground-truth data for LULC classification. Therefore, the Jemma option was quickly eliminated because of the unfavorable issues involved with stream gauge data, which are needed to assess the accuracy of the estimated streamflow data with RS data.

The Lake Tana subcatchment was then considered as the second study area. This subcatchment consists of many small catchments. The main catchments of the Lake Tana subcatchment are Gilgel Abbay, Ribb and Gumera. Gilgel Abbay is the largest among

them: however, its streamflow is regulated to generate electricity, and as such Gilgel Abbay was eliminated. The Ribb subcatchment, which is the second largest among them, was selected as the second case study area because it was not regulated and it was still large enough to work with RS data.

3.3 The Macalister catchment

The first case study area, which is shown in Figure 3.1, is a subcatchment of the Thomson-Macalister catchment in Victoria (Australia) (*I* and *II* of Figure 3.1). The Thomson-Macalister catchment (shown as *II* and *III* in Figure 3.1) is an important water resource catchment for the Melbourne Water Corporation, which is responsible for managing and distributing water for industries and domestic purposes in and around Melbourne (Melbourne Water, 2011). Whilst the Thomson catchment serves as a buffer to Melbourne’s water supply by acting as a ‘drought security storage’ (West Gippsland Catchment Management Authority, 2005), the Macalister River does not contribute to Melbourne’s water supply. Instead, it is a vital water source for the Macalister Irrigation District (MID) and industries surrounding Maffra (Southern Rural Water, 2011).

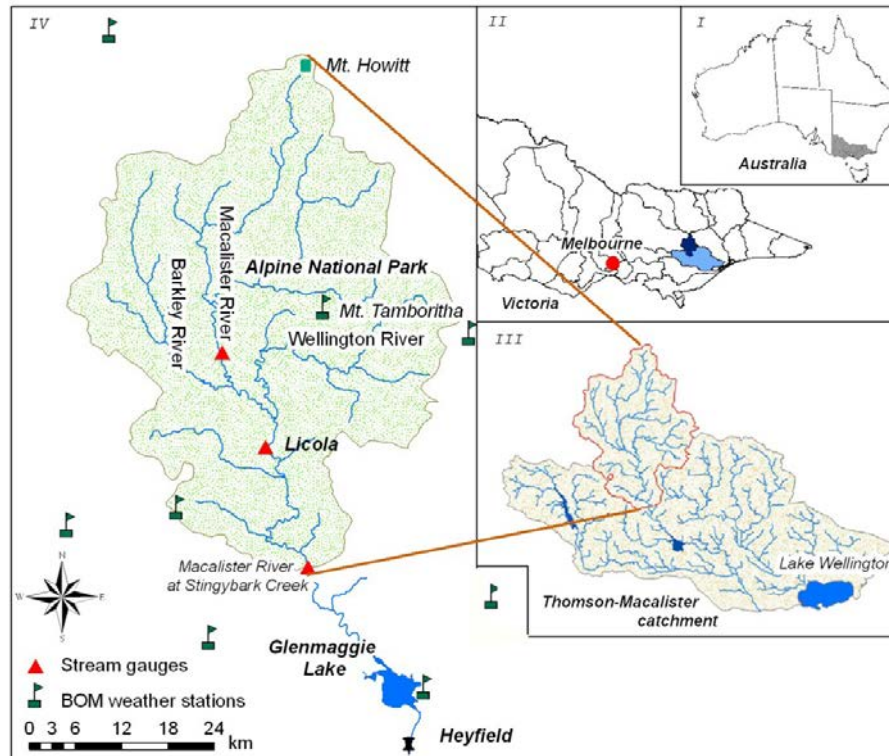


Figure 3.1 Macalister catchment showing relevant meteorological stations

The total Macalister catchment before joining Thomson River is located 250 km east of Melbourne (Figure 3.1 - *II*) and covers an area of 2,250 km². This river flows into Glenmaggie Lake which is located between Heyfield and Licola, and has a capacity of 190,000 ML. The lake is managed by the Southern Rural Water Corporation and its water is distributed for irrigation, domestic and industrial purposes. Further, the Macalister River provides vital environmental flows to Lake Wellington. The upper and middle parts of the Macalister catchment are heritage areas reserved for vital flora and fauna within the west Gippsland catchment area (West Gippsland Catchment Management Authority, 2005). The catchment area above Glenmaggie Lake was selected for this investigation as it did not have any imposed flow regulations. The stream gauge of the Macalister River at Stringybark Creek, which is a few kilometers upstream of the Glenmaggie Lake was selected as the catchment outlet. The catchment area upstream of the Stingybark Creek stream gauge was considered for this study as the case study area and this study catchment is referred to as the Macalister catchment hereafter in this thesis (Figure 3.1 - *IV*).

The Macalister catchment originates from Mt. Howitt in the Alpine National Park located in the Snowy Mountains (Water Resources Overview - Victoria, 2009). It consists of two main tributaries, the Barkly and Wellington Rivers. The Barkly River, which flows from the western part of the catchment, joins the Macalister River at about 15 km northwest of Licola. The Wellington River which originates from the eastern part of the catchment, joins the Macalister River about 1.5 km north of Licola.

The upper part of the catchment is steeply sloped and elevation is over 1,000 m above the Australian Height Datum (AHD). This area is covered with riparian forest. The elevation is approximately 1,000 m AHD in the middle area of the catchment and approximately 250 m AHD in the lower part. The elevation profile of the catchment is shown in Figure 3.2. The middle and lower parts, especially the area close to the river consists of plain areas, which are mostly utilized for grazing and animal husbandry. The areas further away from the river are covered with riparian forest.

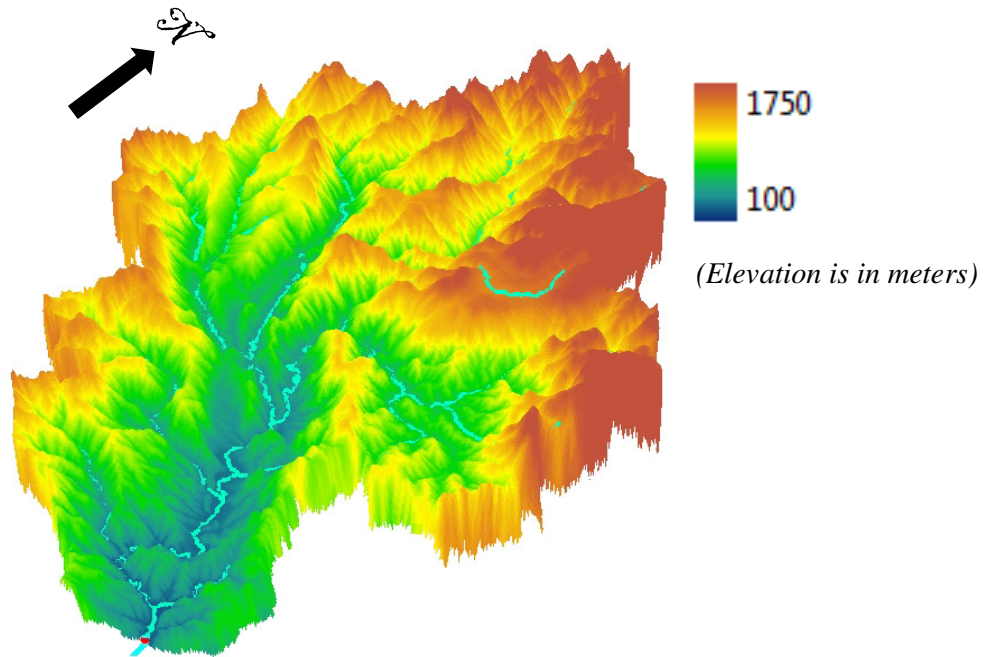


Figure 3.2 Elevation map of the Macalister catchment

Note: Catchment area is slightly rotated clockwise from its original north direction to obtain a better visual of its elevation

The air temperature of the catchment is highly dependent on seasonality and elevation. The mean monthly maximum and minimum temperatures of two different locations—one representing the middle part of the catchment (Mt. Tamboritha) and the other representing the lower part of the catchment (Licola) are shown in Table 3.1. These two locations have nearly a 750 m elevation difference, and as such the lowery situated Licola shows consistently higher temperatures than those of Mt. Tamboritha. The highest temperatures are recorded during January, where the daily temperature of Licola can reach 40 °C and above during some summer days. The lowest temperatures are recorded in July. Even though the mean minimum air temperature values are positive, individual daily minimum air temperatures can be below 0 °C during winter. This is particularly the case on the high altitudes of the catchment during winter months.

Table 3.1 Mean monthly maximum and minimum temperatures at Licola and Mt. Tamboritha

Station	Maximum temperature (°C)		Minimum temperature (°C)	
	<i>Licola</i>	<i>Mt. Tamboritha</i>	<i>Licola</i>	<i>Mt. Tamboritha</i>
January	28.9	23.3	13.2	10.7
February	27.5	22	13.1	10.2
March	25.5	19.7	10.9	8.5
April	21.1	14.9	8.6	5.9
May	17.1	11	6.6	3.8
June	14.3	8	4.5	1.8
July	13.6	6.6	3.9	0.7
August	15.2	8.1	4.3	1.2
September	17.6	10.8	5.6	2.2
October	20.6	14.5	7.1	4.2
November	23.5	17.7	9.9	6.7
December	25.7	19.8	11.4	8.3

Source: Bureau of Meteorology - Australia

The mean annual potential evapotranspiration (PET) varies with altitude and LULC of the catchment, and is shown in Figure 3.3. The upper catchment (north and west) area is rated at nearly 1,050 mm of PET annually, while the lower catchment area is rated at 1,150 mm. The increase of PET is gradual from north to south. The middle part of the catchment, which fundamentally consists of forest, has a rating of nearly 1,100 mm. However, the evapotranspiration within the catchment is highly seasonal with high values in summer and low values in winter.

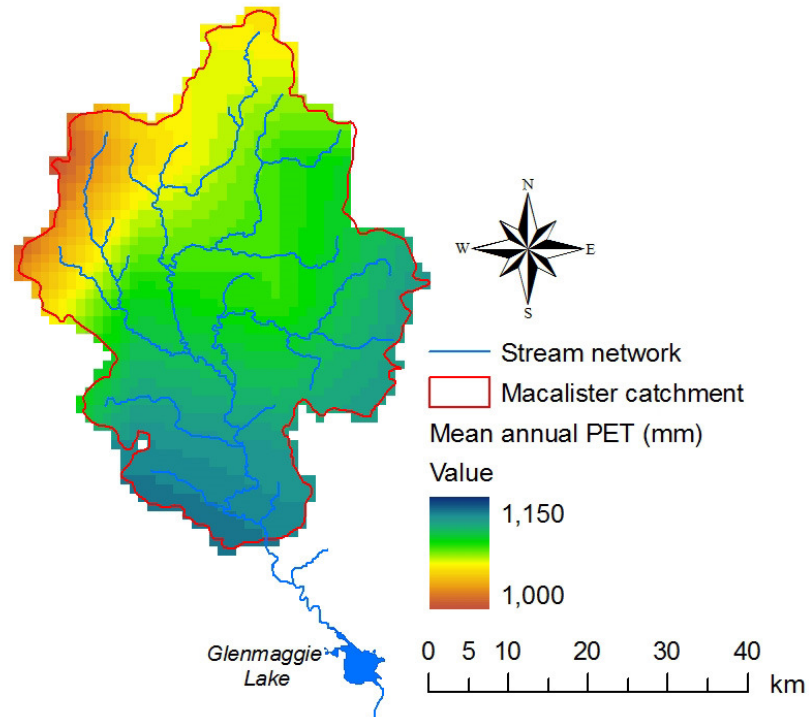


Figure 3.3 Spatial distribution of mean annual potential evapotranspiration over the Macalister catchment
(Adopted from IWMI Climate and Water Atlas - 2000)

While rainfall is the major source of precipitation in the catchment area, patches of snow can be seen in higher mountains (above 1,400 m AHD) especially in winter, but they melt very quickly. The mean annual rainfall reduces in magnitude from north to south as well as west to east, and the highest rainfall occurs in the north and northwest area of the catchment. This is approximately 1,400 mm or more, with 1,000 mm in the middle areas and 600 mm in the lower areas. Figure 3.4 shows the mean monthly rainfall of the catchment at Mt. Tamboritha and Licola. As can be seen from this figure, June to December is the main rainy period in the lower part of the catchment (Licola); however higher rainfall can occur any time during the year in the upper part of the catchment (Mt. Tamboritha). Winter (June to August) shows the highest rainfall over the entire catchment, while the lowest amount of rain is received during autumn (March to May).

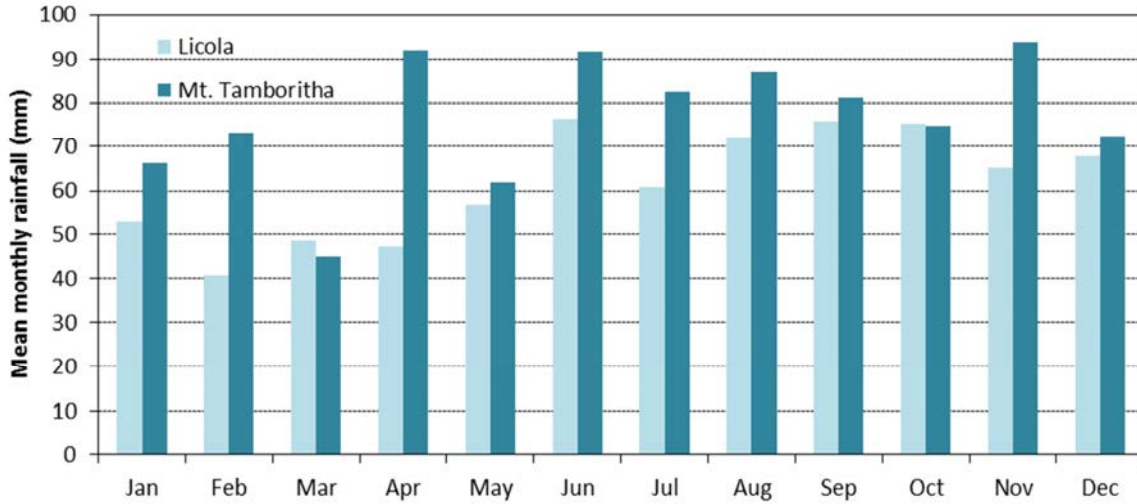


Figure 3.4 Mean monthly rainfall over the Macalister catchment
 (Source: Bureau of Meteorology - Australia)

The mean monthly streamflow of the Macalister River at Stringybark Creek is shown in Figure 3.5. According to this figure, June to November is the high flow period while the remaining period has low flows. September shows the highest average flow, and March has the lowest average. Streamflow peak is not the same as the rainfall peak due to the lag effect of streamflow to rainfall (see Figures 3.4 and 3.5).

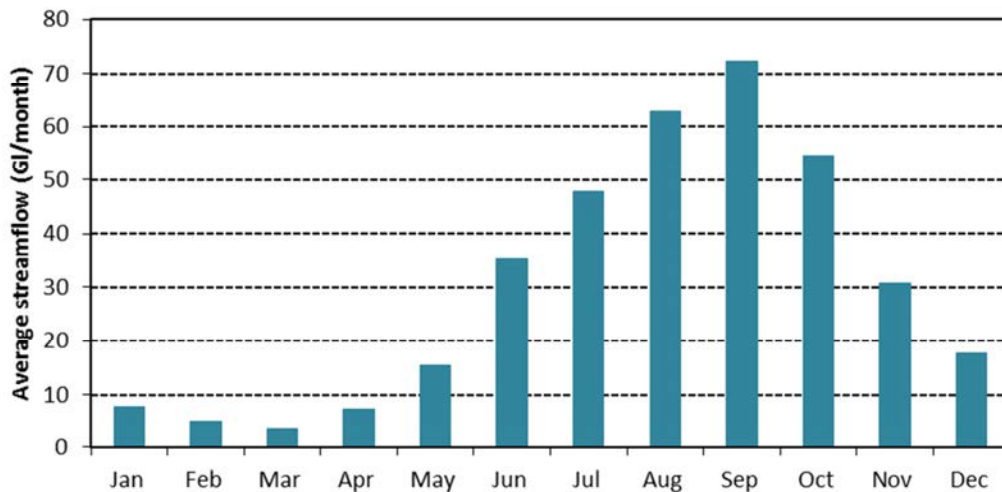


Figure 3.5 Mean monthly streamflow - Macalister River at Stringybark Creek
 (Source: Bureau of Meteorology)

LULC of the catchment is dominated by undisturbed forest (West Gippsland Catchment Management Authority, 2005). It has been reported that Mountain Ash, Alpine Ash and Snow Gum are the dominant species within the catchment area (Peel et al., 2000), and they coexist with various types of bushes and grasses that are present as the under-layer of the forest. Landuse is predominantly for grazing, especially in those lands that are located close to the rivers and streams. There are no major settlements or industries within the catchment.

According to the Australian Soil Classification (Isbell and CSIRO, 1996), Tenosols predominate close to the rivers and streams of the catchment, while Kandosols are the major order in the remaining areas. In addition to these most common soil orders, Ferrosols and Rudosols are also available in some areas. Soil textural data from field experiments are not available for the catchment area other than the general values for major soil types. Finer levels of soil information (suborder, great group, sub group and family) are not available for the catchment area. According to the West Gippsland Catchment Management Authority (2008), soil erosion is dominant in most parts of the catchment area. Sheet and rill type erosion is common because of the intensive rainfall. This is particularly the case in areas where soils are of the Kandosols order because of their weak texture. As a result, nearly 1,200 ha of catchment area consists of gullies and tunnels.

3.3.1 Data

All data which were used in this study were for the period of 1 January 2003 to 31 December 2008. This period was selected because of the availability of RS data at the time the study began. All data used in this study can be broadly categorized into two groups: RS data and ground measured data. Moderate Resolution Imaging Spectroradiometer (MODIS), Tropical Rainfall Measuring Mission (TRMM) and Infrared Global Geostationary Composite (IGGC) data were used as RS data. Rainfall, air temperature, evapotranspiration and streamflow data were collected as ground measured data.

3.3.1.1 Remote sensing data (satellite-based data)

Different types of RS data were used in this study to estimate different meteorological variables and LULC information. All RS data that were used are described in the following sub sections.

MODIS data

Moderate Resolution Imaging Spectroradiometer data are the major set of RS data used in this study. MODIS is the predecessor of Advanced Very High Resolution Radiometer (AVHRR), and was developed for land, ocean and atmospheric applications at regional levels. MODIS provides better sensitivity to vegetation and other ground features because of its specific sensor characteristics (Thenkabail et al., 2004). The MODIS sensor acquires data on a daily basis in 36 spectral bands (Table 2.4), with variable spatial resolution of 250–1,000 meters. Bands 1 and 2 have a 250 m spatial resolution, bands 3 to 7 have a 500 m spatial resolution, and the remaining bands have a 1,000 m spatial resolution. These 36 MODIS bands are generally designed for atmospheric, land and ocean studies, but the first seven bands are considered optimal for land applications (Justice et al., 2002). MODIS was used in this study to acquire information on ground features such as vegetation, surface emissivity and surface temperature as well as brightness temperature of clouds. Both MODIS *Terra* and *Aqua* level 1 data were collected for this study from the Atmospheric Archive and Distribution System (LAADS) web portal of the National Aeronautics and Space Administration (NASA) (<http://ladsweb.nascom.nasa.gov/data/search.html>). However, MODIS data which are on the *Terra* platform were mainly used in this study, while any tilted and absent images from *Terra* were replaced with images from *Aqua*.

TRMM data

The Tropical Rainfall Measuring Mission is a unique program jointly designed and operated by the NASA and the Japan Aerospace Exploration Agency (JAXA) for the purpose of accurately measuring spatial and temporal variation of tropical rainfall. Both optical and microwave sensors are mounted in TRMM, and as such it can acquire information on the magnitude and spatio-temporal variation of precipitation as well as the latent heat over land and ocean (Pierce, 2008). This helps to understand the spatial variation of precipitation and its frequency, as well as the intensity of the precipitation. In

addition, TRMM is used to understand the vertical distribution of hydrometeors, and the convective and monsoonal precipitation categories. TRMM acquires data on a daily basis. Based on these data, NASA and JAXA release various rainfall products with different spatial and temporal resolutions.

In this study, dataset 3B42 of TRMM Multi Satellite Precipitation Analysis (TMPA) was used to generate finer spatial resolution rainfall data. This dataset is $0.25^{\circ} \times 0.25^{\circ}$ degrees in spatial resolution with three hour temporal resolution, and covers 50° N to 50° S of the globe. The 3B42 dataset is primarily a merged product of the microwave and infrared precipitation, which is then calibrated with rain gauge data (Huffman et al., 2007). The microwave data are based on Low Earth Orbital (LEO) satellite microwave sensors, and infrared data are based on Geosynchronous Earth Orbit (GEO) satellite sensors. The microwave sensor data (SSM/I, AMSU-E, AMSU-B and TMI) have higher spatial resolution but only cover 80% of the earth's surface globe in the range of 40° north and 40° south from the equator per day (Huffman et al., 2007). However, GEO infrared data cover the entire globe every 30 minutes with 4 km x 4 km spatial resolution.

In the process of deriving 3B42, instantaneous microwave data are first used to estimate precipitation for the nearest three hour period (0000, 0300, ...). It is then merged with infrared precipitation which is estimated separately. This fills the gaps of microwave precipitation estimates and gives seamless data coverage over the globe. Finally, the merged data are calibrated with TRMM precipitation radar, Global Precipitation Climatology Project (GPCP) monthly rain gauge analysis and Climate Anomaly Monitoring System (CAMS) monthly rain gauge analysis data (Huffman et al., 2007) to produce 3B42. This dataset (3B42) was downloaded at no cost for the entire duration of the study (2003 – 2008) from the Goddard Earth Science and Data Information Centre's web portal (<http://mirador.gsfc.nasa.gov/cgi-bin/mirador/presentNavigation.pl?tree=project&project=TRMM>).

IGGC data

Infrared Global Geostationary Composite (IGGC) data (<https://wist.echo.nasa.gov>), which are available at every 30 minutes intervals, were used to estimate cloud cover in this study, which in turn were used to estimate evapotranspiration. IGGC data are a combination of several geostationary and polar orbiting satellite data, received from the Geostationary

Satellite system (GOES), the Multi-Functional Transport Satellite (MTSAT), and the Meteosat and National Oceanic and Atmospheric Administration (NOAA). All of these data are from the infrared band (11 µm channel) of the aforementioned satellites. The geostationary satellites of GEOS, Meteosat and MTSAT cover the area surrounding the equator, while the NOAA satellite covers the Polar Regions (Goodman, 2011).

Landsat Data

Landsat data were used in this study to classify LULC, as its spatial resolution is sufficient to represent the ground heterogeneity of the study areas compared to MODIS data. Landsat data are also freely available compared to other competitors such as the Indian Remote Sensing (IRS) satellite data and SPOT (Système Pour l'Observation de la Terre) data. Landsat 5 (which was launched on 1 March 1984 and decommissioned on 5 June 2013) and Landsat 7 (which was launched on 15 April 1999 and is still operational) data can be downloaded from the internet.

Landsat 5 is equipped with a Thematic Mapper (TM), and has seven bands. Out of those seven bands, six bands which are visible and short wave infrared have 30 m spatial resolution, while the longwave infrared (thermal) band has 120 m spatial resolution (Lillesand and Kiefer, 1999). The revisit time of the Landsat 5 is 16 days, and Landsat data can be downloaded either from the NASA's Earth Observing System Data and Information System (EOSDIS) web port (<http://reverb.echo.nasa.gov/reverb/>) or from the Global Land Cover Facility (GLFC) web port of University of Maryland (<http://www.landcover.org/index.shtml>).

3.3.1.2 Ground-based data

Meteorological data

The daily meteorological data (such as rainfall, minimum and maximum air temperatures, sunshine hours, wind speed, relative humidity) were acquired from the Bureau of Meteorology – Australia (BOM) and the SILO climatic dataset (<http://www.longpaddock.qld.gov.au/silo/>) for the stations within and in close proximity to the catchment. These stations are shown in Figure 3.1. These meteorological data are quality controlled. In addition, the Penman-Monteith based potential evapotranspiration data were obtained from the SILO database.

Streamflow data

The required daily streamflow data for the Macalister catchment were acquired from the Victorian Water Resources Data Warehouse's (<http://www.viewwaterdata.net/viewwaterdata/home.aspx>) web portal. The Victorian Water Resources Data Warehouse is a dedicated web portal to disseminate up-to-date water information throughout Victoria. There are a number of gauges located along the Macalister River. The Macalister River at Stringybark Creek gauge was selected for this study since it is the last stream gauge installed before Glenmaggie Lake (Figure 3.1).

Soil data

The required soil data for the Macalister catchment was obtained from the United Nations Food and Agriculture Organization's (FAO) Digital Soil Map of the World. This database was originally published in 1974 as the Soil Map of the World (SMW) in a non-digital format but was then converted into a digital map, and later re-projected and converted into a grid format under the Global Resources Information Database (GRID) project of the United Nations Environmental Program (Levick et al., 2004). Initially, the FAO Digital Soil Map had 26 major soil groups containing 106 soil units. However, after adaptation to the International Union of Soil Sciences (IUSS) taxonomy in 1998, the FAO digital soil map was reclassified with 30 reference soil groups. This map is arranged into 10 major continental regions namely Africa, Australasia, Central America, South America, Europe and West of the Ural, North America, Central and North East Asia, Near East, Far East, and South East Asia. The country boundaries within the continental regions have been updated as of 1994. The region of Australasia was used to extract the soil information of the Macalister catchment.

3.4 The Ribb catchment

The Blue Nile River starts from Ethiopian highlands and flows through Sudan before it meets the White Nile in Khartoum in South Sudan. The Ribb catchment, which is a subcatchment of the Blue Nile catchment, originates from the central highland mountains of Ethiopia and is shown in Figure 3.6. This figure shows the Amhara region in Ethiopia (Figure 3.6 - I), the Ribb catchment and the locations of Lake Tana in Amhara (Figure 3.6 - II), and the detailed map of the Ribb catchment (Figure 3.6 - III). In addition, the figure also shows meteorological stations within and near proximity to the catchment, stream

gauge locations as well as the drainage network. The Ribb River flows in a northwest direction until the middle of the catchment and then turns to west and meets Lake Tana.

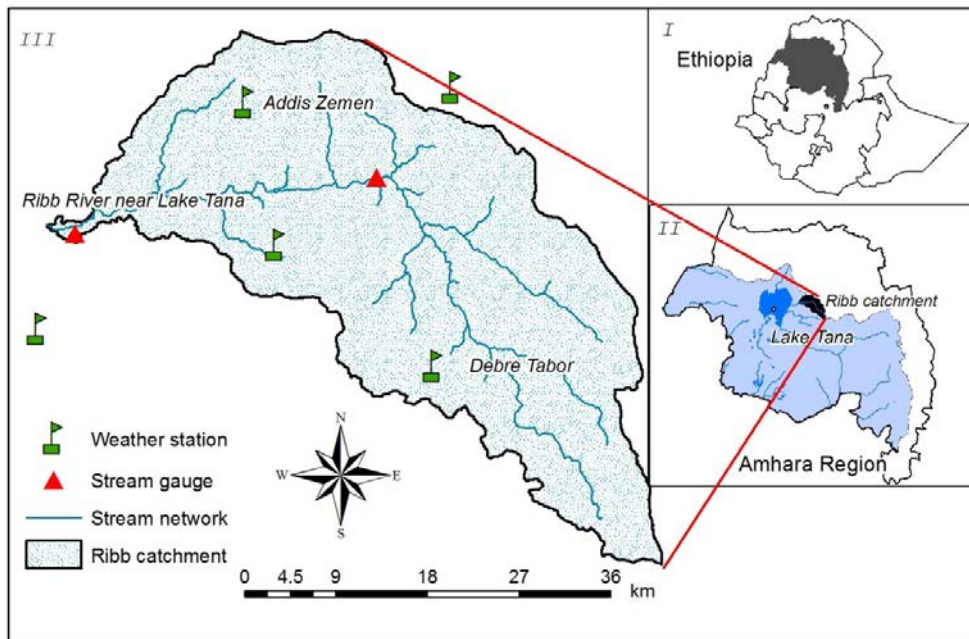


Figure 3.6 Ribb catchment showing meteorological stations in and around the catchment area

Figure 3.7 shows the elevation profile of the Ribb catchment. This figure was generated by the 90 m Digital Elevation Model (DEM) and was rotated anti-clock wise from its normal north oriented position (Figure 3.6 – III), to give a better view. The elevation of the catchment varies between 1,750 m to 4,100 m (Figure 3.7) above the mean sea level (MSL).

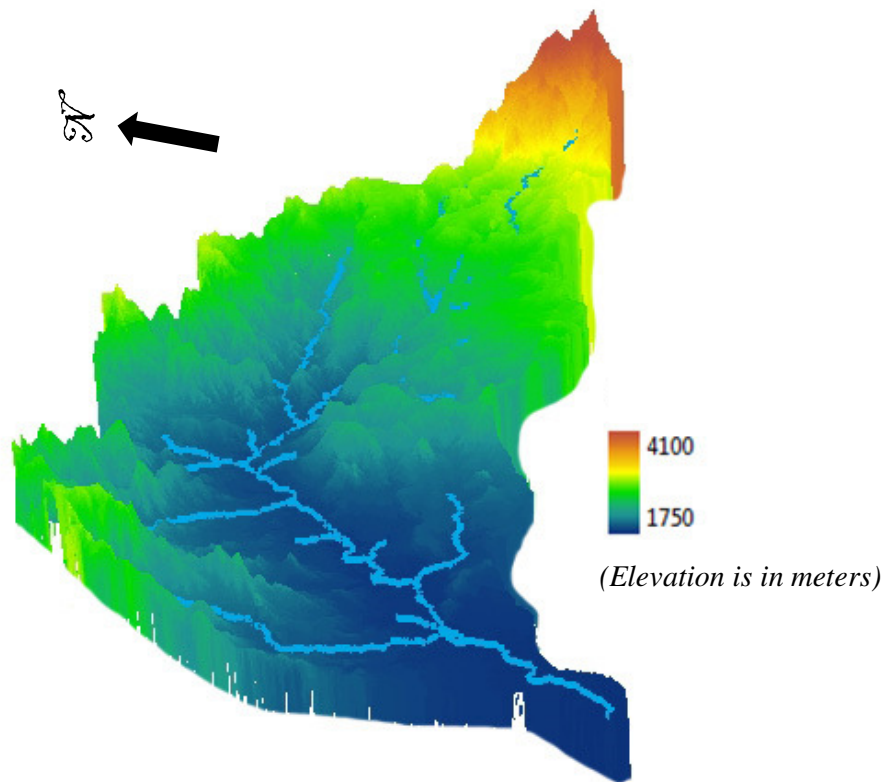


Figure 3.7 Elevation map of the Ribb catchment

The temperature over the catchment changes with seasons as well as with the elevation. The mean maximum and minimum temperature at two different meteorological stations over the Ribb catchment are shown in Table 3.2. The Debra Tabor station is located at a higher elevation than Addis Zemen, and hence its temperature is slightly lower than that of Addis Zemen. Table 3.2 shows that first the half of the year (before the monsoon starts (June)) is warmer than the second half. The table shows that the maximum temperature drops by approximately 3 °C with the start of monsoon. The drop in maximum temperature continues until July, then gradually increases and finally the highest maximum temperature is recorded in March. The minimum temperature pattern in the catchment area is different to the maximum temperature pattern. The lowest minimum temperature is recorded in December, while the highest one is recorded in May.

Table 3.2 Mean monthly maximum and minimum temperatures at two different meteorological stations over the Ribb catchment

Station	Maximum temperature (°C)		Minimum temperature (°C)	
	<i>Addis Zemen</i>	<i>Debre Tabor</i>	<i>Addis Zemen</i>	<i>Debre Tabor</i>
January	31	22.5	9.8	8
February	32.8	23.9	10.6	9.4
March	33.5	24.5	12.8	10.6
April	32.8	23.7	13.8	11.1
May	31.8	23.7	14.1	11.3
June	28.3	21	13.8	10.5
July	25.5	18.4	13.3	9.8
August	25.7	18.5	13.6	9.6
September	27.2	19.6	13	9.3
October	29.3	20.7	10.6	8.2
November	30.2	21.4	9.5	7.8
December	30.3	21.6	8.8	7.6

The mean annual potential evapotranspiration (PET) of the Ribb catchment is shown in Figure 3.8. The PET over the lower catchment area (close to Lake Tana) is as high as 1,800 mm/year, and is around 1,500 mm/year in the upper part of the catchment (i.e. the most southern position). PET significantly varies from month to month with the highest PET being recorded during May and the lowest one during July. From July, PET gradually increases until May of the following year and then drops from May to July.

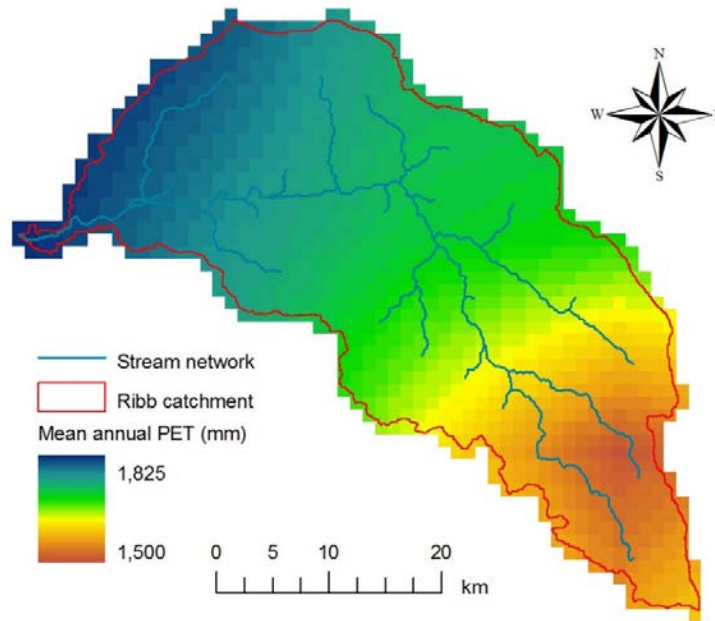


Figure 3.8 Annual potential evapotranspiration over the Ribb catchment
(Adopted from IWMI Climate and Water Atlas - 2000)

The climate of the Ribb catchment is influenced by the tropical highland monsoon. The existence of tropical monsoon makes two clear seasons with regards to rainfall: namely the wet and dry seasons. Figure 3.9 shows the mean monthly rainfall of two stations in the Ribb catchment. These two stations are considered to be representative stations of the Ribb catchment in terms of rainfall. According to this figure, June to September is the wet season, and 75 to 90% of annual rainfall is received during this period when monsoon prevails (based on Addis Zemen and Debra Tabor stations – Figure 3.9). The mean annual rainfall over the catchment is around 1,300 mm. The highest precipitation is received in the month of July as a result of monsoonal activation, but rainfall of August is also close to July. The remaining period (October to May) is predominantly dry, with the driest months being December and January. The rainfall of the catchment varies with the elevation, showing approximately 1,000 mm of annual rainfall near the Lake Tana area (lower catchment) and 1,500 mm in the mountain areas.

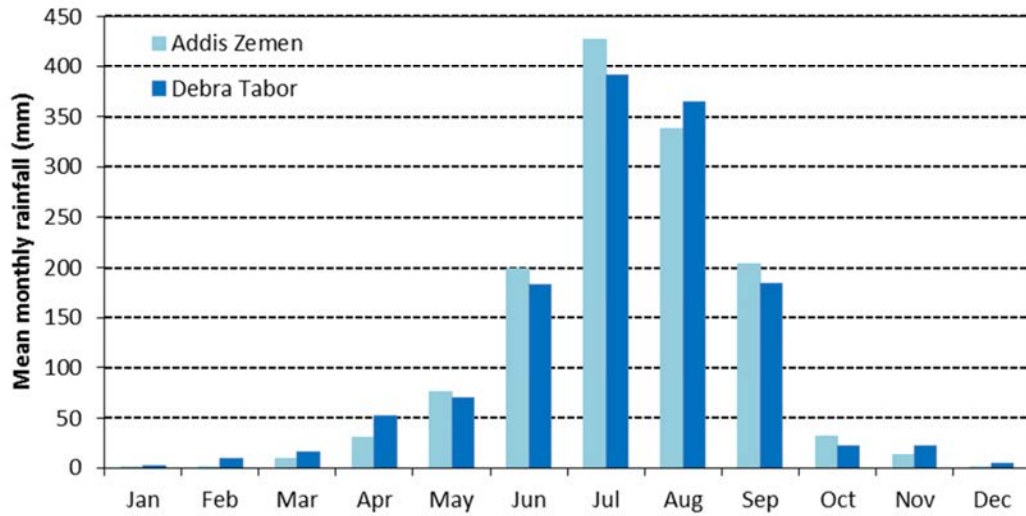


Figure 3.9 Mean monthly rainfall over the Ribb catchment
(Addis Zemen and Debra Tabor)

Figure 3.10 shows the mean monthly streamflow in the Ribb River near the catchment outlet. Streamflow is highly seasonal in the Ribb catchment with its monsoonal rainfall pattern. July to November is the period having high flows and more than 90% of the flow occurs during that period. The rest of the period has low flows. River flow is highest in August, whereas precipitation is highest in July.

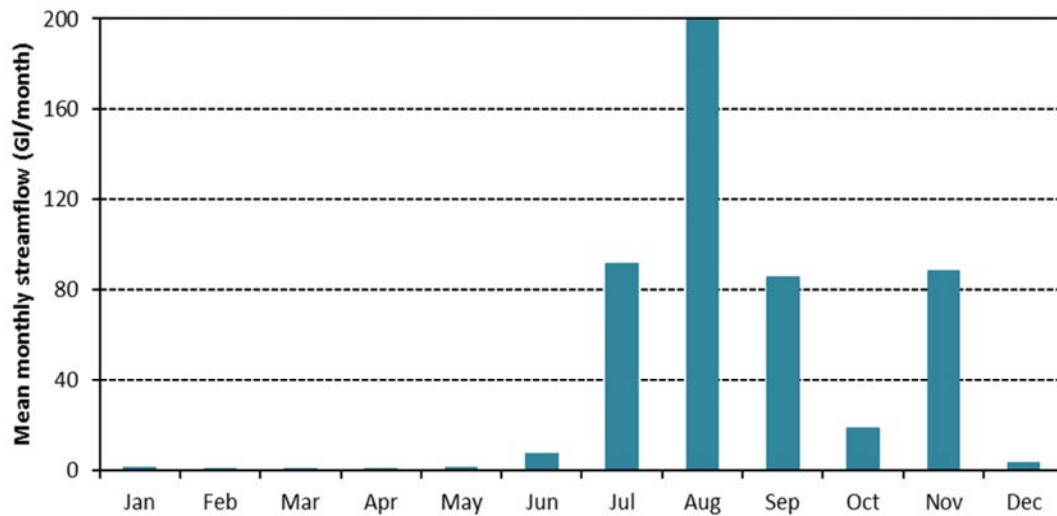


Figure 3.10 Mean monthly streamflow in the Ribb River near Lake Tana
(Based on the period of 1959 to 1992 – source: MoWR Ethiopia)

The landuse of the catchment is predominantly for agricultural crop lands, mostly in the lower parts of the catchment. The middle part of the catchment, which is partially mountainous, consists of moderate cultivation and Afro-alpine forest. The upper part of the catchment is mountainous, and the steep rocky soil there has hindered cultivation. However, this part of the catchment is covered with shrubs and Afro-alpine forest. The agricultural production system in the Ribb River catchment is a crop-livestock mixed system, and the dominant crops are barley (*Hordeum vulgare*), wheat (*Triticum durum* and *Triticum aestivum*), teff (*Eragrostis tef*), millet (*Eleusine coracana*), noug (*Guizotia abyssinica*), maize (*Zea mays*), rice (*Oryza sativa*), chickpea (*Cicer arietinum*) and rough pea (*Lathyrus hirsutus*). The livestock in the catchment are cattle and goat. Soil erosion is the biggest challenge in the Ribb catchment due to intense precipitation, poor agronomical practices and extensive livestock (Mwendera et al., 1997; Hailelassie et al., 2008). As such, the most fertile top soil in the catchment erodes to Lake Tana.

The major soil types in the Ribb catchment are shown in Figure 3.11. Four different soil types i.e. Eutric Leptisols, Chromic Luvisols, Eutric Fluvisols and Eutric Nitisols can be found in the catchment. Out of these, Eutric Leptisols and Chromic Luvisols cover approximately 74%, Eutric Fluvisols covers approximately 25%, and Eutric Nitisols covers the remaining area of the catchment. Eutric Fluvisols can also be found in the lower part of the catchment, which is mostly used for cultivation.

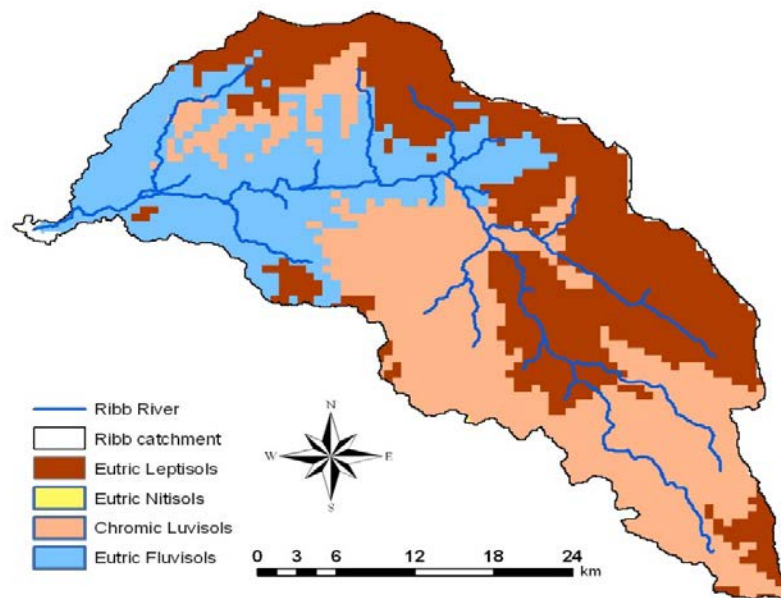


Figure 3.11 Major soil types in the Ribb catchment

3.4.1 Data

Similar to Section 3.3.1, all data that were used in the Ribb catchment to generate streamflows can be broadly categorized into two groups; remote sensing data and ground measured data. The study period was the same as for the first case study period (2003 – 2008).

3.4.1.1 Remote sensing data (satellite-based data)

Similar to the Macalister catchment, MODIS, TRMM and IGCC data which were described in Section 3.3.1.1 were used in the Ribb catchment study. Landsat 5 TM data of cloud free and within the cultivation season (to acquire better representation of all possible LULC classes) were not available in the Ribb catchment, especially for the study period. Therefore, Landsat 7 ETM+ data which is Scan Line Corrector (SLC) off, but gaps filled (which was done by the University of Maryland – USA) was used in the LULC classification.

Landsat 7 is equipped with the Enhanced Thematic Mapper Plus (ETM+). This is an advanced sensor to TM, and has eight bands. Out of those eight bands, seven bands which are visible and short wave infrared have 30 m spatial resolution, while the longwave infrared (thermal) band has 60 m spatial resolution. The remaining panchromatic band has 15 m spatial resolution. Even though ETM+ data are ideal for catchment level applications, its SLC malfunctioned in May 2003, and as such Landsat 7 ETM+ data were unable to scan 100% of the swath areas. As a result of that, the total catchment area was not covered. This deficiency was overcome filling those gaps using the nearest day Landsat ETM+ image and the gap filled data can be downloaded either from the NASA's Earth Observing System Data and Information System (EOSDIS) web port (<http://reverb.echo.nasa.gov/reverb/>) or from the Global Land Cover Facility (GLFC) web port of the University of Maryland (<http://www.landcover.org/index.shtml>). Similar to Landsat 5, the revisit time of the Landsat 7 is 16 days.

3.4.1.2 Ground-based data

Similar variables used in the Macalister catchment to estimate streamflow (Section 3.3.1.2) were used for the investigation of the Ribb catchment.

Meteorological data

The required daily meteorological data for the Ribb catchment were acquired from the National Meteorology Agency (NMA) – Ethiopia for the stations within and in close proximity to the catchment. Those stations are shown in Figure 3.6. Rainfall, minimum and maximum temperatures and sunshine hours of the selected meteorological stations were collected from NMA. Minimum and maximum temperatures and sunshine hours were collected to estimate potential evapotranspiration. However, these data were not quality controlled. Therefore, the data were checked for their quality. It was found that there were a number of missing records within the study period, and it was not possible to fill these data gaps with reasonable accuracy.

One procedural difference between the Ribb catchment and the Macalister catchment is that the Penman-Monteith based evapotranspiration was estimated in the case of the Ribb catchment following Allen et al. (1998).

Streamflow data

There are no major water diversions or regulations along the river except for the intermittent pumping of water for agricultural purposes. The most downstream gauge, which is located just above Lake Tana was selected, for this study as the catchment outlet (Figure 3.6). The required daily streamflow data at this gauging station were acquired from the Ministry of Water Resources (MoWR) in Ethiopia.

Soil Data

The required soil data for the Ribb catchment was obtained from the FAO Digital Soil Map of the World, as was the case for the Macalister catchment.

3.5 Estimation of input variables using remote sensing data for catchment process modelling

In this section, the methods and techniques that were used to estimate rainfall and evapotranspiration, and classify LULC from RS data are presented. In estimating these input variables, RS data were predominantly used. However, a few ground measured meteorological data were also used.

3.5.1 Rainfall estimation

Rainfall is considered as a form of precipitation consisting of liquid water droplets having diameters between 0.5 and 5.0 mm (AMS Glossary, 1999). Rainfall is the most significant variable which determines the amount of streamflow at a given time (Gourley and Vieux, 2005; Su et al., 2008). Therefore, the accurate data of rainfall in a catchment (amount and spatial distribution) is an essential component in streamflow estimation, and the lack of rainfall data significantly hinders the estimation accuracy. Since the networks of meteorological stations (and the number of stations within networks) are shrinking, and because of the difficulties involved in obtaining ground measured meteorological data (as outlined in Chapters 1 and 2), alternatives to measuring rainfall data needed to be considered. The estimation of rainfall data using RS data (Arkin, 1979; Grimes et al., 1999; Grimes et al., 2003; Grimes and Diop, 2003; Coppola et al., 2006; Bocchiola, 2007; Huffman et al., 2007) is one of these alternatives. According to Kuligowski (2002), the RS based rainfall estimation methods can be categorized into four groups, based on the approach used;

1. The use of precipitation index and subsequent adjustment (Arkin, 1979; Arkin and Meisner, 1987),
2. Probability matching (Atlas et al., 1990),
3. Regression modelling (Grimes et al., 1999; Grimes et al., 2003),
4. A combination of infrared, microwave and field data (Huffman et al., 2007).

The first three approaches use visible and/or infrared data to derive rain rates (and then the amount of rainfall). These rain rates are normally estimated from cloud-top properties (i.e. brightness temperature, temperature gradient, etc.). The fourth approach uses microwave observations, and visible and infrared data together to provide rain rates (Huffman et al., 2007). The use of microwave observations in rainfall estimation provides better rain rates in their combined approach than in the other approaches (Kuligowski, 2002). Accordingly, Tropical Rainfall Measuring Mission (TRMM) visible, infrared, microwave and radar data are combined with data from numerous other meteorological satellites such as GEOS and MTSAT to generate TRMM Multisatellite Precipitation Analysis (TMPA) data (Huffman et al., 2007).

Under the TRMM program, several rainfall products are released free of charge to the user community. These rainfall data products vary in their spatial and temporal resolutions. A TMPA data product called 3B42 is used in this study as input data to estimate rainfall. The TMPA 3B42 data cover 50⁰ north to 50⁰ south of the globe. These data are characterised by higher temporal resolution (3 hour), but lower spatial resolution (0.25⁰x0.25⁰ degrees - approximately 625 km² on ground). The low spatial resolution of TMPA 3B42 adversely affects streamflow estimation especially when TMPA 3B42 is used for small and medium scale catchments, since TMPA 3B42 is unable to represent the spatial variability of rainfall over these small and medium scale catchments (Collischonn et al., 2008).

The SWAT hydrological software modelling tool was used in this study for streamflow estimation. SWAT works in several subcatchments and their corresponding hydrological response to estimate streamflow. These hydrological response units are significantly smaller in size than one pixel (625 km²) of TMPA data. As a result of this low spatial resolution, TMPA data do not represent the spatial variability of rainfall within the small subcatchments of study areas. This situation is almost similar to the absence of ground based meteorological stations and ground measured data for streamflow estimation. However, MODIS has radiance data at a spatial resolution of 1 km². Therefore, they can be used to estimate rainfall with better spatial resolution. Furthermore, MODIS data are freely available to the user community, and cover the entire globe on a daily basis (Justice et al., 2002; Thenkabail et al., 2004).

In this study, a methodology is proposed to estimate high spatial resolution (1 km²) but daily rainfall data using MODIS radiance and TRMM 3B42 (hereafter TRMM rainfall in this thesis) data. This methodology is summarized below and is described in detail later on this section.

- The first step is to convert hourly rain rates of TRMM rainfall data into daily values.
- The second step is to separate rain clouds and no-rain clouds from MODIS cloudy images (Section 3.5.1.1).
- The third step is to define the MODIS brightness temperature (BT) threshold to calculate BT difference (Section 3.5.1.2).

- The final step is to estimate high spatial resolution (1 km²) daily rainfall data using daily brightness temperature difference and daily TRMM rainfall data by employing a gamma function (Section 3.5.1.3).

TRMM 3B42 data are available for every three hour period with hourly rain rate. These rain rates were used to calculate daily rain amount and this step does not need further explanation.

3.5.1.1 Rain no-rain cloud separation

The separation of rain clouds from no-rain clouds from all cloudy images is critically important, since all clouds do not yield rain at all times. In particular, thin clouds, such as cirrus which are often categorized as cloudy RS images, do not produce any rain. Therefore, in order to get a higher level of accuracy, such no-rain clouds should not be considered in rainfall estimation. The brightness temperature of MODIS was chosen as an input to identify the no-rain clouds in this study. This is in line with the studies undertaken by Fritsz and Lazsol (1993), Tjemkes et al. (1997) and Kuligowski (2002), who introduced several methods for rain/no-rain cloud separation using BT. The band width used in these previous studies were also considered in this study and they are; (i) 6.53 – 6.89 μm (band 27 of MODIS), (ii) 10.78 – 11.28 μm (band 31 of MODIS) and (iii) 11.77 – 12.27 μm (band 32 of MODIS).

The required BT was calculated using MODIS radiance data (band 27, 31 and 32) as inputs in Plank's formula, which is given as (Oguro et al., 2011):

$$BT_i = \frac{h \times c}{\left(L_i \times k \times \ln \left(\frac{2 \times h \times c^2}{L_i^5 \times R_i} + 1 \right) \right)} \quad (3.1)$$

where L_i is the wavelength of band i , h is the Planck's constant, c is the speed of light, k is the Boltzmann's constant and R_i is radiance value of band i . Band i refers to band 27, 31 and 32 of the MODIS sensor.

The use of constant BT to differentiate rain clouds from no-rain clouds is not always appropriate since the vertical temperature profile changes over time (Kuligowski, 2002). This difficulty has been overcome by using the BT difference of thermal bands (Ba and Gruber, 2001a; Kuligowski, 2002). In line with those studies, differences of (i) band 27 and band 31, and (ii) band 31 and band 32 were used to differentiate rain clouds from no-rain clouds in this study. The reasons for using these BT differences for the separation of rain and no-rain clouds are given below.

According to Fritsz and Lazsol (1993) and Tjemkes et al. (1997), the brightness temperature of band 27 (BT27) is higher than the brightness temperature of band 31 (BT31), when a high amount of water vapour is present on top of the cloud. Based on the above finding, Kuligowski (2002) stated that the bigger the difference between BT27 and BT31, the greater is the probability of having rain clouds.

The difference in brightness temperature between band 31 and band 32 (BT32) is larger for thin clouds than for thicker clouds (Inoue, 1987). This is due to the emissivity differences between band 31 and band 32 which produce minimal differences in brightness temperature for thick clouds (whose emissivity is effectively uniform) but have higher differences for thin clouds. Therefore, Kuligowski (2002) deduced that a higher difference between BT31 and BT32 suggests a higher probability of having no-rain clouds.

Threshold levels for screening rain clouds from no-rain clouds using the above differences have also been highlighted by Kuligowski (2002). According to this study, the spatial median value of BT differences (of both BT27 - BT31 and BT31 - BT32) were used to separate rainy clouds from no-rainy clouds. The same approach was used in this study as thresholds to separate rain clouds from no-rain clouds. Clouds with BT difference values of bands 27 and 31 which are higher than or equal to spatial median values were considered as having rainy clouds. Similarly, clouds with BT difference values of bands 31 and 32 which are less than or equal to spatial median values were considered as rainy clouds.

3.5.1.2 Brightness temperature threshold

The brightness Temperature of rain clouds is considered as a key cloud-top property that is used to estimate rainfall data in this study. Del Beato (1981) observed that the drop in cloud-top temperature (which is slightly different from brightness temperature that was used in this study) from 283 K to 218 K has increased the probability of precipitation over Victoria in Australia. The study of Del Beato (1981) is based on several rainfall events, and 80% of the considered events have yielded rain when the cloud-top temperature dropped from 263 K to 218 K. The findings of Del Beato (1981), that is, low cloud-top temperature results in higher probability of rainfall, could be partially explained by further analysis of the rainfall process as described below.

The occurrence of rain from a cloud depends on several factors, and is mostly determined by the supersaturation process. Supersaturation is a condition that exists in a given portion of the atmosphere when the relative humidity exceeds 100% (AMS Glossary, 1999). The supersaturation process helps the formation of cloud particles. It is driven by ambient temperature, which affects the size of the rain drops. Through a laboratory experiment, Madonna et al. (1961) observed that the supersaturation process is highly dependent on temperature. They found that temperatures above 238 K result in super-cooled water, but those below 238 K form ice crystals. Later, this finding was confirmed by Rosinski and Lecinski (1983) who found that the lower the temperatures the higher the supersaturation percentage. Xinping et al. (2000) found that the lower the temperature, the higher the proportion of ice crystals in the cloud which can in turn increase the probability of having rainfall.

The Global Precipitation Index (Arkin and Meisner, 1987) approach is an earlier approach of estimating precipitation, and is based on a fixed rain rate for clouds when their cloud-top temperature is less than 235 K. According to Rosenfeld (2007), most clouds which have cloud-top temperature less than 235 K are anvils of cumulonimbus clouds. The above studies show that the lower brightness temperature of these clouds the higher the probability of rain. This is because lower BT gives higher BT difference from the threshold (such as 235 K) and thus higher rainfall probability.

The brightness temperature over catchment areas varies accordance latitude and time of the year rather than physical factors. Therefore, the threshold of 235 K for rainfall estimation may not be applicable in all geographical areas. As such, BT of rain clouds was tested with TRMM rainfall data to select the best threshold from several options. The mean seasonal BT, mean monthly BT and 235 K over the catchments were considered as thresholds. The rain clouds of BT less than these thresholds were considered as ‘rainy’ and the other clouds as ‘no-rainy’ (Arkin, 1979; Del Beato, 1981; Arkin and Meisner, 1987; Huffman et al., 1997).

The performances of all above mentioned thresholds were assessed separately with TRMM rain data to find out the best threshold. This assessment was done using the following indices. They are; (i) the Heidke skill score (*HSS*), (ii) the Probability of Detection (*POD*), (iii) the False Alarm Ratio (*FAR*), and (iv) the bias.

HSS measures the optimal fit between BT below the threshold and TRMM rainfall; *POD* determines the fraction of MODIS pixels that were correctly classified as rainy; *FAR* represents the incorrect number of pixels classified as rainy when they are no-rainy; and the bias represents the ratio of the correctly estimated number of pixels in MODIS as rainy compared to total rainy pixels in TRMM. Therefore, all the pixels less than the threshold were classified as rainy and others as no-rainy for this assessment. This classification together was crossed with TRMM rain and no-rain to produce four combinations that were used to calculate the above mentioned indices.

Table 3.3 shows the number of pixels in all four combinations of both MODIS BT and TRMM producing rain and no-rain. In the table, c_1 represents the number of pixels when both MODIS and TRMM have no rain, c_2 represents the number of pixels when MODIS provides rain but TRMM has no-rain, c_3 represents the number of pixels when MODIS has no-rain but TRMM has rain, and c_4 represents the number of pixels when both MODIS and TRMM give rain.

Table 3.3 Contingency matrix of the rain/no-rain combinations of MODIS BT and TRMM

	TRMM no-rain	TRMM rain
MODIS BT no-rain	c_1	c_3
MODIS BT rain	c_2	c_4

HSS is calculated as follows (Kuligowski, 2002),

$$HSS = \frac{2(c_1 \times c_4 - c_2 \times c_3)}{(c_1 + c_2) \times (c_2 + c_4) + (c_3 + c_4) \times (c_1 + c_3)} \quad (3.2)$$

POD, *FAR* and bias are calculated using Equations (3.3), (3.4) and (3.5) respectively (Kuligowski, 2002).

$$POD = \frac{c_4}{(c_3 + c_4)} \quad (3.3)$$

$$FAR = \frac{c_2}{(c_2 + c_4)} \quad (3.4)$$

$$bias = \frac{(c_2 + c_4)}{(c_3 + c_4)} \quad (3.5)$$

The best performing threshold was selected based on the above indices. The results are discussed in Chapters 4 and 5 for the first and second case study catchments respectively. Then the BT difference from the best threshold was used to estimate rainfall in this study (Section 3.5.1.3).

3.5.1.3 Rainfall estimation using gamma function

The BT difference from the threshold (i.e. the difference between the threshold and BT) was then converted to rainfall. This was done by modelling both BT difference and TRMM rainfall through gamma distribution function. The gamma distribution function was used in this study since climatological variables with zeroes are fitted well with a gamma distribution (Thom, 1966). This was the case for the BT difference and rainfall. The gamma probability density function as applicable to this study with respect to BT difference is given below:

$$g(x) = \frac{1}{\beta^\alpha \Gamma(\alpha)} x^{\alpha-1} e^{-(x/\beta)} \text{ for } x > 0 \quad (3.6)$$

where x is the BT difference from its threshold (brightness temperature higher than and equal to the threshold are considered as 0), α is the shape parameter (and $\alpha > 0$), β is the scale parameter (and $\beta > 0$), $\Gamma(\alpha)$ is the ordinary gamma function of α , and e is the natural logarithm (2.71828).

The gamma function can be written as:

$$\Gamma(\alpha) = \int_0^{\infty} x^{\alpha-1} e^{-x} dx \quad (3.7)$$

The following equations were used to determine optimum α and β (Thom, 1966):

$$\hat{\alpha} = \frac{1}{4A} \left(1 + \sqrt{1 + \frac{4A}{3}} \right) \quad (3.8)$$

$$\hat{\beta} = \frac{\bar{x}}{\hat{\alpha}} \quad (3.9)$$

$$A = \ln(\bar{x}) - \frac{\sum \ln(x)}{z} \quad (3.10)$$

where z is the number of observations.

The cumulative probability can be written as:

$$G(x) = \int_0^x g(x) dx = \frac{1}{\hat{\beta} \hat{\alpha} \Gamma(\hat{\alpha})} \int_0^x x^{\hat{\alpha}-1} e^{-\left(\frac{x}{\hat{\beta}}\right)} dx \quad (3.11)$$

Equation (3.11) is valid only when $x > 0$. When x is equal to 0 in Equation (3.11), the equation becomes an incomplete gamma function, since gamma function is undefined at $x = 0$. Thus the cumulative probability ($H(x)$) can be written as:

$$H(x) = p + (1 - p) \times G(x) \quad (3.12)$$

where, p is the fraction of $x = 0$ to the total number of observations:

$$p = \frac{t}{z} \quad (3.13)$$

where, t is the total number of $x = 0$ and z is the total number of observations.

This calculation process produced the cumulative probability function of BT difference for each pixel (which is of 1 km^2 spatial resolution, but in daily temporal resolution) in the study area.

Equations 3.6 to 3.13 were also used to calculate the cumulative distribution of the daily TRMM rainfall at each pixel in the study area. As mentioned in Section 3.5.1, TRMM rainfall data are available as hourly values for every three hours. Therefore, these hourly rates were converted into daily rainfall amount before calculating the cumulative probability.

The cumulative probability distributions of MODIS BT difference data (with high spatial resolution – 1 km^2 , but low temporal resolution - daily) and TRMM rainfall data (with low spatial resolution – 625 km^2 but high temporal resolution) were used to estimate higher spatial resolution (i.e. 1 km^2) daily rainfall data (which are considered to be high resolution). The process is explained in Figure 3.12.

In this process, it was assumed that BT difference is responsible for rainfall, and that higher BT difference results in higher rainfall as explained earlier. This was considered through matching the probability of MODIS BT difference and the probability of TRMM rainfall. This assumption was justified from the findings of Del Beato (1981): that the lower the cloud-top temperature the higher the probability of rainfall.

Figure 3.12 has four separate plots. Plot I shows the daily time series of MODIS BT difference, while plot II contains its cumulative probability. Plot IV shows the TRMM daily rainfall time series while plot III contains its cumulative probability. Plot IV also contains the rainfall estimates at high spatial resolution (1 km^2) derived from combining BT difference data and TRMM rainfall data. Note that plots III and IV are for pixels of 625 km^2 , while plots I and II are for 1 km^2 pixels. Hence, plots I and II are used 625 times

to cover the pixels of plots III and IV. The estimation process is explained below. The arrows between the plots explain the process involved in converting MODIS BT difference data into high spatial resolution daily rainfall data.

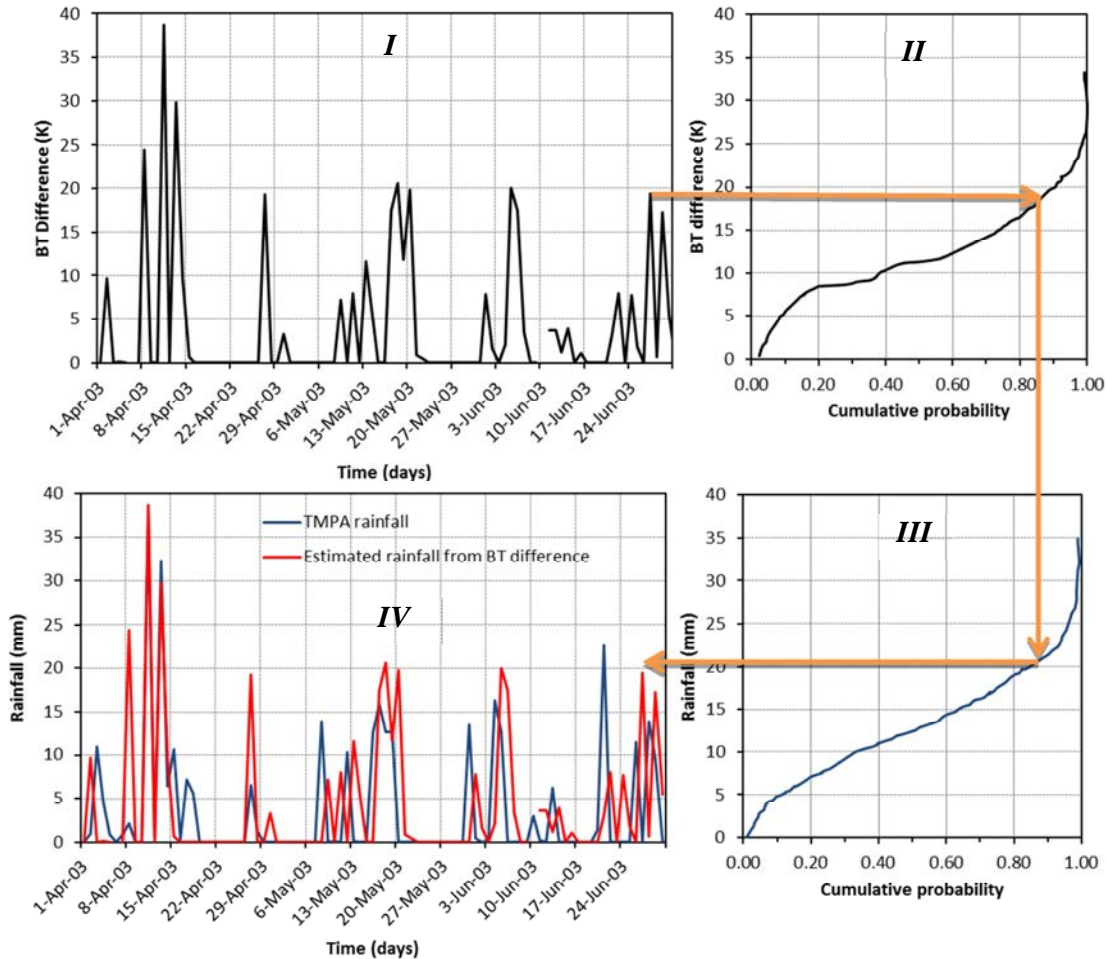


Figure 3.12 Rainfall estimation procedure used in this study

The rainfall estimation starts with calculating cumulative probability of BT difference and TRMM rainfall separately for the study area. Then, for a particular BT difference of a day in plot I, the corresponding cumulative probability is selected from plot II (i.e. cumulative probability of BT difference). Assuming that the cumulative probability of MODIS BT difference is equal to the cumulative probability of TRMM rainfall, the same cumulative probability as BT difference is assigned for rainfall from plot III. This rainfall is considered as the estimated rainfall on that day in plot IV. This process is continued for all days for entire pixels in the BT time series.

3.5.2 Estimation of potential evapotranspiration

Potential Evapotranspiration (PET) is a vital input in streamflow estimation. Recently, RS data have been widely used to estimate PET as well as actual evapotranspiration (AET) (Bastiaanssen et al., 1998a; Camargo et al., 1999; Zhou et al., 2006; Guerschman et al., 2009; Gamage et al., 2011b). Bastiaanssen et al. (1998a) and Su (2002) used RS data in the surface energy balance method to estimate AET by respectively using their Surface Energy Balance Algorithm for Land (SEBAL) and Surface Energy Balance System (SEBS). The surface energy balance method is popular in estimating evapotranspiration due to its low dependency on ground measured data and better representation of evapotranspiration to ground heterogeneity. The surface energy balance method was partly modified and was then used in this study to estimate daily PET.

In the surface energy balance method, the actual evapotranspiration is estimated using both net energy available to evapotranspiration (i.e. net radiation) and sensible heat flux. Net radiation serves as the source of power to drive evapotranspiration, whereas sensible heat flux determines the magnitude of the actual evapotranspiration through its evaporative fraction. Accordingly, actual evapotranspiration (AET_{24}) on any given day can be estimated under SEBAL and SEBS (Bastiaanssen et al., 1998a; Su, 2002) using Equation (3.14):

$$AET_{24} = \frac{86400 \times 10^3}{\lambda \times \rho_w} \times R_{n24} \times \Lambda \quad (3.14)$$

where R_{n24} is the daily averaged net radiation (Wm^{-2}), λ is the latent heat of vaporization (Jkg^{-1}), ρ_w is the density of water (kgm^{-3}) and Λ is the evaporative fraction.

In SEBAL and SEBS, the evaporative fraction is calculated as:

$$\Lambda = \frac{\lambda E}{R_n - G} \quad (3.15)$$

where R_n is the instantaneous net radiation (Wm^{-2}), G is the soil heat flux (Wm^{-2}) and λE is the latent heat flux (Wm^{-2}). According to Bastiaanssen et al. (1998a), the evaporative

fraction is 0 in dry areas where there is no water for evapotranspiration. On the other hand, the evaporative fraction equal to 1 in wet areas where there is sufficient water available for evapotranspiration to take place at its maximum rate (i.e. potential evapotranspiration rate). Hence Equation (3.14) can be modified to estimate the daily potential evapotranspiration PET_{24} (mmday⁻¹) as:

$$PET_{24} = \frac{86400 \times 10^3}{\lambda \times \rho_w} \times R_{n24} \quad (3.16)$$

As can be seen from Equation (3.16), the estimation of PET_{24} requires the calculation of net average radiation (R_{n24}). R_{n24} is calculated differently in this study for non-cloudy days and cloudy days.

3.5.2.1 Estimation of R_{n24} for non-cloudy days

R_{n24} for non-cloudy days is calculated using Equation (3.17) below (Bastiaanssen et al., 1998a; Su, 2002):

$$R_{n24} = (1 - \emptyset) \times K_{day \downarrow} \times \varepsilon_s \times L_{day \downarrow} - L_{day \uparrow} \quad (3.17)$$

where $K_{day \downarrow}$ is the incoming short wave radiation (near the vegetation surface) (Wm⁻²), $L_{day \downarrow}$ is the incoming long wave radiation (near the vegetation surface) (Wm⁻²), $L_{day \uparrow}$ is the outgoing long wave radiation (near the vegetation surface) (Wm⁻²), \emptyset is the surface albedo, and ε_s is the surface emissivity. In Equation (3.17), the $(1 - \emptyset) \times K_{day \downarrow}$ component represents the net short wave radiation, while the remaining components represent the net long wave radiation. PET_{24} can be estimated using Equation (3.16) with R_{n24} estimated from Equation (3.17) for non-cloudy days.

Liang et al. (2002) explained the difficulties involved with the estimation of surface albedo using traditional techniques. Pyranometers or albedometer readings were used to calculate surface albedo under these methods. However, they are site specific, and those readings are not widely available. Therefore, Liang (2001) proposed, and Liang et al. (2002) tested a surface albedo estimation formula with MODIS data using a narrow band to broad band

conversion technique. Using (Equation 3.18):

$$\begin{aligned} \emptyset = & 0.16\lambda_1 + 0.291\lambda_2 + 0.243\lambda_3 + 0.116\lambda_4 + 0.112\lambda_5 + 0.081\lambda_7 \\ & + 0.0015 \end{aligned} \quad (3.18)$$

where, λ_1 , λ_2 , λ_3 , λ_4 , λ_5 and λ_7 are the reflectance values of band 1, 2, 3, 4, 5 and 7 of MODIS data.

The incoming short wave radiation, $K_{day} \downarrow$ of Equation (3.17) is calculated using Bastiaanssen et al. (1998a):

$$K_{day} \downarrow = K_{exo} \times \tau \quad (3.19)$$

where K_{exo} is the extraterrestrial radiation (Wm^{-2}), and τ is the atmospheric transmissivity. K_{exo} can be calculated from Iqbal (1983):

$$K_{exo} = 1367 \times e_0 \times \text{Cos}\theta \quad (3.20)$$

where e_0 is the eccentricity correction factor and θ is the solar zenith angle in radian.

The incoming long wave radiation ($L_{day} \downarrow$) component of Equation (3.17) can be calculated using Equation (3.21) below (Bastiaanssen et al., 1998a; Su, 2002):

$$L_{day} \downarrow = \sigma \times \varepsilon_a \times T_a^4 \quad (3.21)$$

where σ is the Stephan-Boltzmann constant ($5.67 \times 10^{-8} \text{ Wm}^{-2}\text{K}^{-4}$), ε_a is the emissivity of the air as defined by Campbell and Norman (1998) and given by $\varepsilon_a = 9.2 \times 10^{-6} \times (T_a)^2$, and T_a is the atmospheric temperature (K) at the reference height. T_a is obtained from ground measured data.

The outgoing long wave radiation ($L_{day} \uparrow$) component of Equation (3.17) can be calculated

using Equation (3.22) below (Bastiaanssen et al., 1998a; Su, 2002):

$$L_{day} \uparrow = \sigma \times \varepsilon_s \times T_s^4 \quad (3.22)$$

where ε_s is the surface emissivity (unit less) and T_s is the surface temperature (K). Surface emissivity and surface temperature are calculated in this study using RS based vegetation indices and radiance data respectively.

The surface emissivity can be calculated using Equation (3.23) (Bastiaanssen et al., 1998a):

$$\varepsilon_s = 1.009 + 0.047 \times \ln(NDVI) \quad (3.23)$$

where $NDVI$ is the Normalized Difference Vegetation Index. $NDVI$ is calculated using red and near infrared reflectance of satellite images (Tucker, 1979):

$$NDVI = \frac{\lambda_{NIR} - \lambda_{RED}}{\lambda_{NIR} + \lambda_{RED}} \quad (3.24)$$

where λ_{NIR} is the reflectance of near infrared band and λ_{RED} is the reflectance of red band. Theoretically, $NDVI$ values vary from -1 to +1. $NDVI$ values which are less than 0 represent water bodies or clouds, while $NDVI$ values within the range from 0 to 1 represent various LULC classes such as bare soil, sparse vegetation and dense vegetation.

The surface temperature (T_s) in Equation (3.22) can be calculated using MODIS radiance data as:

$$T_s = \frac{T_{rad}}{\varepsilon_s^{0.25}} \quad (3.25)$$

where T_{rad} is the radiant temperature of the surface, which can be calculated using:

$$T_{rad} = [(0.5 \times zPv + 3.1) \times BT_{31} + (-0.51 \times zPv - 2.1) \times BT_{32} + (3.1 - 5.5 \times zPv)] + 0.00627 \times H \quad (3.26)$$

where zPv is the $NDVI$ fraction (unit less), BT_{31} is the brightness temperature of band 31 in MODIS (K), BT_{32} is the brightness temperature of band 32 in MODIS (K) and H is the altitude (m). The altitude value (H) can be obtained from the Shuttle Radar Topography Mission (SRTM) Digital Elevation Model (DEM) over the study area.

zPv of a day can be calculated from $NDVI$ using Equation (3.27) (Valor and Caselles, 1996):

$$zPv = \frac{NDVI - NDVI_{min}}{NDVI_{max} - NDVI_{min}} \quad (3.27)$$

where $NDVI_{min}$ and $NDVI_{max}$ are the minimum and maximum $NDVI$ values of the day respectively.

The brightness temperature of bands 31 and 32 (BT_{31} and BT_{32}) of MODIS can be calculated using the Planck's Equation (i.e. Equation (3.1)).

3.5.2.2 Estimation of R_{n24} for cloudy days

Although the ET process is driven by net radiation, cloud cover reduces the amount of energy reaching the land surface, thereby reducing ET. Young and Sabburg (2006) argued that cloud cover reduces solar radiation (both short and long wave) entering the atmosphere, resulting in a reduction in air temperature and an increase in humidity, irrespective of the time of the day. Reduced air temperature and increased humidity have a direct impact on net long wave radiation.

The R_{n24} of a cloudy day is calculated in this study using the Slob equation, which is given as Equation (3.28) (De Bruin and Stricker, 2000). This equation is similar to Equation (3.17) which was used to estimate R_{n24} for non-cloudy days. Since the Slob equation yields a higher accuracy than other methods such as FAO (Smith et al., 1991; Allen et al., 1998) and KNMI (De Bruin, 1987) in estimating net radiation (De Bruin and Stricker, 2000), it was used in this study.

$$R_{n24} = (1 - \Phi) \times K_{day} \downarrow - \frac{110 \times K_{day} \downarrow}{K_{exo}} \quad (3.28)$$

where \emptyset is the surface albedo, and K_{exo} is the extraterrestrial radiation (estimated using Equation (3.20)). $K_{day} \downarrow$ for a cloudy day is generally computed using the pyranometer readings, which give an indication of cloud cover. If pyranometer readings are not available, as is the case in many areas, the cloud cover can be estimated from RS data. Infrared Global Geostationary Composite (IGGC) images were used in this study to estimate cloud cover with a cloud mask (based on brightness temperature). The duration of cloud cover is calculated from daytime images (every 30 minutes) for each cloudy day. This duration is subtracted from the maximum duration of sunshine hours per day (N), to estimate the actual duration of sunshine hours per day (n). Then, $K_{day} \downarrow$ for a cloudy day is calculated using Equation (3.29) (Allen et al., 1998):

$$K_{day} \downarrow = \left[a + b \frac{n}{N} \right] \times K_{exo} \quad (3.29)$$

where a and b are constants and are respectively equal to 0.25 and 0.5.

The maximum duration of sunshine hours per day (N) is calculated using Equation (3.30) (Allen et al., 1998):

$$N = \frac{24}{\pi} \times \omega_s \quad (3.30)$$

where ω_s is the sunset hour angle.

Albedo (\emptyset) can be calculated only for non-cloudy days using Equation (3.20). The estimation of surface albedo over cloudy days is not possible with reflectance (optical) data since these data do not penetrate through clouds. Assuming that the change of albedo is negligible during a short time (the period of consecutive cloudy days), the nearest non-cloudy day surface albedo is used as surface albedo of the cloudy day to estimate R_{n24} .

3.5.3 Classification of landuse/landcover

Landuse/landcover (LULC) is a key factor that affects evapotranspiration, soil moisture, runoff and groundwater recharge in a catchment (Wegehenkel et al., 2006). RS data have been widely used to produce thematic maps of LULC in field, catchment, regional, country

and global levels (De Fries et al., 1995; Bastiaanssen, 1998; Oetter et al., 2000; Thenkabail et al., 2005; Gamage et al., 2007). The process of making such thematic maps using RS data is called image classification. Two main approaches have been used for image classification. They are: unsupervised classification and supervised classification (Lillesand and Kiefer, 1999). The supervised classification approach was used in this study since it has many advantages over the unsupervised classification approach, as explained in Section 2.4.1.4.

To apply supervised classification on an image, one should have knowledge of existing LULCs over the catchment area. The literature provides ample information on existing LULCs and Table 3.4 shows a broad summary of such LULCs (Lillesand and Kiefer, 1999). Level-I in Table 3.4 describes the broader LULC classes. The initial categorization of available LULC in both catchments (Chapters 4 and 5) shows that all LULC classes in both catchments represent the six classes in Table 3.4. This is contrary to Lillesand and Kiefer (1999) who tabled nine such classes in their original table. Each of these (Level-I) classes can be further divided into sub-classes. This division is important hydrologically since each sub-class responds differently to the runoff generation process. A variety of sub-classes are available in Lillesand and Kiefer's original table, but only relevant sub-classes to both study catchments were extracted and presented under the column labelled Level-II in Table 3.4. A separate field study (or ground-truth data collection) was conducted in each catchment to identify the locations and the signatures of Level-II LULC.

Table 3.4 Landuse/landcover classes
(Adapted from Lillesand and Kiefer, 1999)

Level-I	Level-II
Agriculture	Crop fields
	Pasture (Grasslands)
	Orchards
	Other Agricultural lands (vineyards and nurseries)
Forest	Deciduous forest
	Evergreen forest
	Mixed forest
Urban/buildup	Residential
	Commercial services
	Industrial
	Transportation
Water bodies	Rivers/streams
	Lakes/reservoirs
Wetland	Forested wetland
	Bays/estuaries
Bare/barren	Dry salts
	Beaches
	Dry agriculture

The Landsat 5 TM data (Section 3.3.1.1), which is freely available, were used as RS data for the classification of LULC in the Macalister catchment. Landsat 7 ETM+ (Section 3.4.1.1) data which is gap filled and also freely available were used as RS data for the classification of LULC in the Ribb catchment because of the absence of Landsat 5 TM data. A single image which is free of clouds, haze and distortion was selected for each catchment, since no major changes occurred in LULC during the study period (2003 to 2008).

A methodology slightly different to the one used by Gamage et al. (2007) and Panda et al. (2009) was employed in this study for image classification. The two above mentioned studies used the supervised image classification technique to develop LULC maps for hydrological and agricultural applications respectively. Gamage et al. (2007) used the Principal Component Analysis (PCA) to develop a new, reduced number of variables from the original bands. These new variables were used in LULC classification. In addition to

PCA, they used the Normalized Difference Vegetation Index, (*NDVI*) (Tucker, 1979) to separate vegetation areas from non-vegetation areas. In this study, *NDVI* was used as an additional variable to classify the image, since it can reduce the mountain shadows and improve the sensitivity to vegetation. Furthermore, Feature Space Images (FSI) were used to identify and cluster the signature of each given LULC class. The feature space image is a two-dimensional representation of an image. It is a scatter graph of all pixel values of an image, with different colors representing histogram frequencies of pixels. The main steps of image classification, which were used in this study, are summarized below.

3.5.3.1 Ground-truth data collection

The knowledge of existing ground situation on the catchment is essential for image classification, which includes training, class identification, naming of classes and accuracy assessment (Thenkabail et al., 2008). To achieve this, ground information of the catchments were collected through two separate ground-truth data collection surveys for each catchment. These surveys covered sample areas of each LULC available in those two catchments. Vegetation type, growth stage, soil condition and terrain conditions were collected through these surveys; the survey form used is included in Appendix B. Initially a sample area which was large enough and homogenous in its LULC was selected. Then sample points (i.e. ground-truth data points) within a sample area were carefully selected to represent the different signatures of the particular LULC class.

3.5.3.2 Training of satellite image

The training stage of image classification involved the pre-processing of the satellite image as well as signature identification. As mentioned earlier, the Landsat 5 TM image was used to classify the Macalister catchment's LULC, while the Landsat 7 ETM+ image was used to classify the Ribb catchment's LULC.

The Landsat 5 TM image is georeferenced, and consists of 7 bands. These bands represent visible, infrared, mid infrared and thermal infrared windows of the electromagnetic spectrum. The thermal infrared band (i.e. band 6) of the Landsat TM images was not considered for the classification. This is mainly due to the mismatching of spatial resolutions in thermal and other bands. Indeed, the spatial resolution of the thermal band is

120 m while it is 30 m in all other bands. The remaining 6 bands consist of blue, green, red, near infrared and two mid infrared bands.

The Landsat 7 ETM+ image is also georeferenced, but consists of 8 bands. These bands represent visible, infrared, mid infrared, thermal infrared and panchromatic windows of the electromagnetic spectrum. The thermal infrared band (i.e. band 6) of the Landsat 7 ETM+ images was not considered for classification since its spatial resolution mismatches with the other bands: the spatial resolution of the thermal band is 60 m while it is 30 m in all other bands. The panchromatic band was also eliminated in LULC classification due to its spatial resolution mismatching (15 m). There is some consistency in using TM and ETM+ data which are used to classify LULC over the Macalister and the Ribb catchments respectively, in terms of the 6 bands used (namely the blue, green, red, near infrared and the two mid infrared bands).

Due to the availability of many bands (6 bands in this study), some of the ground information could be repetitive in each band, and may hence adversely affect the classification. Therefore, the Principal Component Analysis (PCA), a mathematical transformation which is based on the linear combination of the band measurements, was used to reduce the number of bands. PCA was used in this study to reduce the number of bands without making useful information redundant (Panda et al., 2009). It was argued that the variables selected using PCA are not correlated, and are often more interpretable with respect to ground information than source data (Faust, 1989); (Jensen, 1996).

In this study, half of the ground-truth data (i.e. half of the sample areas) which was collected through field work was used to train the image for its classification. These data were randomly selected from the ground-truth data. It should be noted that there is no strict rule for the allocation of the number of training samples out of the total samples for classification, with various proportions being found in literature. For example, Shupe and Marsh (2004) and Gamage et al. (2007) respectively used 70 and 50% of ground-truth data for image training. However, the author hereby intends that training samples should fully represent the signatures of each LULC class, irrespective of the above percentages.

One LULC class in a sample area may have a number of different signatures in the image for various reasons. As an example, the signature within the class of pasture could be

different from place to place due to water availability, the soil conditions and management practices. These different signatures within one class could overlap with another class and could lead to a faulty classification. The Feature Space Image (FSI), which is a graphical representation of the band values, was used to avoid such situations, since FSI helps to identify the variation in the signature of a particular LULC class (Gamage et al., 2007). Different signatures which were identified within one class were not merged together, to form one signature since such a merging process can cause inaccuracies in the LULC classification. The output of this stage, which is the trained image for its existing LULC classes, was used as input for the classification stage (Section 3.5.3.3).

3.5.3.3 Classification stage

After the training stage, all pixels of the image are categorized into the LULC classes they mostly resembled. This is the classification stage (Lillesand and Kiefer, 1999). For classification, numerous mathematical approaches such as the maximum distance to mean, the parallelepiped and the maximum likelihood are available, and out of those, the maximum likelihood method was used in this study. This method was specially selected as the accuracy with which it classifies all pixels in an is higher than the other approaches (Lillesand and Kiefer, 1999).

The maximum likelihood classifier assumes that *NDVI* and the PCA component's for each pixel are normally distributed. Under this assumption, the distribution of the pixel values in a given LULC class can be defined with its mean vector and covariance matrix (Lillesand and Kiefer, 1999). Based on these two parameter matrices, the statistical probability of each pixel is computed for a member of the particular LULC class. This process is done for all pixels by taking into account all LULC classes, thereby producing different probabilities of the likelihood of a particular LULC class in each pixel. Then each of the pixel in the image is assigned to the most appropriate LULC class based on the higher probability.

3.5.3.4 Accuracy assessment

The outcome of the classification stage is simply a model of the ground reality based on the LULC signature (Loveland et al., 1999). Therefore, these image classifications have model errors. These errors are due to the loss of information resulting from the

rasterization or simplification of complex ground reality in the model (Maling, 1989). These errors should be considered in identifying the quality of the map, and its suitability and implications to any given application. For this purpose, the remaining half (i.e. sample areas) of the ground-truth data (first half of the ground-truth data was used to train the image) was used to estimate the classification accuracy. Once again, there are no clear guidelines on the required sample size for testing data in the case of estimating the classification accuracies. Congalton (1991) mentioned that a minimum of 50 samples for each class can be used for testing. However, this minimum sample size varies with the size of the study area, homogeneity of LULC classes, and the number of classes in the classification (Gamage et al., 2007).

The accuracy assessment of LULC has been discussed in detail by Congalton (1991), Foody (2002) and Wegehenkel et al. (2006). According to these academics, the accuracy of both individual classes and overall classification is important to understand the strength of the classification. Congalton (1991) stated that the classification accuracy measurement techniques can be categorized into two types: descriptive techniques and analytical techniques.

Descriptive techniques are defined as simple ratios of correctly classified sample points to class total. They give a general idea about the accuracy level, in the producer's and the user's perspective as well as in the overall view of all the classes. The producer's accuracy is the probability of correctly classifying an LULC class relevant to its reference total, and the user's accuracy is the probability of correctly classifying an LULC class in the image that actually represents the same LULC class on the ground. The overall accuracy is the number of correctly classified samples in the total number of samples. These accuracies are further explained in Figure 3.13 (Congalton, 1991).

A particular class can be classified with a higher level of accuracy on a purely random basis, which is not a correct classification. Therefore, analytical techniques are used to address this issue. Both descriptive and analytical techniques were used in this study for both catchments to estimate the level of accuracy of individual LULC classes as well as the overall accuracy of all classes together (i.e. the overall LULC accuracy).

The process of estimating accuracies using test data can be explained using the error matrix of Figure 3.13. This figure shows a matrix of a classified image with a number of classes labelled A, B, C and D. Each blue cell represents the number of pixels that has been classified under a certain class with respect to its actual or reference class. For example N_{BB} refers to the number of pixels that has been classified as class B, from the set which is actually in class B. The total of each class under each row and column are represented by Σ in the matrix. The diagonal view of this figure shows the correctly classified number of points (pixels) of each class. The statistics known as the producer's accuracy, the user's accuracy and the overall classification accuracy (Foody, 2002; Wegehenkel et al., 2006; Gamage et al., 2007) can be estimated based on this matrix.

Predicted Classes	Actual (reference) Classes				
	A	B	C	D	Σ
A	N_{AA}	N_{AB}	N_{AC}	N_{AD}	N_{A+}
B	N_{BA}	N_{BB}	N_{BC}	N_{BD}	N_{B+}
C	N_{CA}	N_{CB}	N_{CC}	N_{CD}	N_{C+}
D	N_{DA}	N_{DB}	N_{DC}	N_{DD}	N_{D+}
Σ	N_{+A}	N_{+B}	N_{+C}	N_{+D}	N

Figure 3.13 Error matrix of classified image in terms of number of pixels

The producer's accuracy (or omission error) measures the probability of correctly classifying an individual class with regard to its reference total (i.e. column total). It gives an indication of how accurately an LULC map is produced. The producer's accuracy (PA) is found by dividing the number of correctly classified samples in an individual class (e.g. N_{AA}) by the total of that class (e.g. N_{+A}). It is calculated using Equation (3.31) by taking class A as an example:

$$PA = \frac{N_{AA}}{N_{+A}} \times 100 \quad (3.31)$$

The user's accuracy (or commission error) indicates whether the LULC of a given location in the classified image actually represents that LULC class on the ground. Therefore, this accuracy is an important indication for subsequent users of the LULC. The user's accuracy

(UA) is calculated by dividing the number of correctly classified samples in an individual class (e.g. N_{AA}) by predicted total of that class (e.g. N_{A+}).

Once again while taking class A as example, UA is calculated using Equation (3.32):

$$UA = \frac{N_{AA}}{N_{A+}} \times 100 \quad (3.32)$$

The overall classification accuracy (OA) is calculated by dividing the number of correctly classified pixels (sum of the diagonal) by the total number of pixels (N). This is calculated using Equation (3.33):

$$OA = \frac{(N_{AA} + N_{BB} + N_{CC} + N_{DD})}{N} \times 100 \quad (3.33)$$

Even though the accuracy of the image classification can be high in terms of PA, UA and OA, there is a possibility of having such a high accuracy by classifying particular pixels into a particular class, purely by chance (Congalton, 1991). This is caused to reduce the faithfulness of the image classification process, leading to incorrect classification and hence adverse effect on applications. In order to account for this chance, the kappa coefficient which is described as an analytical tool (Cohen, 1960; Congalton, 1991; Smits et al., 1999; Foody, 2002), can be used. The Kappa coefficient is calculated using Equation (3.34):

$$\hat{K} = \frac{N \sum_{k=1}^q N_{kk} - \sum_{k=1}^q N_{k+} N_{+k}}{N^2 - \sum_{k=1}^q N_{k+} N_{+k}} \quad (3.34)$$

where \hat{K} is the Kappa coefficient, N is the total number of pixels, N_{kk} is the total of diagonal (total of correctly classified), N_{k+} is the row total in Figure 3.13, N_{+k} is the column total in Figure 3.13, and q is the total number of classes.

Although the accuracy assessment has been widely accepted as a standard practice for image classification, the accepted levels of accuracy (or thresholds) to a given LULC classification vary depending on applications and the scale of the application (Thomlinson

et al., 1999). Considering the scale of the application and spatial resolution of the satellite data used in this study, the following thresholds were used. They are:

- (i) An overall classification accuracy of no less than 85%,
- (ii) An individual class accuracy (both PA and UA) of no less than 70% (i.e. class A, B, C, or D in Figure 3.13). These thresholds were proposed and used by Thomlinson et al. (1999).
- (iii) The kappa coefficient of less than 0.4 is deemed to be poor classification, 0.4 – 0.75 is treated as a good classification and above 0.75 is considered as an excellent classification. These thresholds were proposed and used by Bharatkar and Patel (2013).

Both the accuracy thresholds and the kappa thresholds were used in this study to evaluate the accuracy of the LULC classification.

3.6 Catchment process modelling

The *Soil and Water Assessment Tool* (SWAT) was used to estimate daily streamflow of the two study catchments. Initially, daily streamflow estimation was done with ground measured data. Then, the ground measured data of input variables were replaced with those estimated from RS data, one variable at a time. When setting up the SWAT model with ground measured input variables, all hydrological components such as precipitation, canopy storage, infiltration, redistribution, evapotranspiration, lateral subsurface flow, surface runoff, ponds, tributary channels and return flow were considered.

3.6.1 Brief description of SWAT

SWAT is a deterministic and semi-distributed software tool that can be used for continuous streamflow estimation. SWAT can be used not only to estimate surface flow, but also to estimate subsurface flow, sediment generation, chemical concentration, vegetation growth and the effects of pesticide use. SWAT is freely available to the user community (i.e. it is a public domain software tool), which is supported by the Agricultural Research Service (ARS) Division of the United States Department of Agriculture (USDA) at the Grassland, Soil and Water Research Laboratory in Temple, Texas, USA. SWAT operates in catchment scales, and has the capability of processing data efficiently over large areas,

of supporting spatially distributed catchment details and of simulating land-management scenarios (Arnold et al., 1998). The model can run with various time scales such as daily, monthly and annual. SWAT was used in this study with the daily time step.

SWAT is a water balance model, which is expressed below, when it is used as a daily model (Arnold et al., 1998):

$$SW_t = SW_0 + \sum_{i=1}^t (R - Q_{surf} - E_a - W_{seep} - Q_{ret}) \quad (3.35)$$

where, SW_t is the soil water content at the end of day i , SW_0 is the initial soil water content on day i , t is the time in days from the start of the simulation, R is the amount of precipitation on day i , Q_{surf} is the amount of surface runoff on day i , E_a is the amount of actual evapotranspiration on day i , W_{seep} is the amount of water entering the vadose zone from the soil profile on day i , and Q_{ret} is the amount of return flow on day i . All units are in mm.

Surface runoff (Q_{surf}) is the major component of the water balance in Equation (3.35) and is estimated using the SCS curve number method given below (USDA-SCS, 1972; Arnold et al., 1998):

$$Q_{surf} = \frac{(R - 0.2S)^2}{(R + 0.8S)} \quad (3.36)$$

where R is the rainfall depth for day i and S is the retention parameter. The retention parameter is defined as:

$$S = 254 \left(\frac{100}{CN} - 1 \right) \quad (3.37)$$

where CN is the curve number. More details on the curve number method can be found in USDA-SCS (1972).

The return flow is generated by considering a shallow aquifer (Arnold et al., 1998), and the lateral flow element of the model is estimated using the kinematic storage model. A detailed explanation of all steps and equations used in the estimation of evapotranspiration, seepage, return flow, and their routing techniques together with the model structure can be found in Arnold et al. (1998), Setegn (2010) and Tibebe and Bewket (2011). The model set up and calibration steps are briefly explained in Section 3.6.2.

3.6.2 Model set up and calibration

The setting up of the SWAT model to any catchment begins with “watershed delineation”, and it uses the Digital Elevation Model (DEM). For modelling purposes, SWAT delineates the catchment into several subcatchments with the help of DEM. The size of the subcatchment is automatically determined by SWAT initially. However the user has the freedom to change the subcatchment size.

Once the watershed is demarcated, spatially distributed LULC and soil types are entered as inputs into the model in the grid format. Based on the input percentage of the LULC, soil type and slope (based on DEM) of each subcatchment, SWAT generates several working elements called Hydrological Response Units (HRUs) within each subcatchment (Zhang et al., 2009a).

The next step of the model setup is to enter meteorological data. Measured climate data such as rainfall, minimum and maximum temperature, relative humidity, wind speed and sunshine hours are entered as input variables to the SWAT model. All the above input variables together with their spatial locations are required to be fed into the model (Arnold et al., 1998). The acceptable format and other specifications of these data are explained in the SWAT user manual (Neitsch et al., 2002). In the absence of daily data for the above meteorological input variables (fully or partially), SWAT has the power to generate missing climatic data of a time series. This is based on its *weather generator*, which uses statistical procedures to fill the gaps of missing data.

The SWAT weather generator uses different models to fill/generate missing data of input variables. In the case of rainfall, it uses the Markov chain-skewed (Nicks, 1971) or the Markov chain-exponential (Williams, 1995) models to fill/generate missing rainfall data.

The user has the option to select either model while running the SWAT model. The maximum and minimum temperatures and solar radiation estimations are based on the weakly stationary generating process by Matalas (1967). The Daily average relative humidity values are estimated from a triangular distribution using average monthly relative humidity (Sharpley and Williams, 1990), while mean daily wind speed is generated by the modified exponential equation (Neitsch et al., 2005). More details of the weather generator can be found at SWAT theoretical documentation (Neitsch et al., 2005).

SWAT can estimate potential evapotranspiration (PET) using meteorological data that have been fed into the model. Three prominent PET estimation methods i.e. the Penman-Monteith (PM) method (Allen et al., 1998), the Hargreaves method (Hargreaves et al., 1985) and Priestley-Taylor method (Priestley and Taylor, 1972) are available as in-built options. There is also an option to enter a PET time series that has been computed outside of the SWAT model.

The SWAT model was initially calibrated with 2/3 of the streamflow data. The remaining 1/3 of the measured streamflow data was used to validate the estimation model. Accordingly, data corresponding to years 2003 – 2006 and 2007 – 2008 were respectively used for calibration and validation. Initially, the model calibration was done by manually adjusting various model parameters within the appropriate range. Thus initial manual calibration was then fine-tuned with the auto calibration and validation tool available within the SWAT software tool. The parameter solution (PARASOL) method (van Griensven et al., 2006) available within the SWAT software tool was used as the auto-calibration method in this study.

The accuracy of the daily streamflow estimation (i.e. for calibration and validation separately) was evaluated with Root Mean Square Error (*RMSE*) and Nash-Sutcliffe efficiency (E_f) (Nash and Sutcliffe, 1970; Pala, 2003). The calculation procedures of *RMSE* and E_f are explained in Section 3.9.

3.7 Estimation of remote sensing based indices for statistical modelling

This section will explain the methods of calculating RS based indices (i.e. vegetation and thermal indices) that were used in statistical modelling. The existing literature was carefully studied before selecting indices for statistical modelling purposes.

3.7.1 Selection of remote sensing based indices

Various RS based indices, which are surrogates to hydrometeorological variables, were considered as possible inputs for statistical modelling in this study. Vegetation indices such as the Normalized Difference Vegetation Index (*NDVI*), the Enhanced Vegetation Index (*EVI*) and the Normalized Difference Water Index (*NDWI*), and the brightness temperature at band 31 (*BT31*) and the brightness temperature at band 32 (*BT32*), and thermal indices such as the brightness temperature difference (*BT_{diff}*) (*BT31* – *BT32*) and the brightness temperature gradient (*BT_{grad}*) were used as RS based indices in statistical modelling.

NDVI is the most common and simple RS based vegetation index that has been used in many applications, such as hydrological applications, ET estimation and LULC classification. It represents vegetation density, vigor, vegetation stage and their seasonality (Jackson et al., 2004; Thenkabail et al., 2004). Furthermore, it has been used to estimate the Leaf Area Index (*LAI*), which is a vital variable in hydrological process modelling. Even though *NDVI* is a representative index of vegetation, it does not reflect the vegetation water content. Among various vegetation indices, *NDWI* is simple and sensitive to the vegetation water content (Jackson et al., 2002). Since the vegetation water content is sensitive to moisture availability of the top soil (i.e. the root zone area), *NDWI* is also a surrogate of soil moisture content for that zone. Therefore, *NDWI* was considered in this study as a surrogate to vegetation water content and soil moisture.

NDVI is sensitive to atmospheric noise (Jackson et al., 2004), and can adversely affect on streamflow estimation undertaken through statistical modelling. Therefore, *EVI* was used to overcome this disadvantage of *NDVI*. *EVI* has been developed to overcome atmospheric noise and to optimize the vegetation signal in order to improve the sensitivity to vegetation variability (Huete et al., 2002).

The above mentioned indices are surrogates for vegetation and soil moisture. Thus radiance based BT_{31} , BT_{32} , BT_{diff} and BT_{grad} were used as surrogates to rainfall. The brightness temperature has been used as an input to estimate rainfall since the late 1970s (Arkin, 1979; Grimes et al., 1999; Grimes and Diop, 2003; Huffman et al., 2007). The band width of the brightness temperature data which are used in the above studies are equivalent to MODIS band 31. In addition to this band, MODIS includes band 32. Band 32 of MODIS is adjusted to band 31 in electromagnetic spectrum. This is also a thermal band, and thus was considered in this study as a possible input to streamflow estimation using statistical modelling.

In prior studies, rainfall from a cloud cover (observed from the top of the cloud) was estimated by assigning a constant rain rate to the brightness temperature below a certain threshold. Whilst this constant rate is not the best representation of rainfall yielded from a cloud, Kuligowski (2002) noted that cloud-top textural information can be used better in rainfall estimation. Therefore, BT_{diff} and BT_{grad} , which are representative indices to cloud-top texture, were used as possible input variables in this study.

3.7.2 Equations used to generate remote sensing based inputs for statistical modelling

MODIS reflectance data were used to calculate vegetation indices (i.e. $NDVI$, $NDWI$ and EVI), and MODIS radiance data were used to calculate brightness temperatures (BT_{31} and BT_{32}) and thermal indices (i.e. BT_{diff} and BT_{grad}). Vegetation indices were calculated only on no-cloudy images, while BT and thermal indices were calculated on cloudy images. Cloudy images (or cloudy days) were separated from non-cloudy images (or non-cloudy days) using MODIS cloud mask product.

The calculation procedure and equation for $NDVI$ are explained in Section 3.5.2.1 and Equation (3.24). The calculation of $NDWI$ is similar to the $NDVI$, except bands used in $NDWI$. Indeed, while short-wave infrared was used in $NDWI$ calculations, the red band was used for calculating $NDVI$.

$NDWI$ was calculated using Equation (3.38) (Gao, 1996; Jackson et al., 2004):

$$NDWI = \frac{\lambda_{NIR} - \lambda_{SWIR}}{\lambda_{NIR} + \lambda_{SWIR}} \quad (3.38)$$

where λ_{SWIR} is the reflectance of the short-wave infrared (band 5 of MODIS), and λ_{NIR} is the reflectance of the near infrared (band 2 of MODIS).

EVI on a non-cloudy day was calculated using MODIS reflectance of band 1, 2 and 3 (Huete et al., 2002):

$$EVI = G \times \frac{\lambda_{NIR} - \lambda_{RED}}{\lambda_{NIR} + C_1 \lambda_{RED} - C_2 \lambda_{BLUE} + L} \quad (3.39)$$

where λ_{RED} is the reflectance of MODIS band 1, λ_{BLUE} is the reflectance of MODIS band 3, *G* is the gain factor (2.5), *L* is the canopy background adjustment (for full canopy, *L* = 1), and *C*₁ and *C*₂ are the coefficients of the aerosol resistance term, which uses the blue band (i.e. band 3) to correct for aerosol influences in the red band (i.e. band 1). *C*₁ and *C*₂ are respectively equal to 6 and 7.5 respectively, as suggested by Huete et al. (2002).

As explained in Section 3.7.1, *BT*₃₁, *BT*₃₂, *BT*_{diff} and *BT*_{grad} were considered as surrogates for rainfall in this study. *BT*₃₁ and *BT*₃₂, which were calculated from Equation (3.1) for rainfall estimation purposes (Section 3.5.1.1), were used in statistical modelling. These *BT*₃₁ and *BT*₃₂ were used to calculate *BT*_{diff}. *BT*₃₁ was also used to calculate *BT*_{grad}.

*BT*_{diff} was calculated using Equation (3.40):

$$BT_{diff} = BT_{31} - BT_{32} \quad (3.40)$$

The *BT*_{grad} was initially introduced by Adler and Negri (1988) and has been used by Kuligowski (2002) for rainfall estimation. They calculated *BT*_{grad} by calculating the difference of the average temperature and the minimum temperature of a 5×5 pixel window, and dividing it by the pixel resolution. The use of the average can result in reducing the gradient, which in turn has the potential of identifying the cloud as a cirrus cloud which produces no-rain. Therefore, the difference between the minimum and

maximum values divided by the pixel resolution of a 3×3 pixel window was considered as BT_{grad} in this study.

3.8 Statistical modelling

Artificial neural networks (ANN) were used in this study as the statistical modelling technique to estimate daily streamflow in both study areas. ANN were used in this study since the relationship between vegetation and thermal indices as well as BT with streamflow is very complex, and ANN have the capability to address complex relationships between inputs and output (Govindaraju and ASCE Task Committee on Application of Artificial Neural Networks in Hydrology, 2000; Maier and Dandy, 2000; Samarasinghe, 2006; ASCE Task Committee on Application of Artificial Neural Networks in Hydrology, 2000).

Possible input variables, which were outlined in Section 3.7.1, were considered in daily streamflow estimation using statistical modelling. Catchment average value of each variable was considered in this study for streamflow estimation rather than at a particular pixel. This was mainly to avoid errors in streamflow estimation with noisy pixels. Furthermore, the catchment average gives a better representation for the varying landuse/landcover conditions in the catchment.

The current day, several past days and 8-day average of possible input variables (Section 3.7.1) were considered in statistical modelling. The lagged variables were considered because of the lagged response of rainfall to streamflow, and rainfall to vegetation. On this basis, vegetation indices of seven lag days, and thermal indices and BT of three lag days were considered in this study. In addition to those variables, the previous 8-day average of *NDVI*, *NDWI* and *EVI* were also considered as input variables to model the current-day streamflow. The missing values of previous days are excluded in estimating 8-day average. By doing so, a seamless time series of 8-day average *NDVI*, *NDWI* and *EVI* was generated. Eight day averages were specifically considered since there is no significant difference in vegetation indices within the 8-day period and that is sufficient enough to fill the gaps caused by the clouds.

There are 43 variables present as potential input variables for daily streamflow estimation using statistical modelling by considering the current day, lag times and the average of variables. All those 43 variables are shown in Tables 3.5 (for vegetation indices) and 3.6 (for BT and thermal indices).

Table 3.5 Vegetation indices of current day, lag days and 8-day average

Vegetation indices		
<i>NDVI</i>	<i>NDWI</i>	<i>EVI</i>
1-day lag <i>NDVI</i>	1-day lag <i>NDWI</i>	1-day lag <i>EVI</i>
2-day lag <i>NDVI</i>	2-day lag <i>NDWI</i>	2-day lag <i>EVI</i>
3-day lag <i>NDVI</i>	3-day lag <i>NDWI</i>	3-day lag <i>EVI</i>
4-day lag <i>NDVI</i>	4-day lag <i>NDWI</i>	4-day lag <i>EVI</i>
5-day lag <i>NDVI</i>	5-day lag <i>NDWI</i>	5-day lag <i>EVI</i>
6-day lag <i>NDVI</i>	6-day lag <i>NDWI</i>	6-day lag <i>EVI</i>
7-day lag <i>NDVI</i>	7-day lag <i>NDWI</i>	7-day lag <i>EVI</i>
8-day avg <i>NDVI</i>	8-day avg <i>NDWI</i>	8-day avg <i>EVI</i>

Table 3.6 BT and thermal indices of current day and lag days

BT and thermal indices			
<i>BT31</i>	<i>BT32</i>	<i>BT_{diff}</i>	<i>BT_{grad}</i>
1-day lag <i>BT31</i>	1-day lag <i>BT32</i>	1-day lag <i>BT_{diff}</i>	1-day lag <i>BT_{grad}</i>
2-day lag <i>BT31</i>	2-day lag <i>BT32</i>	2-day lag <i>BT_{diff}</i>	2-day lag <i>BT_{grad}</i>
3-day lag <i>BT31</i>	3-day lag <i>BT32</i>	3-day lag <i>BT_{diff}</i>	3-day lag <i>BT_{grad}</i>

The increased number of input variables (43) can cause input replication in ANN modelling. All the indices outlined in Tables 3.5 and 3.6 are based on seven key indices, and these seven indices are based five bands of MODIS. In addition, the introduction of lag time and the average of indices can further enhanced the issue of ANN input replication to ANN modelling. Since replication and the increased number of input variables can made the ANN model very complex (Bowden et al., 2005a), an input variable selection procedure was followed to identify the most influential input variables that should be used in the ANN model for both catchments.

3.8.1 Influential inputs

Several input variable selection methods have been used with ANN modelling in the recent past (Sharma, 2000; Maier and Dandy, 2000; Bowden et al., 2005a; Maier et al., 2010), especially in water resources applications. They vary from the use of correlation coefficient to the use of genetic algorithms. The calculation of correlation coefficients between independent variables and dependent variables is a direct approach, but may not be suitable to many water resources applications due to the complex non-linear relationship between independent and dependent variables. Accordingly, Sharma (2000) outlined that Mutual Information (MI) could be used to identify influential variables for ANN applications, particularly water-related ones.

The MI criterion is a measure of dependence between any two variables (Sharma, 2000). MI has the ability of capturing all dependencies (linear and/or nonlinear) between independent and dependent variables. With MI, no prior assumption is required to consider the relationship between the dependencies of the variables. More importantly, MI is insensitive to noise of the data and is strong in data transformation (Battiti, 1994; Darbellay, 1999; Soofi and Retzer, 2003; May et al., 2008). The higher the value of MI, the higher the dependence between the variables. The calculation of MI takes place iteratively: as such one disadvantage of MI is the lack of suitable analytical method to decide when the optimal set of variables has been selected. To overcome this disadvantage, Sharma (2000) developed the concept of Partial Mutual Information (PMI) which provides an additional criterion to assist on making decision of when to stop the iteration and select influential variables. PMI can be written as (Sharma, 2000);

$$PMI = \frac{1}{n} \sum_{i=0}^n \log_e \left[\frac{f_{x'_i y'}(x'_i, y'_i)}{f_{x'}(x'_i) f_{y'}(y'_i)} \right] \quad (3.41)$$

where $f_{x'_i y'}(x'_i, y'_i)$, $f_{x'}(x'_i)$ and $f_{y'}(y'_i)$ are the respective marginal and joint probability densities of independent and dependent variables. n denotes the sample size of the data.

PMI applies the partial dependency between independent and dependent variables to the existing prediction model (based on MI). This partial dependency is calculated for each and every potential input variable individually. However, a necessary part of the PMI based input selection method is a criterion that signals which input is influential. Sharma

(2000) has used the 95th percentile of randomized sample PMI as the confidence measure to determine the influential input variables from a pool of input variables. By selecting the 95th percentile, he argued that there is a 5% chance of the input variable to be truly independent. Considering that, the limit that can be truly independent was further reduced to 1% in this study by choosing 99th percentile of a randomized sample PMI as the confidence measure. This step was followed to reduce number of influential variables to its minimum.

3.8.2 Artificial neural networks modelling

Various ANN model architectures have been used in the past for applications in water-related research (Mas and Flores, 2007; Maier et al., 2010). They were discussed Section 2.6. According to the literature, model selection and model construction are the two important steps in developing an ANN model for any application. Model selection involves finding an appropriate model for a given application. Model construction deals with the selection of input variables, and the selection of the number of hidden layers and their nodes, as well as the selection of transfer functions and objective functions to calibrate and validate the model.

The widely used three-layer feed-forward neural networks with back propagation was used in this study. It has the capacity to handle complex relationship between inputs and outputs with sufficient degree of freedom with regards to weights and biases (Maier and Dandy, 2000). Furthermore, it was noted that feed-forward multilayer perceptron models have been widely used in different RS based applications including water resources research (Maier et al., 2010). An illustration of a three-layer feed-forward neural networks model is shown in Figure 3.14. The three layers are the input layer (*I*), the hidden layer (*H*) and the output layer (*O*).

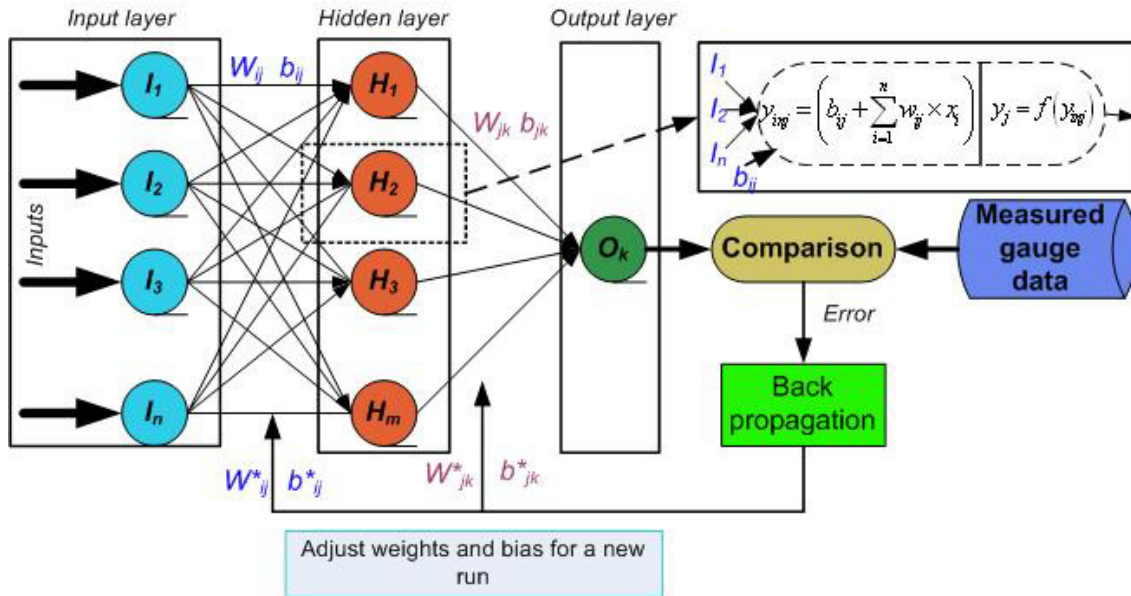


Figure 3.14 Three layer feed-forward ANN used in this study
(Adapted from Kim and Valdes, 2003)

In Figure 3.14, the input nodes are denoted as I_i ($i = 1, 2, 3, \dots, n$) in the input layer, and the hidden nodes are denoted as H_j ($j = 1, 2, 3, \dots, m$) in the hidden layer. n represents the number of nodes in the input layer (this is equal to the number of input variables in this study), while m represents the number of hidden nodes (determined by trial and error during the calibration of the model). The output node in this study is denoted as O_k . A single node is considered (i.e. estimated streamflow) in the output layer. The weights of the feed-forward process are denoted with W_{ij} (input layer to hidden layer) and W_{jk} (hidden layer to output layer), while the new weights at each iteration results from the back propagation process are denoted as W^*_{ij} (input layer to hidden layer) and W^*_{jk} (hidden layer to output layer). Similar to the weights, the biases of the feed-forward process are denoted as b_{ij} (input layer to hidden layer) and b_{jk} (hidden layer to output layer), and new biases in each new iteration resulting from the back propagation process are denoted as b^*_{ij} (input layer to hidden layer) and b^*_{jk} (hidden layer to output layer). There is only one bias between the input and hidden layers, and between the hidden and outputs layers. However, there are $(n \times m)$ weights between the input and hidden layers, and m weights between the hidden and output layers.

Learning rate provides the step size during the gradient descent in updating neural network weights. This controls the rate that weights are allowed to change at any given training

cycle (Raman and Sunilkumar, 1995). It has been observed that higher learning rate increases the convergence process in learning, causing results to be unrealistic. The slower learning rate produces more reliable results (Raman and Sunilkumar, 1995; Maier and Dandy, 1996; Isik et al., 2013) however, such slower learning rate requires high computing power to update the neural network weights. Therefore, an optimum value of 0.3 that had been used in previous studies was used as the learning rate in this study (Maier and Dandy, 1996; Isik et al., 2013).

Figure 3.14 shows that any particular layer is connected to its subsequent layer by relationships whose strengths rely on the magnitudes of the weights (i.e. W_{ij} and W_{jk}) and biases (i.e. b_{ij} and b_{jk}) (Sahoo and Ray, 2006). These weights and biases are optimized through the training procedure to obtain the best simulation result against the output. Nonlinear transfer functions are generally used to transfer the values of the input layer nodes to the hidden layer nodes, whereas the linear transfer functions are generally used to transfer the values from the hidden layer nodes to the output layer nodes (Maier et al., 2010). Among various non-linear transfer functions, Maier et al. (2000), and Sahoo and Ray (2006) stated that TRANSIG was the best function that can be used to transfer the values of the input layer nodes to the hidden layer nodes, particularly in water related applications. Dorofki et al. (2012) tested the performance of several linear transfer functions to transfer the values of the hidden layer nodes to the output layer nodes in runoff estimation and found better performance with the PURELIN transfer function. Sahoo and Ray (2006) in their flow forecasting application also used PURELIN. Therefore, in this study, a non-linear (TANSIG) transfer function combined with the values of the input layer nodes and corresponding weights and biases were used to produce the values of the hidden layer nodes, and a linear (PUERLIN) transfer function combined with the values of the hidden layer nodes and corresponding biases were used to produce the values of the output layer node (Gamage et al., 2011a). The mathematical relationship between input and output can be written as Equation (3.42) (Kim and Valdés, 2003).

$$\widehat{SF} = f_0 \left[\sum_{j=1}^m W_{jk} \times f_h \left(\sum_{i=1}^n W_{ij} x_i + b_{ij} \right) + b_{jk} \right] \quad (3.42)$$

where, \widehat{SF} is the estimated streamflow, f_o is the transfer function of the output neuron, f_h is the transfer function of the hidden neuron, x_i is the input of the input neuron, and i represents an input variable.

It is a general practice that data of all input variables are converted into a standard range (generally 0 to 1) before they are used in an ANN model. This will facilitate the building of more efficient weights between the input layer nodes and the hidden layer nodes (Tran et al., 2009; Maier et al., 2010). The reflectance (vegetation) based input variables of *NDVI* and *NDWI* mostly vary on this range, however, *EVI* and radiance based input variables do not. Therefore, all input variables were standardized into the range of 0.1 to 0.9 (instead of 0 to 1) to avoid the extreme limits of the nonlinear transfer function used to transfer the values of the input layer nodes to the hidden layer nodes (Barua, 2010).

All influential input variables which resulted from the PMI calculation, were used as input variables for ANN modelling. It should be note that the training/testing/validation procedure has become a standard practice in ANN model development. This procedure has two purpose: first to calibrate the model parameters without over fitting, and second to evaluate the calibrated model parameters with a data set that was not used in calibration (i.e. training and testing). Both training and testing were considered as calibration in this study. Of the data collected for the study period from 2003 to 2008, 53.4% was used for training, 13.3% was used for testing, and the remaining 33.3% was used for validation. This is in consistent with the standard practice of ANN modelling which uses 2/3 of the data for calibration (both training and testing) and 1/3 for validation. Accordingly data from 2003 to 2006 were used for calibration, and the remaining years (2007 and 2008) were used for validation.

The suitable number of nodes in the hidden layer, the connection weights and the biases in the network are the parameters to be determined during the calibration process. This is done by minimizing the mean square error (MSE) by considering the difference between the estimated and measured values at the output node (called the error in modelling). The MSE in the ANN model is minimized through back propagation training that is rearranging weights and biases for another run.

The input data of the back propagation neural networks (which was used in this study), are passed forward through the network with appropriate weights and biases, and then the error between the output and the measured values is calculated. This error is thereafter back propagated towards the input layer to adjust the weights. One complete cycle of the forward and backward propagation is called an iteration (epoch). Several such iterations are used to get the optimum MSE (or minimum MSE) during calibration (i.e. both training and testing). The initial weights and biases of the current iteration are considered as the adjusted weights and biases of the previous iteration. Figure 3.15 shows a typical example of how MSE changes with respect to iterations in both training and testing. This figure shows that MSE is reduced with the increasing number of iterations during the training phase, while MSE drops initially and then increases as the number of iterations increases during the testing period. In other words, during the initial stage, MSE goes down with an increase in the number of iterations for both training and testing. However, after several iterations, the MSE of testing starts to increase, while the MSE of training continues to decline. This point is called the early stopping point. Beyond the early stopping point, further training will likely cause over-fitting (Bishop, 1995). Therefore, the weights and biases of that iteration (at the early stopping point) are considered as the optimum weights and biases for the calibration of the model.

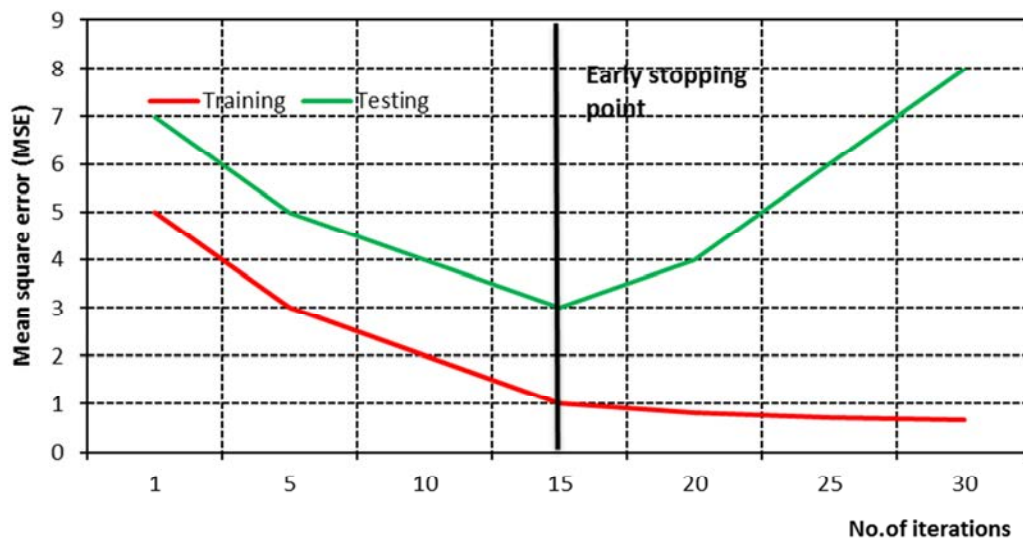


Figure 3.15 MSE of training and testing phases in each iteration

The process of finding the appropriate number of hidden nodes was carried out by the trial and error calibration method. This process was initiated by considering half the number of nodes of the input variables. The output of this model was compared with the measured

streamflow based on the performances indices explained in Section 3.9. Thereafter the number of hidden nodes was gradually increased. The output of each model was compared with measured streamflow as it was done with the first model output. The number of hidden nodes in the model which gives the best performance was selected to estimate streamflow with influential input variables.

3.9 Performance assessment

Indices that were used to assess the performance of estimated rainfall, potential evapotranspiration (PET) and streamflow using RS data will be discussed in this section. The performance of estimated rainfall was calculated using TRMM rainfall data. The performance of estimated PET was calculated using Penman-Monteith (PM) PET data, since observed PET were not available. The required PM based PET were obtained from the SILO database for the Macalister catchment. The required PM based PET for the Ribb catchment was calculated using ground measured data (Allen et al., 1998). The accuracy assessment of LULC was different in the case of rainfall and PET, and was thus explained separately in Section 3.5.3.4. The performance of estimated daily streamflow using both catchment process modelling and statistical modelling was conducted and was compared with observed daily streamflow.

The performance assessment was performed using the Root Mean Square Error (*RMSE*) and Nash-Sutcliffe efficiency (*E_f*) (Nash and Sutcliffe, 1970; Pala, 2003). Both *RMSE* and *E_f* were used in this study, since they represent different measures. *RMSE* is representing error with units, while *E_f* is used to measure the agreement between measured and estimated values.

RMSE and *E_f* were estimated using Equations (3.43) and (3.44):

$$RMSE = \sqrt{\frac{1}{N} \sum_{t=1}^N (x_t - y_t)^2} \quad (3.43)$$

$$E_f = 1 - \frac{\sum_{t=1}^N (x_t - y_t)^2}{\sum_{t=1}^N (x_t - \bar{x})^2} \quad (3.44)$$

where x_t is the observed variable, \bar{x} is the mean value of the observed variable for the total period, and y_t is the simulated or estimated variable, N is the number of days during the study period. In these equations, the observed variable refers to TRMM rainfall, Penman-Monteith PET, and ground measured streamflow.

RMSE gives the error in terms of units of the variables. A zero (0) value for *RMSE* indicates that the estimates have a perfect fit with observations. The main difficulty attached to *RMSE* is to assign the margin of *RMSE* (or low *RMSE*) for the estimates to be sufficiently accurate. This was overcome by treating values of *RMSE* which were less than half of the standard deviation of observed data as ‘low’ *RMSE* (Singh et al., 2004; Moriasi et al., 2007; Singh et al., 2005).

Nash-Sutcliffe efficiency (E_f) ranges from $-\infty$ to +1, where a value close to +1 indicates a higher level of agreement between the estimates and the observations (Krause et al., 2005). When E_f is less than 0, the mean of the observed variable can be considered as a better estimate for the estimated variable than the simulated or estimated variable.

3.10 Summary

This chapter described the study area details for both case studies, particularly in terms of data used (ground measured and satellite data). The methodology used in the estimation of input variables (i.e. rainfall, potential evapotranspiration and LULC) and daily streamflow using RS data was also discussed. The chapter started with a general description of both study areas, followed by catchment climate, hydrology and geomorphology. Whilst both study areas are approximately similar in size, they have different climatic conditions as well as LULC classes.

This chapter proceeded with the description of the data that were used in this study. The first case study area, the Macalister catchment, was a data rich catchment. Thus, the

required meteorological and hydrological data were available for the Macalister catchment. The second case study area, the Ribb catchment, is located in a in a developing country which has very limited ground measured data. The required RS data for both catchments were available free of charge.

The estimation methodologies of rainfall, potential evapotranspiration and LULC, which were used as input variables for catchment process modelling, were explained in detail. These input variables were estimated using RS data. Rainfall estimation is based on the brightness temperature of the clouds and its distribution, while potential evapotranspiration uses the surface energy balance method. Both these variables were estimated using MODIS data, while LULC was estimated using Landsat data which have higher spatial resolution compared to MODIS data. The SWAT model was used to estimate daily streamflow data for both catchments. Initially, model calibration was done with ground measured meteorological data. Then ground measured data were gradually replaced by data which were estimated using RS data, one input variable at a time.

In addition to catchment process modelling using SWAT, statistical modelling was considered in this study to estimate daily streamflow in both catchments. Vegetation indices, the brightness temperature and indices based on the brightness temperature were considered as input variables for statistical modelling. The characteristics of these indices and their calculation procedures were also explained. They are all calculated with MODIS reflectance and radiance data. The artificial neural networks modelling approach was proposed as a better tool for statistical modelling, as this approach performs well in modelling complex nonlinear relationships of the rainfall-runoff process.

In the last section of the chapter, indices that were used for accuracy assessment were explained. For this purpose, the Root Mean Square Error (*RMSE*) and the Nash-Sutcliffe efficiency (*E_f*) were discussed. These indices were used to assess the accuracy of rainfall and potential evapotranspiration estimated using RS data as well as estimated streamflow.

CHAPTER 4: THE MACALISTER CATCHMENT

4.1 Introduction

Streamflow data are immensely important for water resource investigations. However, the limited availability of these data, particularly streamflow measured through streamflow gauges, is a serious impediment to the successful implementation of these water resource investigations (Grimes and Diop, 2003). In the absence of such measured streamflow data, streamflow estimation using measured meteorological data is an alternative. Nonetheless, this alternative is not possible if all required measured meteorological data are unavailable, which is currently the case for most catchments. In the absence of such data, Lakshmi (2004) suggested that the use of RS data could be the answer to generating the required streamflow data. The theories and methodology whereby RS data could be used as such were described in Chapter 3.

A data rich environment, where the appropriate hydro-meteorological ground measured data are available, was selected as the first case study area to test the proposed methodology for daily streamflow estimation using RS data. The selected data rich catchment was the Macalister catchment in Victoria, Australia. The first case study and its results are discussed in this chapter. Then a second case study is conducted with a data poor catchment. The second case study and its results are presented in Chapter 5.

A detailed description of the Macalister catchment (i.e. first case study catchment) was presented in Section 3.3. In this first case study, two streamflow estimation procedures were used, namely: catchment process modelling and statistical modelling. Before using the catchment process modelling procedure, the required data for meteorological variables (i.e. rainfall and potential evapotranspiration) were estimated using RS data. In addition to the above two variables, the LULC of the catchment was classified using RS data. The theory involved in estimating these variables was discussed in Section 3.5. The estimation of these variables for the Macalister catchment is described in Section 4.2, together with the description of the results. These variables were then used in catchment process modelling using the SWAT modelling tool (Section 4.3). The theory behind catchment process modelling was discussed in Section 3.6.

Indices which are based on the reflectance and radiance data, and the brightness temperature were used as inputs in artificial neural networks (ANN) modelling which is the statistical modelling approach in this study. The estimation procedures relating to these input variables were discussed in Section 3.7. The results of the input variable selection and ANN modelling are discussed in Section 4.4.

The study period considered in this study was from 2003 to 2008. Both streamflow estimation approaches were calibrated from data relating to the period of 2003 to 2006, and validated from data pertaining to the period of 2007 to 2008. The performance of estimated rainfall, potential evapotranspiration (PET), streamflow using the catchment process model, and streamflow using the statistical model are presented and discussed in Sections 4.2.1.3, 4.2.2.4, 4.3 and 4.4 respectively. The accuracy of landuse/landcover classification is discussed in Section 4.2.3.3, and finally the performance of the catchment process model was compared with that of the statistical model in Section 4.5.

4.2 Estimation of remote sensing based variables for catchment process modelling

This section presents the results of the estimation of daily rainfall and daily potential evapotranspiration, and the classification of LULC using RS data. These variables were used in estimating daily streamflow with catchment process modelling. Whilst the methods of estimating each variable were discussed in detail in Chapter 3, the results in relation to the Macalister catchment and the performances of these results are discussed in this section.

4.2.1 Rainfall estimation

The methodology outlined in Section 3.5.1 was followed in order to estimate the required rainfall data using RS data. Since this methodology aims at estimating rainfall over areas where ground measured rainfall data are not available, a Tropical Rainfall Measuring Mission (TRMM) based data product, which is called TMPA 3B42 (TRMM rainfall data), was used. These data represent rainfall at near ground level, and are available in high temporal resolution (3-hour). However, the spatial resolution of these data is very low (approximately 625 km²). Therefore, the application of this data directly to daily streamflow estimation, especially for medium and small size catchments, is questionable

(Collischonn et al., 2008). The methodology described in Section 3.5.1 aimed at converting this low spatial resolution (625 km^2) and high temporal resolution (3 hour) data into high spatial resolution (1 km^2) of daily rainfalls (considered to be high resolution), thereby making such converted data ideal for daily streamflow estimation in small and medium size catchments. This was done by combining TRMM rainfall data with the brightness temperature (BT) data obtained from the high spatial resolution (1 km^2) MODIS radiance data of band 31. This process is briefly explained below, but detailed explanations together with results follow in subsequent sub-sections (of Section 4.2.1).

- TRMM rainfall data, which represent hourly rain rates for every three hour period, were converted into equivalent daily rain amounts. These daily rain amounts were used as input data to estimate the high spatial resolution of daily rainfall data.
- Assuming that there is no rain on no-cloudy days, MODIS satellite data which have clouds were used in rainfall estimation. There were 1886 cloudy days within the study period, and according to Mount Tamboritha rain gauge, only 626 days rained within that period in the Macalister catchment. This shows that two third of the total cloudy day number did not yield any rain within the catchment. Since all clouds do not yield rainfall, MODIS BT data of bands 27, 31 and 32 were used in the separation of rain/no-rain clouds in cloudy images (Section 3.5.1.1).
- All rain clouds identified under the above step do not produce rain. Therefore, a BT threshold was defined for using MODIS BT data to separate ‘real’ rain clouds (‘rainy clouds’) that produce rain from rain clouds. No-rain clouds and those clouds which failed with the BT threshold were not further considered in rainfall estimation (Section 4.2.1.1).
- High spatial resolution rainfall was estimated using BT difference and low spatial resolution TRMM daily rainfall by employing a gamma function (Section 4.2.1.2).

4.2.1.1 Brightness temperature threshold

All rain images that were screened through the rain/no-rain cloud mask (i.e. based on BT differences) were further refined with a BT threshold. Del Beato (1981) revealed that clouds with low BT have a higher probability of rain. Some of the rain clouds selected through BT differences may have high BT, which may not yield rain according to Del Beato (1981). Therefore, it is essential to remove such rain clouds with high BT to acquire

accurate rainfalls, as they do not produce rain. To facilitate this, another criterion, (i.e. other than BT differences used in separation of rain/no-rain clouds) based on BT was used to identify clouds that produce rain. A similar criterion has been used in previous studies (Arkin, 1979; Arkin and Meisner, 1987; Grimes et al., 1999; Kuligowski, 2002). In order to remain consistent with those studies, MODIS BT of band 31 (BT31) was used to define the BT threshold that separated rainy clouds from the rain clouds.

Data related to ground measured rainfall (at Mount Tamboritha station), BT31 and 235 K threshold line of BT are shown in Figure 4.1. The BT of 235 K is specially shown in Figure 4.1, since it has been used as the threshold level of BT in estimating rainfall in some previous studies (e.g. Arkin and Meisner, 1987; Huffman et al., 1997). Mount Tamboritha ground station is used as a representative meteorological station as it is located approximately in the middle of the Macalister catchment.

Figure 4.1 indicates that BT31 follows a sinusoidal pattern over the catchment with low BT31 in winter (June to August) and high BT31 in summer (December to February). Winter is the main rain period in the catchment, while rainfall is intermittently distributed in the other seasons. As can be seen from Figure 4.1, rainfall of Mount Tamboritha station varies between 0 to 50 mm during the study period (i.e. 2003 to 2008), and the BT31 values over Mount Tamboritha vary from 190 K to 250 K.

Figure 4.1 demonstrates that BT31 is less than 235 K during most of the study period except during summer months. Therefore, the use of 235 K as a threshold in the Macalister catchment could cause an unwarranted increase in the number of rainy days, which could ultimately overestimate the amount of rain. This could happen particularly in winter since BT31 is always less than 235 K (Figure 4.1). This finding, together with the seasonal pattern of BT31, highlight the notion that the threshold for rainfall estimation should be adjusted seasonally. Hence, in order to achieve a better threshold for local rainfall estimation, two options were tested in this study. They are: (i) the mean seasonal value of BT31 and (ii) the mean monthly value of BT31. The mean annual value of BT31 over the catchment was not considered in this study since it is identical to the 235 K threshold.

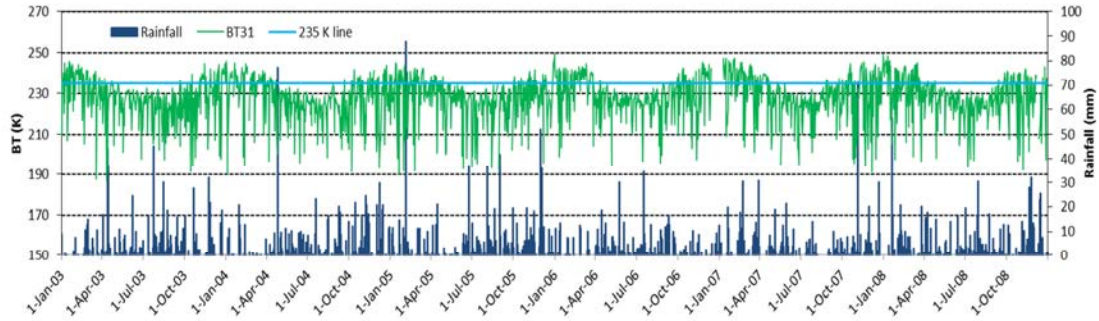


Figure 4.1 Ground measured rainfall and BT of MODIS band 31 at Mount Tamboritha

The values of mean seasonal BT31 and mean monthly BT31 are shown in Table 4.1. This table shows that the mean seasonal BT31 values and the mean monthly BT31 values are always less than 235 K. In this table, summer is defined as December-February, autumn as March-May, winter as June-August, and spring as September-November. Table 4.1 shows that the mean monthly values slightly vary from their mean seasonal value. However, during winter months (Jun-Aug) the mean BT31 is approximately equal to its mean seasonal value.

Table 4.1 Mean seasonal BT and mean monthly BT over the Macalister catchment

Season	Mean BT31 (K)	Month	Mean BT31 (K)	Month	Mean BT31 (K)	Month	Mean BT31 (K)
Summer	231.7	Dec	228.7	Jan	232.7	Feb	233.4
Autumn	229.0	Mar	232.5	Apr	228.5	May	225.9
Winter	223.1	Jun	223.2	Jul	222.7	Aug	223.4
Spring	227.4	Sep	225.5	Oct	227.9	Nov	228.8

In order to determine the best threshold that should be used in this study from the proposed two thresholds (i.e. mean seasonal and mean monthly) and BT of 235 K, the following indices were used: (i) the Heidke skill score (*HSS*), (ii) the Probability of Detection (*POD*), (iii) the False Alarm Ratio (*FAR*), and (iv) the bias. Pixels of BT which are less than these thresholds were considered as ‘rainy’. The estimation procedures of these indices are explained in Section 3.5.1.2.

The estimated *HSS*, *POD*, *FAR* and bias for the Macalister catchment with regards to 235 K, mean seasonal and mean monthly values as thresholds are presented in Table 4.2. In

addition to these calculated indices, the ‘perfect’ value of each index is shown in the table. The best performing value of these three thresholds compared to the perfect index value is also highlighted (in grey) for each index.

Table 4.2 *HSS*, *POD*, *FAR* and bias values for the different thresholds – Macalister catchment

	BT 235 K as threshold	Mean seasonal BT31 as threshold	Mean monthly BT31 as threshold	Perfect value of index
<i>HSS</i>	0.25	0.34	0.31	1
<i>POD</i>	0.87	0.62	0.59	1
<i>FAR</i>	0.44	0.34	0.35	0
<i>Bias</i>	1.57	0.93	0.90	1

Table 4.2 shows that the calculated *HSS* value for BT 235 K as threshold is the lowest in all three thresholds. A detailed observation shows an overestimation of MODIS BT pixels marked as ‘rainy’ when 235 K is used as threshold. This appears to be the main reason to have the lowest *HSS* value with BT 235 K as threshold. This observation is in agreement with Figure 4.1, as there are many days below the 235 K threshold, which are considered as rainy when using BT 235 K as threshold. In turn, this has resulted in a higher number of rain days compared to the actual rain days. Except for *POD*, all evaluation indices of BT 235 K as threshold show poor performance compared to both mean seasonal and mean monthly thresholds. Table 4.2 shows that the mean seasonal BT as threshold performed slightly better than the mean monthly BT as threshold. Given those findings, the mean seasonal BT31 was used as the appropriate threshold for rainfall estimation in this study.

4.2.1.2 Rainfall estimation function and results

All rainy clouds of BT less than the relevant seasonal BT threshold were considered for rainfall estimation (Section 4.2.1.1). Initially, BT and TRMM rainfall data were separated into their relevant seasons. Then, the BT difference on a given day was calculated as the difference of the mean seasonal BT31 (as the threshold) and BT of MODIS band 31.

The above BT difference and corresponding TRMM rainfall data of these days were then used as inputs to estimate rainfall in this study. The theory behind this estimation process was explained in Section 3.5.1.3. The application of this theory to estimate rainfall is

summarized in the following steps and in Figure 4.2 (which is reproduced from Figure 3.12);

1. The cumulative gamma probability function for the BT differences and for TRMM rainfall data was calculated on a seasonal basis (plots II and III). The optimum scale and shape parameters (Equations 3.9 and 3.10) were calculated separately for each season. The calculation of the cumulative probability function was then done for each pixel.
2. The cumulative gamma probability value of the BT difference was selected for a particular day (plots I and II).
3. The corresponding cumulative gamma probability of TRMM rainfall was obtained (plot III).
4. The rainfall corresponding to this cumulative gamma probability to the day under consideration was assigned as the rainfall for that day.
5. Steps 2 – 4 were repeated for all days in the study period.

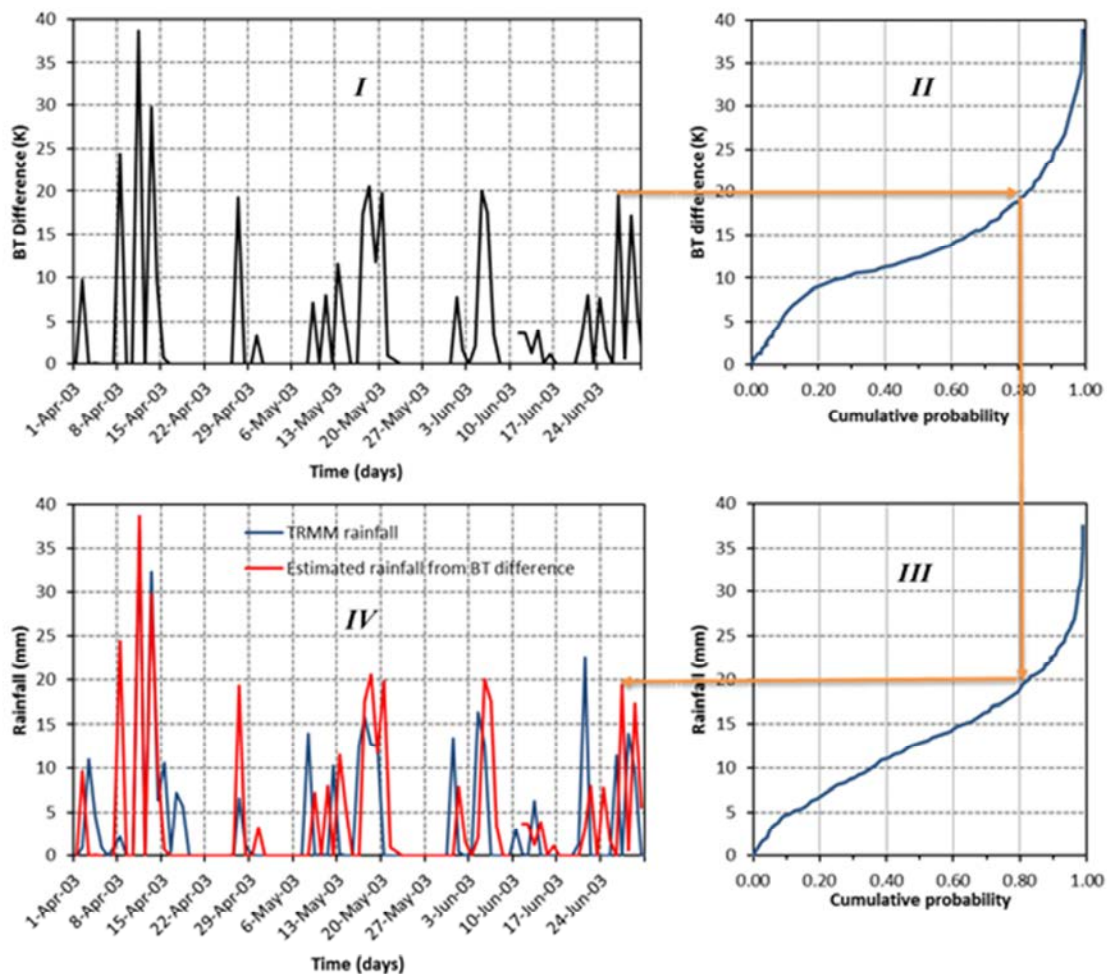


Figure 4.2 Rainfall estimation procedure using BT difference and TRMM rainfall

(Reproduced from Figure 3.12)

The results of rainfall estimated using RS data in this study (hereafter estimated rainfall in this thesis) for a selected day (13 June 2004) are explained below by taking into consideration the spatial distribution of BT and rainfall. This will be followed by a quantitative analysis of estimated rainfall against TRMM rainfall on annual and seasonal bases.

Figures 4.3, 4.4 and 4.5 show the calculated BT on 13 June 2004, TRMM rainfall and estimated rainfall (from MODIS BT data) over the Macalister catchment and its surrounding areas (surrounding catchments). The areas surrounding the Macalister catchment were included to show patterns of the MODIS data and the TRMM data in these figures.

Figure 4.3 shows that BT has decreased from east and southeast to north and northwest. Figure 4.4 shows TRMM rainfall on the same day for the same area. Rainfall in this figure has increased from east and southeast to north and northwest; i.e. in the same direction where BT has decreased. This shows that the rainfall amount has increased (Figure 4.4) when BT has decreased (Figure 4.3).

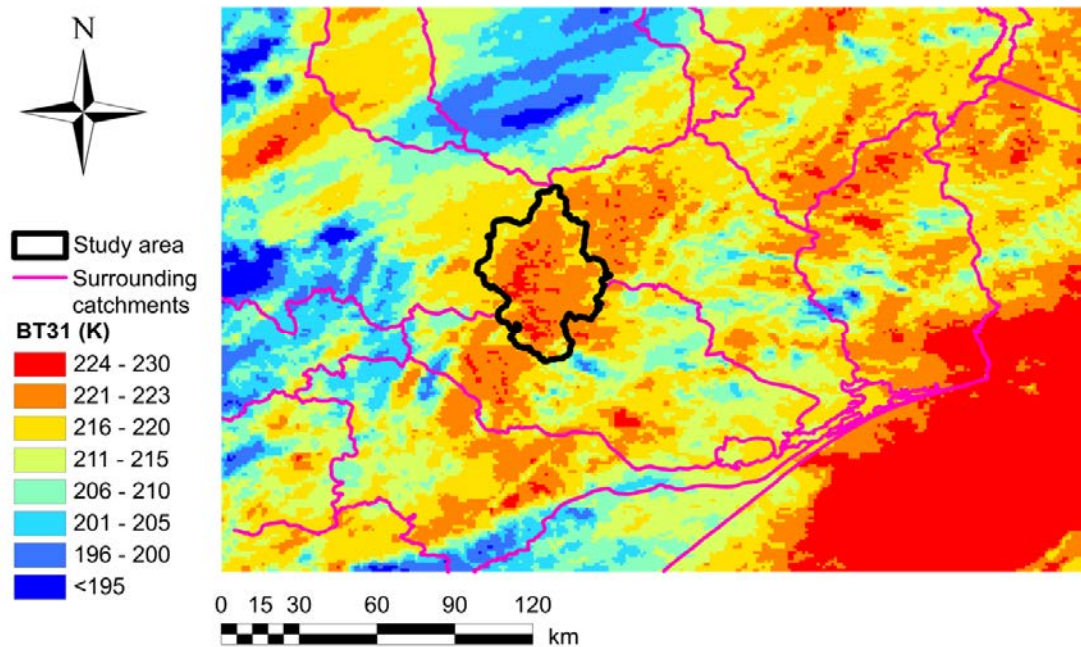


Figure 4.3 BT of band 31 (BT31) on 13 June 2004

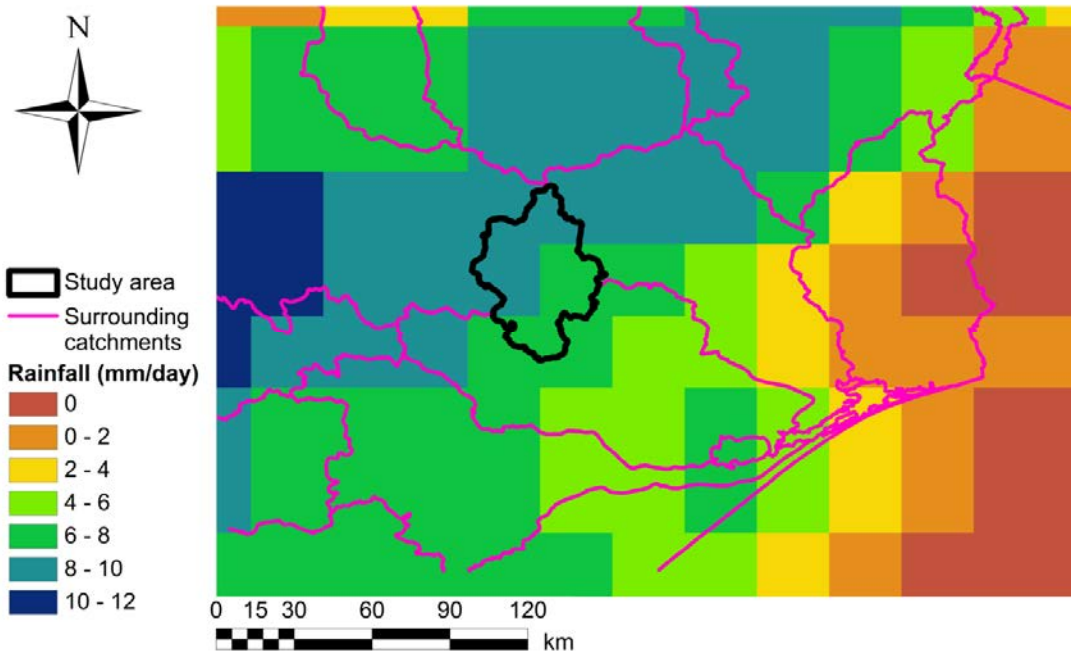


Figure 4.4 TRMM rainfall on 13 June 2004

Figure 4.5 shows the estimated rainfall using MODIS BT data on 13 June 2004. This figure shows that the north and west parts of the Macalister catchment received large amounts of rainfall on that day, but less rain within the Macalister catchment area. A comparison of Figures 4.4 and 4.5 shows that there is a similar pattern (i.e. over all from southeast to northwest) of rainfall between MODIS BT based rainfall estimates and TRMM data. In general, in the southeast area of the Macalister catchment, there has been zero millimeter rainfall, while the northwest area has experienced the highest amount of rainfall. The rainfall amount gradually increases from southeast to northwest in Figure 4.5, which is also the case of TRMM data on that day (Figure 4.4).

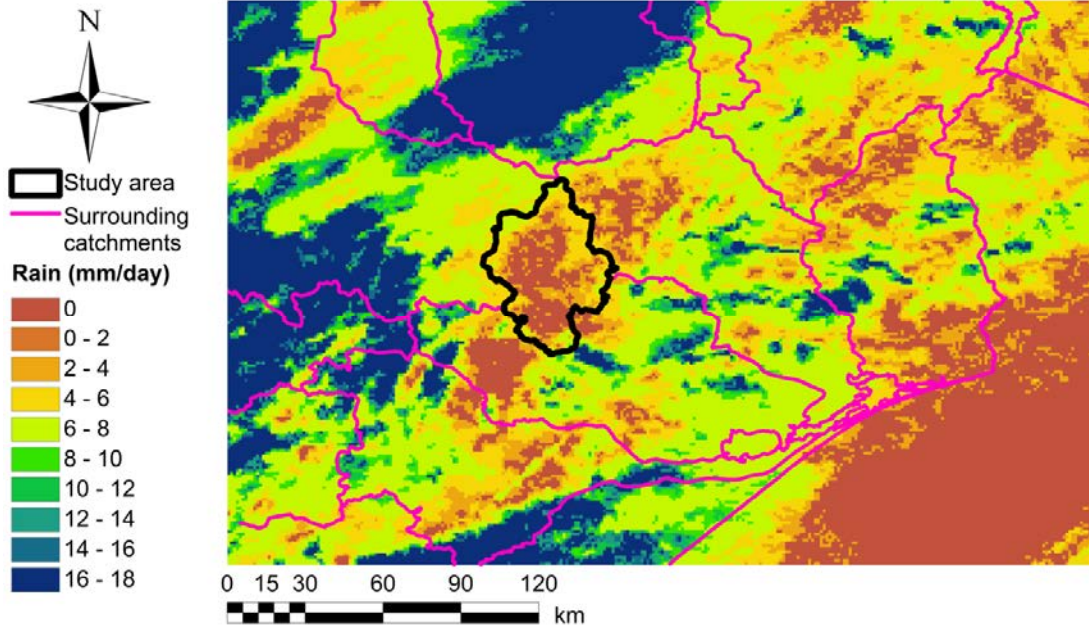


Figure 4.5 Estimated rainfall on 13 June 2004

Figure 4.6 shows the annual values of estimated rainfall and TRMM rainfall data over the Macalister catchment. It should be noted that in this figure, annual rainfall values were calculated based on the spatial mean values of daily TRMM and estimated rainfall data. In general, the estimated rainfall is lower than the TRMM rainfall, except in 2006 which shows the lowest rainfall. The differences are higher in 2007 and 2008.

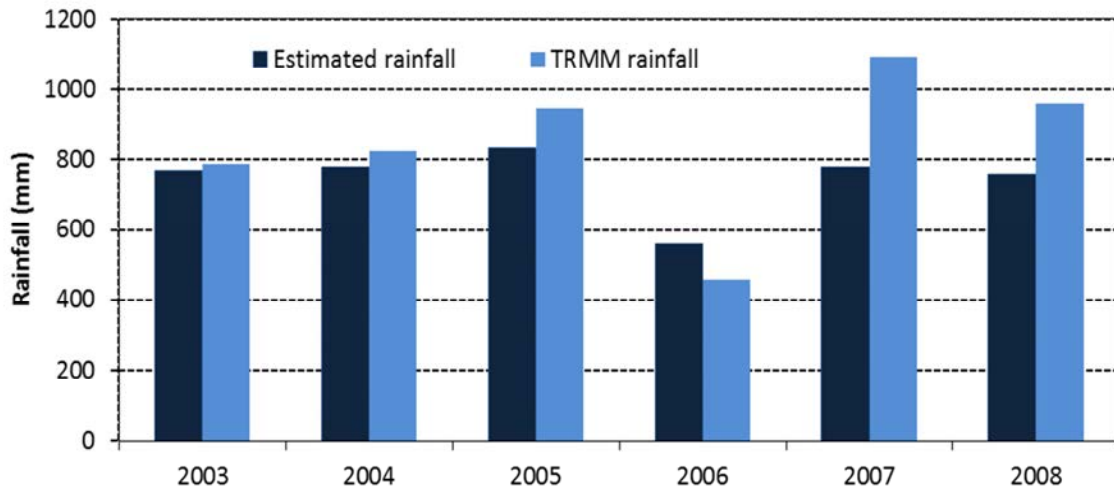


Figure 4.6 Estimated annual rainfall and TRMM annual rainfall – Macalister catchment

In addition to the annual rainfall investigation, seasonal rainfall was also investigated over the catchment. Seasonal rainfall of TRMM and estimated rainfall are shown in Figure 4.7. During the summer seasons of the study period, estimated rainfall over the Macalister catchment yielded mixed results. The summers of 2006/07 and 2007/08 were highly underestimated, while for the majority of the summer seasons estimated rainfalls were underestimated. However, this figure also shows that the summer of 2005/06 was significantly overestimated. In general, during the study period estimated rainfalls for all autumn seasons (except the autumn of 2007) were overestimated. The wettest period of the year in this catchment was winter, and the figure shows that estimated rainfall matched fairly well with TRMM rainfall during the winters of 2003 and 2004. However, the other winter seasons were underestimated. All spring seasons, except in 2006, showed an underestimation in estimated rainfall.

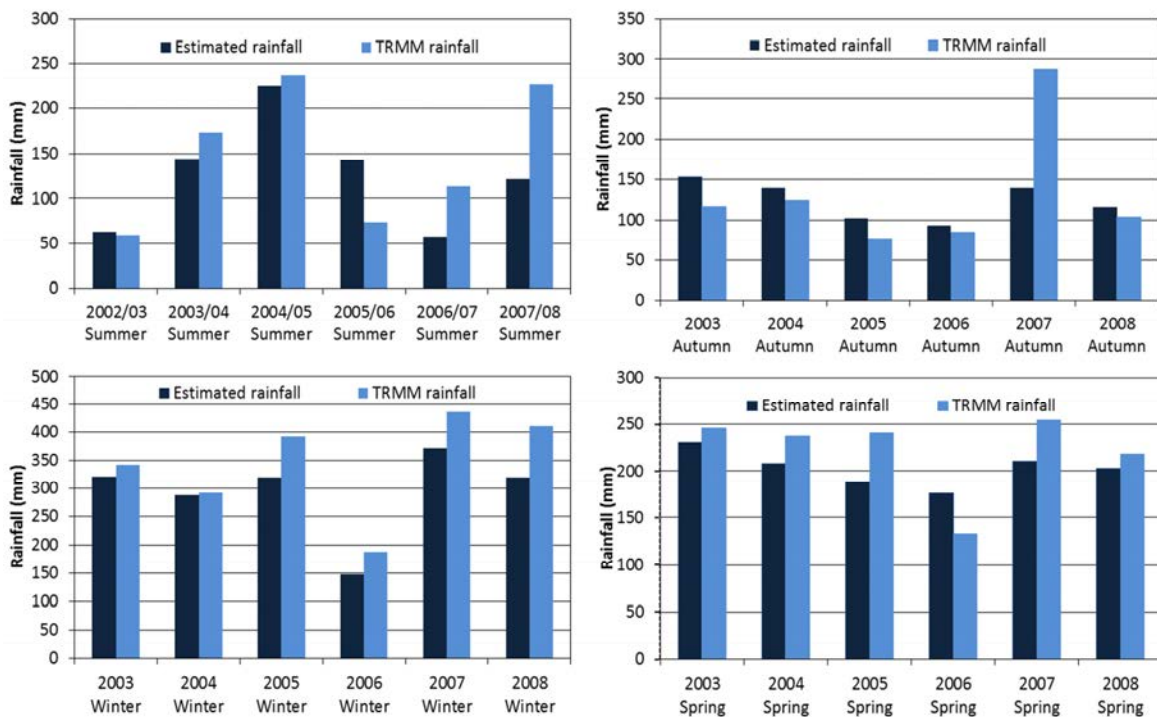


Figure 4.7 Estimated seasonal rainfall and TRMM seasonal rainfall - Macalister catchment

4.2.1.3 Performances of rainfall estimation

The estimated rainfall using MODIS BT data were compared with TRMM rainfall data. Figure 4.8 shows a scatter plot of TRMM rainfall and estimated rainfall, averaged over the catchment area. This figure shows three distinguishing features of rainfall estimation: (i) a reasonable match between TRMM and estimated rainfalls, (ii) zero TRMM rainfall but non-zero estimated rainfall (which means rainfall was not reported under TRMM, but rainfall has been estimated with MODIS radiance data) and (iii) zero estimated rainfall but non-zero TRMM rainfall (which means rainfall was reported with TRMM data but failed to estimate with MODIS radiance data).

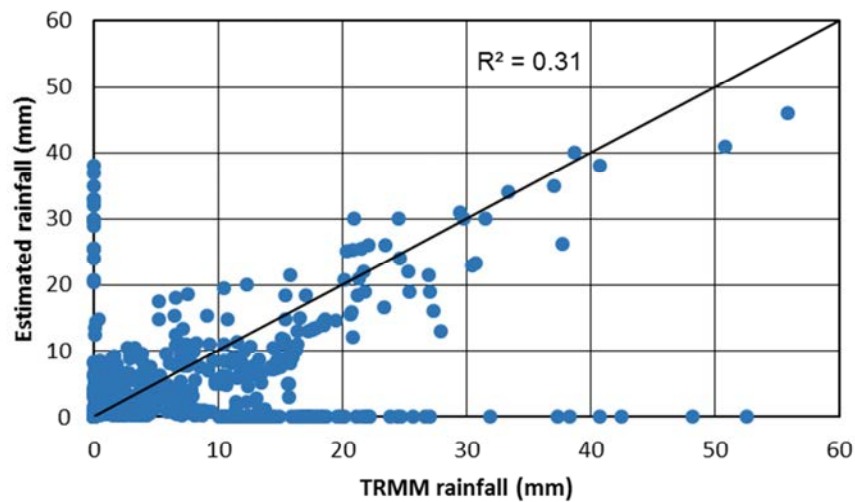


Figure 4.8 Scatter plot of estimated daily rainfall and TRMM daily rainfall

With the methodology described in Section 4.2.1.2 with the aid of Figure 4.2, the major assumption was that there was a good relationship between TRMM rainfall and BT difference for each season of the year. Analysis of TRMM rainfall and BT difference data for different seasons found that these relationships are strong, and even with linear relationships correlation coefficients of 0.45, 0.62, 0.52 and 0.66 were found for Summer (December to February), Autumn (March to May), Winter (June to August) and Spring (September to November) respectively. As can be seen from these correlation coefficients, there are still mismatches between TRMM rainfall and BT difference data. The reason for the above distinguishing features (ii) and (iii) is due to these mismatches which were not explained by the correlation coefficients.

The number of days with no-rain and rain with respect to estimated and TRMM rainfalls are presented in Table 4.3. This table shows that there are 1324 no-rain days during the study period under TRMM rainfalls, and 1250 no-rain days under estimated rainfalls. The table also shows that 448 days have been recorded as rainy days in TRMM within the total 1250 no-rainy days of estimated rainfall. Similarly, 522 days have been recorded as rainy days in estimated rainfall within the total 1324 no-rainy days of TRMM. This shows that only half of the rainy days are correctly detected by the estimated rainfalls approach. As this could lead to miscalculations in streamflow, all mismatch rainfall days (i.e. where there is a mismatch between estimates and TRMM calculations) were investigated further and are presented in Figure 4.8.

Table 4.3 Rain/no-rain days under TRMM and estimated rainfalls during the study period

	TRMM no-rain days	TRMM rain days	Total days
Estimated no-rain days	802	448	1250
Estimated rain days	522	420	942
Total days	1324	868	2192

According to Table 4.3, there are 522 days classified as rainy under estimated rainfall, while there is no rain under TRMM rainfall for these days. Figure 4.9 shows the rainfall amount of these 522 days under estimated rainfall. This figure shows that the majority (more than 300 days) of these 522 rain days in this category (i.e. TRMM no-rain but estimated rain) has less than 1 mm rainfall. Approximately little less than 100 days out of the remaining days have rain in the range of 1 to 2 mm, which means that around 80 % of rain days identified as rainy days under estimated rainfall and no-rainy days under TRMM had rainfall less than 2 mm. Furthermore, Table 4.3 shows that 448 days are recorded with TRMM rain but no-rain under estimated rainfall. This could be the result of either rain clouds not being detected in MODIS data or rain occurring while BT temperature is higher than the particular seasonal threshold. This figure shows that the majority of rainfall under this category is less than 2 mm.

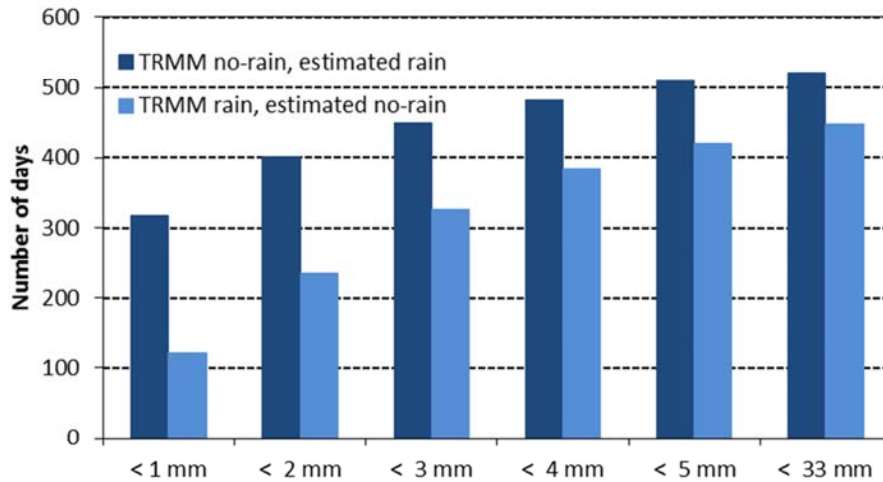


Figure 4.9 Cumulative distribution of mismatching days of rain/no-rain under TRMM and estimated rainfall

Other than rain and no-rain counts, Nash-Sutcliffe efficiency (E_f) and Root Mean Square Error ($RMSE$), which were explained in Section 3.9, were calculated by taking into consideration the TRMM rainfall magnitudes and the estimated rainfall magnitudes. The daily rainfall spatially averaged over the Macalister catchment was considered in the calculation of these performance indices. The E_f value between estimated and TRMM rainfall over the catchment is 0.43. The $RMSE$ is 2.9 mm.

4.2.2 Potential evapotranspiration estimation

The energy balance method, which was explained in Section 3.5.2, was used to estimate potential evapotranspiration (PET) using RS data over the Macalister catchment. As was the case for rainfall estimation, the study period was considered as January 2003 to December 2008.

In estimating PET using the energy balance method, the surface albedo plays an important role. Generally, the pyranometer or albedometer was used to measure the albedo. However, such measurements are site specific and unique to the atmospheric conditions in which the measurement was taken. To avoid these disadvantages, Liang (2001) proposed the RS based narrow band to broad band albedo estimation method. This method, which was explained in Section 3.5.2.1, was used in this study.

The surface albedo values were calculated using RS data by considering non-cloudy day images, and were then compared with the surface albedo values obtained from the literature (Bastiaanssen, 1998; Zhou et al., 2006). Only non-cloudy images were considered in this calculation, since the reflectance of those images originated from ground surface. This comparison was done for different LULC classes within the catchment, and is summarized in Table 4.4. This table shows the minimum, maximum, mean and standard deviation (STD) of the calculated surface albedo values for all non-cloudy days during the study period. The mean surface albedo value was used for comparison purposes. As can be seen in this table, the mean values of calculated surface albedo on shrubs, crop and crop/grassland are similar to those values obtained from the literature. However, the mean value of calculated surface albedo in the evergreen forest areas is low compared to the literature value. These lower values of surface albedo consequently led to an overestimation of net energy available for evapotranspiration, which, in turn, resulted in higher estimates for PET using RS data.

Table 4.4 Comparison of surface albedo of the Macalister catchment

		Evergreen Forest	Shrubs	Crop	Crop/Grassland
Calculated values	<i>Min</i>	0.06	0.09	0.09	0.00
	<i>Max</i>	0.70	0.64	0.56	0.65
	<i>Mean</i>	0.12	0.16	0.17	0.24
	<i>STD</i>	0.05	0.06	0.05	0.08
Literature values*		0.18	0.15	0.15	0.24
				0.20**	

*(Bastiaanssen, 1998) ** Water stressed crops

The estimation of PET for the Macalister catchment during the study period was done separately for cloudy and non-cloudy days. This is because the estimation methods are slightly different for cloudy and non-cloudy days. The theory behind the estimation of PET over cloudy and non-cloudy days using RS data was explained in Sections 3.5.2.1 and 3.5.2.2 respectively.

4.2.2.1 PET of non-cloudy days

On average, 14 % of the days per year in the Macalister catchment were non-cloudy days during the study period. This represents nearly one non-cloudy day a week, but during winter (i.e. June to August) the gap between non-cloudy days was generally longer and during summer it was shorter.

In this study, PET estimated using RS data (hereafter estimated PET) took place spatially at each grid point of the catchment. However, the four test locations in the catchment, each having a different LULC class, were selected in order to compare estimated PET with Penman Monteith (PM) based PET estimates. The PM based PET was considered as the base PET against which estimated PET was to be compared, since it is widely used (Allen et al., 1998; Utset et al., 2004; Allen et al., 2011) and readily available for the study area. The four test locations considered in this comparison process are Mt. Howitt, Mt. Tamboritha, Licola and Barkley River point. The required PM based PET was acquired from the SILO dataset for the selected locations. These selected test locations for the Macalister catchment are shown in Figure 4.10.

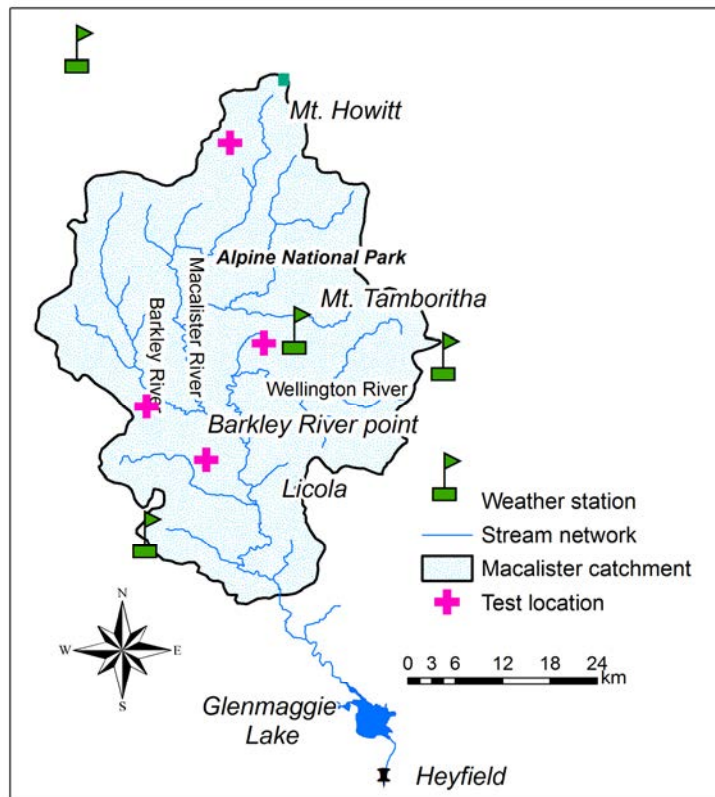


Figure 4.10 Test locations within the Macalister catchment

The selected test locations have differing LULC classes, which markedly affect evapotranspiration, and it is therefore important to specify the ground conditions to fully appreciate the detailed analysis. Evergreen forest is the predominant LULC class in Barkley River point and Mt. Tamboritha, while grassland and forest are predominant in Mt. Howitt. Grassland (pasture) is the dominant LULC class at Licola, but it is mixed with bushes and farmhouses.

Figure 4.11 shows the comparison of estimated and PM based PET for non-cloudy days. This figure also shows that the estimated PET for non-cloudy days is in reasonable agreement with PM based PET. The estimated PET shows a better agreement in the range of $3.0 - 6.5 \text{ mm day}^{-1}$ compared to $0.0 - 3.0 \text{ mm day}^{-1}$. A detailed examination of the PET in the $3.0 - 6.5 \text{ mm day}^{-1}$ range shows that there was better agreement between estimated PET and PM based PET during spring (September to November) and the first two months of summer (December and January). Although there are different LULC classes in these test locations, Figure 4.11 shows that for all test locations, the same pattern of PET is followed during the study period. However, slight differences in the magnitude of PET are observed at different locations due to the change of LULC and elevation.

Figure 4.11 also shows that the maximum PET values estimated with RS data in all test locations are less than 6.5 mm day^{-1} . This maximum value arises from Equation (3.16) during summer days. Furthermore, this figure shows that there are a few days of PM based PET which are greater than 6.5 mm day^{-1} , and which appear to have been underestimated using the RS method. A detailed analysis of the results showed that these underestimated days were warmer (air temperature was mostly above $30 \text{ }^{\circ}\text{C}$) than usual. Although the PET is affected by both net available energy and advective effect, the advective effect was not considered in the RS method in this study (since the relevant data to compute the advective effect cannot be obtained from RS data). The advective effect is higher on warmer days with high wind speed, thereby leading to an underestimation in estimated PET. The advective effect is considered in the PM method.

Figure 4.11 further shows that the estimated PET was slightly underestimated compared to the PM based estimates, when PET is less than 3.0 mm day^{-1} in all test locations. A detailed analysis of these values showed that this occurred mostly in later part of autumn (late April to May) and winter (June to August). These are cooler days, and on such cool

days, as Barton and Meyer (2008) noted, the PM based PET is slightly overestimated, although net radiation is low and advective effect is less.

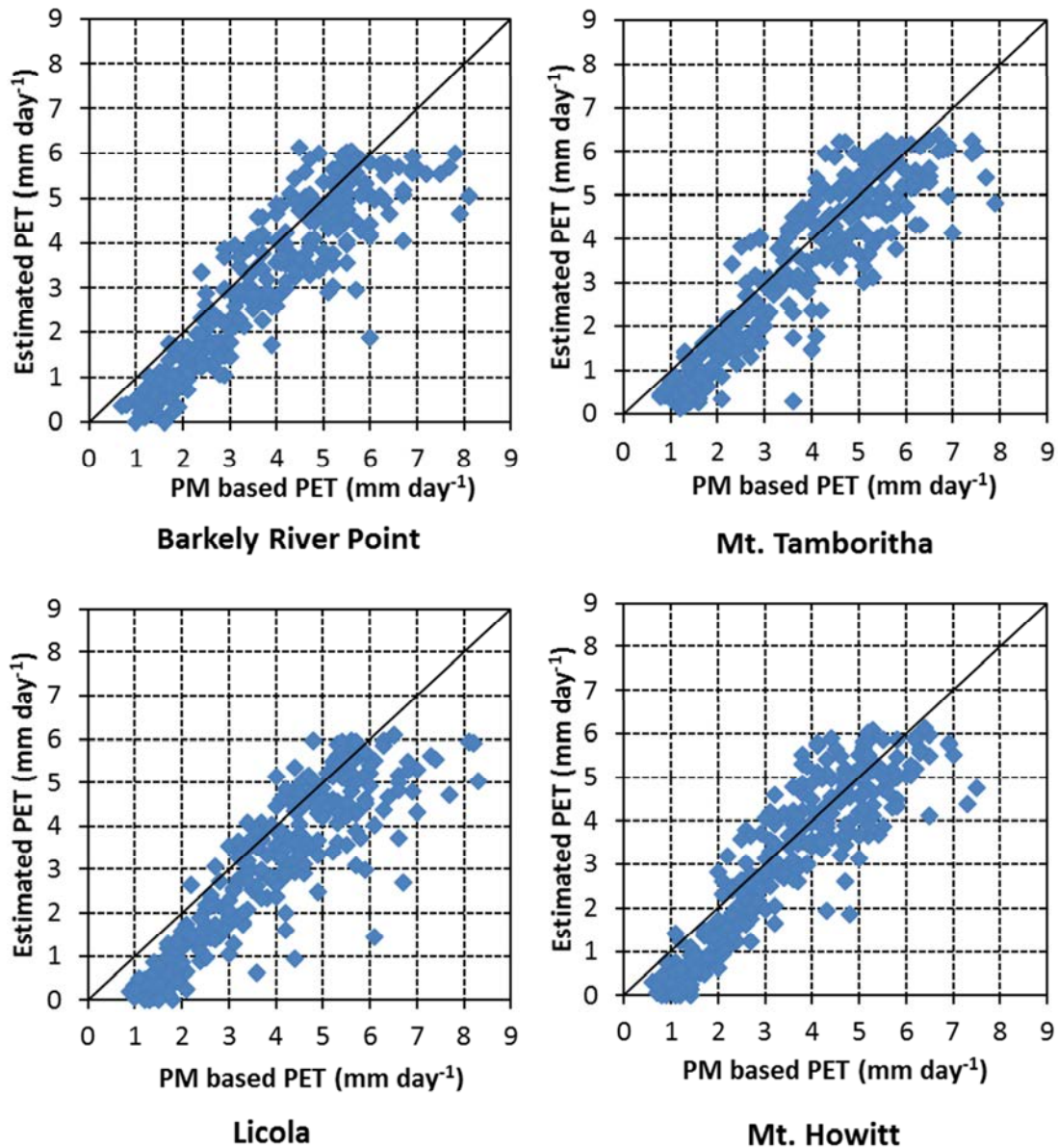


Figure 4.11 A comparison of estimated PET and PM-based PET for non-cloudy days - Macalister catchment

Additionally, Figure 4.11 shows a few highly underestimated days at each of the test locations. A day was defined as highly under or over-estimated in this chapter if the estimated PET deviates from PM based PET by at least one standard deviation of the PM based PET. This definition was used for both the Macalister and Ribb catchments and for both non-cloudy and cloudy days. Licola, Mt. Tamboritha, Barkley River Point and Mt.

Howitt show 9.4, 5.3, 3.3 and 5.3 % of highly underestimated days respectively. As can be seen from the above values, Licola has the highest percentage of highly underestimated days. The detailed examination of calculated surface albedo in the region represented by Licola showed that the calculated albedo values were also higher than the literature values. It is thought that this higher calculated surface albedo value could be a result of the mixed LULC class around Licola. Estimated higher albedo values produce low available net radiation energy evapotranspiration, thus reducing the magnitude of evapotranspiration. In contrast, these low albedo values when used in PM based estimates produce higher evapotranspiration values. Highly overestimated days were not observed in any test location in the Macalister catchment.

4.2.2.2 PET of cloudy days

Similar to non-cloudy days, the estimated PET was computed at every grid point of the catchment for cloudy days, and these values were compared with the PM based PET values at the same test locations. These comparisons are shown in Figure 4.12. This figure illustrates that on some cloudy days, the estimated PET are nearly zero as a result of very low net energy available to PET. Mostly they represent either the total or the partial cloudy days during the winter season. During these days, the estimated cloud cover was overestimated, and as such reduced the actual sunshine hours. The reduced number of sunshine hours was directly related to the net energy available for evapotranspiration. Therefore, the RS based estimates produced PET which were of lesser magnitude than those of PM based PET.

Similar to PET for non-cloudy days (Section 4.2.2.1), it was seen that the maximum PET estimated from RS data had not exceeded 6.5 mm/day, while the PM based estimates had a maximum of around 8 mm/day. As explained in Section 4.2.2.1, the PET is affected by both net available energy and advective effect. The advective effect was not considered in the RS method in this study (since the relevant data to compute the advective effect cannot be obtained from RS data). The advective effect is higher on warmer days with high wind speed, thereby leading to an underestimation in estimated PET. The advective effect is considered in the PM method. In estimating PET from RS data, the net available energy is computed from solar radiation and the maximum amount of solar radiation produces a maximum PET of 6.5 mm/day.

It is also observed in Figure 4.12 that some of the estimated PET during cloudy days were overestimated especially with the PM based PET ranging between 1.0 to 5.0 mm day^{-1} . These days are mostly during mid and late spring (October and November) and the early days of summer (in December). An examination of the results during this overestimated period showed that the actual net radiation (measured by BOM) was significantly less compared to the values calculated from the RS based method. The actual net radiation was used to generate PM based PET in the SILO database; thus these PET values were found to be lower than estimated PET. The measured low net radiation values may be associated with localized haze which was not accounted for in the medium spatial resolution RS data used in this study. Furthermore, the low net radiation could have been measured as a result of smaller clouds which are not sensitive to the medium spatial resolution of the RS data used in this study.

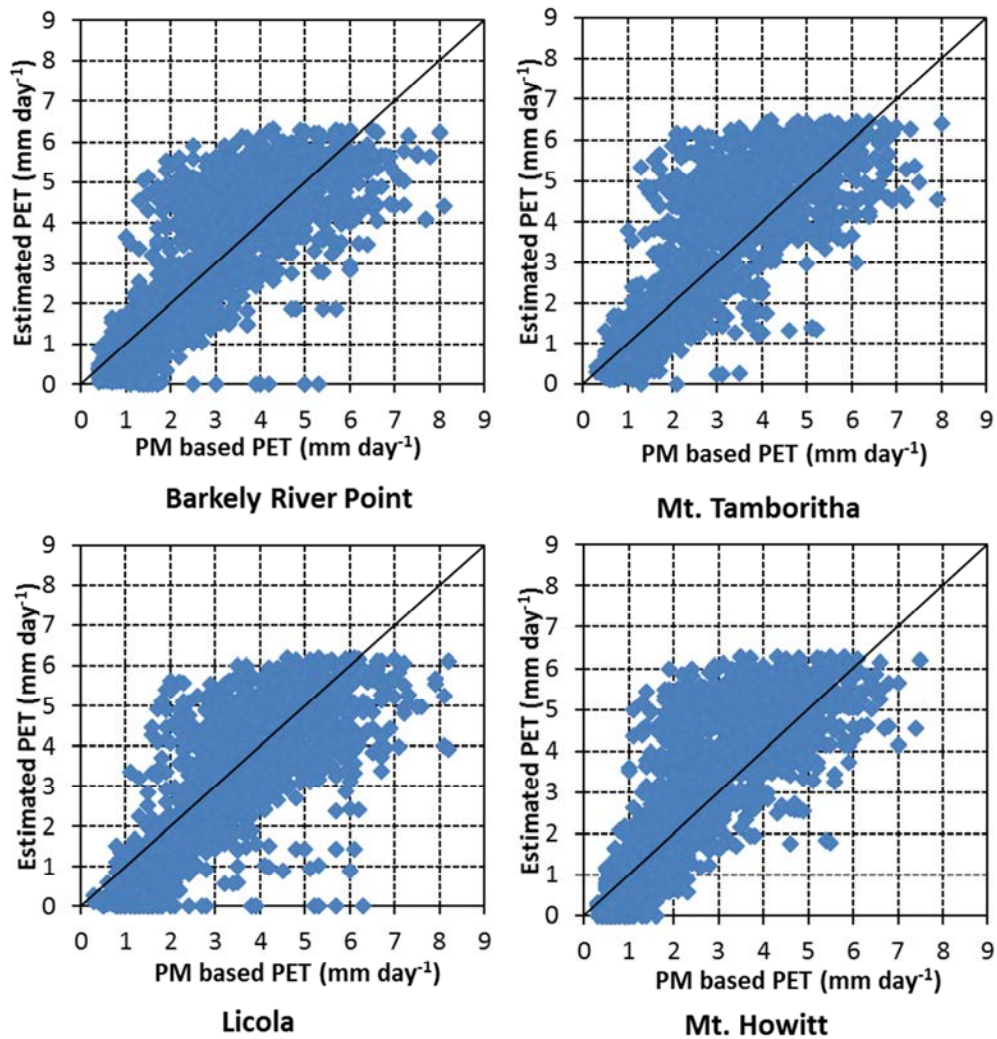


Figure 4.12 PM based PET and estimated PET for cloudy days - Macalister catchment

All test locations show a similar pattern in the comparison of PET estimation on cloudy days. A detailed analysis of the test locations revealed that Licola, Mt. Tamboritha, Mt. Howitt and Barkley River Point have 5.1%, 2.8%, 1.9% and 3.2% highly underestimated days respectively, whilst the percentages of highly overestimated days were 4.6%, 11.2%, 13.3% and 7.6%. These values show that highly overestimated days are greater than the highly underestimated ones during cloudy day PET estimation.

4.2.2.3 Mean annual PET

Mean annual PET values (calculated by considering both non-cloudy and cloudy days together) at each test location are shown in Table 4.5. Considering the percentage difference, this table shows that the estimated PET on the mean annual basis at Mt. Howitt and Mt. Tamboritha are slightly higher compared to the PM based estimates. In contrast, the estimated PET is slightly lower than the PM based PET at Barkley River Point. The difference at Licola is considerably high. This large difference at Licola may be due to the existing mix class of LULC, (i.e. bushes and farm houses) which may have led to overestimated surface albedo values in estimated PET, which in turn underestimated the estimated PET compared to the PM based PET.

Table 4.5 Estimated and PM based mean annual PET-Macalister catchment

Test Location	Mean Annual PET (mm)		Difference (mm)	% difference
	<i>RS</i>	<i>PM</i>		
Barkley River	1001.3	1051.8	-50.5	- 4.8
Mt. Tamboritha	1070.5	1036.4	34.1	3.3
Licola	940.1	1098.2	-158.1	- 14.4
Mt. Howitt	978.9	928.6	50.2	5.4

4.2.2.4 Comparison of PET estimates for total period and seasons

The potential evapotranspiration is mostly affected by physical factors such as net radiation (i.e. net available energy for PET), air temperature, pressure deficit and wind speed in the environment. RS data and air temperature were used as input data to compute net radiation in estimated PET estimation. However, wind speed and pressure deficit were not considered, and this may have caused differences in the estimated PET for both non-cloudy and cloudy days compared to the PM based estimates, which specifically accounted for wind speed and pressure deficit. Similarly, the net short wave radiation is the most

significant component in estimating net available energy, which was calculated using the surface albedo in the estimated PET estimation, and hence the surface albedo is the most significant single variable in determining PET (Liang, 2001). The surface albedo was calculated from RS data which accounted for actual LULC on the surface. These calculated surface albedo values showed a difference from those values available in the literature corresponding to different LULC classes (Table 4.4). This difference may also have contributed to differences in the estimated PET compared to the PM based estimates which used literature values for surface albedo uniformly across the catchment. Allen et al. (2011) also noted that each PET estimation procedure has deficiencies because of the way these procedures model the complexity of the ET process, but the difference between estimated PET and real PET should be minimized for applications. They also reported that the range of this difference depends on the estimation procedure, and that the typical range for RS based estimates varies from 10 to 40 %. The mean annual PET comparison in Table 4.5 for the Macalister catchment showed that the differences of estimated PET were within this range.

The estimated PET and PM based PET estimates were considered as base values in comparing the estimated PET; however the accuracy of the PM based PET has been questioned especially on days with extreme PET values (Barton and Meyer, 2008). The PM method uses a uniform surface albedo value to estimate net available energy spatially and temporally. However, the RS based surface albedo considered the actual spatio-temporal changes in the catchment. Furthermore, the PM method uses uniform values for soil heat flux and slope of saturation pressure curve for the entire catchment, which were not considered at all in RS based estimates. Therefore, the handling of surface albedo, soil heat flux and slope of the saturation curve in the two methods were different, and consequently produced different results.

The RS based and PM based estimates were compared in statistical terms at the selected four test locations of the Macalister catchment (in Figure 4.10), and are shown in Table 4.6. The comparison is shown for both the total period and the seasons. Winter, spring, summer and autumn are defined in this table by their monthly blocks of June-August, September-November, December-February and March-May respectively. Winter is the wettest period during the year followed by spring, while summer and autumn are drier.

The performance measures used in this table – Root Mean Square Error (*RMSE*) and Nash-Sutcliffe efficiency (*E_f*) – were explained in Section 3.9.

Table 4.6 Performance indices of estimated PET and PM based PET - Macalister catchment

Location	Day Condition	Total Period		Seasons							
				Winter		Spring		Summer		Autumn	
		<i>RMSE</i> *	<i>E_f</i>	<i>RMSE</i>	<i>E_f</i>	<i>RMSE</i>	<i>E_f</i>	<i>RMSE</i>	<i>E_f</i>	<i>RMSE</i>	<i>E_f</i>
Barkley River	Non-cloudy days	0.99	0.68	0.89	-0.85	0.73	0.42	1.19	-0.66	0.79	0.52
	Cloudy days	1.02	0.61	0.63	-1.61	1.14	0.04	1.40	-0.30	0.98	0.28
	Both	1.02	0.64	0.66	-1.40	1.09	0.12	1.36	-0.23	0.82	0.50
Mt. Tamboritha	Non-cloudy days	0.93	0.72	0.74	-0.19	0.70	0.51	1.08	-0.49	0.90	0.42
	Cloudy days	1.10	0.56	0.48	-0.63	1.31	-0.22	1.49	-0.51	1.04	0.26
	Both	1.08	0.60	0.51	-0.47	1.24	-0.08	1.43	-0.37	0.92	0.42
Licola	Non-cloudy days	1.15	0.56	1.04	-1.94	0.81	0.24	1.41	-1.28	1.02	0.16
	Cloudy days	1.08	0.57	0.77	-2.82	1.01	0.23	1.39	-0.31	1.15	-0.13
	Both	1.09	0.58	0.80	-2.57	0.98	0.25	1.39	-0.33	1.04	0.13
Mt. Howitt	Non-cloudy days	0.86	0.73	0.87	-0.59	0.71	0.48	0.98	-0.22	0.76	0.53
	Cloudy days	1.11	0.48	0.50	-0.95	1.33	-0.38	1.53	-0.63	0.89	0.38
	Both	1.09	0.53	0.52	-0.76	1.26	-0.20	1.44	-0.45	0.78	0.52

**RMSE* is expressed in mm day⁻¹

Table 4.6 shows that the calculated *RMSE* for the total period varies from 0.86 mm day⁻¹ to 1.15 mm day⁻¹ for all day conditions (i.e. non-cloudy, cloudy, and both cloudy and non-cloudy). All locations except Licola showed slightly lower *RMSE* during non-cloudy days compared to the cloudy days. Table 4.6 also shows that the magnitude of *RMSE* changes with season, with the highest *RMSE* occurring during summer. Spring shows the highest variation in seasonal *RMSE* (0.70 to 1.33) and autumn shows the lowest (0.76 to 1.15), irrespective of the day conditions. The *RMSE* of non-cloudy days is less than in other day conditions in all seasons except winter.

Table 4.6 shows that *E_f* over the Macalister catchment during the total period represents higher values irrespective of the day conditions, but is reduced with seasons. The Nash-Sutcliffe efficiency values vary from 0.48 to 0.72 during the total period over all test locations. Generally, *E_f* of non-cloudy days at all test locations show higher values compared to cloudy days and both non-cloudy and cloudy day conditions during the total period, due to more accurate estimates of surface albedo and net available energy on non-

cloudy days than on cloudy days. The highest E_f value was observed for non-cloudy days at Mt. Tamboritha and the lowest at Licola for the same day condition. The findings in terms of $RMSE$ and E_f values are consistent at each location, showing the expected inverse correlation of $RMSE$ and E_f .

The seasonal analysis shows a mixed result in E_f values. Autumn shows highest E_f value in all test locations irrespective of the day condition. Spring has comparatively higher E_f than winter and summer, and both winter and summer seasons show negative E_f under all day conditions. Table 4.6 shows that non-cloudy day E_f values perform better than those of the other day conditions during seasons. When E_f values for the total period are compared with those of the seasons, it was found that the total period E_f values were not within the range of seasonal E_f values. This has also been observed by Wang et al. (2006) and Sachindra et al. (2013). This is because of the significant difference between the total period mean (which was used to calculate E_f for the total period) and the seasonal mean of the particular seasons (which was used to calculate for the seasonal E_f).

Mt. Tamboritha and Mt. Howitt show better results than the other locations for both total period and seasons. Both these locations have relatively homogenous LULC class, while the other two locations have mixed LULC classes. This show that the estimated PET are relatively closer to the PM based PET over homogenous LULC classes during the total period as well as the seasons. This is mainly due to the similarity and consistency of surface albedo values computed from RS data for the catchment (used in estimated PET) and obtained from literature (used in PM based PET estimates). Furthermore, Licola shows the poorest performance with both $RMSE$ and E_f compared to the other locations during the total period as well as the seasons. This is because Licola has mixed LULC, which has been considered in the RS based method in estimating surface albedo. Mixed LULC information is, however, not considered in the PM method in estimating surface albedo.

4.2.3 Landuse/landcover classification

The spatial distribution and the extent of the landuse/landcover (such as forests, meadows, agricultural land, urban, bare and water bodies) in a catchment influence the spatio-temporal dynamics of evapotranspiration, surface runoff, soil moisture and ground water recharge. Therefore, related landuse/landcover (LULC) information in a catchment is

essential to successfully estimate streamflow using a catchment process model (Wegehenkel et al., 2006). In order to classify LULC, the RS based image classification approach was proposed in Section 3.5.3. A single image (Landsat 5 TM image taken on 23rd November 2006) which is free of clouds, haze and distortion, was selected for the LULC classification of the Macalister catchment. A single image was used in this study since no major changes occurred in the LULC in the Macalister catchment during the study period (2003 to 2008).

Seven bands of Landsat TM (Table 4.7), except the thermal band (band 6), were considered in the classification process. The thermal band was not considered in this study since its spatial resolution is considerably different (120 m) to the other bands (30 m). The remaining six non-thermal bands were used in the Principal Component Analysis (PCA) to produce a reduced number of variables to use in the LULC classification. PCA produces a reduced number of variables without losing information of the original variables. This step was followed, since LULC classification is difficult with many variables.

Table 4.7 Band information of the Landsat 5 TM sensor

Band number	Band name	Band width (µm)	Spatial resolution (m)
1	Blue	0.45~0.52	30
2	Green	0.52~0.60	30
3	Red	0.63~0.69	30
4	NIR*	0.76~0.90	30
5	MIR**	1.55~1.75	30
6	Thermal	10.4~12.50	120
7	MIR	2.08~2.35	30

* NIR – Near infrared, ** MIR- Mid infrared

4.2.3.1 Principal Component Analysis

Principal Component Analysis can be used to transform correlated image bands in to a new set of uncorrelated variables that are arranged based on the magnitude of variance explained in the original data (Eastman and Fulk, 1993). Therefore, PCA has been used in image classification to reduce the number of bands and to enhance the information on the image (Gamage et al., 2007; Madugundu et al., 2014). As outlined in Section 4.2.3, PCA employed six bands of the Landsat 5 TM image. The results of the PCA are presented in

Figure 4.13. This figure represents the cumulative variance of each Principal Component (PC), with the x-axis showing the PCs. Note that $\Sigma PC_i = PC_1 + PC_2 + \dots + PC_i$ in the x-axis, where $i = 2, 3, 4, 5$ and 6 . It shows that the first PC represents almost 85% of the image variability, and the first three PCs represent more than 99% of its variability. This implies that first three PCs can be used to adequately represent all the bands of the original image without losing content information. Therefore, the first three PCs were selected to classify LULC over the catchment. In addition to these three PCs, *NDVI* which was calculated separately to PCA, was used in the classification. *NDVI* was used in the classification, since it facilitates the identification of vegetation information and reduces the effect of mountain shadows. Hence, a final image with four variables (i.e. the above first three PCs and *NDVI*) was used in the LULC classification.

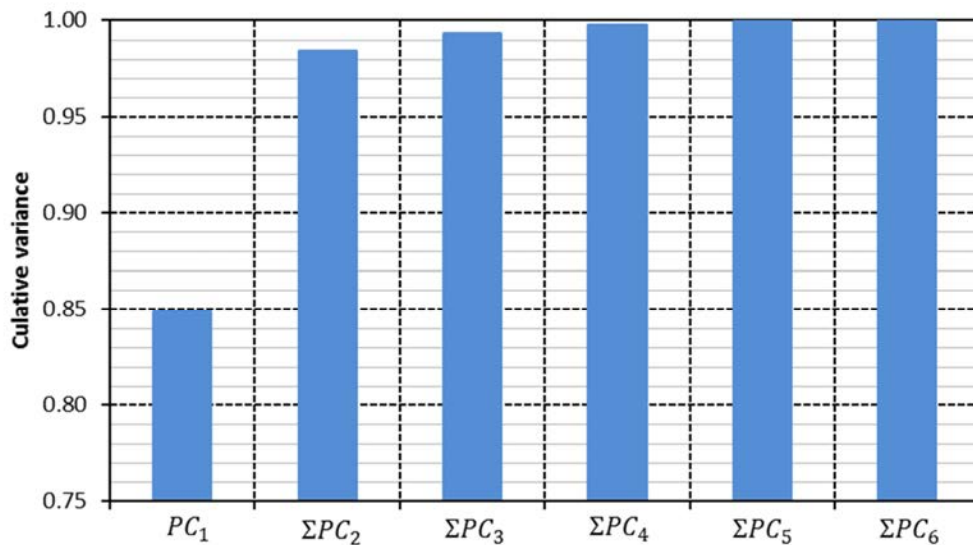


Figure 4.13 PCA components and their cumulative variance

4.2.3.2 Results of landuse/landcover classification

The above mentioned final image was used to classify the LULC classes in the Macalister catchment. The available LULC classes were identified during the field data collection survey (ground-truth data collection). The survey covered sample areas of each LULC available within the catchment area. Half of the field data (i.e. ground-truth data) was used in image training (Section 3.5.3.2). Then, all pixels of the trained image were categorized into LULC classes they mostly resemble using the maximum likelihood classifier. The remaining half of the ground-truth data (i.e. sampling areas) was used to assess the

classification accuracy (Section 3.5.3.4). A detailed description of the methodology of LULC classification was given in Section 3.5.3.3.

The results of the LULC classification of the Macalister catchment are shown in Figure 4.14. The area covered by each LULC class is presented in Table 4.8. As can be seen from Figure 4.14 and Table 4.8, forests represent the majority of LULC. Forest in the Macalister catchment can be divided into three classes based on the area covered by its crown canopy (i.e. top canopy cover). They are: closed forest (81%-100% crown canopy); open forest (50%-80% crown canopy); and woodland forest (20%-50% crown canopy) (Bureau of Rural Sciences, 2009).

According to the classification results (Figure 4.14), 51.1% of the catchment area is covered with closed forest, which can be seen from north to south of the catchment along its west and east borders. Open forest covers 33.7% of the catchment area and is mostly located in the middle part of catchment. Woodlands forest is the least within all forest classes and is scattered all over the catchment. Eucalyptus is the dominant plant species in all three classes of forest in this catchment, and represents nearly 93% of the catchment area.

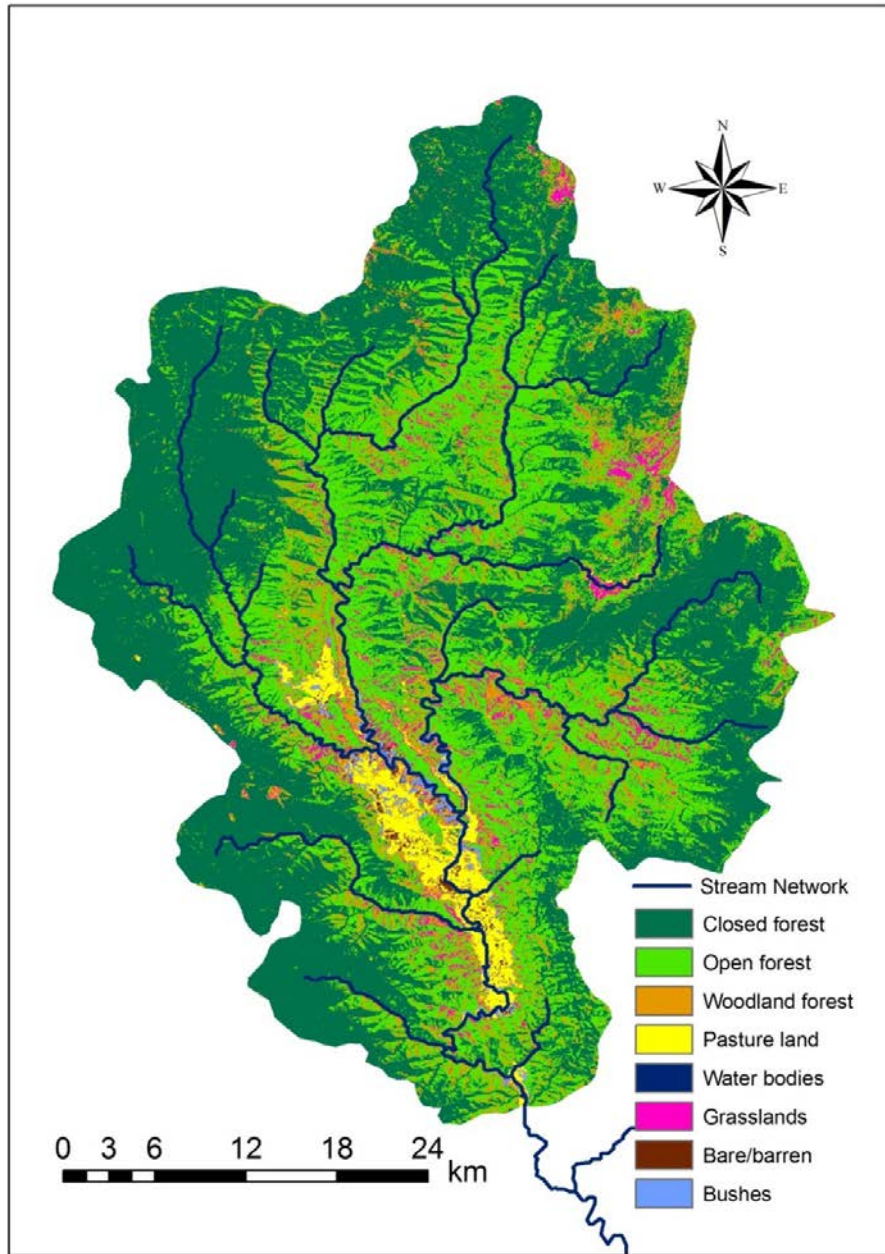


Figure 4.14 Landuse/landcover classes of the Macalister catchment (after image classification)

Following the forest cover (i.e. closed forest, open forest and woodlands forest), pasture and grasslands are the next dominant LULC classes. They cover approximately 6% of the catchment area. A magnified view of the classified LULC image shows that they are mixed with each other. This is mainly because of the similar signature of these LULC classes. Whilst pasture is dominant along the Macalister River, grasslands are scattered throughout the catchment. The remaining areas represent bushes, bare/barren lands and

water bodies, which cover a little more than 1% of the catchment area. Rivers, streams and a few farm ponds represent the water bodies, but they cover a negligible area. Other than these classes of vegetation, roads and houses are present but in insignificant proportions. Therefore, a great attention was not paid to classify these classes.

Table 4.8 Areas of the catchment covered by different LULC classes (after image classification)

LULC class	Area (ha)	Percentage
Closed forest	76931.8	51.1
Open forest	50713.2	33.7
Woodland forest	12297.0	8.2
Pasture land	4258.2	2.8
Water bodies	1.7	0.0
Grasslands	4646.2	3.1
Bare/barren land	526.1	0.3
Bushes	1201.8	0.8
Total	150576.0	100.0

4.2.3.3 Accuracy assessment of the landuse/landcover classification

Both descriptive and analytical techniques which were described in Section 3.5.3.4, were used to assess the accuracy of LULC classification using the half of the data that was not used for image training purposes. They are discussed separately in the following subsections.

(a) Descriptive techniques

With regards to the descriptive techniques, the producer's accuracy (the probability of correctly classifying an LULC class relevant to its reference total), user's accuracy (the probability of correctly classifying an LULC class in line with the image that actually represents that LULC class on the ground) and overall accuracy (the number of correctly classified samples in the total number of samples), notions of which have been explained in Section 3.5.3.4, were calculated. These accuracy figures were compared using that half of the ground-truth data (i.e. sample area) that was not used for training purposes (i.e. for identifying the signature of each LULC class in the satellite image) of the LULC

classification. The results of the LULC classification accuracy are traditionally presented as a matrix (which is called the contingency matrix), and is shown in Table 4.9.

Even though Congalton (1991) mentioned that each LULC class should have a minimum of 50 samples for accuracy assessment (as a rule of thumb), it is believed that the number of sample points used in this study is sufficient to accurately represent the study area because of its relative size, less heterogeneity and less number of LULC classes. Table 4.9 shows that the number of sample points which was used to assess the LULC accuracy is higher than 50 in all forest classes and pasture lands (refer to producer's total), while grasslands were close to that margin. The number of sample points which was used for accuracy assessment is significantly less in the remaining LULC classes, but they represent an insignificant area in the catchment. Thomlinson et al. (1999) have suggested setting the individual LULC class accuracy threshold as 70% and the overall accuracy threshold as 85%.

Table 4.9 Contingency matrix of the landuse/landcover classification – the Macalister catchment

		1	2	3	4	5	6	7	8	9	10
		Closed forest	Open forest	Woodland forest	Pasture land	Water bodies	Grasslands	Bare/barren land	Bushes	User's total	User's accuracy
1	Closed forest	61	3	5	0	0	3	0	2	74	82.4
2	Open forest	3	59	6	3	0	2	0	1	74	79.7
3	Woodland forest	2	4	51	1	0	4	1	2	65	78.5
4	Pasture land	1	3	2	51	0	1	2	0	60	85.0
5	Water bodies	0	0	0	0	3	0	0	0	3	100.0
6	Grasslands	0	1	1	4	0	37	0	2	45	82.2
7	Bare/barren land	0	0	0	2	0	0	16	2	20	80.0
8	Bushes	0	0	0	6	0	0	2	20	28	71.4
9	Producer's total*	67	70	65	67	3	47	21	29	369	
10	Producer's accuracy	91.0	84.3	78.5	76.1	100.0	78.7	76.2	69.0		80.8

*Producer's total represent the number of samples used in accuracy assessment

Table 4.9 shows that the individual accuracy level of all three forest classes (which cover about 93% of the catchment area) is more than 78.5% in both producer's perspective of accuracy and user's perspective of accuracy. For example, the producer's accuracy and user's accuracy of closed forest is 91% and 82.4% respectively. This can be explained by the fact that although 91% of closed forest areas have been correctly identified as closed forest, only 82.4% of the areas called closed forest are actually closed forest.

Closed forest shows the highest producer's and user's accuracy in all three forest classes followed by open forest and woodland forest. This table also shows that the samples used to assess the accuracy of a given class can falsely be found in some other classes. A high proportion of such false classification in a given forest class falls under the remaining two forest classes (cells covered by the first three columns and the three rows in the table). This is especially due to the similar signatures of these classes in the image used to for classification purposes. Other than that, this table shows that all forest types (the first three rows) signatures are mixed with grasslands (column 5) which is the main reason to have less user's accuracy in comparison with producer's accuracy.

The producer's accuracy of the pasture is approximately 76% (Table 4.9). Table 4.9 also shows that the samples of this particular class of LULC is also classified with open forest, grasslands, bare/barren lands and bushes (column number 4). This is mainly because the pasture lands have a diverse signature which overlaps with those classes. Pasture lands are more similar to grasslands in vegetation structure (grass height, density and seasonality), thereby making it difficult to separate the signature of those two classes. It is also observed that bushes are more vulnerable to be classified as pasture lands as bushes are located at the edges of pasture lands. User's accuracy of the pasture is as high as 85% whilst signature is mixing with other LULC classes such as open forest, grasslands and bare/barren lands.

Water bodies represent a negligible area in the catchment, being represented only by the Macalister River, its tributaries and farm ponds. Grassland shows 78.7% and 82.2% of producer's accuracy and user's accuracy respectively (Table 4.9). The table also shows that the signature of grassland is mixed with all three forests classes (column number 6). This is

possible since grasslands can depict a very bright signature (higher *NDVI* value) which is equivalent to dense forest during its growth stage (especially during late winter to early summer). Furthermore, grassland is erroneously classified with pasture, since both classes share a common grass signature.

The results show that bare/barren LULC class represents a small percentage (0.3%) of land in the Macalister catchment. The levels of accuracy in both producer's and user's classification are higher in this LULC class than the recommended level (Thomlinson et al., 1999).

Table 4.9 shows that the overall accuracy, which represents the correctly classified samples (i.e. the sum of the diagonal values in the contingency matrix) in relation to the total number of samples, of the LULC classification is 80.8%. This figure is marginal to the threshold highlighted by Thomlinson et al. (1999).

(b) Analytical techniques

The kappa coefficient, an analytical measurement of the classified LULC map accuracy is calculated, and presented in Table 4.10, together with user's accuracy. This is presented with user's accuracy since user's accuracy is important in further applications. This coefficient is an indicator for measuring the significance of the contingency metrics (in Table 4.9) against the chance agreement which arises due to a given LULC class randomly classified to correct LULC class. The kappa coefficient value varies from 0 to 1. 1 means that observed classification accuracy (user's accuracy) in the classified map is 100 times better than the one resulting from chance. At most times, the kappa coefficient (converted to a percentage) is a little less than the observed classification accuracy value due to the fact that both contingency calculations and the kappa coefficient use different forms of information from the Table 4.9. However, a large difference between the contingency matrix and the kappa coefficient reveals that the classification is not reliable. Table 4.10 shows that differences between those two accuracy indices are small.

Table 4.10 Kappa statistics and user’s accuracy of the landuse/landcover classification

LULC class	Kappa coefficient	User’s accuracy
Closed forest	0.79	82.4
Open forest	0.75	79.7
Woodland forest	0.74	78.5
Pasture land	0.82	85.0
Water bodies	1.00	100.0
Grasslands	0.80	82.2
Bare/barren land	0.79	80.0
Bushes	0.69	71.4
Overall	0.77	80.8

According to Bharatkar and Patel (2013), a kappa coefficient less than 0.4 represents a poor classification, 0.4 to 0.75 represents a good classification, and more than 0.75 represents an excellent classification.

Table 4.10 shows that the kappa coefficients of all individual LULC classes are either good or excellent based on Bharatkar and Patel (2013). The kappa coefficient of open forest, woodland forest and bushes can be rated as ‘good’ while that of closed forest, pasture lands, grasslands, water bodies and barren lands can be rated as ‘excellent’. The overall kappa coefficient is 0.77, and can thus be rated as ‘excellent’.

Both the descriptive and analytical techniques used in this study for the accuracy assessment of image classification showed that the results of the classification are reliable and suitable for further applications. On this basis, this LULC classification results were subsequently used as input data for the catchment process model to estimate streamflow in the Macalister catchment (Section 4.3).

4.3 Catchment process modelling

As outlined in Section 3.6, the Soil and Water Assessment Tool (SWAT) was used to estimate daily streamflow in catchment process modelling. Several SWAT models of the Macalister catchment were developed with different data to investigate how RS based input data perform

on daily streamflow estimation. Initially, ground measured meteorological data with LULC data (Section 4.2.3) and FAO-based soil data were used to set up the model.

Daily rainfall, minimum and maximum temperature, solar radiation, wind speed and relative humidity were used as ground measured meteorological variables for this study. All variables except rainfall were used to compute PET within the SWAT model. The Penman-Monteith method which is an in-built option of SWAT was used in this regard. The SWAT model set up with these ground measured data (including SWAT derived PET data) was considered as the base model in this study.

The objective of the base model is to calibrate the model parameters. Then these calibrated model parameters were used with later models which had used RS based variables as inputs. Estimated rainfall and estimated PET from RS data were used as RS based input variables in this process. RS based LULC and FAO-based soil data were kept unchanged throughout the modelling process. The sequence below was used for replacing ground measured inputs with RS based inputs.

- (1) PET which was computed internally by SWAT model (hereafter SWAT derived PET) using ground measured data was replaced with PET estimated using RS data, while keeping ground measured rainfall data unchanged in the model.
- (2) Ground measured rainfall data were replaced with estimated rainfall, while keeping SWAT derived PET unchanged.
- (3) Both ground measured rainfall and SWAT derived PET were replaced with estimated rainfall and estimated PET.

The setting up of a SWAT model to a catchment was discussed in Section 3.6.2. The hydrological response unit (HRU) is the basic element which generates runoff in a subcatchment of the SWAT model. Defining HRUs in a subcatchment is based on that subcatchment LULC, soil class and slope (Neitsch et al., 2002). There are three options available to define HRUs with LULC, soil class and slope. They are:

- I. Through the use of dominant LULC, soils or slope – One HRU is created to represent a subcatchment. This HRU will represent the dominant LULC, soil, and slope class in the subcatchment.
- II. The dominant HRU – One HRU is created to represent a subcatchment. However, this HRU represents the dominant unique combination of LULC, soil, and slope class in the subcatchment.
- III. Multiple HRUs – Multiple HRUs are created in the subcatchment, based on the user's defined percentage of LULC, soil, and slope class.

The third option was used in this study to define HRUs, since the catchment elevation and LULC of the Macalister catchment vary significantly from upstream (north) to downstream (south). In the case of the Macalister catchment, 30% of LULC over subcatchment, 20% of soil class over LULC, and 20% of slope class over soil area were used to define HRUs. LULC was given a higher weight since this variable has more effect on the SCS curve number. As explained in Section 3.6.1, surface runoff is the major component of water balance in the SWAT model (Equation 3.35) and is estimated through the SCS curve number method.

The results and performances of each of the aforementioned models are discussed in the following sub sections. This performance comparison shows the effectiveness of the catchment models which used RS based input data of rainfall and PET.

4.3.1 Model calibration and validation with ground measured data

The procedures outlined in Section 3.6.2 was followed to set up the SWAT model of the Macalister catchment with ground measured data. Then the model was calibrated for the period 2003 - 2006 and validated for the period 2007 - 2008. Observed streamflow data of the Macalister River at Stingybark Creek were used during the calibration period to optimize the calibration parameters. Then, the model was run with those optimum parameters for the period of validation. The theoretical ranges which are allowed in the SWAT model and the optimum value of the most sensitive parameters obtained at the end of auto-calibration are given in Table 4.11. The existing literature shows that many of those parameters listed on Table 4.11

are the most sensitive parameters in streamflow estimation with SWAT (Sther et al., 2008; Setegn, 2010; Betrie et al., 2011a; Bastiaanssen et al., 1998a).

CN2 varies according to different LULC, hydrologic condition (poor or good) and Hydrologic Soil Group (i.e. A, B, C, D) (Chow, 1959; Neitsch et al., 2002). The Hydrologic Soil Group (HSG) in this modelling exercise was determined based on FAO soil class over the catchment area. The hydrologic condition depends on various ground conditions such as the density and canopy of vegetative areas, the amount of year-round vegetation cover, the percentage of residue vegetation cover on the land surface and the degree of surface roughness (USDA, 1986). The hydrological condition is categorized as poor if these conditions impair infiltration and cause higher runoff, and as good if these conditions encourage infiltration and reduce runoff. The LULC generated with RS data imply that the Macalister catchment is in 'good' hydrologic condition throughout the year. Different CN2s were used to represent different LULC within this study. The remaining parameters in Table 4.11 were considered to have a single value for the entire catchment. This is due to the unavailability of data at a finer spatial scale in the catchment. These parameters are also more relevant to the entire catchment than for individual subcatchments, HRUs or different LULC classes.

Table 4.11 SWAT model parameters used for calibration purposes

Parameter	Description	Range*	Optimum value
Parameters the govern surface water response			
CN2	Curve Number II	35-98	48 ¹ , 55 ² , 60 ³ , 58 ⁴ , 85 ⁵ , 65 ⁶
ESCO	Soil evaporation compensation factor	0-1	0.2
SOL_AWC	Available soil water capacity	0-1	0.57
Parameters that govern subsurface water response			
GW_REVAP	Groundwater re evaporation coefficient	0.02-0.2	0.16
REVAPMN	Threshold depth of water in the shallow aquifer for re evaporation to occur (mm)	0-500	90.9
GWQMN	Threshold depth of water in the shallow aquifer required for return flow to occur (mm)	0-5000	605.16
GW_DELAY	Groundwater delay (days)	0-50	5.38
ALPHA_BF	Base flow recession constant	0-1	0.44
RCHRG_DP	Deep aquifer percolation fraction	0-1	0.83
Parameters that govern catchment response			
CH_K2	Effective hydraulic conductivity in main channel alluvium (mm h ⁻¹)	0.01-150	13.8
SURLAG	Surface runoff lag coefficient (day)	0-10	6.78

¹closed forest, ²open forest and woodlands, ³pasture, ⁴grasslands, ⁵bare/barren and ⁶bushes

*(Neitsch et al., 2010)

Figure 4.15 shows measured streamflow and the results obtained from the base model (i.e. estimated daily streamflow for the model developed with ground measured data including SWAT derived PET data) of the Macalister catchment for the period 2003 to 2008 (i.e. both calibration and validation periods). Measured streamflow of the Macalister catchment (i.e. the gauge near Stringybark Creek) shows that streamflow is high during the ‘July to November’ period of every year. The lowest streamflow in a given hydrological year is recorded during the ‘March to May’ period. According to these observations, a hydrological year can be divided into two main seasons: wet (i.e. winter and spring) and dry (i.e. summer and autumn). Out of measured streamflow during the study period, years 2003 to 2005 reveal the average streamflow conditions. The streamflow of year 2007 is above average (extremely high flow) while years 2006 and 2008 are below average.

It was observed (Figure 4.15) that streamflow estimation over the Macalister catchment with the base model is in good agreement with the measured streamflow, both for the calibration and validation periods. However, estimated daily streamflow is overestimated in the wet season of year 2006 which is the driest year in the catchment within the study period. Figure 4.16 shows the scatter plots of estimated streamflow versus measured streamflow with their coefficient of determination, separately for calibration and validation periods. The scatter plot of the calibration period shows a slight overestimation in low flows, while a slight underestimation in high flows. The coefficient of determination of estimated and measured streamflows in the validation period is slightly better than that of the calibration period.

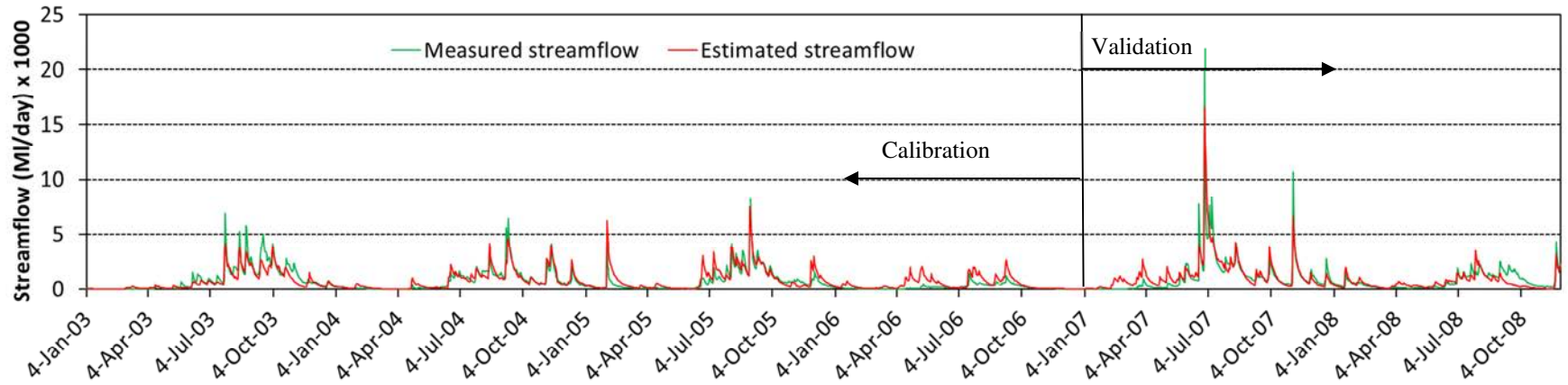


Figure 4.15 Measured and estimated streamflow of the Macalister catchment – base model

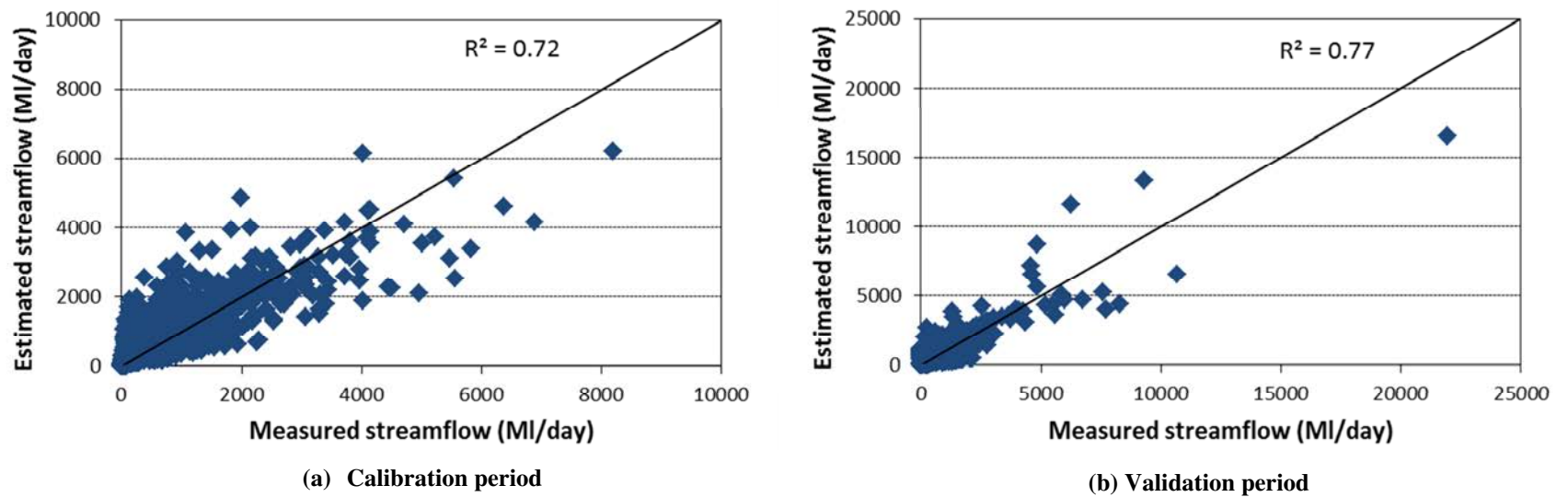


Figure 4.16 Scatter plots of the measured and estimated streamflow of the Macalister catchment – base model

Figure 4.17 shows the same result as the base model with measured streamflow for the seasons during the study period. It should be noted that December–February, March–May, June–August and September - November are considered as summer, autumn, winter and spring respectively in this study. The seasons during calibration period and validation period are shown separately in this figure.

In general, Figure 4.17 shows that the streamflow of the dry season (i.e. summer and autumn seasons) is mostly overestimated, especially during the calibration. SWAT does not allow different parameters for different months or seasons, and therefore the parameter set obtained from calibration was the best in modelling streamflows in all seasons, which include both dry and wet seasons.

The streamflow of the wet season (i.e. winter and spring) is well estimated in both the calibration and validation periods. It is noted that the magnitude of streamflow during the calibration period of winter is much lower than that of the validation period. This is in line with the observation of Figure 4.15, with very high flows in year 2007.

The estimated streamflow of the base model was further analyzed with the Root Mean Square Error (*RMSE*) and the Nash-Sutcliffe efficiency (E_f), other than the coefficients of determination which were shown in Figures 4.16 and 4.17. The estimation procedure of *RMSE* and E_f were explained in Section 3.9. Table 4.12 summarizes all performance indices for both the total period (both calibration and validation separately) as well as individual seasons (both calibration and validation separately for each season).

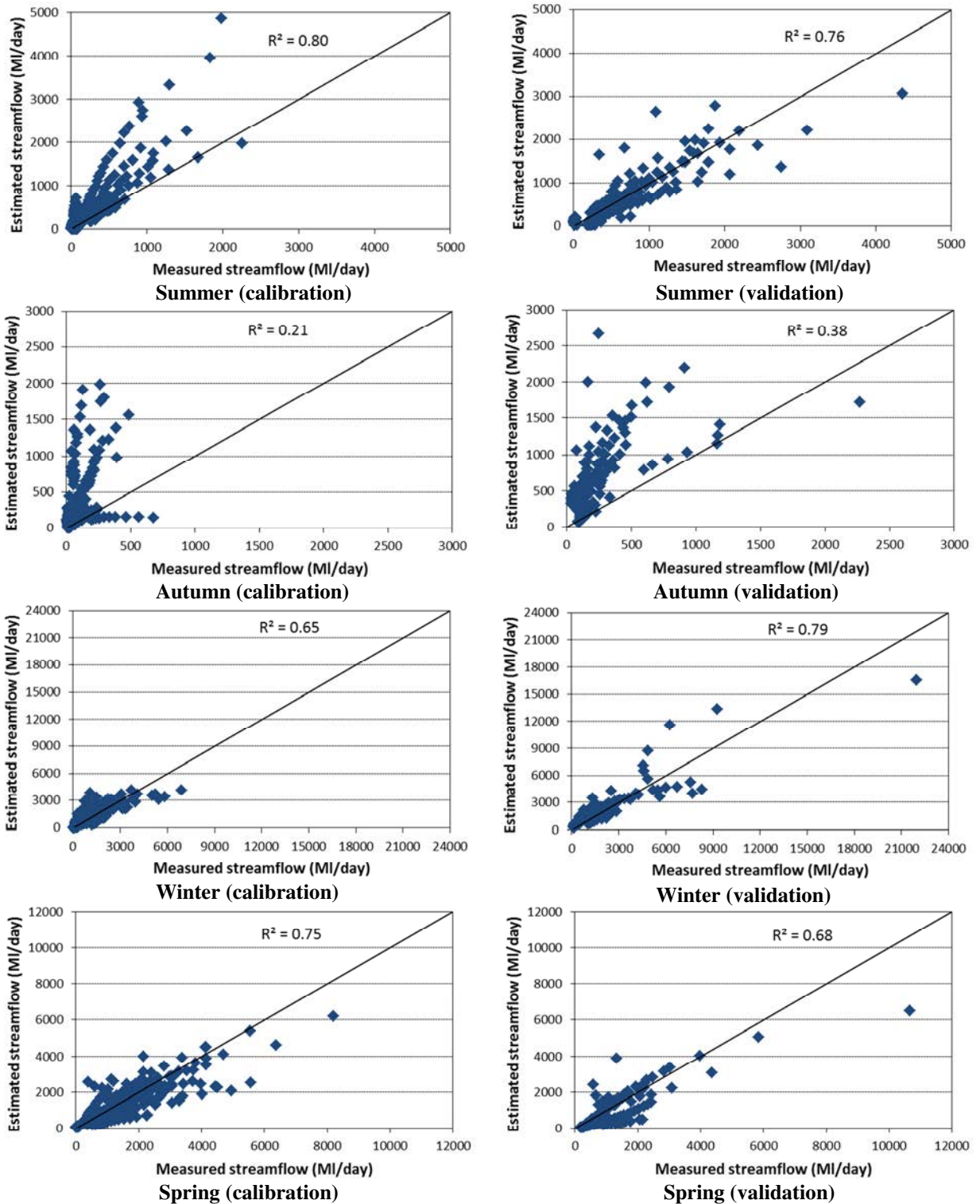


Figure 4.17 Scatter plots of the measured and estimated streamflow for different seasons of the Macalister catchment – base model

The performance indices of the total period show slightly better streamflow estimation during the validation period compared to the calibration period. However, the seasonal performance indices are different to the total period values and they are different in different seasons. The performance indices of Table 4.12 show that streamflow estimation during the wet season (i.e. winter and spring) is better than that of the dry season (i.e. summer and autumn). Among all seasons, autumn is estimated with a negative E_f . It was observed that the magnitude of measured streamflow of autumn seasons is either very low or zero during the calibration period. During these extremely low streamflow periods, the SWAT model overestimated the streamflow, thereby producing a negative E_f . The streamflow of autumn of 2007, which is wet compared to other autumn seasons during the study period, has modeled well. This has had a favourable impact on the performance of the validation period during the autumn season.

Table 4.12 *RMSE* (in MI/day) and E_f values of the streamflow estimation using measured data
- base model

Period	Performance Index	Calibration	Validation
Total	E_f	0.73	0.76
	<i>RMSE</i>	469	487
Spring	E_f	0.74	0.62
	<i>RMSE</i>	584	677
Summer	E_f	0.35	0.75
	<i>RMSE</i>	214	313
Autumn	E_f	-17.25	-2.66
	<i>RMSE</i>	365	482
Winter	E_f	0.65	0.78
	<i>RMSE</i>	562	1005

4.3.2 Streamflow estimation with remote sensing based input variables

After setting up and calibrating the SWAT model with ground measured data (i.e. the base model in Section 4.3.1), the ground measured rainfall, and SWAT derived evapotranspiration were replaced with estimated rainfall (Section 4.2.1) and estimated PET (Section 4.2.2). These substitutions were initially done one at a time, and then together. The results of these different SWAT configurations are discussed in the subsections below. The different configurations are:

- A model with estimated PET and ground measured rainfall
- A model with estimated rainfall and SWAT derived PET
- A model with estimated rainfall and estimated PET

In these models, there were no separate calibrations and validations, thus the models were run from 2003 to 2008. The calibrated model parameters of the base model were used as model parameters (Section 4.3.1) in these model runs.

4.3.2.1 Model with estimated PET and ground measured rainfall

The PET of the base model which were computed using ground measured meteorological data (SWAT derived PET) were replaced with estimated PET to generate daily streamflow in this model. The results of the model run are shown in Figures 4.18 and 4.19. The calibration and validation periods are shown in Figure 4.18 to maintain the consistency with the base model (Figure 4.15). Figure 4.18 shows that the estimated daily streamflow is in a good agreement with the measured streamflow, which is similar to Figure 4.15. Figure 4.19 shows the same results in scatter plots separately for calibration and validation periods of the base model; this is consistent with Figure 4.16. This figure shows that the coefficients of determinations of calibration and validation periods are also similar to those of base model.

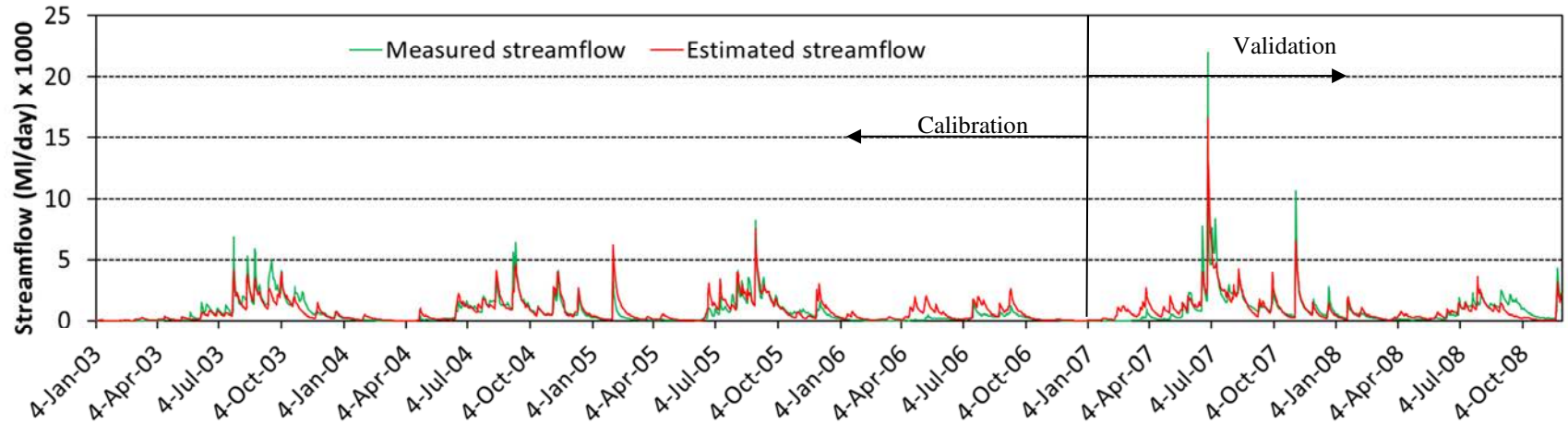


Figure 4.18 Measured and estimated streamflow of the Macalister catchment – model with estimated PET and ground measured rainfall

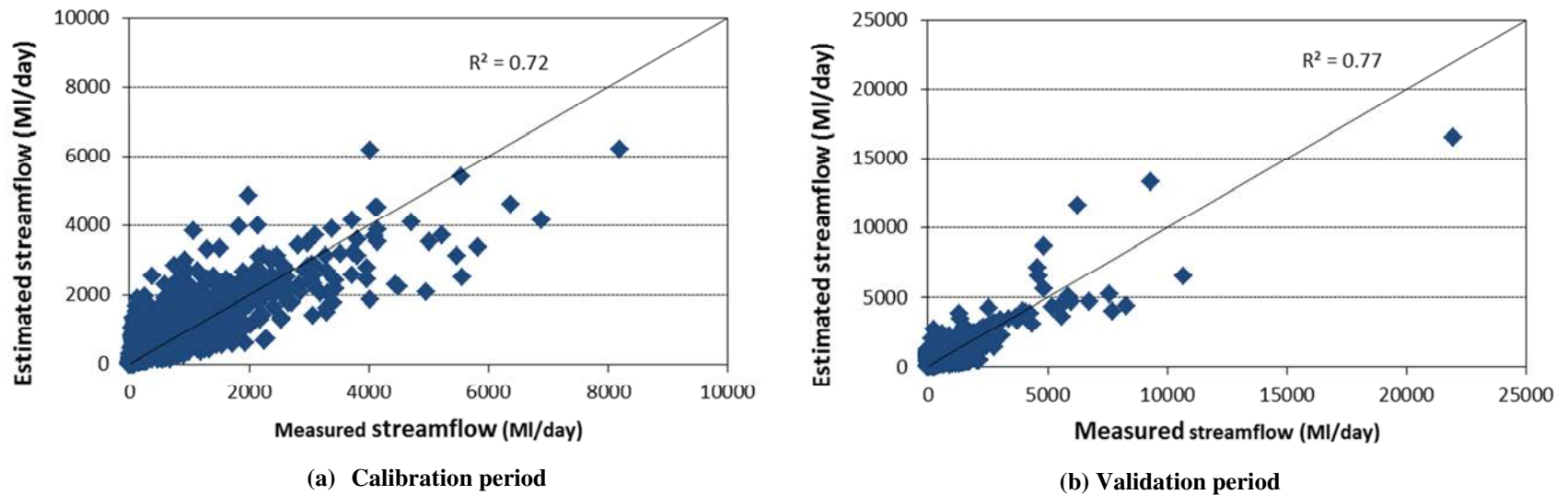


Figure 4.19 Scatter plots of the measured and estimated streamflow of the Macalister catchment with estimated PET and ground measured rainfall

The output of the model run was used with observed (or measured) streamflow to assess the performance of this version of the model. They are presented in Table 4.13. A comparison of Table 4.12 and Table 4.13 shows similar results in both estimations, not only for the total period but also for individual seasons.

Table 4.13 Performance indices of the streamflow estimation – model with estimated PET and ground measured rainfall data

Period	Index	Calibration period	Validation period
Total period	E_f	0.66	0.77
	<i>RMSE (Ml/day)</i>	538	477
Spring	E_f	0.74	0.62
	<i>RMSE (Ml/day)</i>	582	677
Summer	E_f	-0.24	0.74
	<i>RMSE (Ml/day)</i>	409	314
Autumn	E_f	-17.5	-3.24
	<i>RMSE (Ml/day)</i>	367	519
Winter	E_f	0.46	0.78
	<i>RMSE (Ml/day)</i>	699	1005

The scatter plots of seasons in Figure 4.18 (the model with estimated PET and ground measured rainfall) were not considered since the estimated daily streamflow of the base model and the model with estimated PET are almost similar.

4.3.2.2 Model with estimated rainfall and SWAT derived PET

Daily rainfall which is estimated using RS data were used as input in this model. Daily values of the estimated rainfall were spatially averaged within each subcatchment and fed into the SWAT model at the centroid of the subcatchment. PET derived by the SWAT model was not replaced in this model. The estimated streamflow from this model and measured streamflow are shown as a line plot in Figure 4.20. The same results are shown as scatter plots for the calibration and validation periods (although calibration and validation were not done separately for this model) separately in Figure 4.21.

Figures 4.20 shows a poor estimation of streamflow with estimated rainfall. Streamflow during the wet season is more poorly estimated than the dry season with estimated rainfall. Figure 4.21 shows that most of the streamflow greater than 3000 MI/day are underestimated in both the calibration and validation periods. When comparing Figures 4.20 and 4.21 with their counterpart figures of the base model (i.e. figures 4.15 and 4.16), it is seen that the estimation of streamflow from this version of the model is not as good as that of the base model or the model with estimated PET (Section 4.3.2.1). Note that the model with the estimated PET had produced similar results to these of the base models (Section 4.3.2.1).

Figure 4.22 is based on the same model results, but they are shown separately for seasons and calibration and validation periods. This figure also shows that streamflow is poorly estimated with estimated rainfall. Streamflow was mostly overestimated during the dry season (i.e. summer and autumn). Similar overestimation was also observed in the dry season of the base models. Estimated streamflow of this model was mostly underestimated during the wet season (i.e. winter and spring).

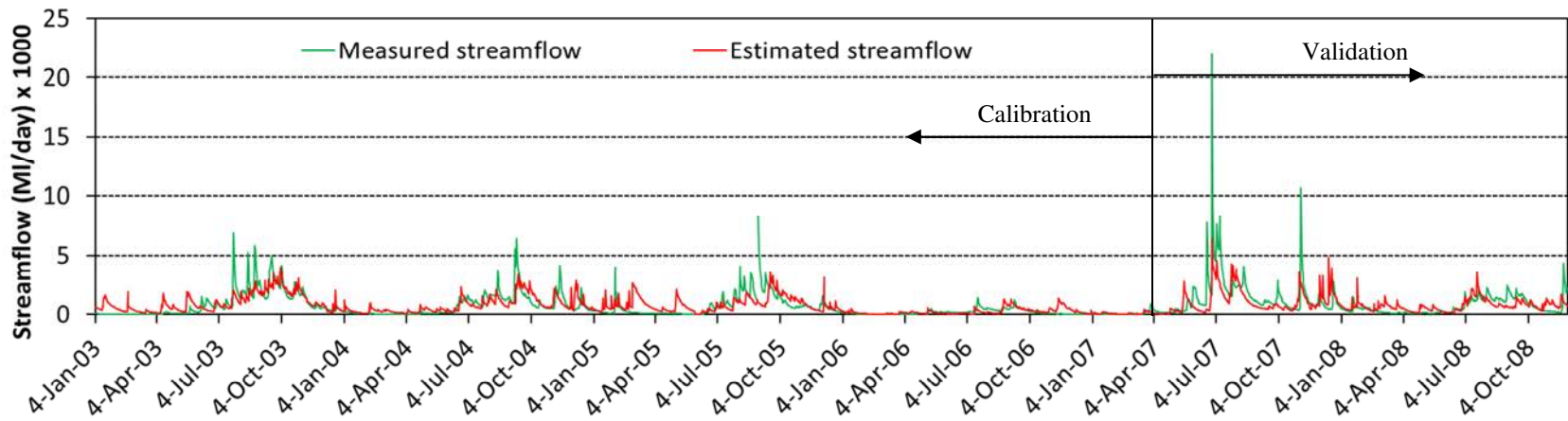


Figure 4.20 Estimated and measured streamflow of the Macalister catchment – model with estimated rainfall and SWAT derived PET

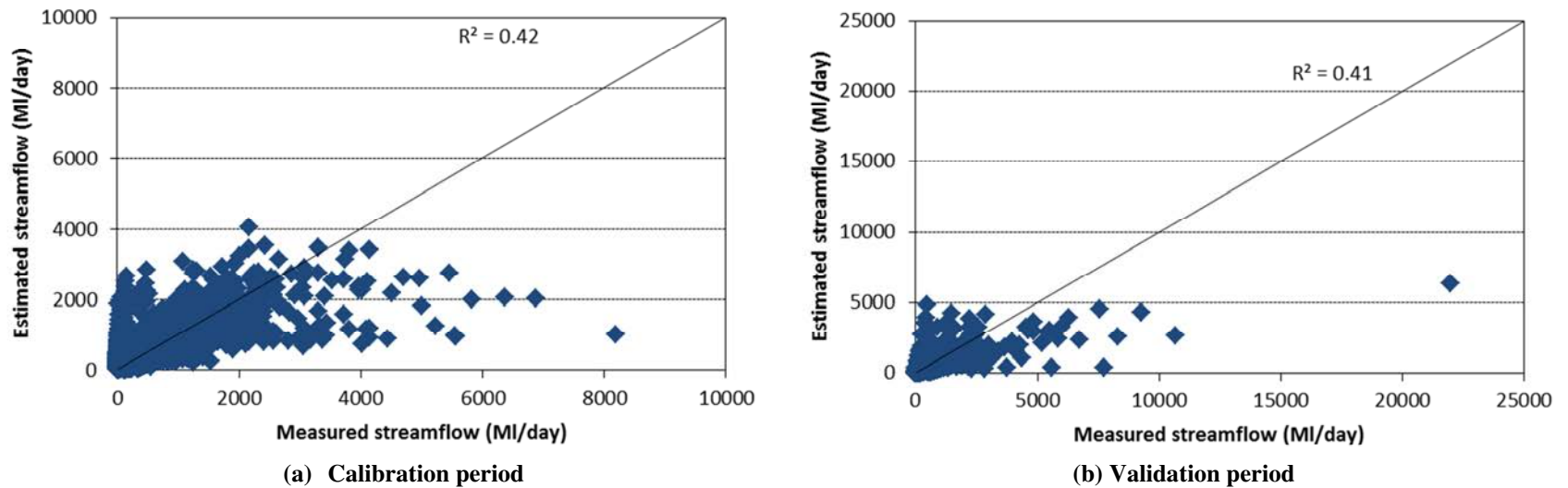


Figure 4.21 Scatter plots of the estimated and measured streamflow of the Macalister catchment - model with estimated rainfall and SWAT derived PET

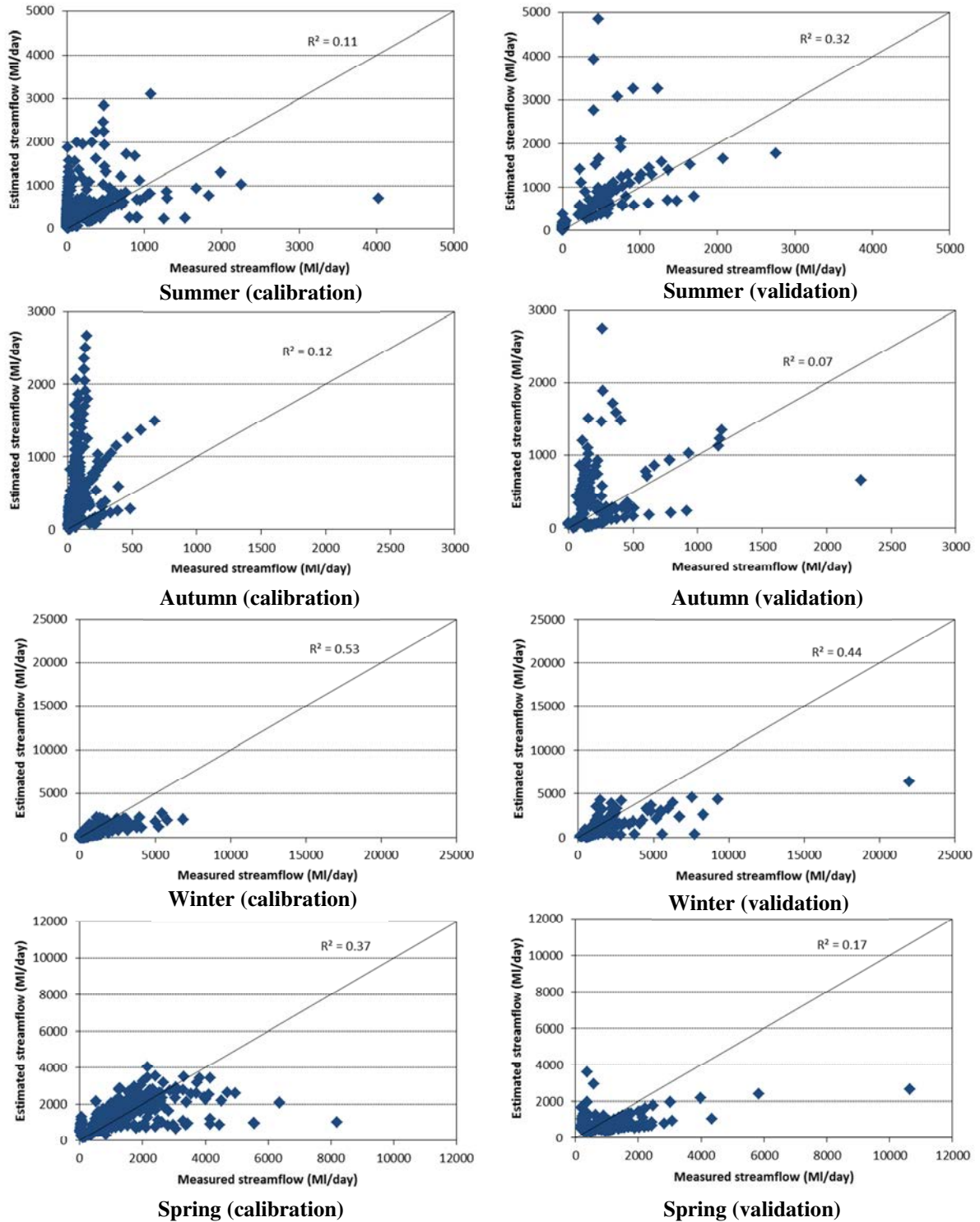


Figure 4.22 Seasonal scatter plots of measured and estimated streamflow of the Macalister catchment – model with estimated rainfall and SWAT derived PET

4.3.2.3 Model with estimated rainfall and estimated PET

Both estimated rainfall and estimated PET were used together to estimate daily streamflow data in the SWAT model. This was done by replacing both ground measured rainfall and SWAT derived PET by the above mentioned estimated rainfall and estimated PET. Similar to Sections 4.3.2.1 and 4.3.2.2, the calibrated model parameters of the base model were used in this model run. Results of the model run are shown in Figures 4.23 and 4.24. The calibration and validation periods were shown in these figures, as it was done with the previous model results (Sections 4.3.2.1 and 4.3.2.2) to maintain consistency. A comparison of Figures 4.23 and 4.24 with the corresponding figures of the model with estimated rainfall in Section 4.3.2.2 (i.e. Figures 4.20 and 4.21) show that the results of both models are similar (which is also poor relative to those of the base model and the model with estimated PET, which are similar). The same results were plotted on a seasonal basis, and are shown in Figure 4.25. This figure shows that streamflow during the wet season is fairly well estimated compared to streamflow during the dry season.

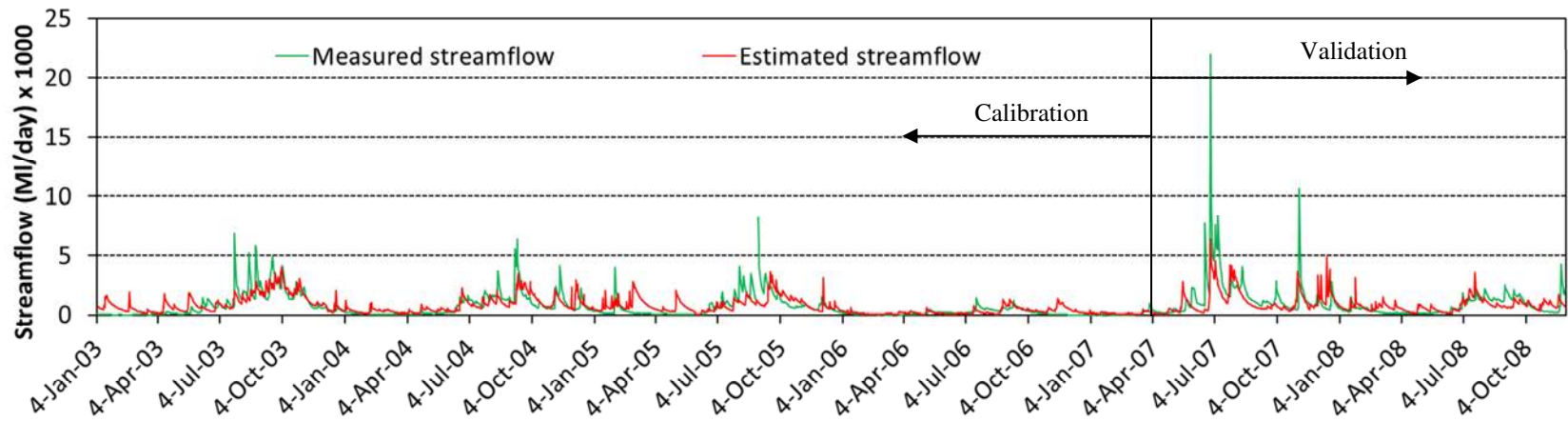


Figure 4.23 Measured and estimated streamflow of the Macalister catchment - model with estimated rainfall and estimated PET

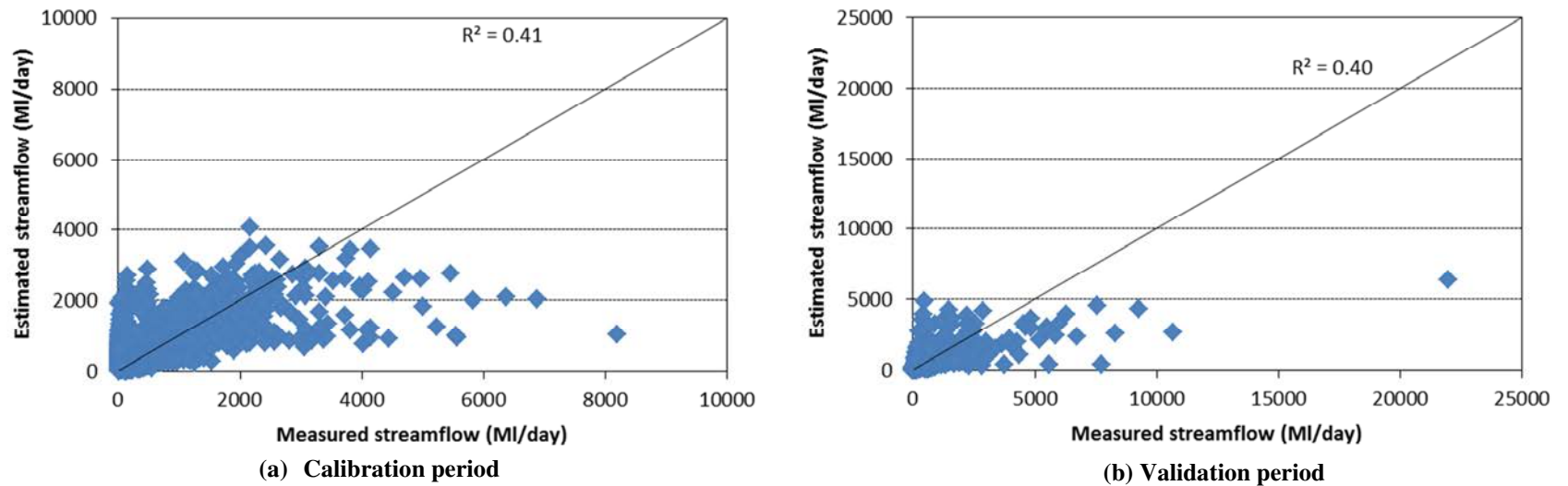


Figure 4.24 Scatter plots of the measured and estimated streamflow – model with estimated rainfall and estimated PET

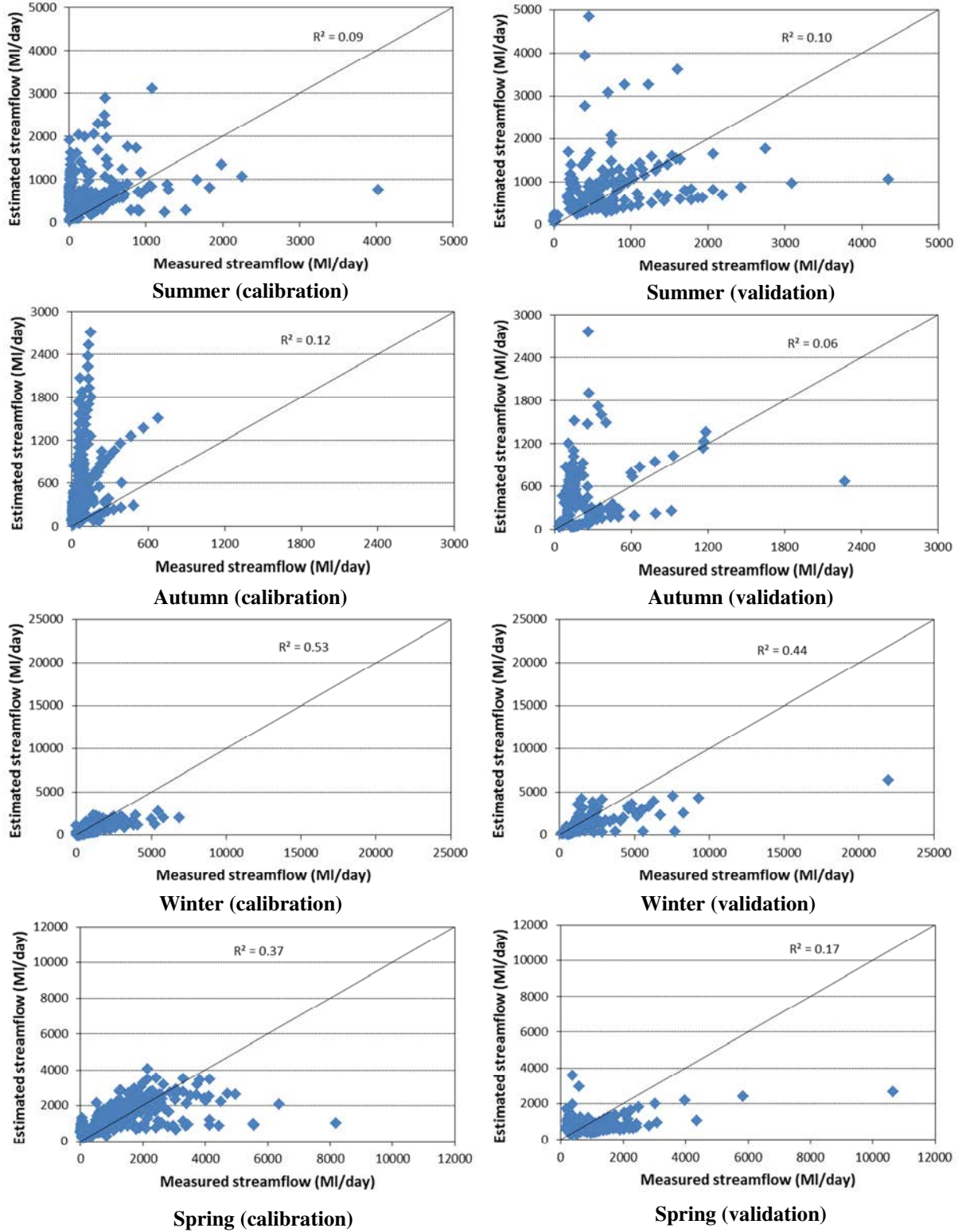


Figure 4.25 Seasonal scatter plots of the measured streamflow and estimated streamflow using estimated rainfall and estimated PET

The performance indices calculated for the models run under Sections 4.3.2.2 and 4.3.2.3 are summarized in Table 4.14. This table shows that the performance indices are almost identical in both models. The E_f values of the total period and the wet season (i.e. winter and spring) show some confidence in streamflow estimation with estimated rainfall and estimated PET, but poor results during the dry season (i.e. summer and autumn). The poor result in the dry season (especially in calibration) is mainly due to the overestimation of rainfall during this period (as can be seen Figure 4.7). If the estimated rainfall from RS data can be improved, then the performance of these catchment models will be improved.

Table 4.14 Performance indices of estimated streamflow using a model with estimated rainfall, and a model with both estimated rainfall and PET

		Model with estimated rainfall		Model with both estimated rainfall and estimated PET	
Period	Index	Calibration	Validation	Calibration	Validation
Total period	E_f	0.40	0.39	0.39	0.38
	$RMSE (Ml/day)$	712	785	717	785
Spring	E_f	0.36	0.12	0.36	0.10
	$RMSE (Ml/day)$	917	1007	919	1009
Summer	E_f	-1.13	-0.60	-1.24	-0.60
	$RMSE (Ml/day)$	535	747	549	1033
Autumn	E_f	-41.85	-2.53	-43.11	-2.52
	$RMSE (Ml/day)$	562	463	570	463
Winter	E_f	0.40	0.33	0.39	0.32
	$RMSE (Ml/day)$	741	1772	739	1771

4.3.2.4 Flow duration curves for all models

The results of all models were further analyzed with flow duration curves (FDCs). The notion of a flow duration curve can be explained as a relationship between any given streamflow value and the percentage of time that the streamflow is equaled or exceeded (Smakhtin, 2000). Furthermore, the FDC is capable of summarizing the streamflow variability in a given catchment and is recognized as an informative method of displaying a complete range of streamflow from low flows to high flows (Smakhtin, 2000).

The FDC with 17 fixed percentage points was generated using measured and estimated streamflow, and is shown in Figure 4.26. The 17 points describe the probability range from

0.1% (representing rare events) to 99.9% (representing frequent streamflow values). It should be noted that the streamflow of this plot is in log scale. Figure 4.26 shows that high flows are underestimated with the models of estimated rainfall from RS data. All models estimate streamflow well during the exceedance range of 1 to 50%, and they all overestimate streamflow in the range of 50% to 99.90% of exceedance. Among all models, the model with estimated rainfall and estimated PET shows the highest overestimation.

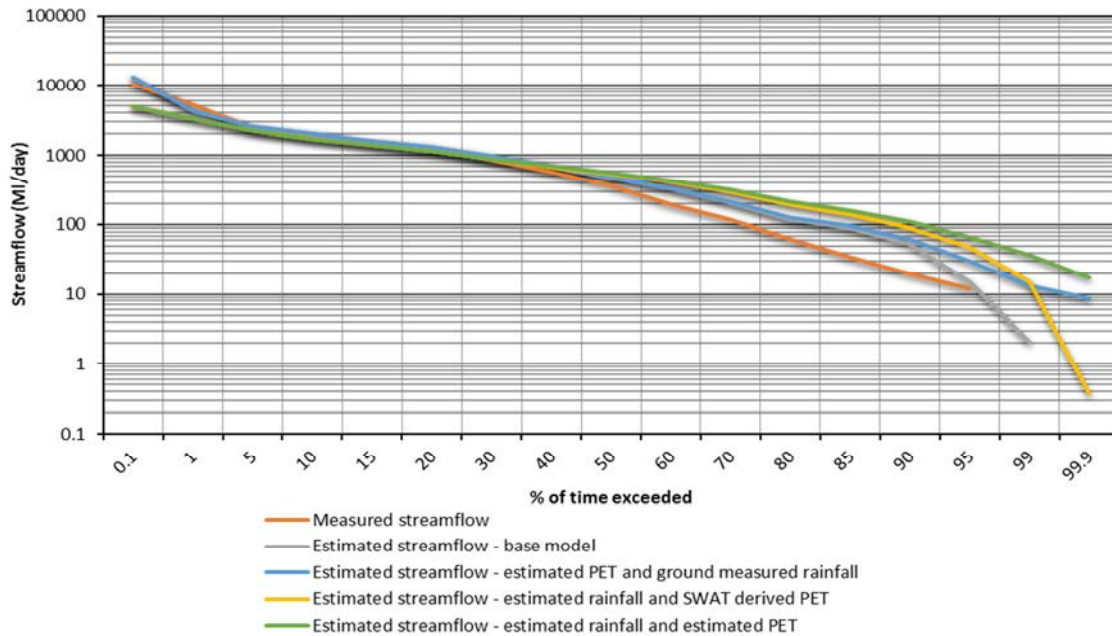


Figure 4.26 Flow duration curves – Macalister catchment

4.4 Streamflow estimation using statistical modelling

This section discusses the estimation of streamflow using statistical modelling, through the use of Artificial Neural Networks (ANN), with RS-based (RS based) variables as inputs. Both RS-based vegetation and thermal indices were used as input variables in the estimation of streamflow. The Normalized Different Vegetation Index (*NDVI*), the Normalized Difference Water Index (*NDWI*) and the Enhanced Vegetation Index (*EVI*) were used as vegetation indices. These variables were selected because they represent some features of surface vegetation such as vegetation vigor, vegetation water content and leaf area index (Teillet et al., 1997; Huete et al., 2002; Thenkabail et al., 2004) which are linked to the physical processes of streamflow generation. The brightness temperature of band 31 (*BT31*), band 32 (*BT32*), and brightness temperature difference (*BT_{diff}*) and brightness temperature gradient (*BT_{grad}*) were

also used as potential input variables for streamflow estimation. BT_{diff} and BT_{grad} were considered as thermal indices in this study. All BT and thermal indices were considered as surrogate for rainfall since the brightness temperature was central to rainfall estimation using RS data (Arkin, 1979; Del Beato, 1981; Diop and Grimes, 2003; Huffman et al., 2007).

4.4.1 Remote sensing based input variables and streamflow

Before commencing streamflow estimation using ANN, all potential input variables outlined in Section 4.4 were analyzed to understand their patterns and relationship with measured streamflow. This was done using time series plots of each RS-based variable with respect to streamflow of the Macalister catchment. Catchment averages of daily RS-based indices for the period of 2003 to 2008 were used in this analysis. However, there were some small gaps (e.g. December 2006) in the time series of these indices as the quality of the RS data was insufficient to calculate these indices.

The 8-day average of *NDVI*, *NDWI* and *EVI* are displayed in Figures 4.27 to 4.29. These vegetation indices are available only for non-cloudy days. Considering that non-cloudy days lead to gaps in the time series of these indices, an 8-day average (considering the values of the present day and the previous seven days) of the indices was used to fill the gaps. This 8-day interval was specially selected since it was sufficient enough to cover most of the gaps during the cloudy days.

The catchment average of 8-day average *NDVI* and daily streamflow are shown in Figure 4.27. As demonstrated in this figure, streamflow starts to rise in May of each year and reaches its peak during August and September. It then gradually recedes until January. During the period between January and May, streamflow remains low and steady because of the prevailing dry conditions. Compared to streamflow, the 8-day average *NDVI* shows a different response in the Macalister catchment. This is shown in Figure 4.27, where the 8-day average *NDVI* starts to increase in early spring (September to November) and continues to increase until January-February in the following year. This pattern of the influence of vegetation on streamflow demonstrates that vegetation is more sensitive to the effects of seasonality rather than simply the amount of rainfall over the catchment, which is responsible for streamflow.

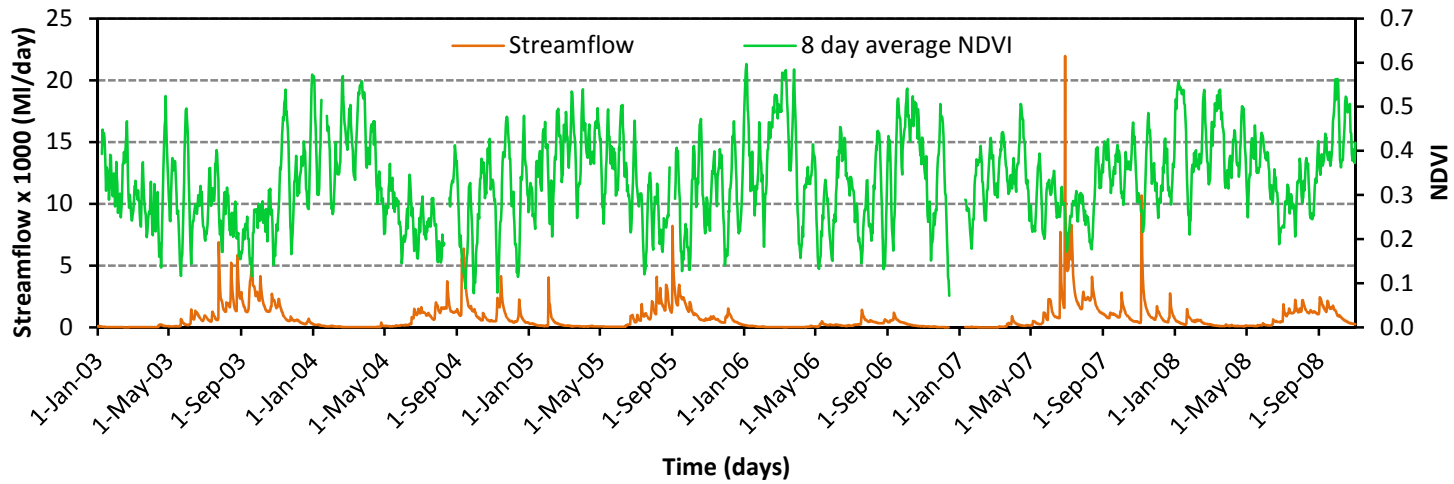


Figure 4.27 Streamflow and 8-day average *NDVI* - Macalister catchment

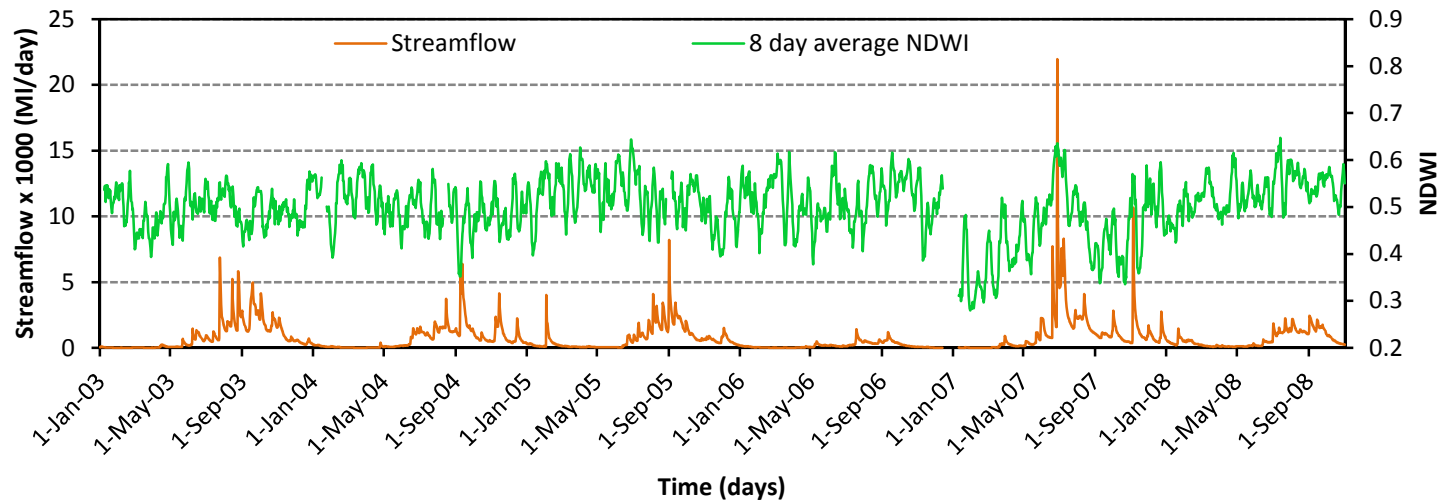


Figure 4.28 Streamflow and 8-day average *NDWI* - Macalister catchment

Figure 4.28 shows the catchment average time series plot of 8-day average *NDWI* and daily streamflow for the study period over the Macalister catchment. *NDWI* is a representative index of the vegetation water content (Jackson et al., 2004), and indirectly represents the amount of water available in the root zone of the soil. In general, this figure shows that the fluctuation of *NDWI* is less than that of *NDVI* (Figure 4.27). As such, it can be assumed that the soil moisture content of the root zone of the catchment is mostly unchanged.

The time series of catchment average 8-day average *EVI* and streamflow are laid out in Figure 4.29. According to this figure, the 8-day average *EVI* follows the same trend of the 8-day average *NDVI* (Figure 4.27). This may be a result of both indices being dependent on the measured quantity of energy emerging in the near infrared and red bands from the vegetation. However, as an index, the 8-day average *EVI* shows less fluctuation when compared to 8-day average *NDVI*.

Figure 4.30 shows the time series plot of catchment average daily *BT31* with streamflow. Daily brightness temperature of clouds over the Macalister catchment varies from 190 K to 250 K, and it can be seen from this figure that the daily brightness temperatures over the catchment have a strong seasonality. The mean brightness temperature during winter (June to August) drops below approximately 230 K, while in summer (December to February) it increases to approximately 240 K. Additionally, Figure 4.30 shows the brightness temperature of the clouds over the Macalister catchment can unpredictably drop at any time of the year for a day or two. Finally, it is also found from Figure 4.30 that streamflow is high during the winter and spring seasons when brightness temperature of clouds is low.

Figure 4.31 demonstrates the relationship between the brightness temperatures of both band 31 and band 32. It was found that the estimated temperatures using each band differ slightly. These temperature differences are mainly based on the manufacturing features of the bands. Although there is correlation between two bands, both were used in this study to estimate streamflow.

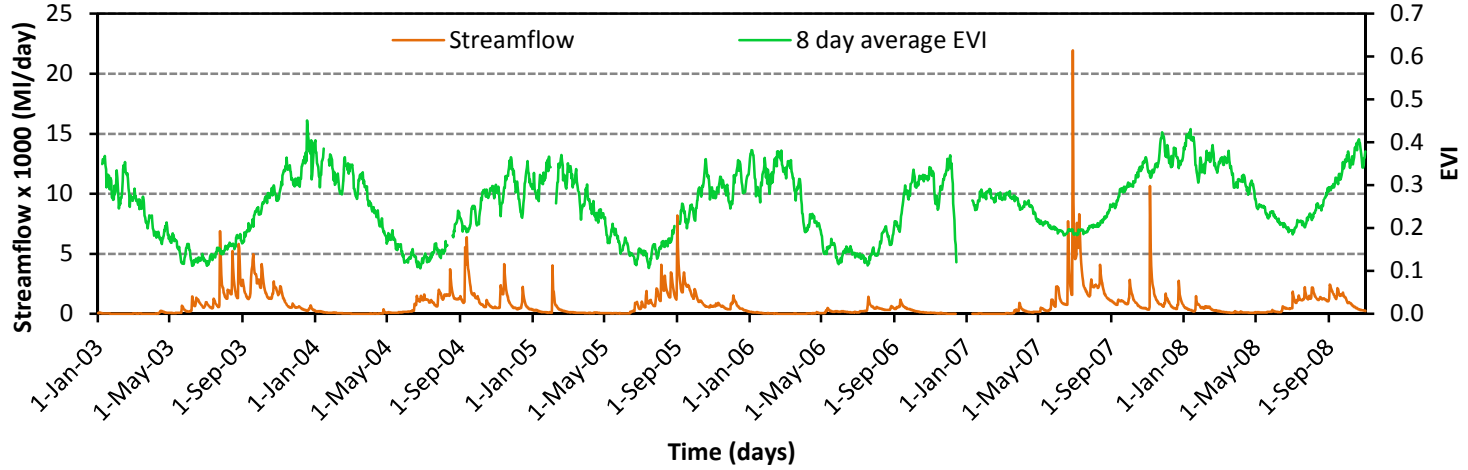


Figure 4.29 Streamflow and 8-day average *EVI* - Macalister catchment

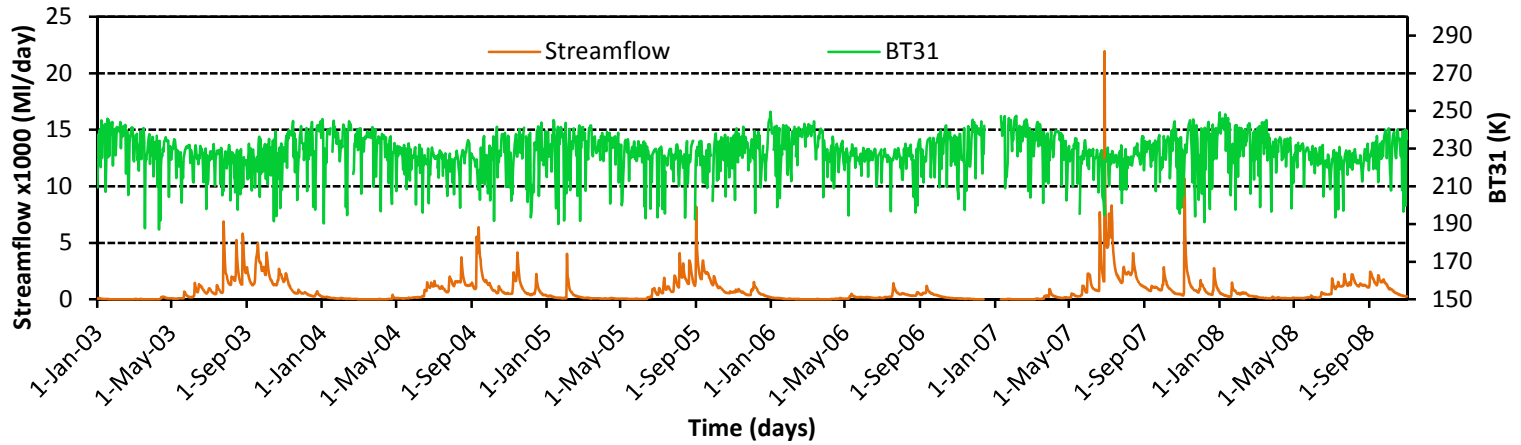


Figure 4.30 Streamflow and brightness temperature of band 31 (*BT31*) - Macalister catchment

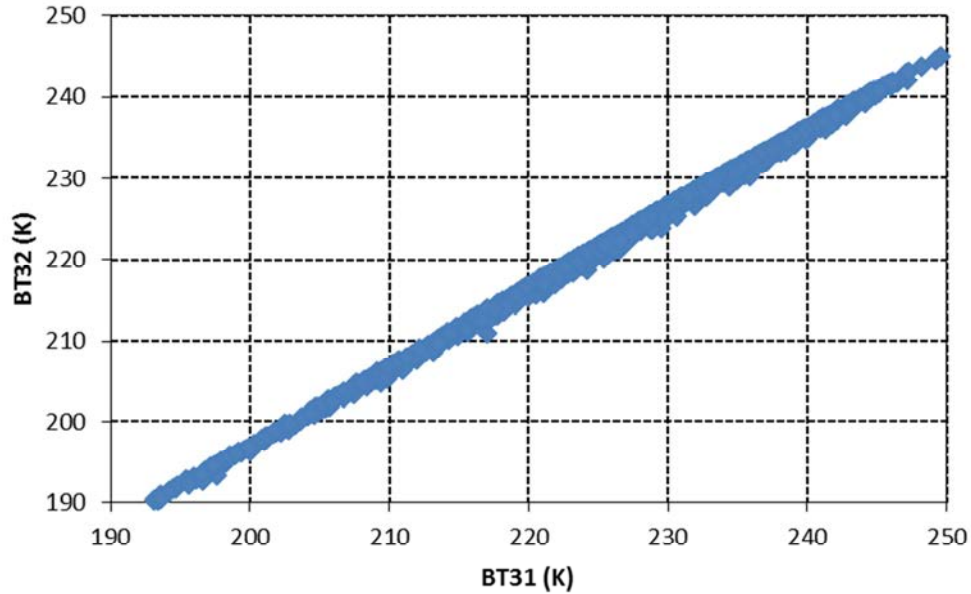


Figure 4.31 Brightness temperature of band 31 and band 32

Figure 4.32 shows the time series plots of BT difference (BT_{diff}) and streamflow. The BT difference varies between the range of 3 to 5 K. However, the variation of BT_{diff} is generally higher in summer (December to February) and autumn (March to May) seasons compared to winter (June to August) and spring seasons (September to November). According to Inoue (1987), the difference in BT between these bands (Band 31 and 32) is greater for thin clouds (cirrus clouds) than for cloud-free areas and for thicker clouds (cumulonimbus). The thin clouds such as cirrus do not produce any rain, but are dominant in summer and autumn. As such, streamflow during these seasons shows its lowest values, even though the BT difference is comparatively high.

The plot of BT gradient (BT_{grad}) and streamflow over the catchment is demonstrated in Figure 4.33. The BT_{grad} shows a higher variability than the BT_{diff} . According to Kuligowski (2002), higher values of BT gradient are an indication of convective rains.

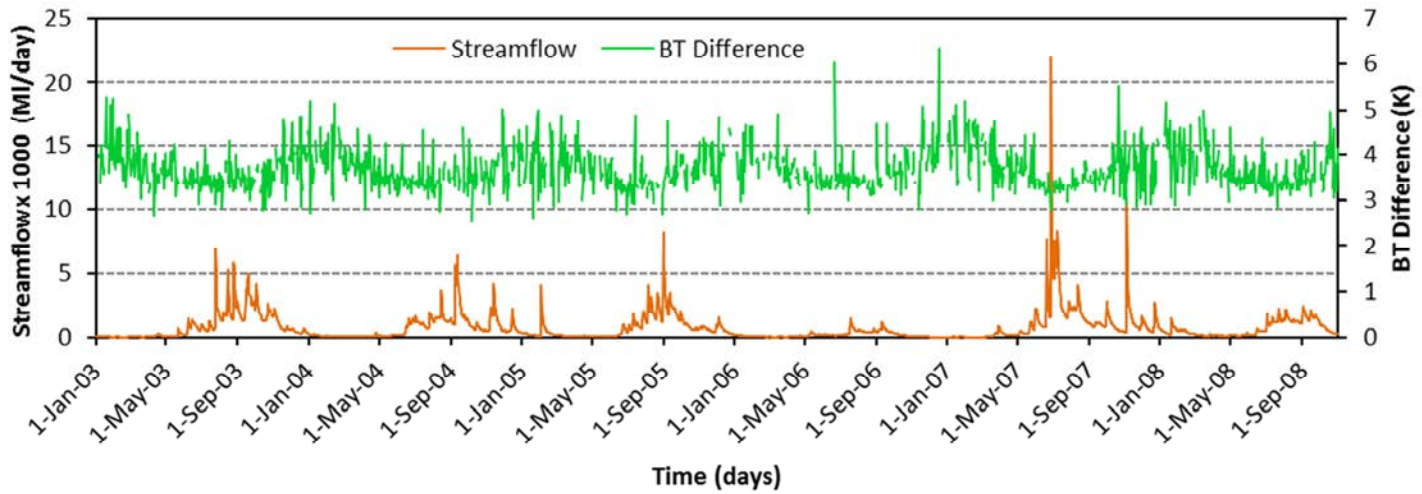


Figure 4.32 Streamflow and BT difference (BT31-BT32) -

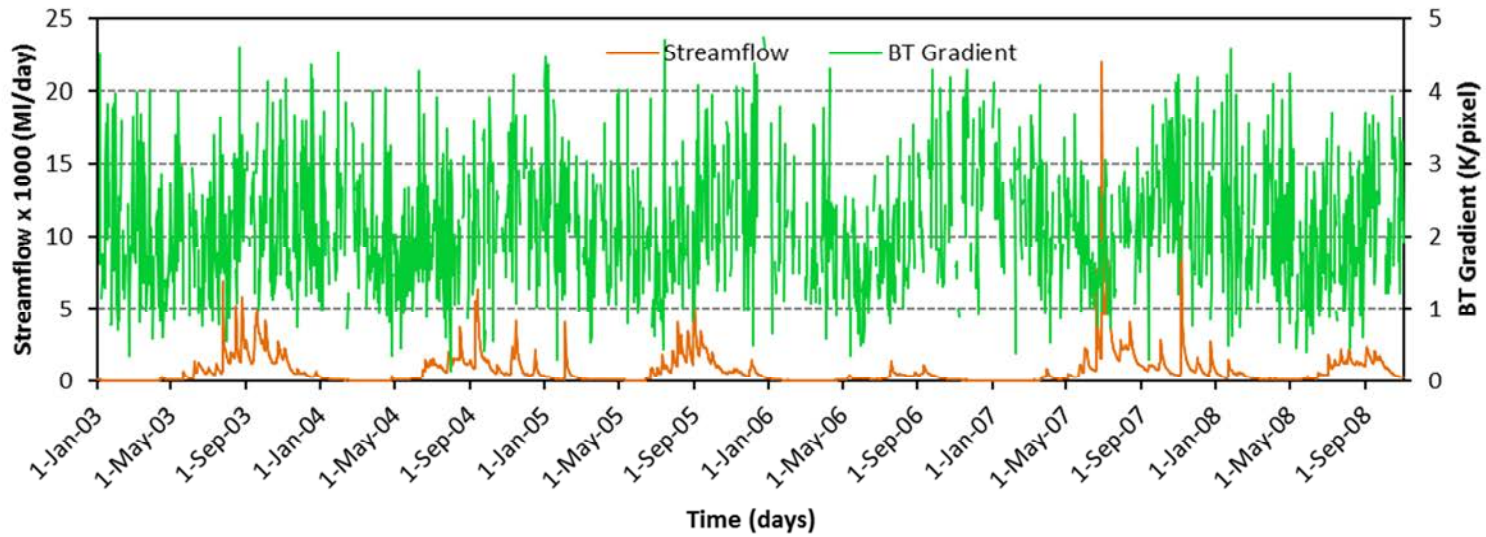


Figure 4.33 Streamflow and BT gradient - Macalister catchment

4.4.2 Determination of influential variables

The current day of RS based vegetation and thermal indices, and BT (Section 4.4.1) together with their lagged days were considered as potential variables for Artificial Neural Networks (ANN) modelling of daily streamflow. In the case of vegetation variables (i.e. *NDVI*, *EVI* and *NDWI*), a lag time up to seven days was considered. In contrast, for the BT and thermal indices (i.e. *BT31*, *BT32*, *BT_{diff}* and *BT_{grad}*), a lag time of up to three days was considered. The reason for the difference in lag time between vegetation and thermal variables is that the vegetation indices are slower to respond to water availability than those related brightness temperature and thermal indices. After considering the lag time of each variable and the average of vegetation indices, it was found that altogether there are 43 variables present as potential input variables for ANN modelling. Tables 3.5 and 3.6 show those variables separately on the vegetation and thermal bases.

As outlined in Section 3.8, the use of all 43 variables for ANN modelling can cause various issues. Amongst them, feature input data replication, complexity of the ANN model and high demand for computational memory. Since those issues can ultimately contribute to difficulties in understanding and interpreting model results (Bowden et al., 2005a), a variable selection approach was followed to determine influential input variables from these 43 potential variables for use in the ANN model.

Several authors (Maier and Dandy, 2000; Sharma, 2000; Bowden et al., 2005a; Maier et al., 2010) have highlighted the importance of the input selection in water related applications, and Bowden et al. (2005a) have given a comprehensive description of the available input variable selection methods. Among those input selection methods, the calculation of Pearson correlation coefficient between potential dependent variables and independent variables is the simplest and most efficient approach. Hence, the Pearson correlation coefficients between streamflow and all potential RS-based variables were computed with the intention of selecting the influential input variables for the ANN model (Section 4.4.3). An analysis of Pearson correlation between streamflow and potential RS-based variables was carried out separately for the total study period and individual seasons, because most of the RS-based input variables revealed a high seasonality (Figures 4.27, 4.29, 4.30 and Figures 4.32 – 4.33).

The results of the Pearson correlation coefficient analysis of streamflow with all potential input variables (including their lags) are shown in Table B1 of Appendix B. This table also shows the level of significance of each coefficient. The Pearson correlation coefficient analysis between potential input variables and streamflow revealed that all correlation coefficients were similar in magnitude. This makes the selection of highly influential variables for streamflow estimation somewhat difficult. According to Sharma (2000), such kind of similar correlation coefficients adversely affect the purpose of selecting input variables. Therefore, the Partial Mutual Information (PMI) method was used in selecting influential input variables. A detailed explanation of the calculation procedure of the PMI has been provided in Section 3.8.1.

The results of the PMI calculations are shown in Table 4.15. This table shows the calculated PMI values and their 99th percentile values. The potential input variable column is arranged according to the category of input variable. The influential input variables (PMI > 99th percentile) are highlighted in this table. According to Table 4.15, there are 17 influential input variables, and they were used as input variables for ANN modelling.

The majority of influential variables are derived from the reflectance based indices. Among all of influential input variables (i.e. both vegetation and thermal based), the 8-day average *NDVI* shows the highest level of dependency to streamflow.

Table 4.15 RS-based input variable, PMI and their 99th percentile

Potential input variable	PMI	99 th percentile
<i>NDVI</i>	0.0573	0.0514
1-day lag <i>NDVI</i>	0.0511	0.0458
2-day lag <i>NDVI</i>	0.0584	0.0493
3-day lag <i>NDVI</i>	0.0644	0.0433
4-day lag <i>NDVI</i>	0.0451	0.0471
5-day lag <i>NDVI</i>	0.0459	0.0349
6-day lag <i>NDVI</i>	0.0532	0.0758
7-day lag <i>NDVI</i>	0.0487	0.0543
8-day avg <i>NDVI</i>	0.1314	0.0365
<i>NDWI</i>	0.0486	0.0467
1-day lag <i>NDWI</i>	0.0405	0.0594
2-day lag <i>NDWI</i>	0.0512	0.0684
3-day lag <i>NDWI</i>	0.0422	0.0400
4-day lag <i>NDWI</i>	0.0372	0.0323
5-day lag <i>NDWI</i>	0.0515	0.0695
6-day lag <i>NDWI</i>	0.0404	0.0531
7-day lag <i>NDWI</i>	0.0489	0.0483
8-day avg <i>NDWI</i>	0.0641	0.0407
<i>EVI</i>	0.0446	0.0624
1-day lag <i>EVI</i>	0.0303	0.0537
2-day lag <i>EVI</i>	0.0561	0.0719
3-day lag <i>EVI</i>	0.0495	0.0605
4-day lag <i>EVI</i>	0.0380	0.0615
5-day lag <i>EVI</i>	0.0463	0.0697
6-day lag <i>EVI</i>	0.0410	0.0466
7-day lag <i>EVI</i>	0.0430	0.0655
8-day avg <i>EVI</i>	0.0563	0.0654
<i>BT31</i>	0.0503	0.0564
1-day lag <i>BT31</i>	0.0544	0.0689
2-day lag <i>BT31</i>	0.0598	0.0755
3-day lag <i>BT31</i>	0.0619	0.0423
<i>BT32</i>	0.0548	0.0563
1-day lag <i>BT32</i>	0.0474	0.0465
2-day lag <i>BT32</i>	0.0601	0.0571
3-day lag <i>BT32</i>	0.0453	0.0489
<i>BT_{diff}</i>	0.0595	0.0361
1-day lag <i>BT_{diff}</i>	0.0634	0.0674
2-day lag <i>BT_{diff}</i>	0.0526	0.0479
3-day lag <i>BT_{diff}</i>	0.0459	0.0515
<i>BT_{grad}</i>	0.0390	0.0600
1-day lag <i>BT_{grad}</i>	0.0501	0.0478
2-day lag <i>BT_{grad}</i>	0.0445	0.0529
3-day lag <i>BT_{grad}</i>	0.0327	0.1458

*Influential variables are highlighted in the table

4.4.3 Artificial Neural Networks modelling

The Artificial Neural Networks (ANN) modelling approach which was discussed in detail in Section 3.8.2, was used to estimate streamflow. Model selection and model construction are the two basic important steps in developing an ANN model. The widely used three layer (i.e. input, hidden and output) feed-forward neural networks with back propagation was selected in this study to estimate streamflow, since it has the capacity to handle complex relations between inputs and output with a sufficient degree of freedom with regards to weights and biases (Maier and Dandy, 2000). A full description of the three-layer feed-forward neural networks was given in Section 3.8.2.

Model construction (or building) of the model deals with the selection of input variables, and the selection of a number of neurons in the hidden layer, as well as the selection of the transfer function and the objective function to calibrate and validate the model. The selection of input variables was discussed in detail in Section 4.4.2. The influential input variables which were highlighted in Table 4.15 were used as input variables. The trial and error calibration method was applied to determine the optimum number of hidden neurons in the hidden layer of model. A non-linear (*TANSIG*) transfer function was used to compute the value of the hidden layer nodes from the values of input layer nodes, and a linear (*PUERLIN*) transfer function was used to compute the values of the output layer node from the values of hidden layer nodes. The mean square error (*MSE*) was used as the objective function in this study (Gamage et al., 2011a). A detailed description of the model selection and construction was given in Section 3.8.2.

The ANN models were developed separately for the total period and each season. The ANN model for the total period was configured using data of the entire study period. In the seasonal model, a separate ANN model was configured for each season (summer – December to February, autumn – March to May, winter – June to August and spring – September to November). Particular seasons of each year (from 2003 to 2008) were combined to have seasonal time series of RS-based indices (independent variables) and streamflow (dependent variable) in the seasonal model.

ANN modelling involves a standard procedure of model training, testing and validation. Training and testing periods were considered together as model calibration in this study. The data from 2003 to 2006 data were used to calibrate the ANN models, while 2007 and 2008 were used to validate the models. These periods were also used for calibration and validation under the catchment process modelling approach in Section 4.3.

4.4.3.1 Streamflow estimation - total period model

Data of seventeen significant input variables (Table 4.15) were used as input data (which means 17 input nodes) for the trial and error calibration method to determine the optimum number of hidden neurons. The degree of agreement between measured streamflow and output (i.e. estimated streamflow) was assessed using the performance indices outlined in Section 3.9.

The trial and error calibration method showed that the model with 26 hidden neurons gives the best results in daily streamflow estimation. The result of this ANN model is shown in Figures 4.34, 4.35 and 4.36. In Figure 4.34, the line graph shows measured streamflow and estimated streamflow time series for both the calibration and validation periods. Figure 4.35 shows the same result in scatter plots separately for the calibration and validation periods with a 1:1 line, while Figure 4.36 shows the flow duration curves of measured and estimated streamflows.

Both Figures 4.34 and 4.35 show poor results in streamflow estimation. A detailed analysis of the results showed that most of the underestimation occurred during the winter and spring seasons with high flows, and overestimation occurred during summer and autumn with low flows. A careful observation of the results of the ANN model for the total period revealed that most of this overestimation occurred during summer and autumn seasons. These two seasons are recorded as dry seasons in which streamflow is significantly less than its mean value. As such, it shows that the ANN model for the total period does not model the effects of seasonality in streamflow well in the Macalister catchment. Therefore, separate ANN models for each season were developed.

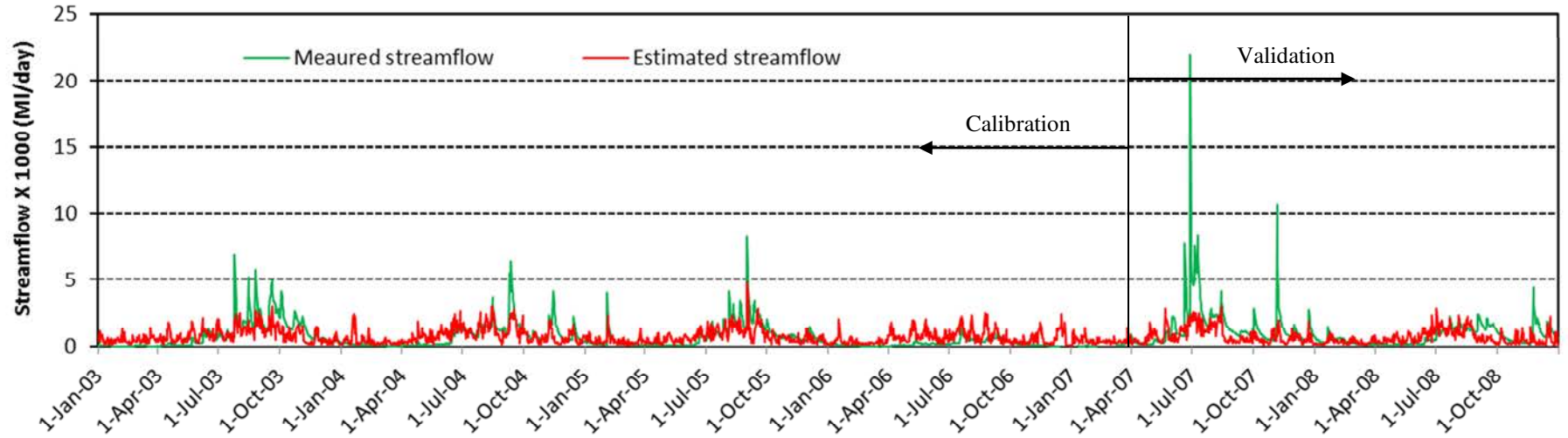


Figure 4.34 Measured streamflow and estimated streamflow using ANN model for total period – Macalister catchment

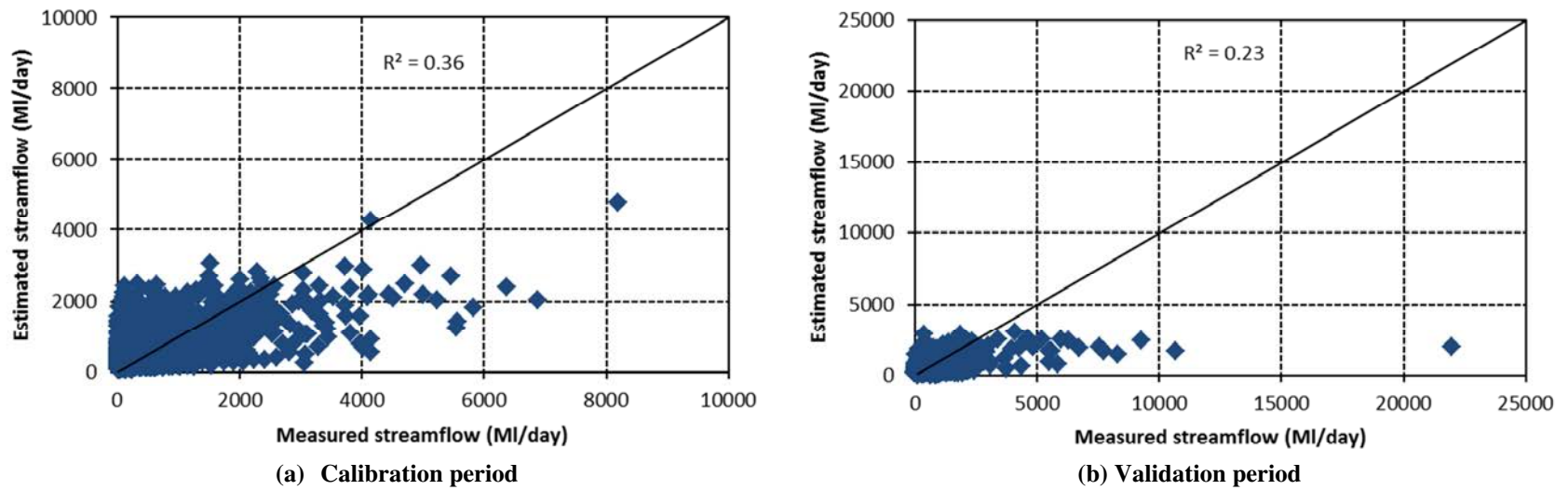


Figure 4.35 Scatter plots of measured, and estimated streamflow using ANN model for the total period – Macalister catchment

Figure 4.36 shows that the extreme high flows (i.e. streamflows of % time exceeded less than 5%) are underestimated (this was also shown in Figures 4.34 and 4.35). Furthermore, it shows that the streamflows exceeded 50% of the time are overestimated, and the degree of overestimation is increased with lower flows. Note that the vertical axis of Figure 4.36 is in logarithmic scale.

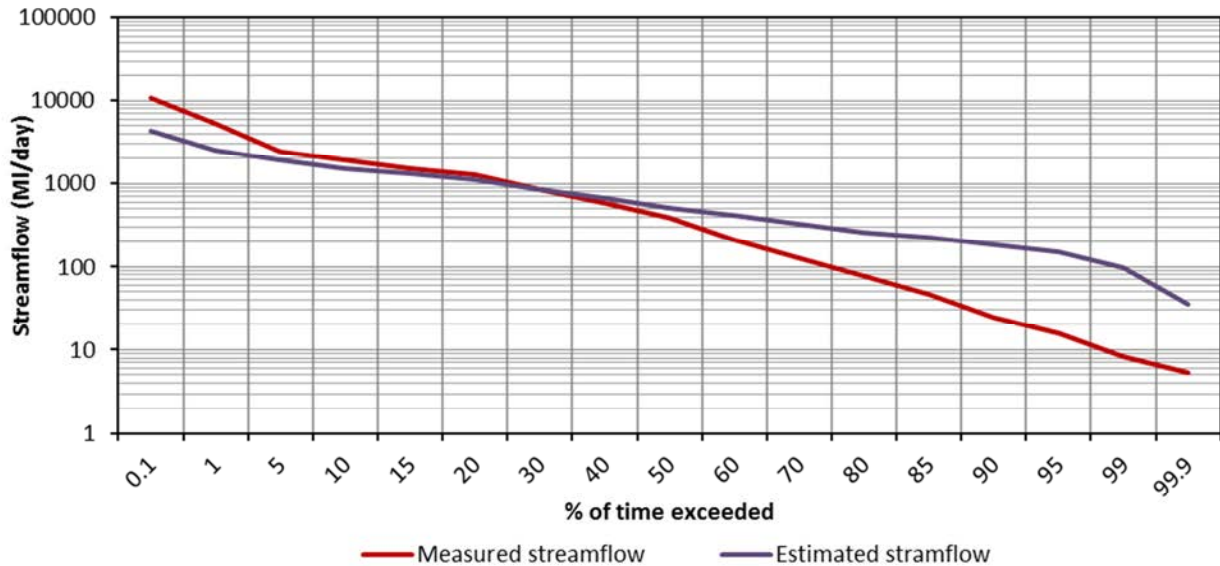


Figure 4.36 Flow duration curve of the measured and estimated streamflow – Macalister catchment

4.4.3.2 Streamflow estimation with seasonal ANN models

The results of Section 4.4.3.1 show that the ANN model developed for the total period does not model adequately the hydrological behaviors of the Macalister catchment. Therefore, seasonal ANN models were developed to represent each season. This was carried out with the same input variables which were used in Section 4.4.3.1. The trial and error calibration method was used to develop the ANN models for each season to obtain the optimum number of hidden neurons.

Initially, the total time series (i.e. data of selected input variables in Section 4.4.2) was separated into four seasons (winter, spring, summer and autumn), and a time series for observed streamflow and for the 17 input variables corresponding to each season was

constructed. Then, the same range of hidden neurons (8 to 34) that was considered in the ANN model for the total period, was tested in seasons to determine the optimum number of hidden neurons for seasonal models. As in Section 4.4.3.1, a non-linear (*TANSIG*) transfer function was used in computing the values of hidden layer nodes from the values of input layer nodes, and a linear (*PUERLIN*) transfer function was used for computing the values of the output layer node from the values of hidden layer nodes. The mean square error (MSE) was used as the objective function, and the calibration and the validation periods were also maintained as in Section 4.4.3.1 (calibration period – 2003 to 2006 and validation period – 2007 to 2008). Performance indices were calculated with estimated and measured streamflow, and the ANN model which gives the best performances was considered as the final model for a given season with the optimum number of hidden neurons.

The trial and error calibration method yielded different number of hidden neurons for the final model in different seasons. Models with 13, 24, 18 and 24 hidden neurons yielded the best performance for summer, autumn, winter, and spring seasons respectively.

The scatter plots of the measured and estimated streamflow for each season are shown in Figure 4.37 for the calibration and validation periods. This figure shows a reasonably good agreement between measured and estimated streamflow in autumn and spring seasons during the calibration period. The results of the calibration period in summer and winter show weak agreement between measured and estimated streamflow. High flows in all seasons except autumn are highly underestimated during the calibration period, while low flows show a mixed result. The results of the validation period during summer and winter show better results than those of the calibration period. Even though autumn shows the best result in the calibration period, spring shows overall best results in both the calibration and validation periods.

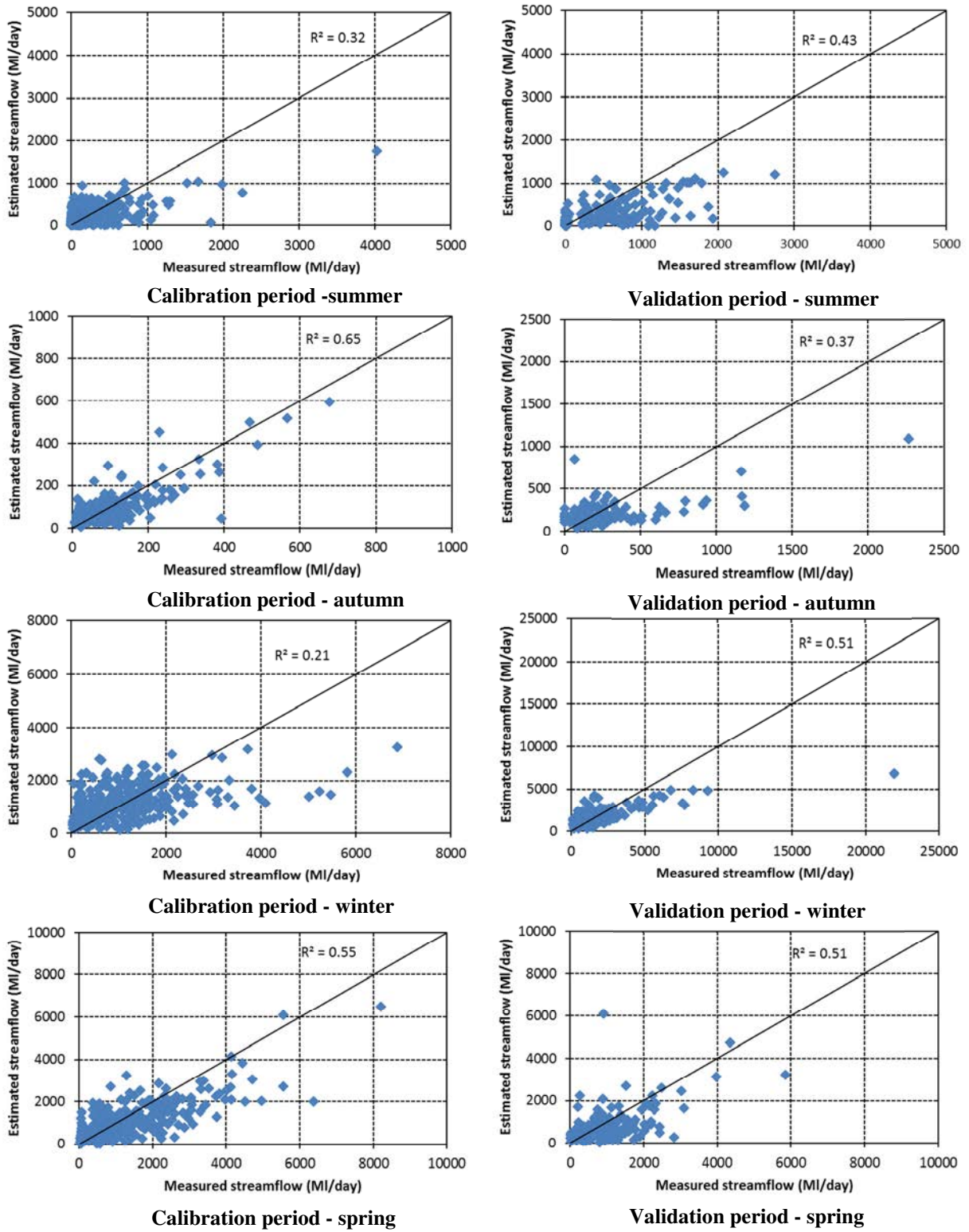


Figure 4.37 Scatter plots of measured and estimated streamflow for calibration and validation periods during each season – Macalister catchment

In addition to separating seasonal model results, all of estimated streamflow from seasonal models were combined to compile a single time series. The outcome (seasonal-combined) is shown in Figure 4.38 as a line graph and Figure 4.39 as a scatter plot separately for the calibration and validation periods. In general, Figure 4.38 shows a better estimation of streamflow during both calibration and validation, compared to Figure 4.34 which is based on the ANN model for the total period. This is further explained in the scatter plots between measured and estimated streamflow in Figure 4.39. The calibration period in Figure 4.39 shows less underestimation compared to the calibration period in Figure 4.35. This observation is also the same in the validation periods in Figure 4.39 and Figure 4.35.

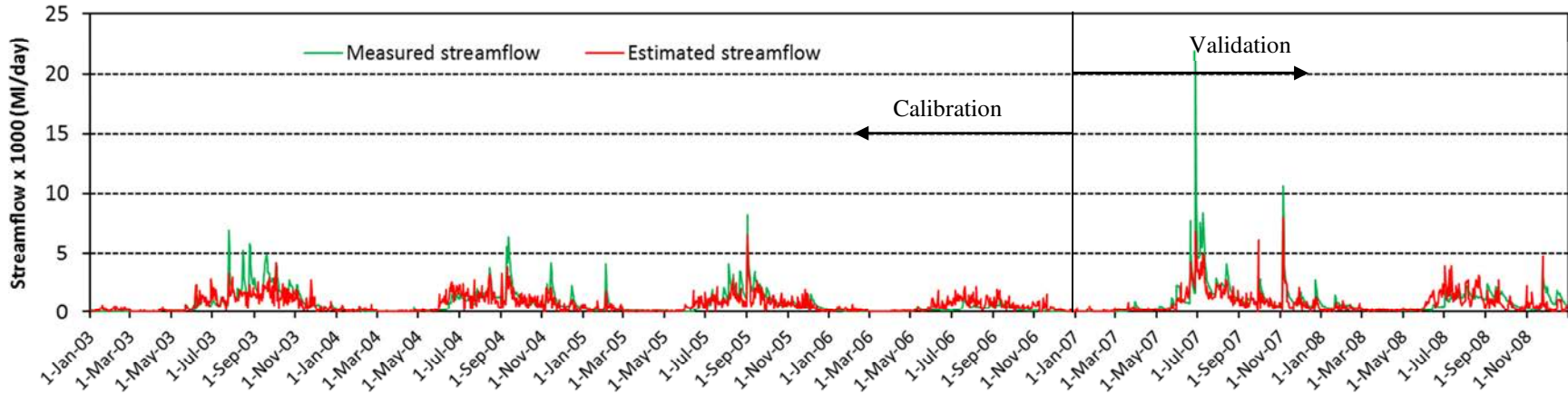
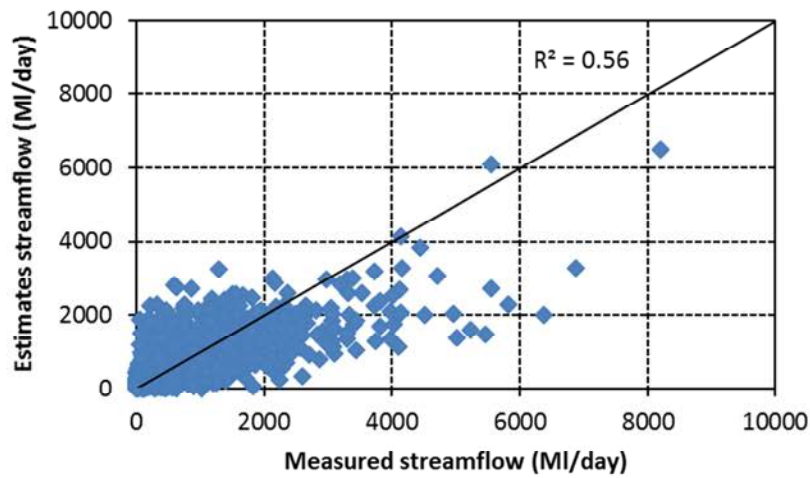
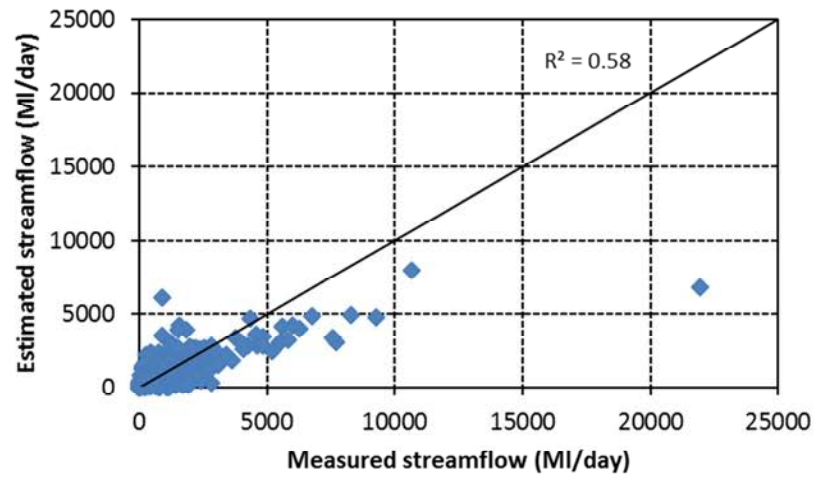


Figure 4.38 Measured streamflow and estimated streamflow (based on seasonal-combined results) - Macalister catchment



(a) Calibration period



(b) Validation period

Figure 4.39 Scatter plot of the measured streamflow and estimated streamflow (based on seasonal-combined results) – Macalister catchment

Figure 4.40 shows the flow duration curve of measured and estimated streamflow which is based on the seasonal-combined results. This figure shows a better agreement between measured and estimated streamflows. It also shows that high flows are still underestimated, however the magnitude of the underestimation of high flows is less on the seasonal-combined results than that of the ANN model for the total period (Figure 4.36). Figure 4.40 shows slight overestimation of estimated streamflow beyond 85% of exceedance level. This is a significant improvement in streamflow estimation with the seasonal ANN models compared to the ANN model for the total period, which showed large overestimations beyond the exceedance level of 50% (Figure 4.36). Note that the vertical axis of Figure 4.40 is in logarithmic scale.

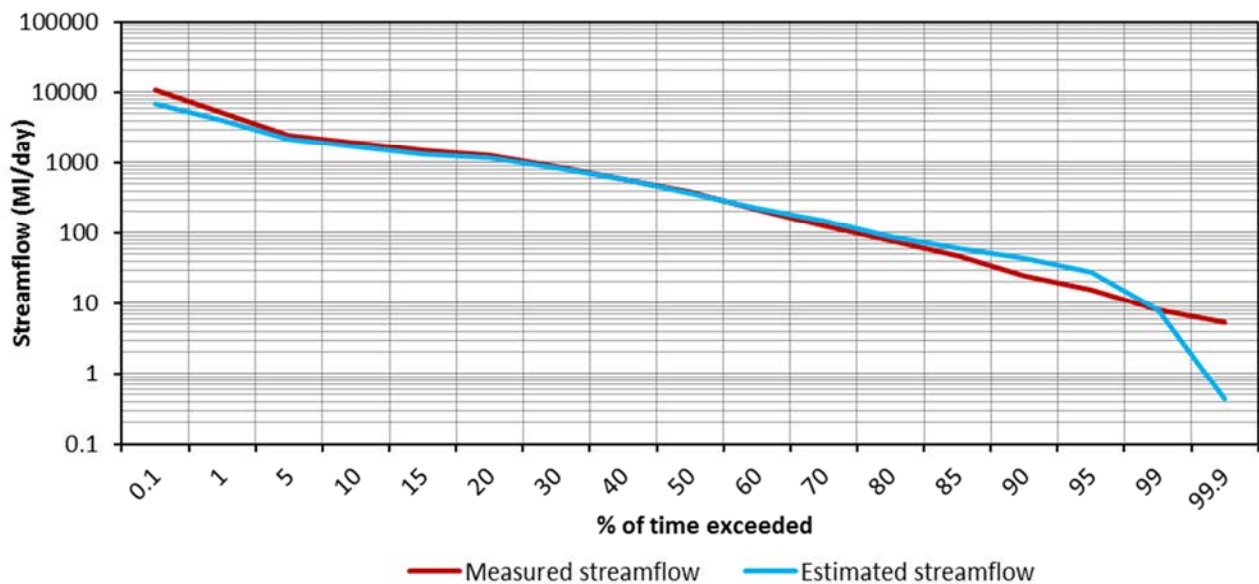


Figure 4.40 Flow duration curve of observed and estimated (with the seasonal ANN model) streamflow – Macalister catchment

4.4.3.3 Performance assessment of ANN models

Table 4.16 shows all performance indices which have been calculated for estimated streamflow using ANN models. This table shows performance indices calculated separately for the model outputs of total period, seasonal and seasonal-combined. In general, this table reveals that the results of seasonal models are mixed, while the results of seasonal-combined are better than the results of the total period model. This is consistent with the line plots,

scatter plots and flow duration curves of Sections 4.4.3.1 and 4.4.3.2. The weak performance even with the seasonal-combined ANN model (which has performed better than all other ANN models) is due to less number of year's data used both in calibration and validation. The performance of these models can be improved with additional data.

Table 4.16 Performance indices of the estimated streamflow from various ANN models – Macalister catchment

Estimation type		<i>RMSE (MI/day)</i>	<i>E_f</i>
ANN model for total period	Calibration	730	0.35
	Validation	1255	0.18
Seasonal models			
Summer	Calibration	306	0.31
	Validation	456	0.09
Autumn	Calibration	51	0.64
	Validation	204	0.34
Winter	Calibration	863	0.17
	Validation	1602	0.45
Spring	Calibration	790	0.52
	Validation	809	0.43
Seasonal-combined	Calibration	607	0.55
	Validation	932	0.55

4.5 Comparison of catchment process modelling and statistical modelling

The aim of this section is to compare the outcomes of both catchment process modelling and statistical (ANN) modelling which represent approaches used to estimate daily streamflows in the Macalister catchment. Flow duration curves and performance indices of both modelling techniques were used in this comparison.

Figure 4.41 shows the flow duration curves of measured streamflow, streamflow estimated using the catchment process models (the base model and the model with estimated rainfall and estimated PET) and streamflow estimated with seasonal ANN models. Note that the results of seasonal ANN models were combined together to have a total time series. All streamflow values plotted in this figure are in logarithmic scale. This figure shows that high flows with

exceedance probability less than 1% are underestimated in streamflows estimated with estimated rainfall and estimated PET and with the seasonal ANN models that used influential RS-based indices as inputs. However, it shows that estimated streamflow with ground measured data matches well with measured streamflow for these high flows, but are overestimated with low flows. All the estimated streamflows match well with the measured streamflow in the probability exceedance range of 1 to 50%. Then figure shows that all estimated streamflow (except under seasonal-combined) are overestimated in various amounts when the percentage of time exceeded is larger than 50. It shows that the seasonal-combined model starts its overestimation after 80% of time exceeded.

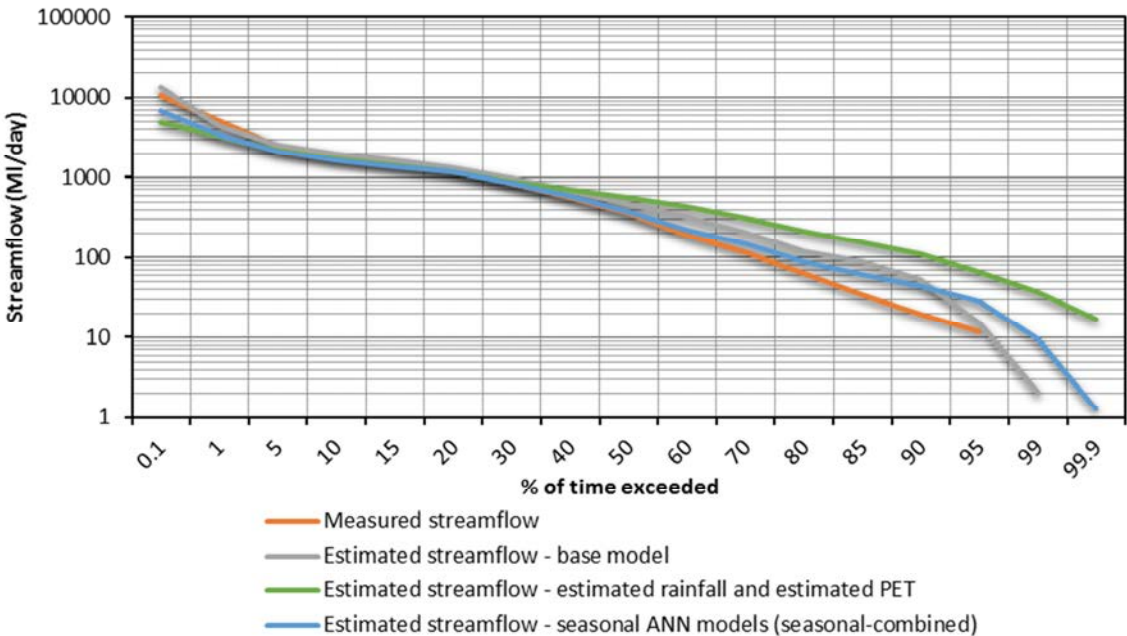


Figure 4.41 Comparison of flow duration curves of measured and estimated streamflow from catchment process and statistical models

This figure also shows that the highest overestimation is with the model with estimated rainfall and estimated PET. Importantly, after combining all the results of the seasonal models, the figure shows slightly better results than both the base model and the model with the estimated rainfall and estimated PET when it comes to the low flow section of the FDC.

In contrast to this figure, the calculated performances indices of the above discussed models are also summarized in Table 4.17. According to Table 4.17, streamflow estimated with ground measured data shows highest performances. In contrast to this, streamflow estimates with estimated rainfall and estimated PET shows the weakest performances. Importantly, this table shows that the performance indices of the dry seasons (i.e. Summer and Autumn) in the seasonal-combined ANN model are better than the remaining two models. This indicates that seasonal calibration addresses catchment behaviors more precisely than total period in ANN modelling.

Table 4.17 Performance indices of estimated streamflow-model with ground measured data, model with both estimated rainfall and PET, and seasonal-combined ANN

		Base model (model with ground measured data)		Model with estimated rainfall and estimated PET		Seasonal-combined ANN	
Period		E_f	$RMSE$ (ML/day)	E_f	$RMSE$ (ML/day)	E_f	$RMSE$ (ML/day)
Total period	Calibration	0.73	469	0.39	717	0.55	607
	Validation	0.76	487	0.38	785	0.55	932
Spring	Calibration	0.74	584	0.36	919	0.52	790
	Validation	0.62	677	0.1	1009	0.43	809
Summer	Calibration	0.35	214	-1.24	549	0.17	863
	Validation	0.75	313	-0.6	1033	0.45	1602
Autumn	Calibration	-17.25	365	-43.11	570	0.64	51
	Validation	-2.66	482	-2.52	463	0.34	204
Winter	Calibration	0.65	562	0.39	739	0.31	306
	Validation	0.78	1005	0.32	1771	0.09	456

As can be seen from Table 4.17, the E_f values for both calibration and validation for the catchment process models with ground measured data and estimated rainfall/PET data (estimated from RS data) in autumn and in some cases with summer have negative values. These poor results in autumn and summer are because SWAT does not allow different parameters for different months or seasons. If different parameters for different seasons are

allowed, then individual seasons can be better modelled, which allows autumn and summer to be better modelled. This has been discussed in Section 4.3.1.

4.6 Summary

This chapter described the results which were generated for the Macalister catchment based on the methodology explained in Chapter 3. Two separate modelling methods, catchment process modelling and statistical modelling, were used in estimating streamflow in the Macalister catchment using RS data.

The appropriate input variables (rainfall, potential evapotranspiration and LULC) for catchment process modelling were estimated using RS data. High spatial resolution rainfall data were estimated in this study using MODIS brightness temperature and TRMM data. The cumulative gamma probability distribution was employed to estimate rainfall using those inputs. Estimated rainfall shows a reasonable agreement with TRMM rainfall data. Potential evapotranspiration (PET) over the catchment was estimated using the energy balance method. Both, MODIS reflectance and radiance data were used in PET estimation. Estimated PET shows higher agreement with the Penman-Monteith (PM) PET estimates. Landsat TM data were used to classify LULC of the Macalister catchment. The supervised image classification approach was followed with ground-truth data to classify LULC in this study. A single image was used to classify LULC, since there is no major change in LULC during the study period.

The SWAT modelling tool was used for catchment process modelling to estimate streamflow. The SWAT model was initially set up with ground measured data to calibrate the model parameters, and this was considered as the base model. Then, ground measured rainfall and SWAT derived PET of the base model were replaced with RS based estimated rainfall and estimated PET, which produced three models (i) a model with estimated PET and ground measured rainfall (ii) a model with estimated rainfall and SWAT derived PET, and (iii) a model with estimated rainfall and estimated PET. It was found that the base model is the closest to measured streamflow and the performance of the models was gradually reduced from the base model to the model with estimated rainfall and estimated PET using RS data.

Both vegetation and thermal indices were used as inputs in the statistical modelling approach. The Normalized Difference Vegetation Index, the Normalized Difference Water Index and the Enhance Vegetation Index were used as vegetation based indices. Not only the current day values of those indices, but also the values of lag days (i.e. up to seven days) as well as the 8-day average of these indices were considered as potential inputs for statistical modelling. The brightness temperature of MODIS bands 31 and 32 on cloudy days, the brightness temperature difference between bands 31 and 32 on cloudy days, and the brightness temperature gradient of band 31 on cloudy day, with lag time up to three days were used as thermal indices. A detailed examination shows that all of these indices are highly seasonal and have varying degrees of relationship to streamflow in the catchment. The consideration of current day, lag days and 8-day average of variables accumulated 43 input variables for statistical modelling. Since accumulated input variables can complicate the ANN modelling, the Partial Mutual Information method was used to obtain influential variables to estimate daily streamflow.

Artificial neural networks (ANN) models were used as statistical models in this study. The trial and error calibration method was used to obtain the optimum number of hidden neurons in each model. The same calibration and validation periods as the catchment process modelling were also maintained in the statistical modelling. The seasonal ANN models showed better results in streamflow estimation than the single ANN model developed for total study period.

The results of both catchment process modelling and statistical modelling were then compared. This comparison shows that results of seasonal ANN models combined to a complete time series were as good as the results of the base model, used in the catchment process modelling.

The overall results of the chapter showed that RS data can be used in streamflow estimation successfully. Therefore, both catchment process modelling and statistical modelling approaches were used in the Ribb catchment to estimate streamflow data.

CHAPTER 5: THE RIBB CATCHMENT

5.1 Introduction

The methodologies tested in the first case study (study area – the Macalister catchment) were applied in the second study. The Ribb catchment was selected as the second study area, where ground measured data are limited for streamflow estimation. The limitations are not only restricted to inadequate observation points in both meteorological and stream gauges, but also to the poor quality of the recorded data. In some stations, data are not available to have a continuous time series.

The rationale behind the selection of the Ribb catchment as the second case study area was explained in Section 3.2.2. As tested in the first case study, both catchment process modelling and statistical modelling techniques were used in this case study. Catchment process modelling was undertaken using the SWAT model, while the artificial neural networks modelling technique was used as the statistical modelling approach. The same study period as the first case study (i.e. 2003 - 2008) was considered in the second case study. The period of 2003 – 2006 was considered as the calibration period, while the period of 2007 - 2008 was considered as the validation period, for both catchment process and statistical modelling.

For catchment process modelling, first rainfall and potential evapotranspiration (PET) data of the catchment were estimated using RS data (Sections 3.5.1 and 3.5.2 respectively). Furthermore, landuse/landcover (LULC) was classified using RS data (Section 3.5.3). The results of rainfall and PET estimation, and LULC classification are discussed in Sections 5.2.1, 5.2.2 and 5.2.3 respectively. Catchment process modelling of the Ribb catchment including the calibration and validation, and the model results with RS based input data (i.e. rainfall, potential evapotranspiration and LULC) are discussed in Section 5.3.

As practised in the first case study, the RS based input variables for statistical modelling approach were calculated for the Ribb catchment (Section 5.4.1). The results of the statistical modelling approach together with the performances of streamflow estimation in calibration and validation periods are discussed under Section 5.4.3.

A comparison of the results of catchment process modelling and statistical modelling of the Ribb catchment is presented in Section 5.5, followed by the summary of the chapter in Section 5.6.

5.2 Estimation of remote sensing based variables for catchment process modelling

5.2.1 Rainfall estimation

The main steps of the rainfall estimation procedure were outlined in Section 4.2.1. These steps were followed for the Ribb catchment, and briefly described below under various sub-sections.

5.2.1.1 Separation of rain and no-rain clouds

As was the case for the Macalister catchment, the MODIS based brightness temperature (BT), was calculated using MODIS bands 27, 31 and 32 to separate rain clouds from no-rain clouds. These brightness temperatures were used to calculate the brightness temperature difference of band 27 and 31, and the brightness temperature difference of band 31 and 32. The median values of these differences were used as thresholds to separate rain clouds from no-rain clouds (Kuligowski, 2002). Clouds with BT difference of bands 27 and 31 equal and higher than its median value and/or clouds with BT difference of bands 31 and 32 equal and less than its median value were considered as rainy clouds.

5.2.1.2 Brightness temperature threshold

As explained in Section 4.2.1.1, the brightness temperature of band 31 was used in the rainfall estimation of the Macalister catchment using rainy clouds, and the same approach was used for the Ribb catchment. Figure 5.1 shows the brightness temperature of band 31 (mean value for the catchment) of rain clouds and ground measured rainfall (i.e. Addis Zemen station) over the Ribb catchment for the study period. It is noted that the magnitude of rainfall in the catchment varies from north to south (Figure 3.8), but temporal rainfall pattern of the catchment is same as in the Addis Zemen station. BT31 values in the figure are not continuous since there are many no-rain cloud days in a given year in the Ribb catchment. This figure

indicates that the rainfall over the Ribb catchment is limited to the monsoon season which is from June to September (Setegn, 2010). This is a clear difference from the Macalister catchment which receives rainfall throughout a year. This situation in the Ribb catchment depicts clear wet (June to September) and dry (October to May) seasons. The BT of the Ribb catchment also shows a sinusoidal pattern, same as was in the Macalister catchment. The lowest BT of the Macalister catchment was counted in winter (June to August). Almost the same period (i.e. June to August) extended to September, and records the lowest BT in the Ribb catchment, causing monsoonal rains.

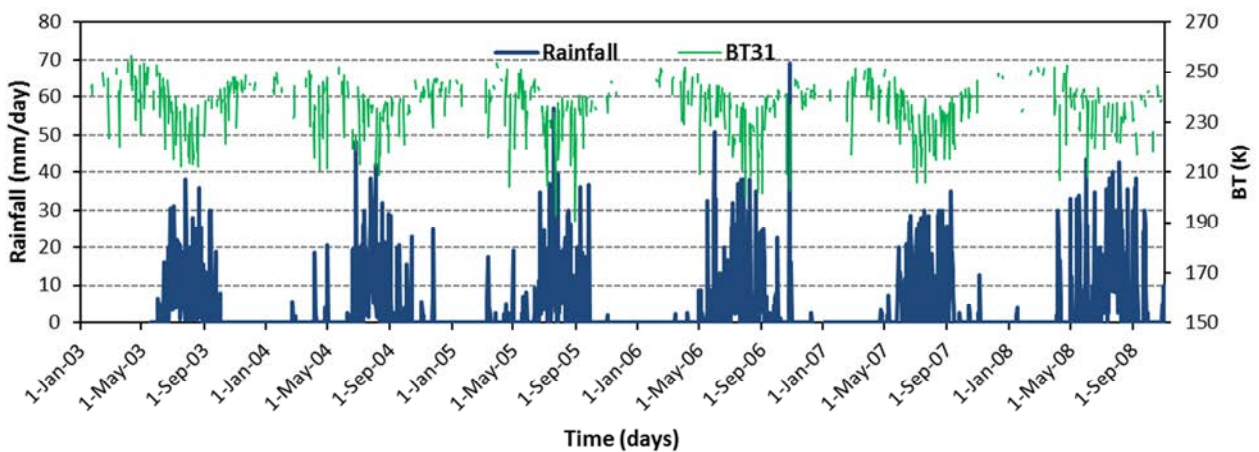


Figure 5.1 Ground measured rainfall and brightness temperature of the Ribb catchment

The Heidke skill score (*HSS*), Probability of Detection (*POD*), False Alarm Ratio (*FAR*) and bias were used as skill indices to identify the ability of proposed thresholds in producing rainfall in the Macalister catchment. These skill indices were calculated with TRMM rainfall pixels and ‘rainy’ pixels in rain clouds. TRMM rainfall data were used in this study as a substitute for the observed rainfall data due to their availability, accessibility and accuracy (Section 3.3.1). The mean seasonal BT values yielded the best results on the skill indices in the Macalister catchment. Therefore, the mean seasonal BT value was considered as the threshold for rainfall estimation in the Ribb catchment considering four seasons; since BT profile is the same in both catchments. Four seasons considered were: summer – June to August, autumn – September to November, winter - December to February and spring – March to May. Note that the terminology of summer, autumn, winter and spring are arbitrary in the case of the Ribb catchment, since the concept of seasons does not strongly exist in

Ethiopia. The calculated mean seasonal brightness temperature as thresholds for the Ribb catchment are shown in Table 5.1.

Table 5.1 Mean seasonal brightness temperature over the Ribb catchment

Season	Months	Mean seasonal BT (K)
Summer	Jun-Aug	231.3
Autumn	Sep-Nov	239.6
Winter	Dec-Feb	246.0
Spring	Mar-May	245.4

Table 5.1 shows that the mean seasonal BT values are higher than 235 K in all seasons except summer, when monsoon prevails. Summer in the Ribb catchment shows the lowest mean seasonal BT. Furthermore, this table shows the mean seasonal BT of winter and spring (i.e. prominent dry periods) are approximately equal.

5.2.1.3 Rainfall estimation function and results

Rainfall over the Ribb catchment for the study period was estimated following the procedure applied to estimate rainfall in the Macalister catchment (Section 4.2.1). The cumulative gamma probability functions were first calculated for the brightness temperature differences and TRMM rainfall data on a seasonal basis. Then, for a particular day, the brightness temperature difference and its cumulative gamma probability value was selected. The TRMM rainfall which had the same cumulative gamma probability was then obtained. This rainfall was then considered as the rainfall for that day. These steps were repeated for all days in the study period. This step-wise procedure was explained in Sections 3.5.1.3 and 4.2.1.2. The estimated rainfall data were compared with TRMM rainfall data to assess the accuracy of estimates, as was done in Section 4.2.1.2.

As an example, Figure 5.2 shows TRMM rainfall over the Ribb catchment and its surrounding areas on 07 August 2006. It shows that TRMM rainfall vary from 0 to 14 mm mainly from northeast to southwest in that figure, and 0 to 2 mm in the Ribb catchment. The estimated rainfall data on the same day are presented in Figure 5.3. This figure shows the same pattern

of rainfall from northeast to southwest as in Figure 5.2, but the magnitude of the estimated rainfall is slightly higher than the TRMM rainfall.

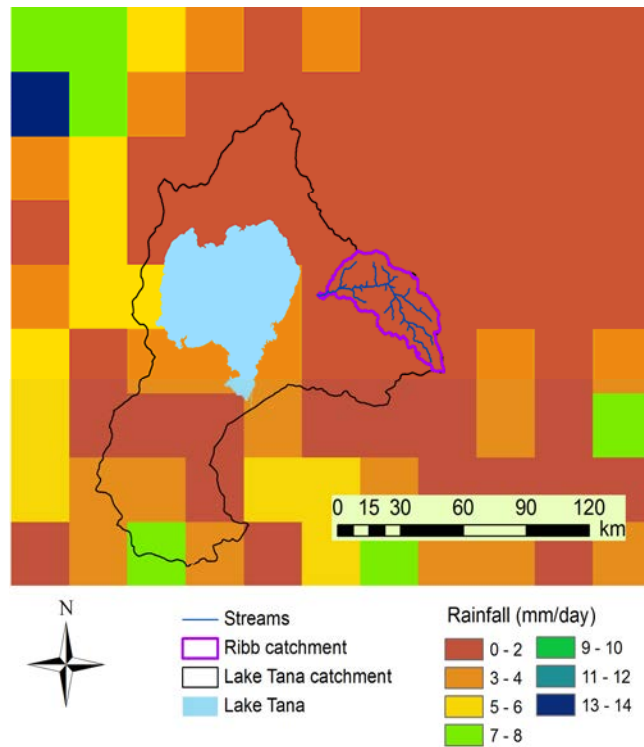


Figure 5.2 TRMM rainfall data over catchment area and its surrounding areas

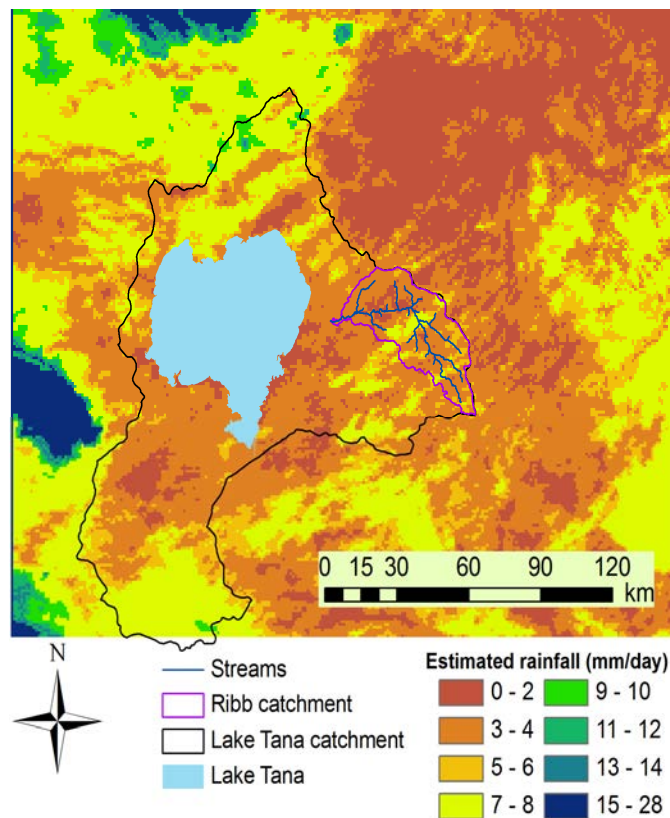


Figure 5.3 Estimated rainfall over the Ribb catchment and its surrounding areas

Figure 5.4 shows the annual estimated rainfall and TRMM rainfall in the Ribb catchment. This figure shows that year 2005 is the wettest year, while year 2007 is the driest within the study period. It is also observed in general that the estimated rainfall matches reasonably well with the TRMM rainfall on an annual basis except in year 2005.

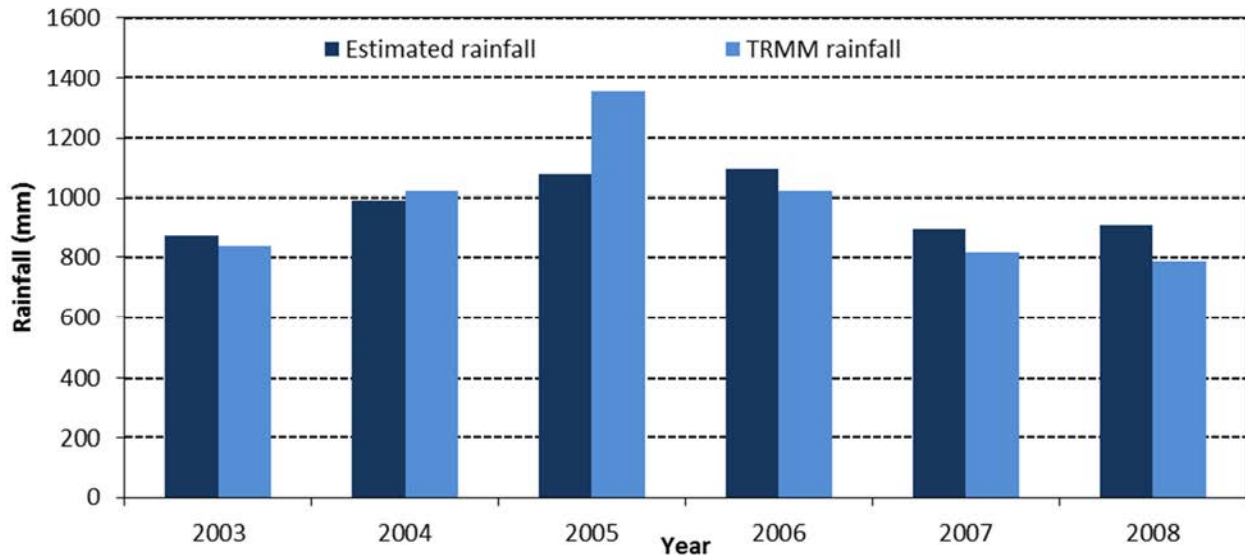


Figure 5.4 Annual rainfall of the Ribb catchment – TRMM and estimated rainfall

The estimated rainfall were further analysed with respect to its wet and dry seasons to understand how well estimated rainfall matches with the TRMM rainfall. The results of estimated and TRMM rainfall are shown in Figure 5.5.

The estimated rainfall during the wet season shows a slight overestimation compared to TRMM rainfall except year 2003. However, the estimated rainfall during the dry season of the study period shows a mixed result. The estimated rainfall during the dry season of 2003 is highly overestimated, while it is highly underestimated during the dry season of 2005. Note the scale difference of the vertical axis of the two figures in Figure 5.5.

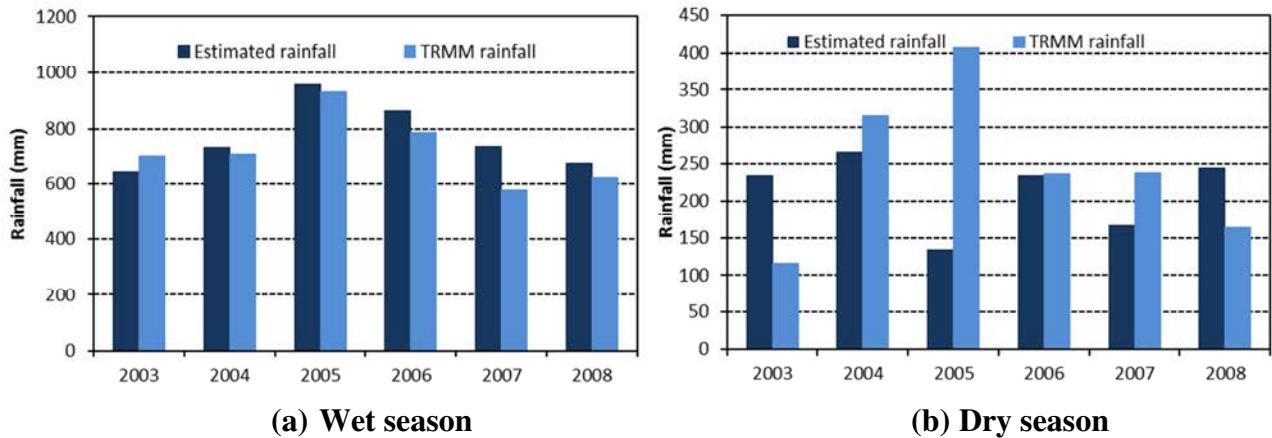


Figure 5.5 Seasonal rainfall (estimated and TRMM) over the Ribb catchment

5.2.1.4 Performance of rainfall estimation

The estimated rainfall data were further analysed with respect to TRMM rainfall data. Rain and no-rain days were counted separately in both estimated and TRMM rainfall data, and are presented in Table 5.2.

Table 5.2 Rain/no-rain days under TRMM and estimated rainfall during the study period

	TRMM no-rain days	TRMM rain days	Total days
Estimated no-rain days	1249	144	1393
Estimated rain days	191	608	799
Total days	1440	752	2192

This table reveals that there are 752 days of rain and 1440 days no-rain in TRMM data in the Ribb catchment during the study period. In contrast, there are 799 days of rain and 1393 days no-rain under estimated rainfall. It shows that the number of rain days in estimated rainfall is slightly higher than TRMM rain days. The close match of rain days between estimated and TRMM (80%) in the Ribb catchment is significantly better than that of the Macalister catchment as was shown in Table 4.3 (48%). These statistics show that the rate of detection of rain and no-rain is higher in the Ribb catchment than in the Macalister catchment.

It is observed that there are 191 days with estimated rainfall when there was no rain recorded in TRMM data. Similarly, there are 144 days with no rainfall estimates, when TRMM had recorded rainfall. Figure 5.6 shows the mismatching of rainfall days with respect to several classes of magnitudes of rainfall. This figure shows that the magnitude of the majority (approximately 70%) of days estimated of having rainfall when TRMM did not record rainfall are less than 2 mm. This was also observed in the Macalister catchment. On the other hand, the magnitude of the majority (approximately 52%) days estimated of having no rain when TRMM showed rainfall are less than 2 mm.

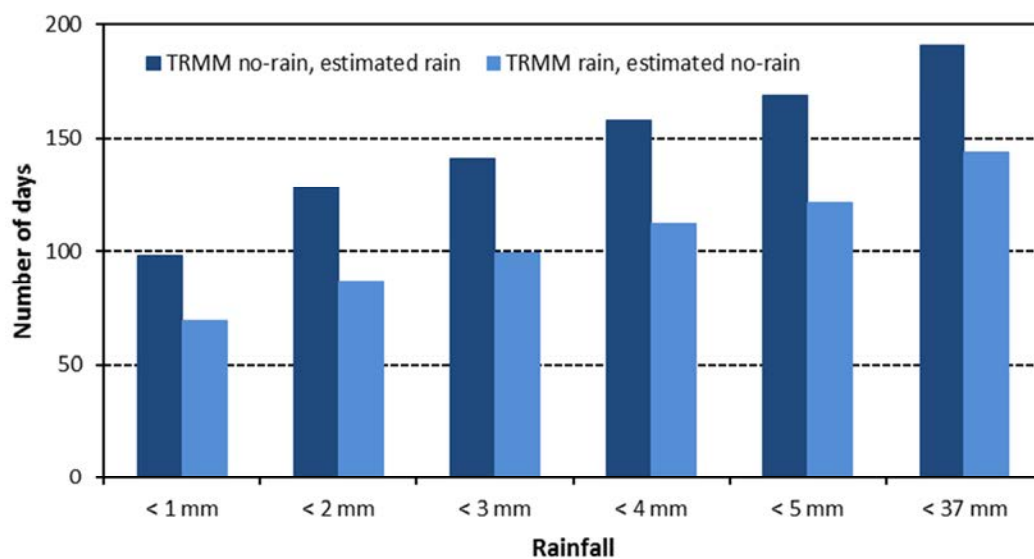


Figure 5.6 Cumulative distribution of mismatching days of rain/no-rain under TRMM and estimated

The Nash-Sutcliffe efficiency (E_f) and Root Mean Square Error ($RMSE$), which were explained in the Section 3.9, were also calculated with TRMM and estimated rainfall. TRMM rainfall data were considered as observed rainfall in these calculations. The E_f was 0.34 and $RMSE$ was 5.3 mm in estimating rainfall over the Ribb catchment.

5.2.2 Potential evapotranspiration estimation

Potential evapotranspiration (PET) data were estimated using RS data as an input to catchment process modelling. The proposed method used minimum ground measured variables to

estimate PET, and was tested in the Macalister catchment (Section 4.2.2). The same method was applied to the Ribb catchment to estimate PET. The estimated PET in the Macalister catchment was compared with Penman-Monteith (PM) based PET which was obtained through the SILO database. However, such database or calculated PM based PET data are not available for the Ribb catchment. Therefore, the PM based PET was estimated using ground measured data for the meteorological stations shown in Figure 5.7.

The collected ground measured data (i.e. minimum and maximum temperature, wind speed and sunshine hours) for those stations have missing information. Minimum and maximum temperature were available for all stations with a small percentage of missing data for the study period. Wind speed and sunshine hours are available only for the Debra Tabor meteorological station but with a very small percentage of missing data. Therefore, these data of Debra Tabor were used for the other stations assuming that there are no significant differences in these data in the catchment. The days which data were absent (i.e. missing or not collected) were not considered in the PM based PET estimation. Required saturated vapour pressure to calculate PM based PET was estimated using air temperature (Allen et al., 1998). The actual vapour pressure or relative humidity over the study area was absent, and therefore relative humidity data were obtained from the *IWMI Climate and Water Atlas*.

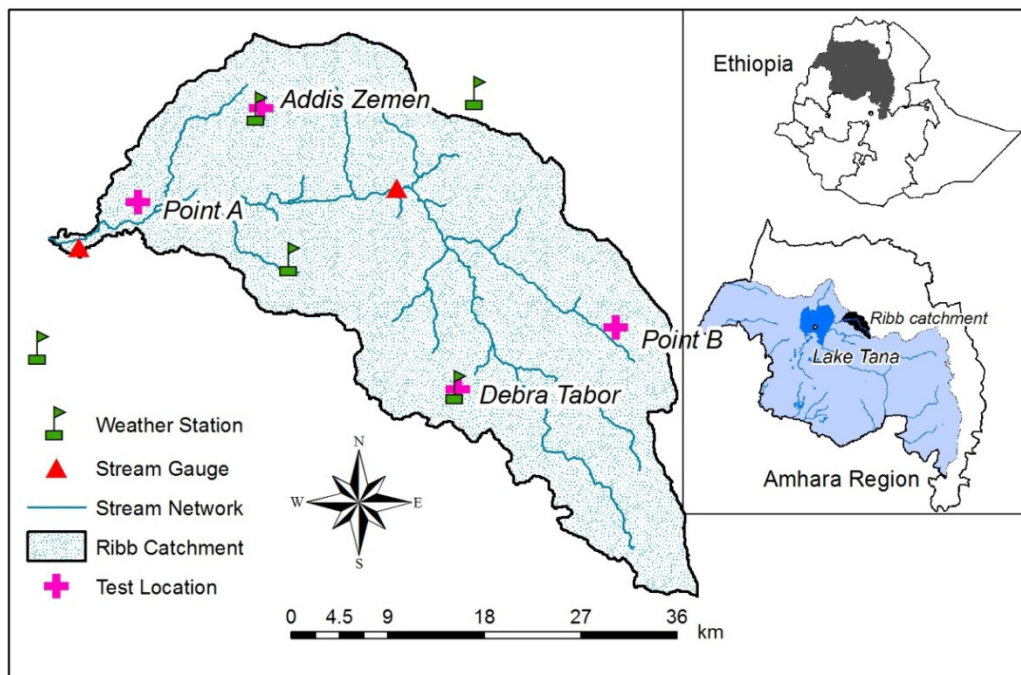


Figure 5.7 Meteorological stations and test locations over the Ribb catchment

Surface albedo values which are most important in estimation of PET using RS data were calculated, and compared against the values listed in the literature, and are shown in Table 5.3. In Section 4.2.2, the calculated surface albedo and existing literature values were compared for the Macalister catchment considering the existing LULC classes at test locations. Although the Macalister catchment is largely covered with evergreen forest, the dominant LULC class in the Ribb catchment was cultivation lands. The Afro-alpine forest can be seen as evergreen forest in the upper part of the Ribb catchment. Table 5.3 shows that mean value of the estimated surface albedo is less than the existing literature value in all LULC classes except the shrubs where it is equal.

Table 5.3 Comparison of estimated surface albedo values for different LULC of the Ribb catchment with literature values

		Afro-alpine forest	Shrubs	Crop	Crop/Grassland
Calculated values	<i>Min</i>	0.01	0.00	0.05	0.00
	<i>Max</i>	0.66	0.45	0.28	0.69
	<i>Mean</i>	0.10	0.15	0.13	0.16
	<i>STD</i>	0.05	0.04	0.02	0.05
Literature values*		0.18**	0.15	0.20***	0.24

*Values are not site specific

**Stressed crop

***(Bastiaanssen, 1998)

The estimated PET values of the Ribb catchment were computed separately for non-cloudy days and cloudy days as explained in Section 3.5.2. The results and their performance are discussed separately for non-cloudy days and cloudy days.

5.2.2.1 PET of non-cloudy days

Surface albedo, surface emissivity and surface temperature values were calculated using RS data for the Ribb catchment for non-cloudy days. These variables were used to estimate PET for the catchment. On average, the Ribb catchment had 23 percent of non-cloudy days per year during the period of study, which is significantly higher than the non-cloudy days of the

Macalister catchment (14%). Most of these non-cloudy days were evenly distributed during a given year except in June to September when the monsoon is active.

The estimated PET and PM based PET for the selected test locations (in Figure 5.7) of non-cloudy days are shown in Figure 5.8. This figure shows that the estimated PET on non-cloudy days is in the range of 4.0 to 9.0 mmday^{-1} . Also, the estimated PET are overestimated in most days compared to the PM based PET at all four test locations. This overestimation is due to the low values of surface albedo (Table 5.3) when they are computed with RS data during non-cloudy days; sparse vegetation produces low values of estimated surface albedo from RS data.

A difference in the pattern and magnitude of the estimated PET is seen across locations as a result of different LULC. Point A represents cultivation lands, while Point B is predominantly shrubs and forest. Addis Zemen has mix LULC class with cultivation land and urban. Debra Tabor is highly mixed with cropping, urban and riparian lands.

The underestimation and overestimation of the PET was further analysed using the same procedure applied in the Macalister catchment. A day was defined as highly under or over-estimated if the estimated PET deviates from PM based PET by at least one standard deviation of the PM based PET. Accordingly, the percent of highly overestimated days for Point A, Addis Zemen, Point B and Debra Tabor are 26.7, 29.8, 23.2 and 18.8 respectively. Furthermore, few highly underestimated days (i.e. 0.8, 0.8, 1.9 and 2.9 percent respectively) are also observed.

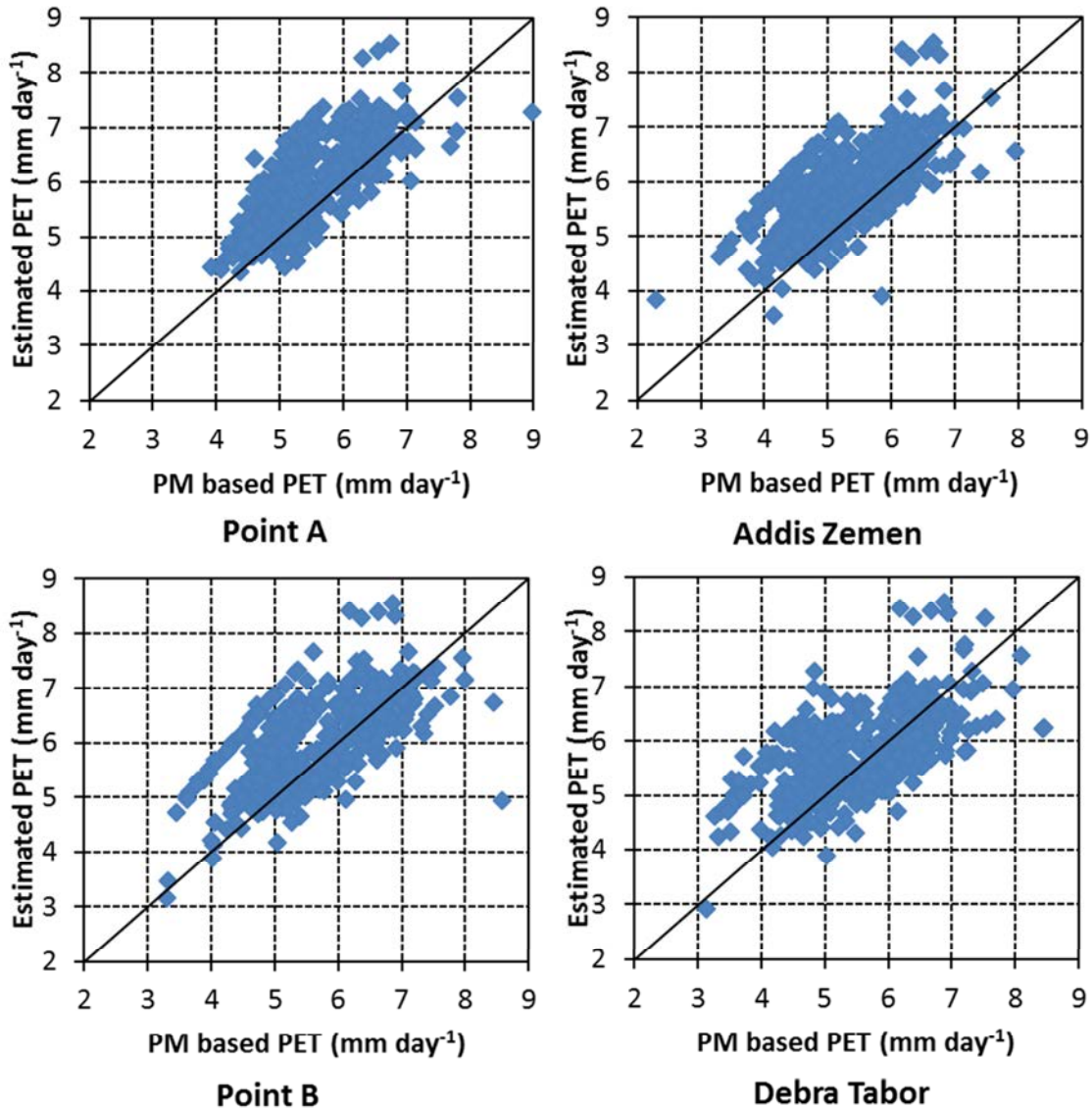


Figure 5.8 PM based PET and estimated PET for non-cloudy days at selected test locations in the Ribb catchment

5.2.2.2 PET of cloudy days

The PET of cloudy days were estimated using the methodology explained in Section 3.5.2.2, and this methodology was applied in the Macalister catchment (Section 4.2.2.2). These estimated PET and PM based PET over the Ribb catchment for cloudy days are shown in Figure 5.9 for the same test locations.

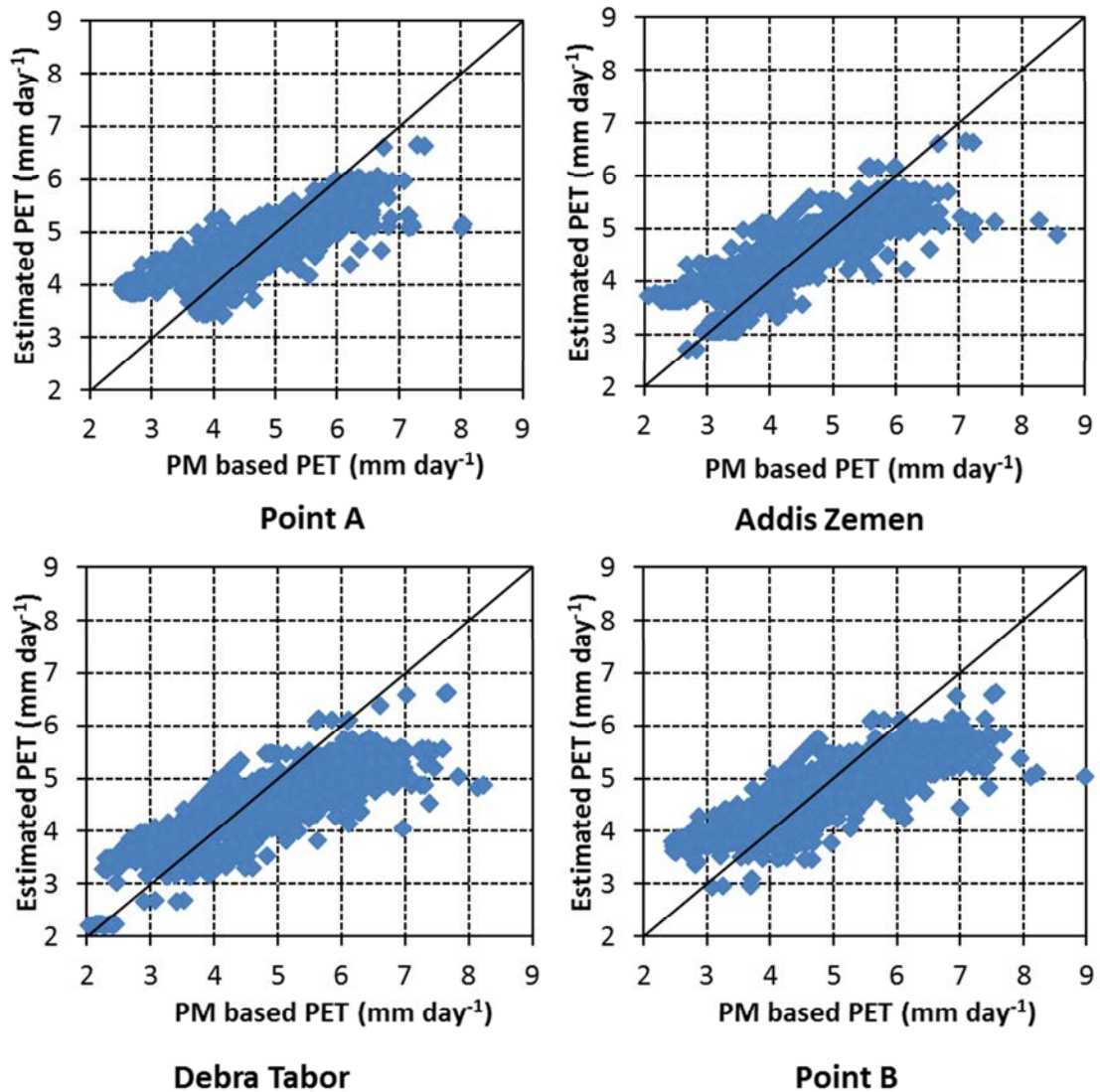


Figure 5.9 PM based PET and estimated PET for cloudy days at selected test locations in the Ribb catchment

According to Figure 5.9, the minimum estimated PET of cloudy days is around 2.0 mmday⁻¹ (fully cloudy day). It shows that most PET which are greater than 4 mmday⁻¹, are underestimated with estimated PET. Detailed analysis shows Point A, Addis Zemen, Point B and Debra Tabor have 12.8, 9.9, 13.3 and 15.0 percent of cloudy days as highly underestimated. In addition, 6.6, 4.5, 4.3 and 4.3 percent days are highly overestimated in the Ribb catchment on cloudy days.

5.2.2.3 Mean annual PET

Mean annual values of the estimated PET for the study period over the Ribb catchment were calculated and are shown in Table 5.4. This table shows that estimated PET are slightly underestimated compared to PM based PET estimates in all test locations. However, this underestimation is less than 5% in all test locations. The performance of PET estimates in the Ribb catchment is well within the general guidelines stated by Allan et al. (2010), which stated that the estimated PET can be accepted for further applications if they are within the range of 10% - 40% of measured PET. When measured PET is not available, the PET estimated through Penmann-Monteith method can be used for ground measured PET. Non-cloudy days in Figure 5.8 show overestimation over the catchment and cloudy days in Figure 5.9 show a mixed results with more underestimations. However, the percentage of non-cloudy and cloudy days in the Ribb catchment are 23% and 77% respectively. Therefore, the slight underestimation in annual estimated PET values in Table 5.4 is due to the effect of underestimations in cloudy days.

Table 5.4 Mean annual PET over selected test locations

Test Location	Annual PET (mm)			
	RS	PM	Difference (mm)	% of Difference
Point A	1792.2	1826.1	-33.9	-1.8
Addis Zemen	1705.0	1762.9	-57.9	-3.3
Point B	1756.6	1800.6	-44.1	-2.4
Debra Tabor	1678.1	1756.5	-78.4	-4.5

5.2.2.4 Performance of PET estimates for total period and seasons

Similar to the Macalister catchment (Section 4.2.2.4), the performance of PET estimation was calculated for the Ribb catchment. As explained in Section 5.2.1, wet (i.e. June to September) and dry (i.e. October to May) seasons were considered for this analysis. Wet season and early months of dry season are the main cultivation period in the catchment. Crops such as paddy and maize are cultivated predominantly during this period. As such, the PET during this period is higher than that of the dry period. The main cultivation season of wet period is followed by a minor cultivation season during December to February depending on water

availability. Cultivation lands are turned into bare lands during latter part of the dry season due to the lack of water. Results of the performance in relation to the Ribb catchment are shown in Table 5.5 for the selected test locations (Figure 5.7).

Table 5.5 shows that *RMSE* values are significantly lower during the non-cloudy days compared to the cloudy days in the total period for all test locations. The *RMSE* values for the non-cloudy days of the wet season also less than those of the cloudy days. However, there is no significant difference in *RMSE* of cloudy days.

As can be seen from Table 5.5, the E_f values of the Ribb catchment vary with respect to seasons and day condition. Higher E_f values were observed for non-cloudy days, during the total period. Seasonal E_f values show a mix result from very high to negative.

Table 5.5 Performance of PM-based PET and estimated PET for non-cloudy days at selected test locations in Ribb catchment

Location	Day condition	Total period		Wet season		Dry season	
		<i>RMSE</i> *	E_f	<i>RMSE</i>	E_f	<i>RMSE</i>	E_f
Point A	<i>Non-cloudy days</i>	0.37	0.49	0.27	0.28	0.62	0.15
	<i>Cloudy days</i>	1.02	0.04	1.13	0.24	0.68	-0.09
	<i>Both</i>	0.56	0.44	0.35	0.27	0.64	0.08
Addis Zemen	<i>Non-cloudy days</i>	0.38	0.55	0.36	0.73	0.66	0.18
	<i>Cloudy days</i>	1.07	0.23	0.47	0.51	0.69	0.05
	<i>Both</i>	0.58	0.51	0.39	0.54	0.67	0.15
Point B	<i>Non-cloudy days</i>	0.49	0.46	0.31	0.48	0.84	0.73
	<i>Cloudy days</i>	1.37	0.21	0.38	0.46	0.97	0.15
	<i>Both</i>	0.75	0.41	0.38	0.46	0.88	0.48
Debra Tabor	<i>Non-cloudy days</i>	0.53	0.47	0.28	0.78	0.98	-0.08
	<i>Cloudy days</i>	1.51	-0.14	0.39	0.71	0.97	-0.34
	<i>Both</i>	0.82	0.40	0.38	0.78	0.97	-0.15

* Units of *RMSE* is mm day⁻¹

5.2.3 Landuse/landcover classification

Landuse/landcover (LULC) classification over the Ribb catchment was done using the methodology explained in Section 3.5.3. This was also applied to the Macalister catchment for

its LULC classification Landsat 7 ETM+ image, acquired on 23 October 2005 was used to classify LULC classes in the Ribb catchment. This particular day was specially selected since image on that day was cloud free, and gives a better representation of the existing LULC classes in the Ribb catchment.

The classification process that was used can be summarized as follows. Initially, the Landsat ETM+ bands were used to generate the principal component of the bands, which reproduced the number of bands used in the classification. The same Landsat ETM+ image was then used to calculate *NDVI*. The selected principal components (layers) and *NDVI* (layer) were stacked as an image to classify existing LULC classes in the Ribb catchment. This image was used as the final image in the classification.

A field survey was conducted in the Ribb catchment to identify the existing LULC classes. During this survey, several sample points were considered to define LULC classes. These are called ground-truth data. One half of the ground-truth data that were collected in the field survey was used to train the final image. The trained image was then used to classify into LULC classes in the catchment using the maximum likelihood classifier. Finally, the remaining half of ground-truth data were used to calculate the accuracy of classified LULC.

5.2.3.1 Principal Component Analysis

Landsat 7 ETM+ consists 8 bands and the first 7 bands of Landsat 7 ETM+ are similar (i.e. in terms of band widths) to Landsat 5 TM. The eighth band of the Landsat 7 ETM+ is the panchromatic band (0.52 ~ 0.90 μm). Six bands, out of eight of Landsat 7 ETM+, (i.e. excluding the thermal band - band 6 and panchromatic band - band 8) were considered in the image classification. The panchromatic and thermal bands were not considered due to the mismatching of their spatial resolution (15/60 m) with other bands (30 m). This was also the case with the thermal band of Landsat 5 TM that was used in LULC classification of the Macalister catchment. As mentioned in the classification summary (Section 5.2.3), PCA was used to further reduce the number of bands. The results of PCA are presented in Figure 5.10. This figure represents the cumulative variance explained by principal components of Landsat 7 ETM+ bands, except thermal and panchromatic. Note that $\Sigma PC_i = PC_1 + PC_2 + \dots + PC_i$ in

the x-axis, where $i = 2, 3, 4, 5$ and 6 . The Figure 5.10 shows that the first principal component represents almost 97% of the image variability, and the first three principal components of the image represent more than 99% of its variability. Therefore, the first three principal components and *NDVI* (which represents vegetation information) were used to classify the LULC over the Ribb catchment.

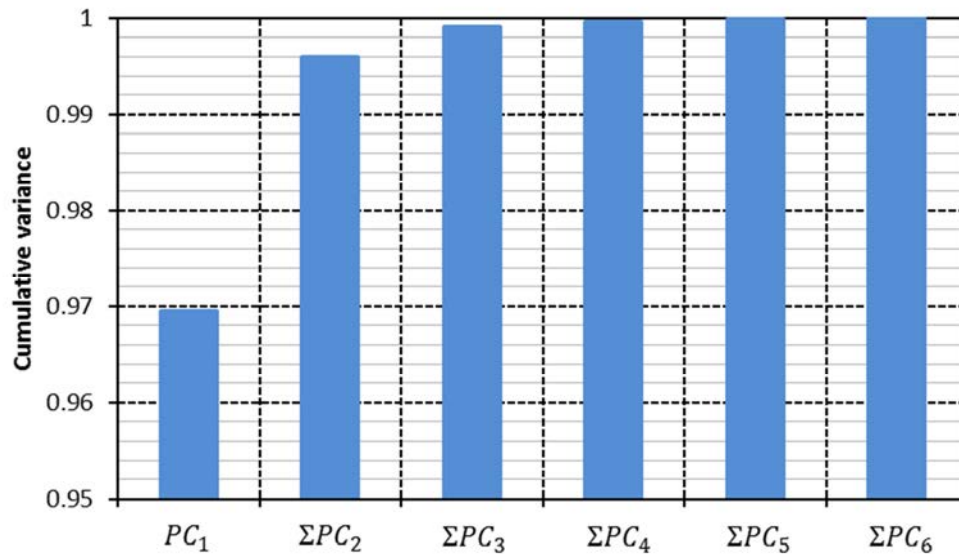


Figure 5.10 Principal components of the selected six bands of Landsat 7 ETM+ and their cumulative variability

5.2.3.2 Results of landuse/landcover classification

As outlined in Section 5.2.3, the train image was classified into LULC classes using the maximum likelihood classifier. Figure 5.11 shows the classified image of the Ribb catchment. This figure shows that the cultivated area which is covered by teff (a cereal crop) is the dominant LULC class in the lower catchment area (close to the catchment outlet). The signatures of grasslands and grassland/shrubs in the catchment are mixed with teff, since teff also a type of grass. LULC of the middle part of the catchment is a mix of cultivation lands and natural vegetation. Moderately slope lands are common in this area, and most of them are under teff cultivation during the main cultivation season. Marginal land (i.e. land close to natural vegetation) are used as grasslands or sometimes for teff cultivation. However, these lands are highly eroded (Betrie et al., 2011b), as such unfertile for cropping. The afro-alpine

forest is the dominant LULC class in upper catchment area, and this area is not suitable for cultivation because of slope.

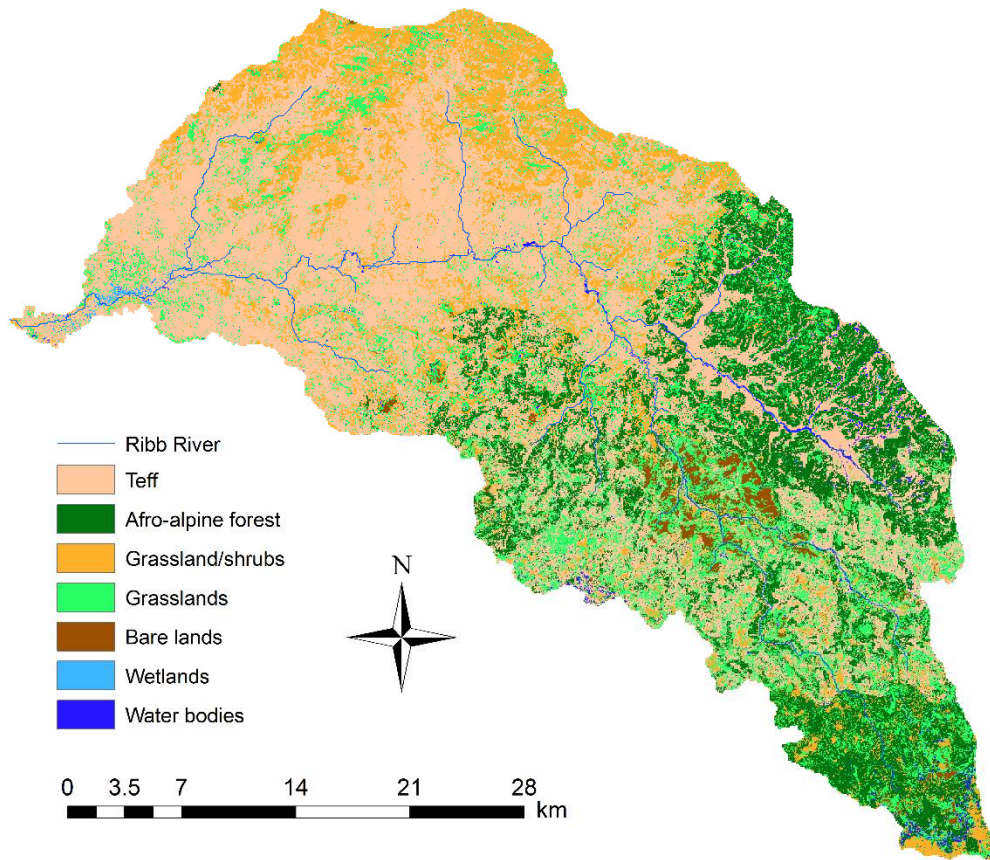


Figure 5.11 Landuse/landcover classes of the Ribb catchment

Table 5.6 shows the areas of each LULC class that covers the Ribb catchment. The table shows, teff covers little less than half of the Ribb catchment. The Afro-alpine forest which is mostly located in mountains, grassland/shrubs and grasslands cover approximately in equal areas in the Ribb catchment.

Table 5.6 Extent and percentage of each LULC class obtained through classification

LULC class	Area (ha)	Percentage
Teff	60638.4	47
Afro-alpine forest	23189.9	17.9
Grassland/shrubs	20848.6	16.2
Grasslands	20800.8	16.1
Bare land	2036.8	1.6
Wetlands	249.9	0.2
Water bodies	1360.7	1
Total	129125.1	100

Table 5.6 shows bare lands are less than 2 percent of the total land area of the catchment. There are no major water bodies in catchment other than the Ribb River. However, some of the lowlands which are close to Lake Tana, become wetlands during the monsoon period. Again, they are seasonal and prevails a short period.

5.2.3.3 Accuracy assessment of the landuse/landcover classification

Both descriptive and analytical techniques were used in the accuracy assessment as in the Macalister catchment. The remaining half of the ground-truth data which was not used in the image training was used in calculation of accuracy indices (which were described in Section 3.5.3.4).

(a) Descriptive technique

Table 5.7 shows the calculated contingency matrix for existing LULC classes in the Ribb catchment. This table shows the sample size (i.e. Producer's total) of the LULC classes of teff, afro-alpine and grassland/shrubs used in classification accuracy calculation is higher than the threshold (i.e. minimum 50 sample points per class) outlined by Congalton (1991). Less number of samples in grasslands, bare land, wetlands and water bodies were noted even during the ground-truth data collection survey. An effort was made to increase these numbers, however, this was not achieved due to inaccessibility with difficult terrain conditions in the upper catchment areas.

The contingency matrix shows both producer's accuracy (9th row) and user's accuracy (9th column), as well as overall accuracy (in the cell of 9th row and column). As explained in Section 4.2.3.3 (a), the producer's accuracy is used to assess the accuracy of image classification, and the user's accuracy is used to assess the accuracy of LULC in classified image for further applications (i.e. water resources planning, urban planning and agricultural applications).

In the contingency matrix, teff shows 77.8 and 88.5 percent of producer's and user's accuracy respectively. Producer's accuracy is less than the user's accuracy in teff as its signature mixed with afro-alpine forest, grassland/shrubs and bare land. A magnified view of the classified image shows that mostly these signature mixings occur near to the edges of all three LULC classes. In user's perspective, the teff signature can be mixed with grassland/shrubs which their signatures are almost similar. Teff itself is a type of a grass which is not much different to ordinary grass types.

Table 5.7 Contingency matrix of the landuse/landcover classification of the Ribb catchment

		1	2	3	4	5	6	7	8	9
		Teff	Afro-alpine forest	Grassland/shrubs	Grasslands	Bare land	Wetlands	Water bodies	User's total	User's accuracy
1	Teff	77	0	4	1	2	2	1	87	88.5
2	Afro-alpine forest	5	54	0	2	0	0	2	63	85.7
3	Grassland/shrubs	7	2	46	5	2	1	0	63	73.0
4	Grasslands	2	3	5	31	2	2	1	46	67.4
5	Bare land	7	0	0	0	24	0	0	31	77.4
6	Wetlands	0	0	0	0	0	15	1	16	93.8
7	Water bodies	1	0	0	0	0	0	9	10	90.0
8	Producer's total	99	59	55	39	30	20	14	316	
9	Producer's accuracy	77.8	91.5	83.6	79.5	80.0	75.0	64.3		81.0

The afro-alpine forest, which is second to teff in its coverage, shows 91.5 and 85.5 percent of producer's accuracy and user's accuracy respectively. The producer's accuracy is higher in this LULC class with its clear signature but slightly mixed with grasslands and grassland/shrubs, as can be seen in Table 5.7. A similar situation occurs with the user's accuracy, in terms of mixed signature, but mixed with the signature of teff (Table 5.7). Grasslands shows the producer's accuracy of 83.6% while its signature is mixing with teff and grasslands. The user's accuracy (67.4%) of this class is relatively less than teff and afro-alpine forest, mainly due to the mixing with teff and grasslands. The producer's accuracies of grasslands and bare land are equal. The contingency matrix shows that signature of grasslands is mixed with Afro-alpine forest and grasslands/shrub, while bare land signature is mixed with grasslands/shrub and grasslands. The user's accuracy of the grasslands is the lowest user's accuracy among all classified classes. The table shows that grasslands can be found in any LULC of the classified image. The user's accuracy of bare land is mostly affected by teff. The overall accuracy of the LULC classification is 81 percent. Thomlinson et al. (1999) stated that the LULC classification can be accepted for further application, if it has an overall accuracy and individual accuracies not less than 85 percent and 70 percent respectively. This was the case for the Ribb catchment in most LULC classes, as seen in Table 5.7.

(b) Analytical technique

The kappa coefficients were calculated to measure the validity of the observed classification accuracy to the random classification accuracy due to chance agreement of classification (Lillesand and Kiefer, 1999), and then are shown in Table 5.8. The author of this thesis outlined the threshold for kappa coefficient based on the existing literature in Section 3.5.3.4 (Bharatkar and Patel, 2013). According to those thresholds grasslands and grassland/shrubs classes can be rated as 'good' while all other classes as 'excellent'. Kappa coefficient of the overall classification can also be rated as 'excellent' according to these thresholds. As explained in Section 3.5.3.4, small difference between user's accuracy and kappa coefficient for individual LULC class and for overall classification reveal that the classification is reliable.

Table 5.8 Kappa statistics of the landuse/landcover classification

LULC class	Kappa coefficient	User's accuracy
Teff	0.83	88.5
Afro-alpine forest	0.82	85.7
Grassland/shrubs	0.67	73.0
Grasslands	0.63	67.4
Bare land	0.75	77.4
Wetlands	0.93	93.8
Water bodies	0.90	90.0
Overall	0.77	81.0

* Kappa coefficient less than 0.4 is considered 'poor', 0.4 – 0.75 is considered 'good' and above 0.75 is considered 'excellent' (Bharatkar and Patel, 2013).

The accuracy of the classified LULC which are presented in the contingency matrix (Table 5.7) and Table 5.8 show that LULC classification over the Ribb catchment is reliable enough for further applications, and used in catchment process modelling (Section 5.3).

5.3 Catchment process modelling

The methodology which was explained in Section 3.6 with regard to catchment process modelling, and tested in the first case study (Section 4.3) was applied to the second case study area (i.e. Ribb catchment). The SWAT model was used in catchment process modelling to estimate streamflow. As was explained in Section 4.3, the model was calibrated for 2003-2006 and validated for 2007-2008. Initially, the model was calibrated with available ground measured data. This was analysed as the base model. Then, keeping calibrated model parameters of the model unchanged, the ground measured rainfall and model derived PET were replaced with the estimated rainfall and estimated PET using RS data, and the model was run.

The results of the model run with ground measured rainfall and estimated PET, and the model run with estimated rainfall and model derived PET are not described in this section since the results of these two model runs were identical to those of the base model and the model run

with estimated rainfall and estimated PET. This behavior of results was the same with the Macalister catchment.

5.3.1 Model calibration and validation using ground measured data

The SWAT model setting up, calibration and validation processes were discussed in detail in Section 3.6. These processes were used up for the Macalister catchment, and the results were discussed in Section 4. 3. The same procedure was applied to set up, calibrate and validate the SWAT model for the Ribb catchment. The LULC information obtained from the LULC classification (Section 5.2.3) and the FAO-based soil data were used to set up the SWAT model.

The model calibration and validation were done using the available ground measured meteorological data. As stated earlier, this model was considered as the base model for the Ribb catchment. The purpose of this step was to obtain a set of calibrated model parameters. Major parameters that were used in the calibration are listed in Table 5.9 together with the software defined ranges of the model parameters and the optimum values obtained after the auto-calibration. This table shows that different CN2 values were used for different LULC classes in the model. This was possible with the available information, however, single parameter values were used in each of the remaining parameters for the entire catchment, because of lack of data available to calibrate these parameters at subcatchment level. This was also the case with the Macalister catchment.

Figures 5.12 and 5.13 show the results of the base model of the Ribb catchment. Figure 5.12 shows measured streamflow and estimated daily streamflow as line graphs. Measured streamflow of the catchment reveals that high flow prevails during the wet period from July to late September in almost every year. Streamflow is in its low flow phase from early October to late June. The base model has estimated daily streamflow well during both calibration and validation periods, except the early part of the wet season in 2008.

Table 5.9 SWAT model parameters used for calibration purposes – Ribb catchment

Parameter	Description	Range*	Optimum value
Parameters the govern surface water response			
CN2	Curve Number II	35-98	72 ¹ , 65 ² , 81 ³ , 86 ⁴ , 85 ⁵
ESCO	Soil evaporation compensation factor	0-1	0.86
SOL_AWC	Available soil water capacity	0-1	0.8
Parameters that govern subsurface water response			
GW_REVAP	Groundwater re evaporation coefficient	0.02-0.2	0.14
REVAPMN	Threshold depth of water in the shallow aquifer for re evaporation to occur (mm)	0-500	282
GWQMN	Threshold depth of water in the shallow aquifer required for return flow to occur (mm)	0-5000	577
GW_DELAY	Groundwater delay (days)	0-50	8
ALPHA_BF	Base flow recession constant	0-1	0.28
RCHRG_DP	Deep aquifer percolation fraction	0-1	0.05
Parameters that govern catchment response			
CH_K2	Effective hydraulic conductivity in main channel alluvium (mm h ⁻¹)	0.01-150	14.2
SURLAG	Surface runoff lag coefficient (day)	0-10	3

¹Teff, ²Afro-alpine forest, ³Grasslands/shrubs, ⁴Grasslands and ⁵Barelands

*(Neitsch et al., 2010)

Figure 5.13 shows the same results as scatter plots, separately for calibration and validation periods. Additionally this figure shows the high values of the coefficient of determination (R^2) between measured and estimated streamflow. However, the calibration period of Figure 5.13 shows more overestimations, while the validation period shows both overestimations and underestimations.

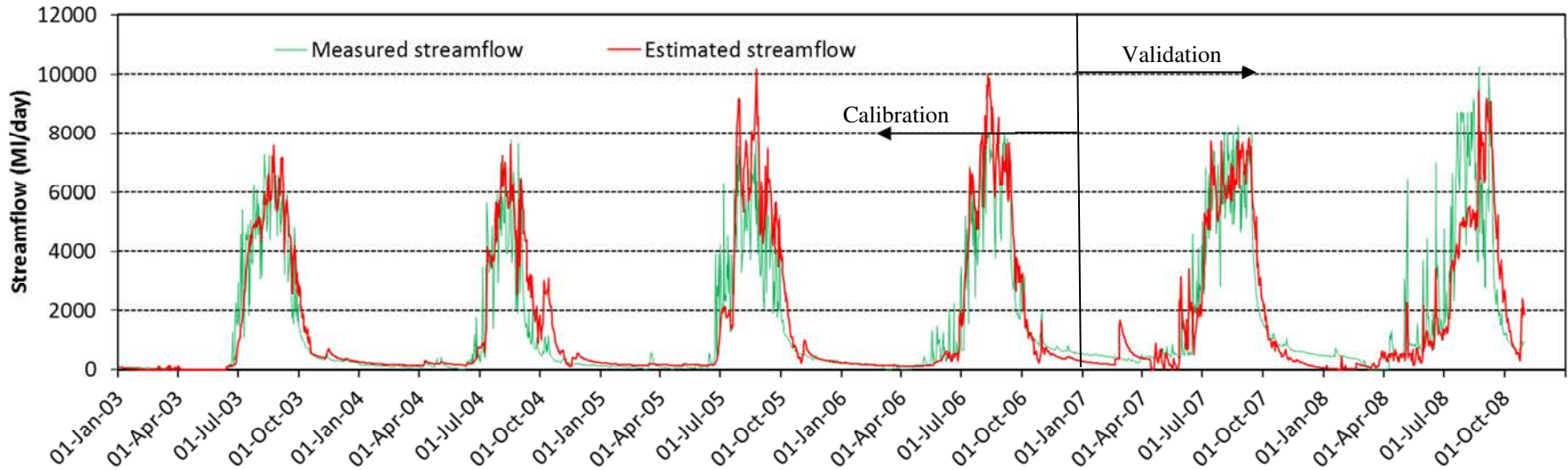
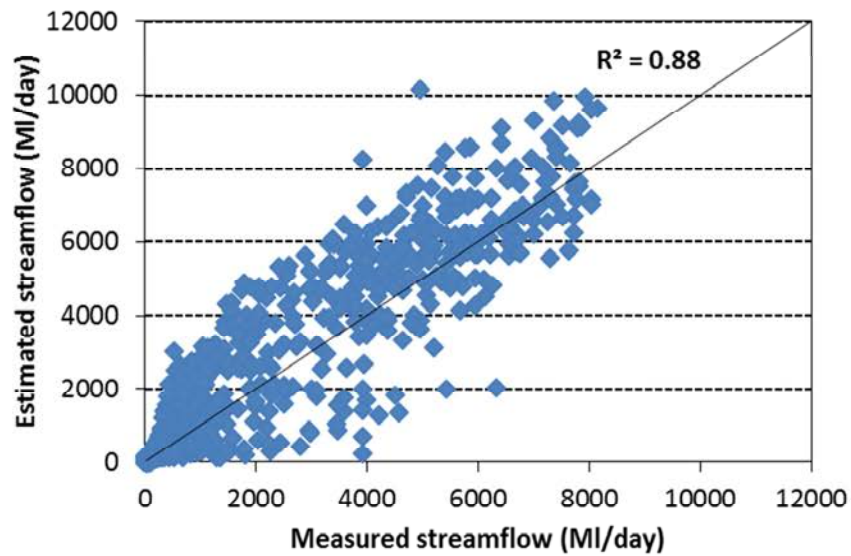
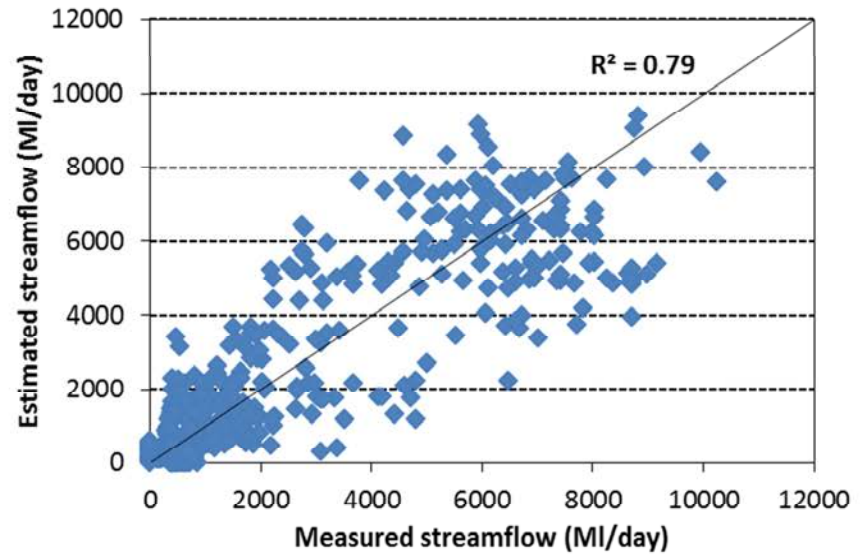


Figure 5.12 Measured and estimated streamflow of the Ribb catchment – base model



(a) Calibration period



(b) Validation period

Figure 5.13 Scatter plots of the measured and estimated streamflow of the Ribb catchment – base model

These results are separately presented for wet and dry seasons in Figure 5.14, again for calibration and validation periods. This figure shows that streamflow has mostly overestimated at the calibration period of the wet season. Estimated streamflow during validation period during the wet season shows a mixed result. However, their coefficients of determination remain very high. Compared to the wet period, the model results are different during the dry period. Estimated streamflow of the dry season during the calibration is mostly overestimated. In comparison to the calibration period, the validation period shows very poor performance in streamflow estimation. This figure shows the base model was significantly underestimated the streamflow during the validation period of the dry season.

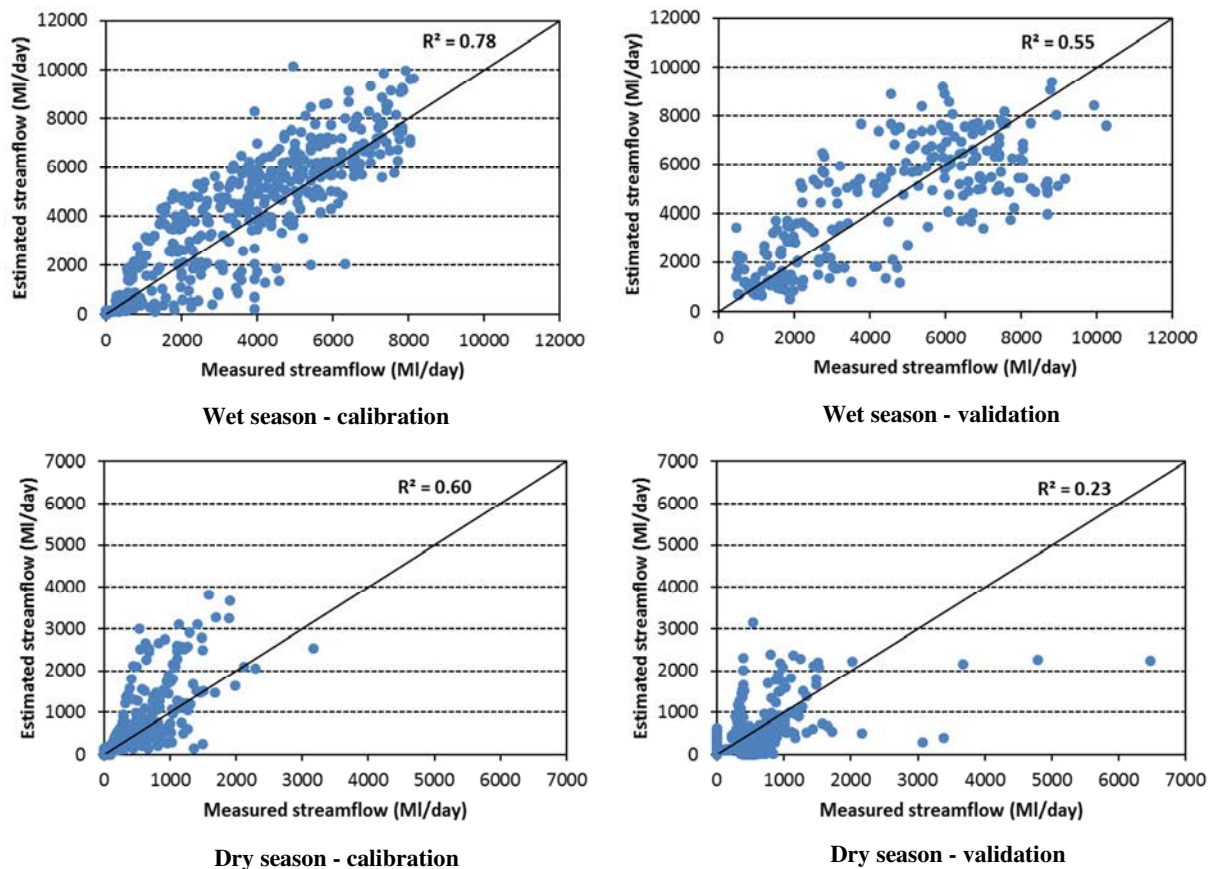


Figure 5.14 Scatter plots of the measured and estimated streamflow of wet and dry seasons in the Ribb catchment – base model

5.3.2 Model with estimated rainfall and estimated PET

As was done in the first case study, the estimated rainfall and estimated PET (Sections 5.2.1 and 5.2.2) were extracted on a subcatchment basis, and replaced the ground measured rainfall and the model derived PET in the base model. As explained in Section 4.3.2, the model with estimated rainfall and estimated PET was not calibrated, but run with the calibrated model parameters obtained from the base model (Section 5.3.1).

Figure 5.15 shows the results of the model run with estimated rainfall and estimated PET (from RS data). Although there were no separate calibration and validation done in this model run, they are marked in the figure to maintain the consistency with Figure 5.12. This figure shows that the estimated streamflow is highly underestimated during all wet seasons except the wet season of 2005. Estimated streamflow during the wet season shows that the model was delayed to response to rainfall. However, this figure also shows that the model has responded quickly to recession of streamflow. The same results are presented as scatter plots in Figure 5.16, separately for the calibration and validation periods with coefficient of determination. Figure 5.16 shows that estimated streamflow is mostly underestimated though the coefficient of determination is high during the validation period.

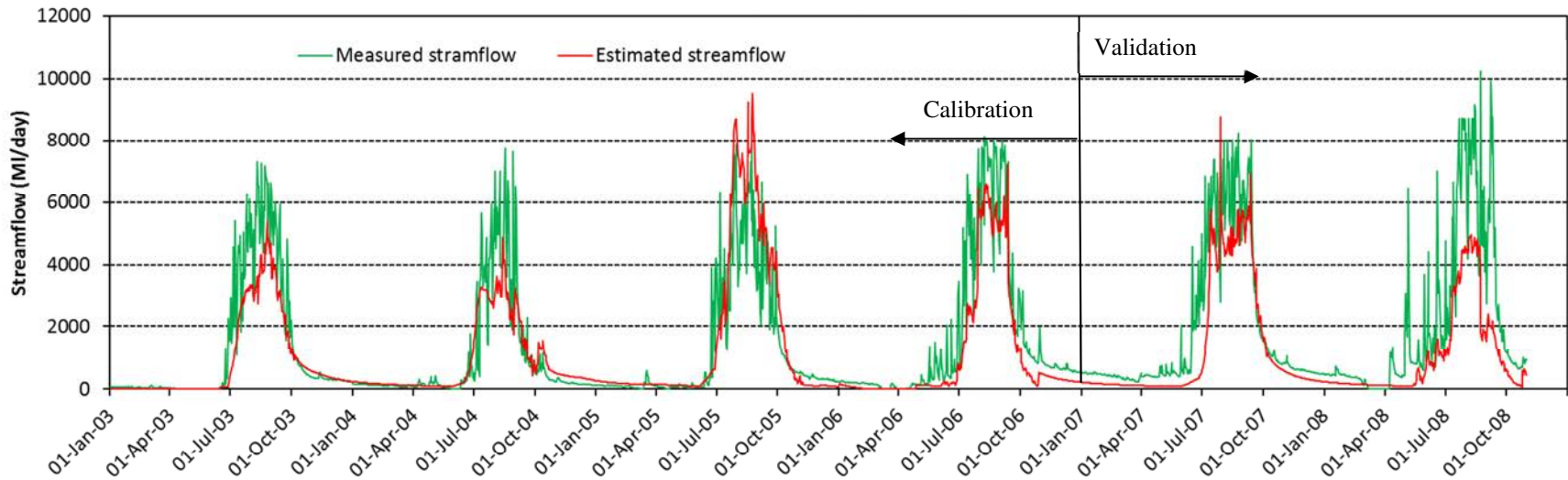


Figure 5.15 Measured streamflow, and estimated streamflow with both estimated rainfall and PET – Ribb catchment

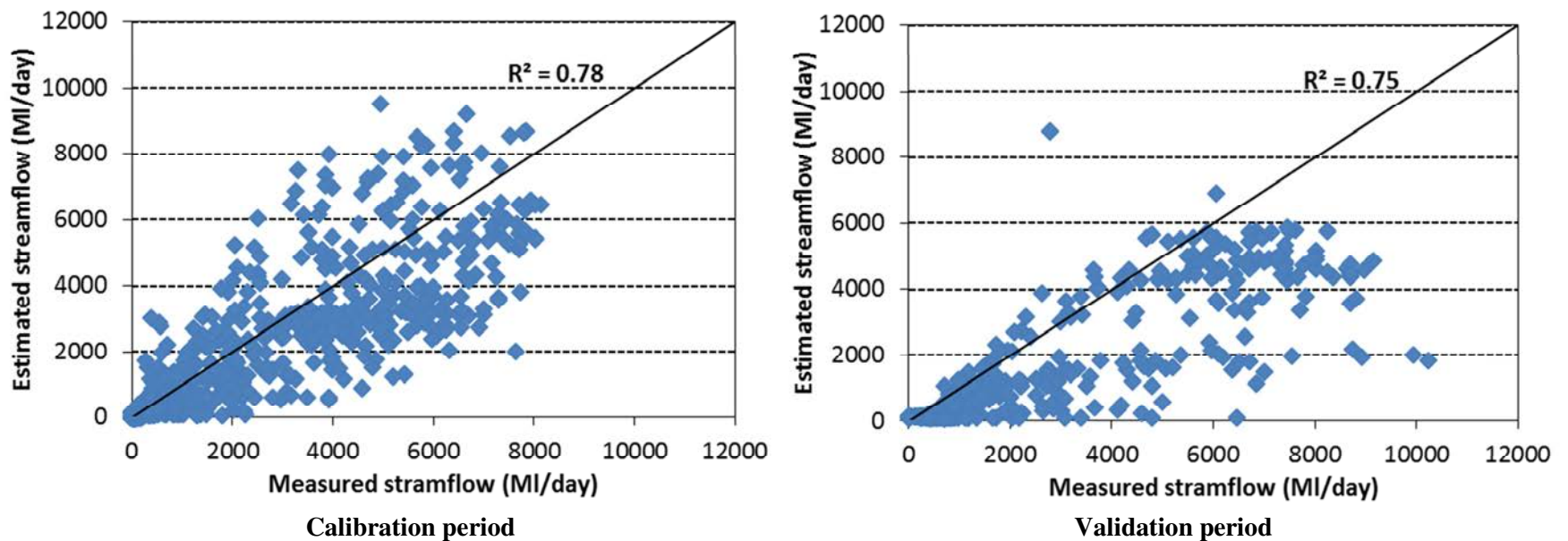


Figure 5.16 Scatter plots of the measured and estimated streamflow of the Ribb catchment with both estimated rainfall and PET

The results of the model run with estimated rainfall and estimated PET were plotted separately on seasonal basis, for calibration and validation periods, and are shown on Figure 5.17. Estimated daily streamflow of during calibration period of the wet season shows a mixed result. However, the estimated daily streamflow is highly underestimated during the validation period of the wet season, though the coefficient of determination is reasonably good. Furthermore, figure shows that streamflow estimation during dry season is weaker than that of wet season. The coefficients of determination are further low in dry season compared with wet season. Additionally, the estimated streamflow of the validation period during the dry season shows a significant underestimation compared to calibration period of the same season. Comparing the results in Figure 5.17 with those of Figure 5.14, it is seen that overestimations during the calibration period have reduced, but still producing a lower coefficient of determination for both wet and dry seasons. Similar observation is made for the validation period.

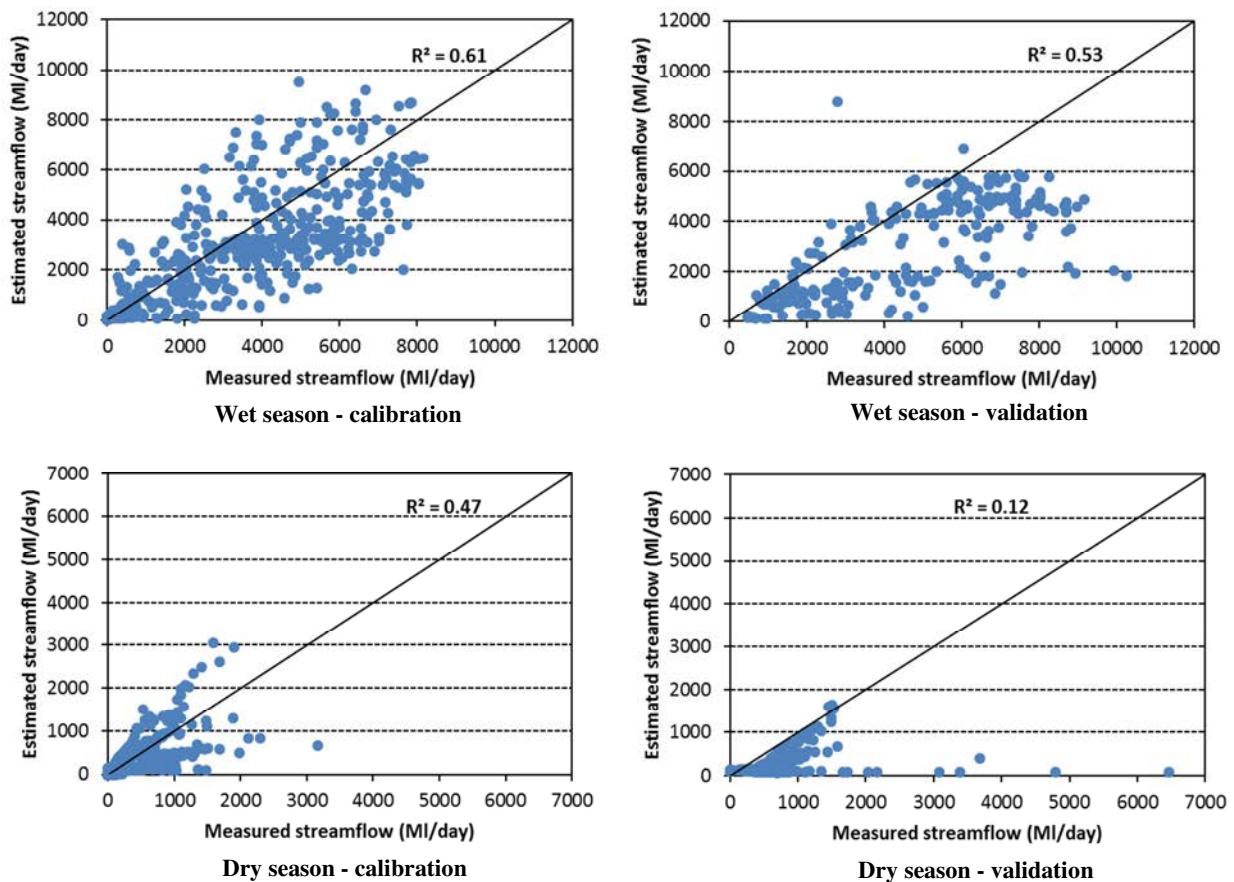


Figure 5.17 Scatter plots (seasonal) measured and estimated streamflow of the Ribb catchment – model with both estimated rainfall and PET

5.3.3 Comparison of results of base model and model with estimated rainfall and estimated PET

The performance indices (Nash-Sutcliffe efficiency and Root Mean Square Error) were also calculated for both base model and model with estimated rainfall and estimated PET. The calculation procedures of these indices were explained in Section 3.9, and the calculated indices for the Ribb catchment are shown in Table 5.10. This table shows the performance indices calculated separately for the total period as well as for seasons, for both calibration and validation periods.

Table 5.10 shows that the performances of the calibration period are consistency higher than those of the validation period for both models except the *RMSE* of the total period in the base model. This is consistent with the discussion in Section 5.3.1 and 5.3.2. It is also seen from this table that the performance of the model with estimated rainfall and estimated PET is consistency lower than that of the base model. Similarly it is seen that the wet period is modelled better than the dry period. These findings are consistent with the discussion in Sections 5.3.1 and 5.3.2.

Table 5.10 Performance indices of the estimated streamflow with catchment process modelling

		Model based on ground measured data		Model based on estimated rainfall and estimated PET	
Period	Index	Calibration	Validation	Calibration	Validation
Total period	E_f	0.83	0.78	0.77	0.61
	<i>RMSE</i> *	833	784	975	1536
Wet period	E_f	0.68	0.51	0.53	0.10
	<i>RMSE</i> *	1354	1783	1639	2437
Dry period	E_f	-0.03	-0.06	0.37	-0.31
	<i>RMSE</i> *	341	548	267	608

*units are in Ml/day

Figure 5.18 shows the flow duration curves of measured streamflow and estimated daily streamflow using the base model and model with estimated rainfall and estimated PET. This

figure shows that the high flows in estimated streamflow using the base model slightly overestimated (streamflows with an exceedance probability greater than 80%). The estimated daily streamflow using the model run with estimated rainfall and estimated PET shows underestimations for very low flows. Note the logarithmic scale of the y-axis of Figure 5.18.

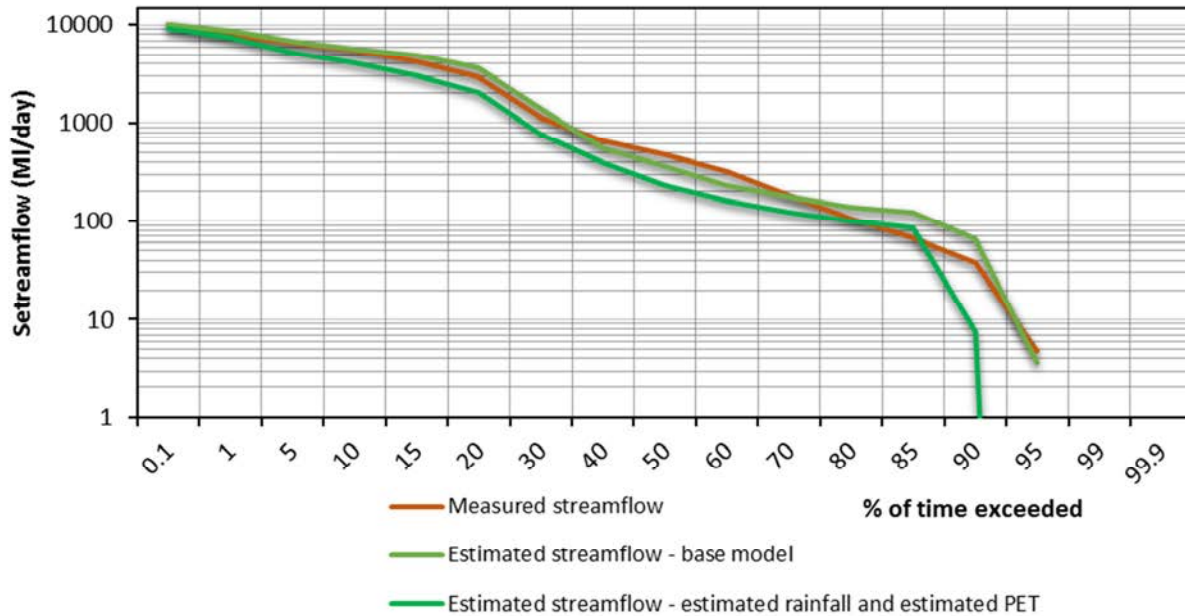


Figure 5.18 Flow duration curves of measured and estimated streamflows – Ribb catchment

5.4 Streamflow estimation using statistical modelling

This section discusses the behaviours of streamflow, vegetation indices and brightness temperature of the Ribb catchment. Then the discussion is focused on estimation of streamflow using artificial neural networks (ANN) (which is the statistical modelling technique used in this study).

Vegetation indices of Normalized Different Vegetation Index (*NDVI*), Normalized Difference Water Index (*NDWI*) and Enhanced Vegetation Index (*EVI*) were used as potential input variables, in developing the ANN models. The rationale behind the use of these variables was discussed in Sections 3.7.1 and 4.4.1. Current day seven lag days and 8-day average of these indices were considered as it was practised in the first case study area. The radiance-based brightness temperature of band 31 (*BT31*), band 32 (*BT32*), brightness temperature difference

(BT_{diff}) and brightness temperature gradient (BT_{grad}) were used as surrogate variables for rainfall in ANN modelling. Current day and three lag days of BT and thermal indices were also considered as potential inputs in statistical modelling. Partial Mutual Information (PMI) method which was explained in Section 3.8.1, and applied in the Macalister catchment to obtain influential input variables (Section 4.4.2) were also used in the Ribb catchment to obtain the influential input variables for the statistical modelling.

5.4.1 RS based input variables and streamflow

Before developing the ANN models, the 8-day average $NDVI$, 8-day average $NDWI$ and 8-day average EVI were carefully analysed to understand their behaviours in relation to streamflow of the Ribb catchment, and they are shown in Figure 5.19.

Figure 5.19 shows that the streamflow is in its peak during the period from June to October in each year. Monsoon rain occurs during this period. As can be seen from the figure, the peak flow could reach as high as 6000 MI/day. This figure also shows that all vegetation indices follow the same pattern. Vegetation indices show their lowest values during April and May. Water availability to vegetation during April and May is very low. The figure also shows that the Ribb River also records its minimum streamflow during this period. After May, the vegetation indices start to increase and peaks around August and September because of available water from monsoon rains. Then they gradually recede until early April/May next year. A clear lag between streamflow and $NDVI$ is shown in Figure 5.19 in the Ribb catchment. However, this lag is shorter than the lag observed in the Macalister catchment (Section 4.4.1). This could be because of the dominant agricultural crops (such as teff, maize and vegetables) and grasslands in the Ribb catchment that respond faster to rainfall than forest and bushes which are dominant LULC in the Macalister catchment.

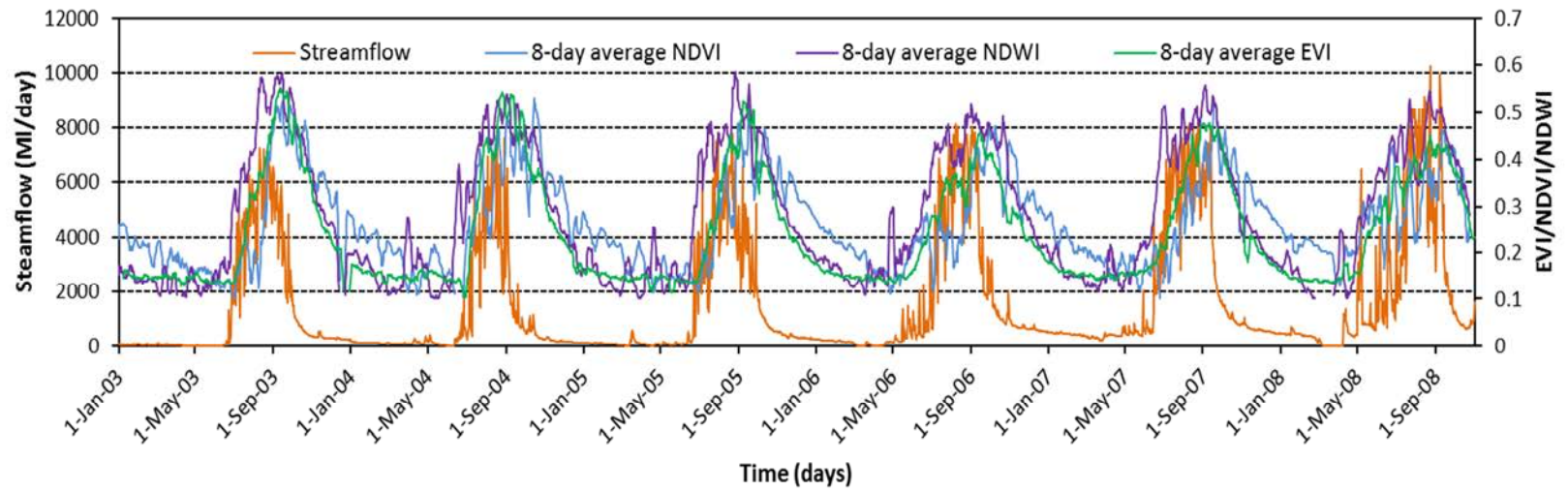


Figure 5.19 Streamflow and 8-day average of *EVI*, *NDWI* and *NDVI* in the Ribb catchment

Figure 5.19 shows that 8-day average $NDWI$ respond quicker to streamflow (i.e. rainfall) than the 8-day average $NDVI$ and 8-day average EVI . This shows the higher sensitivity of $NDWI$ to the soil moisture than EVI and $NDVI$.

Similar to the vegetation indices, the brightness temperature and its derivatives were analysed with respect to streamflow to examine the behaviours of these variables. The time series plot of streamflow and BT_{31} is shown in Figure 5.20. This figure shows BT_{31} is lower in the monsoon period compared to the non-monsoon period. August and September records the lowest brightness temperature over the catchment area. After September, the brightness temperature gradually increases until the April of next year, and then decreases until September. Even though, the wet season is the period of peak solar energy available to the catchment area, the monsoonal clouds which are rich with super cooled water/ice particles could reduce the brightness.

Similar to the brightness temperature, BT_{diff} (difference between brightness temperature of band 31 and band 32) was plotted with streamflow and is shown in Figure 5.21. The brightness temperature difference over the catchment shows a similar pattern to BT_{31} . The lowest BT_{diff} can be seen during the monsoon period with some noise in the data, while the highest BT_{diff} is seen before the monsoon starts. Furthermore, this figure shows that BT_{diff} highly fluctuates before the start of the monsoon period.

The time series plot of BT_{grad} and streamflow is shown in Figure 5.22. This figure shows that BT_{grad} is highly varying over time and in general BT_{grad} is higher before the start of the monsoon. Then it gradually reduces; however, remains highly variable.

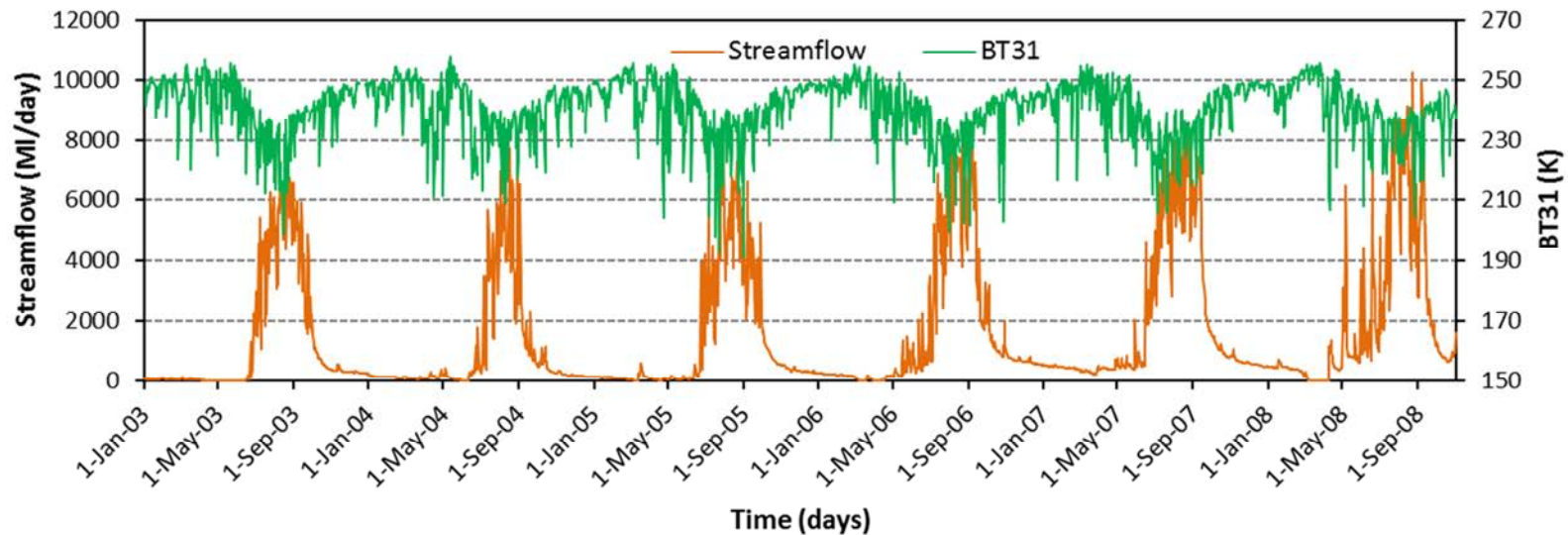


Figure 5.20 Streamflow and BT_{31} of MODIS in the Ribb catchment

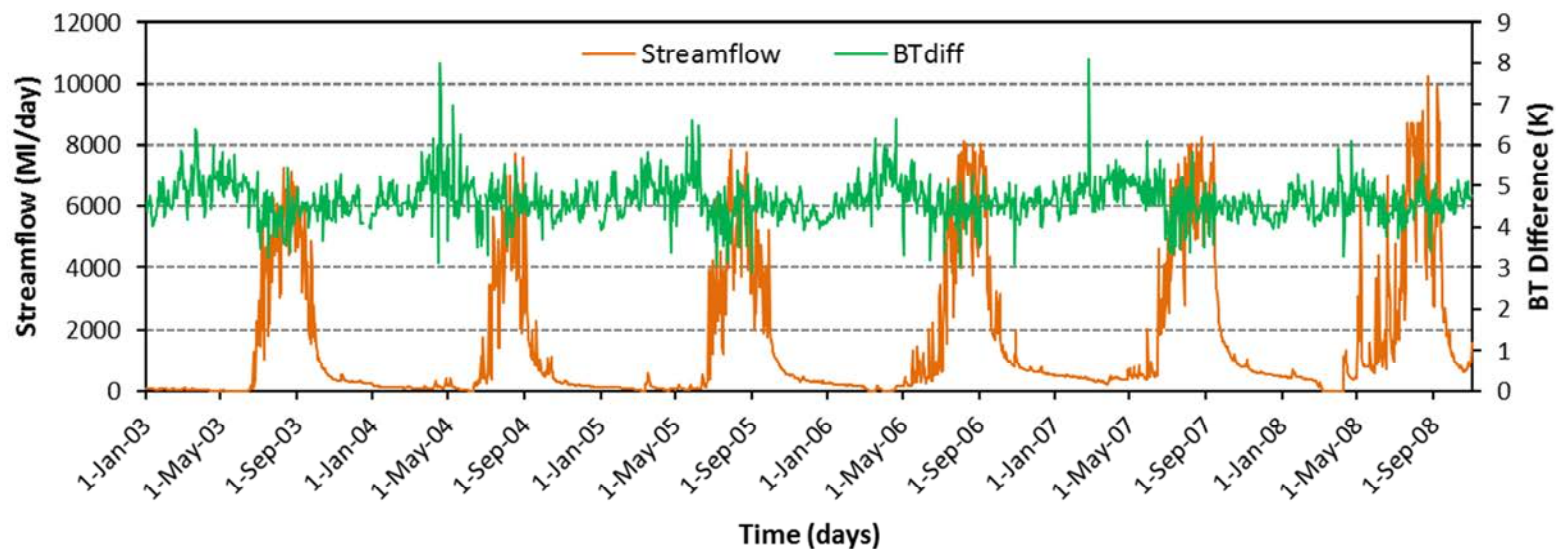


Figure 5.21 BT_{diff} and streamflow in the Ribb catchment

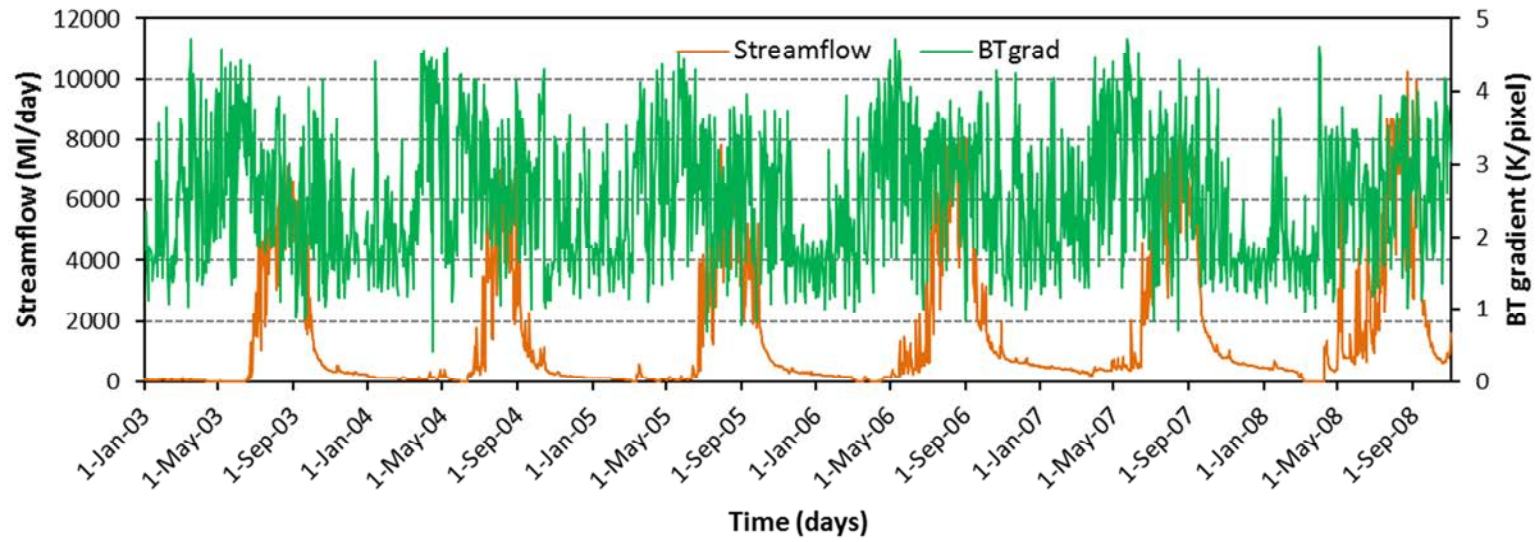


Figure 5.22 BT_{grad} and streamflow in the Ribb catchment

5.4.2 Determination of influential input variables

As was practised in the Macalister catchment, the PMI method was used to obtain the influential input variables for use in ANN modelling. Potential 43 input variables which were outlined in Tables 3.5 and 3.6. were used in this selection. The results of the PMI calculation are shown in Table 5.11. This table shows that only two variables (highlighted) out of 43, are significant in relation to streamflow in the Ribb catchment. They are the 8-day average *NDVI* and the 8-day average *NDWI*. Therefore, these two variables were used as input variables for ANN modelling of the Ribb catchment.

Table 5.11 PMI results of input variables

Potential input variable	PMI	99 th percentile
<i>NDVI</i>	0.0963	0.1931
1-day lag <i>NDVI</i>	0.0647	0.3398
2-day lag <i>NDVI</i>	0.0971	0.1473
3-day lag <i>NDVI</i>	0.1034	0.1952
4-day lag <i>NDVI</i>	0.0755	0.2047
5-day lag <i>NDVI</i>	0.0825	0.1928
6-day lag <i>NDVI</i>	0.0570	0.2797
7-day lag <i>NDVI</i>	0.0820	0.1811
8-day avg <i>NDVI</i>	0.2322	0.1680
<i>NDWI</i>	0.0771	0.3349
1-day lag <i>NDWI</i>	0.0577	0.2813
2-day lag <i>NDWI</i>	0.0492	0.2949
3-day lag <i>NDWI</i>	0.0448	0.2795
4-day lag <i>NDWI</i>	0.0588	0.3560
5-day lag <i>NDWI</i>	0.0587	0.2795
6-day lag <i>NDWI</i>	0.0376	0.1798
7-day lag <i>NDWI</i>	0.0404	0.2879
8-day avg <i>NDWI</i>	0.3477	0.1999
<i>EVI</i>	0.0885	0.1433
1-day lag <i>EVI</i>	0.0782	0.3194
2-day lag <i>EVI</i>	0.0692	0.2067
3-day lag <i>EVI</i>	0.0621	0.1958
4-day lag <i>EVI</i>	0.0772	0.3492
5-day lag <i>EVI</i>	0.0641	0.3631
6-day lag <i>EVI</i>	0.0840	0.2043
7-day lag <i>EVI</i>	0.0509	0.2902
8-day avg <i>EVI</i>	0.2673	0.3357

Table 5.11 Continuation...

<i>BT31</i>	0.0291	0.2732
1-day lag <i>BT31</i>	0.0295	0.1120
2-day lag <i>BT31</i>	0.0164	0.2443
3-day lag <i>BT31</i>	0.0171	0.2108
<i>BT32</i>	0.0281	0.0877
1-day lag <i>BT32</i>	0.0202	0.2671
2-day lag <i>BT32</i>	0.0327	0.1170
3-day lag <i>BT32</i>	0.0337	0.0901
<i>BT_{diff}</i>	0.0151	0.1915
1-day lag <i>BT_{diff}</i>	0.0187	0.0984
2-day lag <i>BT_{diff}</i>	0.0143	0.2026
3-day lag <i>BT_{diff}</i>	0.0127	0.1046
<i>BT_{grad}</i>	0.0111	0.1105
1-day lag <i>BT_{grad}</i>	0.0177	0.1042
2-day lag <i>BT_{grad}</i>	0.0192	0.0930
3-day lag <i>BT_{grad}</i>	0.0047	0.3861

5.4.3 Artificial Neural Networks modelling

The significant input variables (i.e. 8-day average *NDVI* and the 8-day average *NDWI*) which were obtained from the Partial Mutual Information analysis (Section 5.4.2) were used as input variables to estimate daily streamflow with ANN modelling for the Ribb catchment. The ANN modelling in the Macalister catchment (Section 4.4.3) showed that seasonal models performed better than the model of total period. There are no four distinguishable seasons in the Ribb catchment as explained in Section 5.2.1, but two seasons with respect to rain availability. These two seasons (i.e. wet and dry) were considered for building the ANN models in the Ribb catchment. The same procedure which was explained in Section 3.8.2 was followed for building these models. Similar to catchment process modelling, the period from 2003 to 2006 was considered as the calibration period, while years 2007 and 2008 were considered as the validation period.

5.4.3.1 Streamflow estimation with seasonal ANN models

The ANN models were built using a trial and error calibration method by systematically changing the number of hidden neurons. This trial and error calibration method revealed that the best results can be obtained with 8 hidden neurons for both wet and dry season ANN

models. The results of seasonal ANN modelling in the Ribb catchment are shown in Figure 5.23 as scatter plots. This figure shows the calibration and validation periods separately for each season with their coefficients of determination.

Figure 5.23 shows that seasonal ANN models estimate streamflow moderately well in the calibration period with respect to the coefficients of determination. The wet season model shows higher coefficient of determination in both calibration and validation. However, high flows (>6000 MI/day) are underestimated in both calibration and validation periods. This shows that the model is not sensitive to the higher flows during the wet season. The reason for not capturing these high flows during the wet season well in the ANN model could be the less high flows used in the calibration of the model.

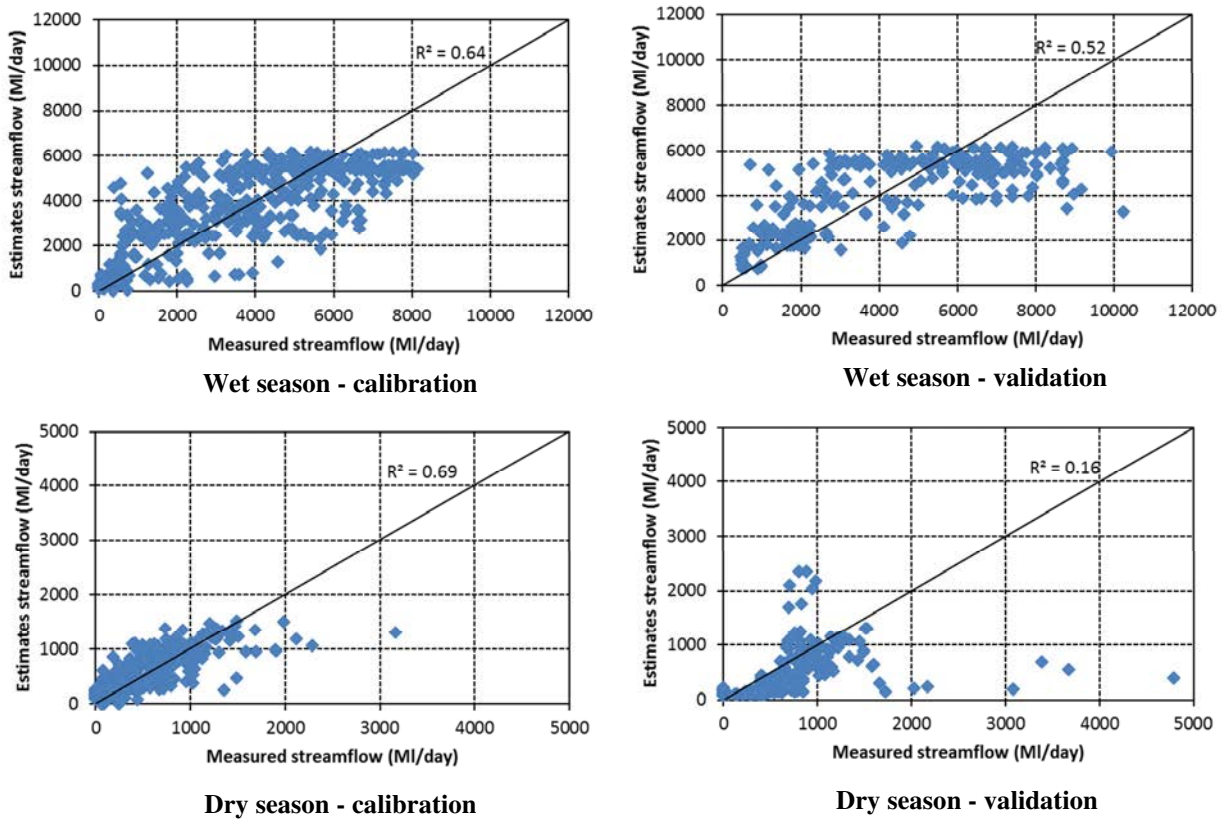


Figure 5.23 Scatter plots of the measured and estimated streamflows – Ribb catchment

The result of the dry season shows that streamflow in the calibration period is estimated slightly better than the calibration period of wet season. However, streamflow of dry season in validation period is poorly estimated. It also shows that higher flows in the dry season are underestimated both calibration and validation periods.

To facilitate the calculation of performances indices and comparison, the results of the two seasonal models were combined to have a single time series, and this time series is shown in Figure 5.24. Scatter plots of these time series data separately for the calibration and validation periods are shown in Figure 5.25. Figure 5.24 reveals that estimated streamflow match well with the measured streamflow during its calibration period, and high flows are highly underestimated during both calibration and validation periods. This is also seen in Figure 5.25.

Similar to Figure 4.40 in the Macalister catchment, a flow duration curve was drawn using the streamflow data obtained from the seasonal model of the Ribb catchment for the period of 2003 to 2008, and is shown in Figure 5.26. Note that the streamflow axis in Figure 5.26 is in logarithmic scale. This figure shows that the estimated streamflow matches well with measured streamflow, especially when the flow exceedance is less than 70%, and higher than 10%. This figure also shows that the estimated streamflow of exceedance level is more than 70% is overestimated, and the streamflow with exceedance level less than 10% is underestimated.

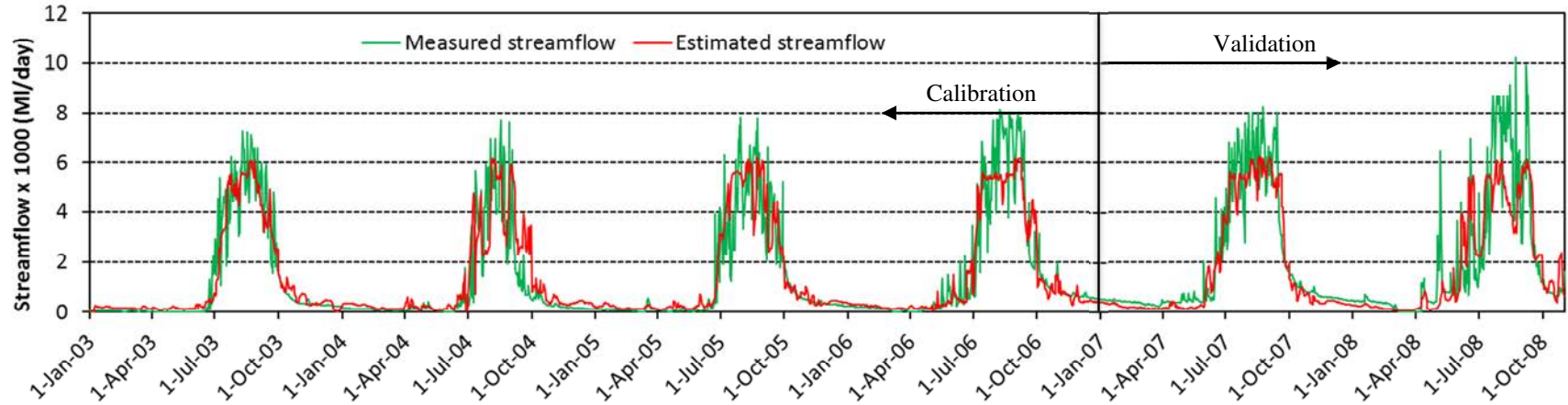


Figure 5.24 Estimated (combined) and measured streamflows with their calibration and validation periods – the Ribb catchment

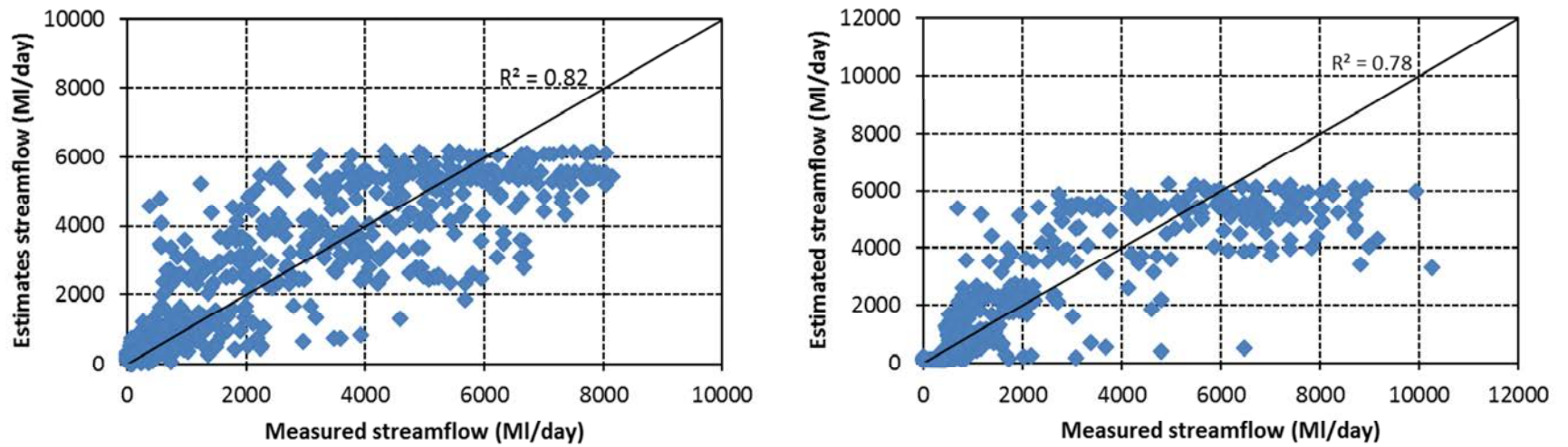


Figure 5.25 Scatter plots of the measured streamflow and estimated streamflow – Ribb catchment

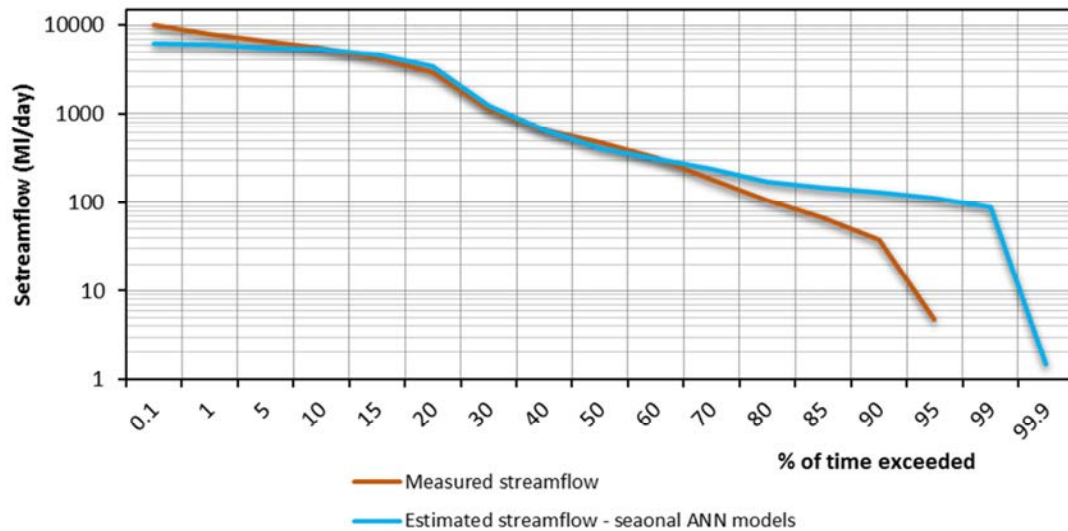


Figure 5.26 Flow duration curve of the seasonal ANN models

5.4.3.2 Performances of ANN based streamflow estimation

The models performances were evaluated in this study using Root Mean Square Error ($RMSE$) and Nash-Sutcliffe efficiency (E_f) and the results are shown in Table 5.12. The table shows that the performance of both calibration and validation period is better in the wet season than in the dry season in terms of E_f . Furthermore, the performances of calibration during the dry season is much better than that of the validation period. Both wet and dry seasonal model outcomes were combined to have a time series of the total period, and the performance indices were also calculated for the total period time series, which are shown in Table 5.12. The table shows, that E_f of both calibration and validation periods are very high for the total period.

Table 5.12 Performance indices of the estimated streamflow using ANN models – Ribb catchments

Estimation type		$RMSE$ (MI/day)	E_f
Wet	<i>Calibration</i>	1447	0.62
	<i>Validation</i>	1823	0.50
Dry	<i>Calibration</i>	199	0.64
	<i>Validation</i>	548	-0.15
Total period	<i>Calibration</i>	868	0.81
	<i>Validation</i>	1101	0.79

5.5 Comparison of results from catchment process modelling and statistical modelling

Figure 5.27 (redrawn using Figures 5.18 and 5.26) shows the flow duration curves (FDCs) of both catchment process modelling (i.e. the base model and the model with Estimated rainfall and estimated PET) and statistical modelling (i.e. seasonal ANN models), and measured streamflow. The figure shows that the base model is the closest to measured streamflow, and then estimated streamflow using estimated rainfall and estimated PET. Estimated streamflow using ANN models shows the most underestimation and overestimations. This figure shows that high flows estimated using the seasonal ANN models has slightly underestimated compared to estimated streamflow using estimated rainfall and estimated PET. With increasing percentage of exceed time, the seasonal ANN model estimates show an improvement. According to this figure, the estimated streamflow using seasonal ANN models shows almost same result of estimated streamflow using ground measured data. All models deviate from the measured streamflow with respect to very low flows (note the logarithmic scale of y-axis and the deviation is highest with seasonal ANN modelling).

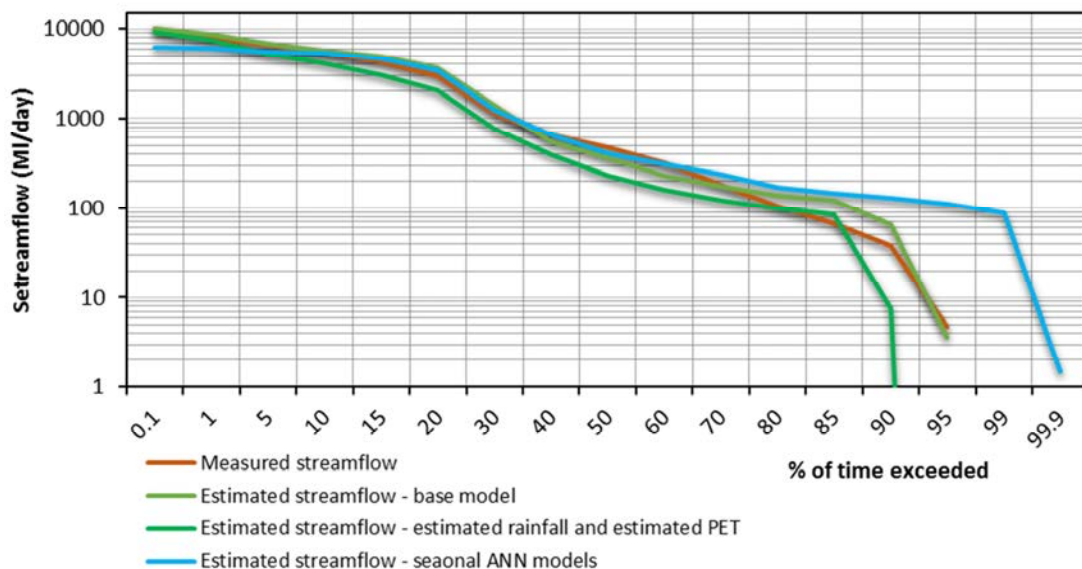


Figure 5.27 FDCs of catchment process models and statistical model

Table 5.13 is a combination of Tables 5.10 and 5.12 for the purpose of comparison. This table shows that the performance of seasonal ANN model is as good as base model. However, validation period of the dry season is poorly estimated by all models.

Table 5.13 Performance indices of all the models

		Model based on ground measured data (base model)		Model based on estimated rainfall and estimated PET		Model based on seasonal ANN	
Period	Index	Calibration	Validation	Calibration	Validation	Calibration	Validation
Total period	E_f	0.83	0.78	0.77	0.61	0.81	0.79
	$RMSE^*$	833	784	975	1536	868	1101
Wet period	E_f	0.68	0.51	0.53	0.1	0.62	0.50
	$RMSE^*$	1354	1783	1639	2437	1447	1823
Dry period	E_f	-0.03	-0.06	0.37	-0.31	0.64	-0.15
	$RMSE^*$	341	548	267	608	199	548

5.6 Summary

This chapter discussed the results obtained in the second case study i.e. the Ribb catchment. Both catchment process modelling and statistical modelling were used to estimate daily streamflow using the methods followed in the first case study. Period of 2003 to 2008 were also considered in the second case study to maintain the consistency with the first case study. The period of 2003 to 2006 were considered as the calibration period while 2007 to 2008 were considered as the validation period in both modelling processes.

Before commencing daily streamflow estimation, rainfall and PET data were estimated using RS data. Almost similar level of accuracy as of rainfall estimation in the Macalister catchment was obtained in the Ribb catchment. Estimated PET using RS data showed a slight overestimation on non-cloudy days, while slight underestimation on cloudy days. In addition, LULC of the Ribb catchment was also derived using a RS image over the second case study area. The results of LULC classification showed that the individual LULC class accuracy is satisfy the accuracy thresholds available in the literature.

Estimated rainfall and PET, and classified LULC were then used to estimate daily streamflow of the Ribb catchment with the catchment process model. The SWAT model

(which was used as catchment process model in the Macalister catchment) was also used in this catchment. Before estimating streamflow using estimated rainfall and estimated PET, a base model was developed to obtain best calibration parameters on the Ribb catchment with limited ground measured data. Then these parameters were used with estimated rainfall and estimated PET to estimate daily streamflow in the Ribb catchment. The results revealed that the base model performed better than the model with estimated rainfall and estimated PET.

RS based vegetation and thermal indices, and BT were calculated for the Ribb catchment, same as it was done in the Macalister catchment. Current day, seven lag days and 8-day average of indices were considered from vegetation indices, while current day and 3 lag days were considered from BT and thermal indices. Partial Mutual Information method was used in this study area as well to obtain influential variables. The influential variables (i.e. 8-day average *NDVI* and 8-day average *NDWI*) were then used as input variables to ANN modelling. The seasonal ANN models were developed for the second case study, since the seasonal ANN models showed the best results with statistical modelling in the Macalister catchment.

The comparison of catchment process modelling and statistical modelling results showed that seasonal ANN models are as good as catchment process model, in fact equal performance with model based on ground measured data. This is a significant achievement in daily streamflow estimation with available limited ground measured streamflow data.

CHAPTER 6: SUMMARY, CONCLUSIONS AND RECOMMENDATIONS

6.1 Summary

The aim of this study was to investigate the use of Remote Sensing (RS) data to estimate daily streamflow, especially when ground measured data are scarce. This study was carried out in two different catchments. They are the Macalister catchment in Victoria - Australia and the Ribb catchment in Ethiopia. The Macalister catchment had sufficient ground measured data, such as rainfall, air temperature, wind speed and sunshine hours to estimate streamflow, while the Ribb catchment had least ground measured data to analyse the performance of estimates. Catchment process modelling and statistical modelling were used with input variables computed using RS data, to estimate daily streamflows in both catchments.

The Soil and Water Assessment Tool (SWAT) was used as the catchment process model in this study. SWAT is a semi-deterministic hydrological model. It uses ground measured meteorological data such as rainfall, surface temperature, relative humidity and wind speed. SWAT has the power to fill the gaps of meteorological variables caused by missing data and interpolate data through its in-built weather generator despite model and data uncertainties.

Model uncertainties are common in hydrological modelling. SWAT was selected in this study to estimate streamflows as it supports the remote sensing based variables (e.g. rainfall, potential evapotranspiration and landuse/landcover) on grid scales as input to SWAT. In addition, the in-built weather generator of SWAT is an added advantage that can immensely benefit the data scarce catchments. All standard procedures were taken in to account while calibrating the SWAT model for both catchments to reduce the model parameter uncertainties. This was carefully done with the assistance of existing literature. The manual calibration approach was first used to calibrate the most sensitive model parameters, and then the auto-calibration was used to fine-tune the manually calibrated parameters. This procedure helps to reduce model uncertainty. Data uncertainty arises from inadequate gauging stations especially in data-poor catchments. In addition, equipment calibration issues/sensor malfunctioning for the existing gauge locations can

hinder the quality of data that had been collected. The data uncertainty affects the model parameter uncertainty, since the model parameters are determined using the available data. Data uncertainty was minimized by quality checking of data before they were used in modelling.

Daily rainfall and potential evapotranspiration were estimated with RS data in this study to run SWAT models of the two catchments. In addition to these two variables, landuse/landcover (LULC) of both catchments were classified using RS data.

The Artificial Neural Networks (ANN) modelling technique was used as the statistical modelling tool in this study. The vegetation and thermal indices together with brightness temperature (BT) computed from RS data were used as inputs in this study. These indices were especially selected as they can be treated as surrogates for meteorological variables that are responsible for streamflow generation. The summary and conclusions related to the estimation of input variables (for both catchment process modelling and statistical modelling), and the estimation of daily streamflow resulting from catchment process modelling and ANN modelling are briefly presented in following sections, followed by recommendations for future work.

6.1.1 Catchment process modelling using remote sensing data

Rainfall and potential evapotranspiration were estimated, and LULC were classified using RS data as inputs to catchment process modelling in both catchments. They were then used with the SWAT models to estimate streamflows in both catchments.

6.1.1.1 Rainfall estimation using remote sensing data

Although the Tropical Rainfall Measuring Mission (TRMM) rainfall data (3B42) are available at a global scale at finer (3 hours) temporal resolution, their spatial resolution is coarse (approximately 625 km²), and do not represent the heterogeneity of rainfall in small and medium scale catchments. However, the MODIS BT, which can be used as surrogate for rainfall, is available at finer spatial resolution (approximately 1 km²), but has a coarser temporal resolution (1 day). Therefore, the TRMM rainfall data and the BT of band 31 were combined in this study to estimate daily rainfall data with a spatial resolution of 1 km².

All non-cloudy images were considered to represent no-rain, and therefore all cloudy images of MODIS were considered in the rainfall estimation. However, all clouds do not yield rain. A cloud mask based on the BT difference was used in the initial separation of rain/no-rain clouds. Brightness temperatures of band 27, 31 and 32 were used in this masking process. All of the images passed on these cloud masks were further refined using a BT threshold, since warm clouds do not yield rain.

Three thresholds were tested in identifying rain making clouds. The thresholds were the BT of 235 K (traditional threshold), the mean seasonal BT, and the mean monthly BT. The results showed that the mean seasonal threshold captured rain producing clouds better than the other two thresholds. The BT difference with respect to the mean seasonal threshold and TRMM rainfall data were combined through their cumulative gamma distribution functions to estimate high spatial daily rainfall.

The Macalister catchment receives rainfall throughout the year, with winter and spring being the wettest periods. It was found that these two wet seasons were marginally underestimated in the rainfall estimation using RS data. Compared to these wet seasons, the dry seasons (i.e. summer and autumn) showed a mixed result. The majority of the estimated rainfall during summer showed both over- and under-estimation, while the majority of the estimated rainfall during autumn was overestimated.

In contrast to the four seasons of the Macalister catchment, the Ribb catchment is characterised by two strong seasons (i.e. the wet season – monsoon period and the dry season – non-monsoon period). The same procedure that was applied to the Macalister catchment was used to estimate rainfall in the Ribb catchment. The results showed that the estimated rainfall was slightly underestimated during the wet season, but yielded a mixed result during the dry season.

The performance analysis showed that the method used in this study to estimate rainfall using RS data has worked well for both catchments. However, the Macalister catchment shows a slightly better performance than the Ribb catchment in daily rainfall estimation via high spatial resolution data.

6.1.1.2 Estimation of potential evapotranspiration using remote sensing data

In the absence of ground measured data, RS data and globally available climate datasets were used in this study to estimate daily PET (estimated PET). These data were used to calculate the available energy for latent heat, which was used to convert liquid water to water vapour. On that basis, the surface energy balance method was modified to estimate PET over both catchments. The PET estimates computed from RS data were compared against the Penman-Monteith (PM) estimates for both catchments to assess the accuracy of the PET estimates computed from RS data. The PM method is still the most widely accepted method to produce the best estimates of PET especially in the absence of direct measurements of PET.

Surface albedo is a significant variable in PET estimation since it determines the amount of net energy available to PET, and it accounts for spatially and temporally non-uniform LULC in the catchment. The two way surface albedo estimation procedure was used in this study to compute surface albedo with RS data on non-cloudy days. The estimated surface albedo values for a given LULC class were compared with the corresponding surface albedo values used in the PM method to estimate PET, which were obtained from the literature. The results in both catchments showed that the mean value of surface albedo computed from RS data matched well with the literature values in the majority of LULC classes. Furthermore, the results showed that the range of surface albedo computed from RS data was significantly larger. However, the standard deviation of the surface albedo computed from RS data was very small; thus the effect of extreme values of surface albedo on PET estimation was negligible.

The PET estimation was done separately for non-cloudy and cloudy days. The estimated PET and PM based PET were compared at selected locations that have different LULC. The overall agreement between estimated PET and PM based PET was higher in the total period of non-cloudy days. This was common for both catchments in all LULC classes. The nearest non-cloudy day surface albedo values were used to estimate PET on cloudy days in both catchments, since surface albedo was able to be computed only for non-cloudy days. The estimated PET data on cloudy days showed an overestimation in the Macalister catchment. This was mostly due to localized issues such as haze not being accounted for with the RS based method. Meanwhile, the estimated PET data of the Ribb

catchment on cloudy days were mostly underestimated. Extreme PET values during cloudy days were always underestimated in both catchments, as a result of not accounting for the advection effect in the RS based method. However, these differences were within the accepted range. The results show that the methodology used in this study worked very well in estimating PET on non-cloudy days and reasonably well on cloudy days.

The seasonal comparison of estimated PET results did not vary much in the Ribb catchment irrespective of cloudiness; however they produced mixed results in the Macalister catchment. More localized climatological conditions (inherent to the seasons of winter and spring in the Macalister catchment) such as haze and heat waves could have reduced the accuracy of the estimated PET data compared to the Ribb catchment. However, the seasonal results of the non-cloudy days were strong in both catchments. Furthermore, the highest accuracy was noted during the vegetation season (spring in the Macalister catchment and wet in the Ribb catchment). The vegetative seasons in both catchments were relatively free from extreme climate events, producing high accuracy in PET estimates computed from RS data, and were comparable to PM based estimates.

The results also revealed that the estimated PET data agreed well with the PM based PET estimates within the range of 3.0 to 6.5 mmday^{-1} for both catchments. It was also noted in the literature that the PM based PET tends to overestimate low PET values (on cooler days). The PET estimates computed from RS data on cooler non-cloudy days in the Macalister catchment showed a lower value than the PM based PET estimates, which could be an indication that the RS based PET estimation method had produced more accurate PET values.

6.1.1.3 Landuse/landcover classification using remote sensing data

Since RS data provide rapid and continuous temporal and spatial information of the land surface, they were used in this study to develop the LULC maps that can be used in catchment process modelling, and various other applications.

A Landsat 5 TM image and a Landsat 7 ETM+ image were used to classify LULC in the Macalister catchment and the Ribb catchment respectively. The Principal Component Analysis (PCA) was used in pre-image processing together with the Normalized

Difference Vegetation Index, (*NDVI*) to prepare the final images for classification purposes. The supervised classification approach was used in image classification, with the maximum likelihood method as classifier.

Separate ground-truth data collection surveys were conducted for each catchment to identify existing LULC class signatures. Each catchment was found to be unique in terms of LULC and weather patterns. The Macalister catchment is dominant with forest classes, while the remaining areas are mainly pasture and grasslands. These are permanent LULC classes. Though the biomass amount of grasslands and pasture changes according to seasonal effects, their extent in the catchment remains constant over time. Compared to the Macalister catchment, the Ribb catchment is dominated by cultivation lands. As a result, the vegetation cover in the Ribb catchment changes significantly over the seasons. The wet season (monsoon) is the main cropping season; thus the entire catchment is fully covered during the wet season with agricultural crops (in the lower and middle parts of the catchment) and natural vegetation (mainly in the upper part of the catchment).

The first half of the collected ground-truth data was used in image training and the remaining half was used in classification accuracy assessment. Both descriptive (user's accuracy, producer's accuracy and overall accuracy) and analytical (kappa statistics) techniques were used to assess the accuracy of classified LULC. The results of both catchments showed that the individual classification accuracy was better in terms of the threshold used in this study for almost all LULC classes. The overall classification accuracy of the LULC classification was also at a satisfactory level. The calculated kappa statistics also showed higher level of accuracy in the classified maps. The accuracy estimation of LULC classification showed that the methodology used in this study in classifying LULC worked well for both catchments, although each catchment had different LULC classes.

6.1.1.4 Catchment process modelling

The SWAT was used as a catchment process modelling tool to estimate daily streamflow. Initially, ground measured data (such as rainfall and air temperature) were used to calibrate the model. Other than meteorological data, the Digital Elevation Model, the FAO-soil map, and classified LULC information were used in calibrating this model. Initially the

model was manually calibrated. Thereafter, this manually calibrated model was auto-calibrated for fine tuning. The calibrated model was considered as the base model. Three further SWAT models were considered by replacing ground measured data with corresponding data computed from RS. The calibrated model parameters of the base model were used in these three models. The three models were:

- (1) PET which was derived by the SWAT model using ground measured data, was replaced with estimated PET data, while keeping ground measured rainfall data unchanged in the model.
- (2) Ground measured rainfall data were replaced with estimated rainfall, while keeping SWAT derived PET unchanged.
- (3) Both ground measured rainfall and SWAT derived PET were replaced with estimated rainfall and estimated PET.

From the four models (including the base model), it was found that the base model performed better than the rest of the models in daily streamflow estimation. The seasonal analysis of the results (of the base model) showed that estimated daily streamflow has been accurately estimated during the winter and spring seasons in the Macalister catchment and the wet season in the Ribb catchment, but has been underestimated during extreme events in both catchments. Moreover, estimated daily streamflow during summer and autumn has been overestimated.

It was further observed that streamflow estimation in the Macalister catchment remained largely unchanged when the SWAT model derived PET was replaced with estimated PET. However, the model run with estimated rainfall and estimated PET led to a significant change in estimated streamflow in comparison to measured streamflow. The calculated performance indices revealed that performance was significantly reduced from the base model to the model with estimated rainfall and SWAT derived PET. Similar results were observed with the model run with estimated rainfall and estimated PET. This model run yielded the poorest performance in all three options that aimed to estimate streamflow through the use of estimated rainfall and estimated PET.

For the Ribb catchment, a base model, which was developed with existing limited ground measured data, provided the calibrated model parameters. The results showed a very high

performance in the base model for the total period. The seasonal analysis of the results indicated that estimated streamflow was accurately estimated during the wet season, but was underestimated during extreme events. Estimated daily streamflow during the dry season was overestimated. These results are identical to the results of the Macalister catchment for the base model.

The calibrated model parameters of the Ribb catchment were then used with estimated rainfall and estimated PET to estimate streamflow. Intermediate models (the first two models of the previously mentioned models) were not considered in the case of the Ribb catchment, since the results of the intermediate models in the Macalister catchment were found to be identical to the base model and the model with estimated rainfall and estimated PET. The base model showed the best performance in the Ribb catchment also.

Estimated daily streamflow using the above mentioned model options were compared using the Flow Duration Curves (FDC) in both catchments, other than performance indices. In the Macalister catchment, it was found that extreme flows such as the percentage of exceedance less than 1 %, were underestimated by the model with estimated rainfall. This was mainly due to the fact that estimated rainfall figures failed to reflect extreme rainfall events properly. On other side of the FDCs, it was found that streamflow, which percentage of time exceeds more than 50 was overestimated with estimated rainfall. This observation was common in the case of the base model which was developed to calibrate model parameters. Compared to the Macalister catchment FDCs, the Ribb catchment FDCs showed a continuous underestimation of daily streamflow after 5 % of exceedance level. However, this underestimation was less when compared to the underestimation of the Macalister catchment.

6.1.2 Statistical modelling using remote sensing data

As mentioned in Section 6.1, the artificial neural networks (ANN) model was used as a statistical modelling tool. RS based vegetation and thermal indices, and BT were considered as inputs for this modelling approach.

6.1.2.1 Calculation of vegetation and thermal indices

Both RS based vegetation, thermal indices, and BT were considered as input variables in the statistical modelling approach to estimate daily streamflow. The Normalized Difference Vegetation Index (*NDVI*), the Normalized Difference Water Index (*NDWI*) and the Enhanced Vegetation Index (*EVI*) were used as vegetation indices and brightness temperature difference (*BT_{diff}*) and brightness temperature gradient (*BT_{grad}*) were used as thermal indices. In addition to those, brightness temperatures of band 31 (*BT31*) and band 32 (*BT32*) were also considered as potential input variables. These variables were selected because they represent some features of hydrometeorological variables that contribute to generating streamflow. The vegetation based indices were calculated only for non-cloudy days (since cloud cover arrests ground features fully or partially while stopping light penetration through clouds), while thermal based indices were calculated only for cloudy days (since radiance data were only used to capture cloud features in this section of the study).

Since meteorological variables have a lag effect on streamflow, a lag time of up to 7 days was introduced to vegetation indices, and a lag time of up to 3 days was introduced to thermal indices. A lengthier lag time was catered for in vegetation indices than in thermal indices because vegetation has longer response on streamflow. In addition to those, 8-day averages of vegetation indices were used in this modelling to cover all the gaps in vegetation indices arising from cloud cover.

6.1.2.2 Determination of influential input variables

After considering current day, lagged days and average days, there were 43 potential input variables for statistical modelling. As mentioned earlier in Section 3.8.1, several issues, such as data redundancy, replication and complex model structure can potentially arise with an increased number of input variables. In that regard, it is crucial to accurately identify the influential input variables for streamflow estimation using statistical modelling. In this study, such an identification process was undertaken through the Partial Mutual Information (PMI) method. This method generated seventeen influential variables and two influential variables for the Macalister catchment and the Ribb catchment respectively.

6.1.2.3 Artificial Neural Networks modelling

All seventeen influential variables were used as input variables for daily streamflow estimation with ANN modelling in the Macalister catchment. The use of an adequate number of hidden neurons is of utmost importance in ANN modelling, since too many neurons can cause their weight to control the model, while too few neurons can reduce the effect of input variables on outputs. Therefore, the trial and error calibration method was used in this study to find out the best number of hidden neurons. Performance indices were used to evaluate results in the trial and error calibration method. Accordingly, the model with 26 hidden neurons yielded the best results. These results were compared with measured streamflow data of the Macalister catchment. The dissimilarity between estimated and measured streamflow indicated that the model was not effective when applied singlehandedly for all seasons. Therefore, a separate model for each season was derived using the trial and error calibration method. The best results were obtained with models adopting 13, 24, 18 and 24 hidden neurons for summer, autumn, winter, and spring respectively.

After combining the results of the seasonal models into a total time series, a higher performance of the model was noted in the Macalister catchment. This approach (i.e. seasonal ANN modelling) was replicated to the Ribb catchment by using the two influential variables that resulted from the PMI method. It was found that 8 neurons gave the best performance for both the wet and dry seasons.

6.1.3 Comparison of catchment process modelling and statistical modelling

The results of catchment process modelling were compared with those of ANN modelling for the base models, the model run with RS based inputs and the ANN model (seasonal-combined). Visual comparison was done with flow duration curves, while more analytical comparison was carried out with performance indices. Such a comparison revealed that the base model yielded the best estimates in both catchments. On the other hand, ANN modelling provided better results than catchment process modelling with RS based variables.

6.2 Conclusions

The following conclusions were drawn from this study:

- The proposed methodology to separate rain clouds from no-rain clouds and rainy clouds from rain clouds work well in identifying the majority of rainy clouds.
- The combined use of the TRMM rainfall data and MODIS BT data in generating daily rainfall data via a higher spatial resolution worked reasonably well for both catchments. Majority (80%) of the mismatches in rainfall estimation are less than 2 mm, which means almost all large rainfall events were correctly captured and well estimated. This methodology is particularly suited for estimating rainfall for small and medium scale catchments.
- The surface albedo computed from RS data compared well with the literature values. The RS data give albedo values on grid basis and results revealed that mean value of grids slightly vary, but standard deviation of surface albedo estimated using RS data over uniform LULC is less than 0.1.
- The method used to estimate PET with RS data produced comparable results to the Penman-Monteith based PET, especially for non-cloudy days using the computed surface albedo (of non-cloudy days). The nearest non-cloudy day surface albedo values were used for cloudy days, and they were used with RS data to estimate PET for cloudy days, and they produced reasonable agreement with the Penman-Monteith based PET. The accuracy of PET estimated using RS data for both cloudy and non-cloudy days is within the acceptable range of accuracy (10-40%).
- The methodology used to classify LULC had given sufficient accuracy in individual and overall (of the order of 81%) classification accuracies. Higher kappa coefficient (of the order of 0.77) shows that the LULC classifications are reliable. Thus, this methodology can be used for further applications such as catchment modelling.
- Catchment process modelling showed that the base model which used ground measured rainfall and SWAT model derived PET data performed the best. The performance of catchment models with rainfall and PET computed from RS data was not as good as that of the base model. The catchment model performance with either the SWAT model derived PET using ground measured metrological data or PET estimated from RS data produced similar results in streamflow estimation.

- Replacing ground measured rainfall with rainfall computed from RS data in the catchment process models had a significant effect on the streamflow estimation in both catchments. Streamflows of the wet season were modelled better than those of the dry season.
- The vegetation indices, thermal indices and BT strongly followed the seasonal changes of both catchments.
- The PMI method showed that many vegetation and thermal variables (altogether 17 variables) were influential to streamflow when seasonality is strong. The same method showed that the average of a few vegetation variables (2) were influential when wetness and dryness are strong.
- The ANN modelling revealed that a single non-seasonal model did not sufficiently address the variability of streamflow estimation. However, the seasonal ANN models with the same inputs produced better streamflow estimates.
- A comparison of the results of catchment process modelling and statistical modelling showed that extreme events (such as those having a probability of occurrence less than 1%) were underestimated under both approaches. In addition, low flows were overestimated.
- The streamflow estimates of ANN modelling were as good as the results of the base model (with ground measured rainfall and SWAT model derived PET). Therefore it can be said that ANN modelling had produced better streamflow estimates than catchment process modelling with RS data.

6.3 Limitations and directions for future research

Based on the methodologies and the findings of this study, several limitations were identified. Since these limitations serve as opportunities for future research, a few recommendations for future research are set out in the last paragraph.

The major limitation of streamflow estimation using RS data is the need for a few ground measured data to calibrate both catchment process models and statistical models. Statistical modelling needs only streamflow data; however, the catchment process modelling approach needs streamflow data as well as some meteorological data.

The processing and calculations of this study (i.e. image processing, estimation of rainfall and PET, index calculation) need high level of skills and computer power, which prohibit the use of this method of streamflow estimation by general hydrologists and engineers.

Rainfall, excess moisture, cloud shadow and haze could in reality change the surface albedo during cloudy days, and their effect on PET during cloudy days was not accounted for in this study. In addition, the estimation of cloud cover during cloudy days was difficult (especially during winter in the Macalister catchment), and as such introduced further differences between RS based PET estimates on cloudy days and the PM based PET estimates. Moreover, localized ground conditions such as haze and small clouds could not be recognized because of the cloud mask employed and because of the medium spatial resolution of the RS data used in this study.

In summary, an investigation of the use of microwave data (that has the ability to penetrate clouds to a certain level) to estimate PET is recommended, and then the use of this PET for streamflow estimation with catchment process modelling. It is further recommended to investigate sub-daily rainfall estimation using TRMM rainfall data and IGGC thermal data which is available on an hourly basis. This sub-daily estimates may have a better representation to the temporal variation rainfall, and it could thus improve the accuracy of streamflow estimation. Additionally, since statistical modelling was found to yield promising results, it is also worth investigating how this methodology could be applied to ungauged catchments or neighboring catchments.

REFERENCES

- Abbott, M. B., Bathurst, J. C., Cunge, J. A., O'connell, P. E. and Rasmussen, J. (1986a). An introduction to the European Hydrological System — Systeme Hydrologique Europeen, "SHE", 1: History and philosophy of a physically-based, distributed modelling system. *Journal of Hydrology*, 87(1-2), 45-59.
- Abbott, M. B., Bathurst, J. C., Cunge, J. A., O'connell, P. E. and Rasmussen, J. (1986b). An introduction to the European Hydrological System — Systeme Hydrologique Europeen, "SHE", 2: Structure of a physically-based, distributed modelling system. *Journal of Hydrology*, 87(1-2), 61-77.
- Abbott, M. B. and Refsgaard, J. C. (eds.) (1996). *Distributed Hydrological Modeling*. Kluwer Academic Publishers, Dordrecht, The Netherlands.
- Adeaga, O., Oyebande, L. and Balogun, I. (2005). PUB and water resources management practices in Nigeria. In: Predictions in Ungauged Basins: Promise and Progress, 2005, Brazil, IAHS.
- Adler, R. F. and Negri, A. J. (1988). A Satellite Infrared Technique to Estimate Tropical Convective and Stratiform Rainfall. *Journal of Applied Meteorology*, 27(1), 30-51.
- Ahmad, M. D., Bastiaanssen, W. G. M. and Feddes, R. A. (2005). A new technique to estimate net groundwater use across large irrigated areas by combing remote sensing and water balance approaches. *Hydrogeology Journal*, 13(5-6), 653-664.
- Ahmad, M. D., Turrall, H. and Nazeer, A. (2009). Diagnosing irrigation performance and water productivity through satellite remote sensing and secondary data in a large irrigation system of Pakistan. *Agricultural Water Management*, 96, 551-564.
- Ahn, K.-H. and Merwade, V. (2014). Quantifying the relative impact of climate and human activities on streamflow. *Journal of Hydrology*, 515(0), 257-266.
- Allen, R. G., Pereira, L. A., Raes, D. and Smith, M. (1998). *Crop evapotranspiration - Guidelines for computing crop water requirements*. FAO Irrigation and Drainage Food and Agriculture Organization of the United Nations, Rome, Italy. 293.
- Allen, R. G., Pereira, L. S., Howell, T. A. and Jensen, M. E. (2011). Evapotranspiration information reporting: I. Factors governing measurement accuracy. *Agricultural Water Management*, 98(6), 899-920.
- AMS Glossary (1999). *Glossary of Atmospheric terms* [Online]. American Meteorological Society. [Accessed 10/01/2012]. Available: <http://www.ametsoc.org/amsedu/wes/glossary.html>
- Andersen, J., Dybkjaer, G., Jensen, K. H., Refsgaard, J. C. and Rasmussen, K. (2002). Use of remotely sensed precipitation and leaf area index in a distributed hydrological model. *Journal of Hydrology*, 264(1-4), 34-50.
- Anys, H. and Dong-Chen, H. (1995). Evaluation of textural and multipolarization radar features for crop classification. *IEEE Transactions on Geoscience and Remote Sensing*, 33(5), 1170.
- Arkin, P. A. (1979). The Relationship between Fractional Coverage of High Cloud and Rainfall Accumulations during GATE over the B-Scale Array. *Monthly Weather Review*, 107(10), 1382-1387.
- Arkin, P. A. and Meisner, B. N. (1987). The Relationship between Large-Scale Convective Rainfall and Cold Cloud over the Western-Hemisphere during 1982-84. *Monthly Weather Review*, 115(1), 51-74.
- Arking, A. and Childs, J. D. (1985). Retrieval of Cloud Cover Parameters from Multispectral Satellite Images. *Journal of Climate and Applied Meteorology*, 24(4), 322-333.

- Arnold, J. G. and Allen, P. M. (1996). Estimating Hydrologic Budgets for Three Illinois Watersheds. *Journal of Hydrology*, 176(1), 57- 77.
- Arnold, J. G., Srinivasan, R., Muttiah, R. S. and Williams, J. R. (1998). Large Area Hydrologic Modelling and Assessment Part I: Model Development. *Journal of the American Water Resources Association*, 34(1), 73-89.
- Artan, G., Gadain, H., Smith, J., Asante, K., Bandaragoda, C. and Verdin, J. (2007). Adequacy of satellite derived rainfall data for stream flow modeling. *Natural Hazards*, 43(2), 167-185.
- Asante, K. O., Arlan, G. A., Pervez, S. and Rowland, J. (2008). A linear geospatial streamflow modeling system for data sparse environments. *International Journal of River Basin Management*, 6(3), 233-241.
- ASCE. (1996). *Handbook of hydrology*. ASCE, New York.
- ASCE Task Committee on Application of Artificial Neural Networks in Hydrology (2000). Artificial Neural Networks in Hydrology I: Preliminary concepts. *Journal of Hydraulic Engineering*, 5(2), 115-123.
- Atlas, D., Rosenfeld, D. and Wolff, D. B. (1990). Climatologically Tuned Reflectivity Rain Rate Relations and Links to Area Time Integrals. *Journal of Applied Meteorology*, 29(11), 1120-1135.
- Awulachew, S. B., McCartney, M., Steenhuis, T. S. and Ahmed, A. A. (2008). *A review of hydrology, sediment and water resource use in the Blue Nile Basin*. IWMI Working Paper 131, International Water Management Institute, Colombo, Sri Lanka.81.
- Ba, M. and Gruber, A. (2001a). GOES Multispectral Rainfall Algorithm (GMSRA). *Journal of Applied Meteorology*, 40, 1500–1514.
- Ba, M. B. and Gruber, A. (2001b). GOES multispectral rainfall algorithm (GMSRA). *Journal of Applied Meteorology*, 40(8), 1500-1514.
- Bandara, K. M. P. S. (2003). Monitoring irrigation performance in Sri Lanka with high-frequency satellite measurements during the dry season. *Agricultural Water Management*, 58(2), 159–170.
- Barrett, E. C. (1970). The estimation of monthly rainfall from satellite data. *Monthly Weather Review*, 98, 322-327.
- Barrett, E. C. (1973). Forecasting daily rainfall from satellite data. *Monthly Weather Review*, 101, 215-222.
- Barton, A. B. and Meyer, W. S. (2008). *An Analysis of Method and Meteorological Measurement for Evapotranspiration Estimation Part 1: Results using weather data from Griffith, NSW*. CRC for Irrigation Futures Technical Report, Cooperative Research Centre for Irrigation Futures.
- Barua, S. (2010). *Drought assessment and forecasting using a nonlinear aggregated drought index*. Ph D thesis, Victoria University.
- Bastiaanssen, W. G. M. (1998). *Remote Sensing in Water Resources Management: The State of the Art*. International Water Management Institute, Colombo.
- Bastiaanssen, W. G. M., Ahmad, M. D. and Chemin, Y. (2002). Satellite surveillance of evaporative depletion across the Indus Basin *Water Resources Research*, 38(12), 1-9.
- Bastiaanssen, W. G. M. and Chandrapala, L. (2003). Water balance variability across Sri Lanka for assessing agricultural and environmental water use. *Agricultural Water Management*, 58(2), 171-192.
- Bastiaanssen, W. G. M., Menenti, M., Feddes, R. A. and Holtslag, A. a. M. (1998a). A remote sensing surface energy balance algorithm for land (SEBAL) 1. Formulation. *Journal of Hydrology*, 212-213(1998), 198-212.

- Bastiaanssen, W. G. M., Pelgrum, H., Wang, J., Ma, Y., Moreno, J. F., Roerink, G. J. and Van Der Wal, T. (1998b). A remote sensing surface energy balance algorithm for land (SEBAL) 2. Validation. *Journal of Hydrology*, 212-213, 213-229.
- Battiti, R. (1994). Using mutual information for selecting features in supervised neural net learning. *IEEE Transactions on Neural Networks*, 5(4), 537-550.
- Benny, A. H. and Dawson, G. J. (1983). Satellite imagery as an aid to bathymetric charting in the Red Sea. *Cartographic Journal*, 20(1), 5-16.
- Betrie, G. D., Mohamed, Y. A., Griensven, A. V. and Srinivasan, R. (2011a). Sediment management modelling in the Blue Nile Basin using SWAT model *Hydrological Earth System Science*, 15(807-818).
- Betrie, G. D., Mohamed, Y. A., Van Griensven, A. and Srinivasan, R. (2011b). Sediment management modelling in the Blue Nile Basin using SWAT model. *Hydrology and Earth System Sciences*, 15(3), 807-818.
- Beven, K. J. and Kirkby, M. J. (1979). A physically based variable contributing area model of basin hydrology. *Hydrological Science Bulletin*, 24(1), 43-69.
- Bharatkar, P. S. and Patel, R. (2013). Approach to accuracy assessment for RS Image classification techniques. *International Journal of Scientific & Engineering Research*, 4(12), 79-86.
- Biggs, T. W., Mishra, P. K. and Turrall, H. (2008). Evapotranspiration and regional probabilities of soil moisture stress in rainfed crops, southern India. *Agricultural and Forest Meteorology*, 148(10), 1585-1597.
- Birkett, C. M. (1994). Radar altimetry: A new concept in monitoring lake level changes. *EOS Transactions, American Geophysical Union*, 75(24), 273-275.
- Birkett, C. M. (1995). The contribution of TOPEX/POSEIDON to the global monitoring of climatically sensitive lakes. *Journal of Geophysical Research: Oceans*, 100(C12), 25179-25204.
- Bishop, C. M. (1995). *Neural networks for pattern recognition* Oxford University press, Oxford.
- Bitew, M. M. and Gebremichael, M. (2011). Evaluation of satellite rainfall products through hydrologic simulation in a fully distributed hydrologic model. *Water Resources Research*, 47(6), 1-11.
- Bitew, M. M., Gebremichael, M., Ghebremichael, L. T. and Bayissa, Y. A. (2011). Evaluation of High-Resolution Satellite Rainfall Products through Streamflow Simulation in a Hydrological Modeling of a Small Mountainous Watershed in Ethiopia. *Journal of Hydrometeorology*, 13(1), 338-350.
- Bocchiola, D. (2007). Use of Scale Recursive Estimation for assimilation of precipitation data from TRMM (PR and TMI) and NEXRAD. *Advances in Water Resources*, 30(11), 2354-2372.
- Boegh, E., Thorsen, M., Butts, M. B., Hansen, S., Christiansen, J. S., Abrahamsen, P., Hasager, C. B., Jensen, N. O., Van Der Keur, P., Refsgaard, J. C., Schelde, K., Soegaard, H. and Thomsen, A. (2004). Incorporating remote sensing data in physically based distributed agro-hydrological modelling. *Journal of Hydrology*, 287(1-4), 279-299.
- Bonné, J. (1971). Stochastic simulation of monthly streamflow by a multiple regression model utilizing precipitation data. *Journal of Hydrology*, 12(4), 285-310.
- Bos, M. G. (2004). Using the depleted fraction to manage the groundwater table in irrigated areas. *Irrigation and Drainage Systems*, 18(3), 201-209.
- Bowden, G. J., Dandy, G. C. and Maier, H. R. (2005a). Input determination for neural network models in water resources applications. Part 1--background and methodology. *Journal of Hydrology*, 301(1-4), 75-92.

- Bowden, G. J., Maier, H. R. and Dandy, G. C. (2005b). Input determination for neural network models in water resources applications. Part 2. Case study: forecasting salinity in a river. *Journal of Hydrology*, 301(1-4), 93-107.
- Brandes, D., Hoffmann, J. G. and Mangarillo, J. T. (2005). Base flow recession rates, low flows, and hydrologic features of small watersheds in Pennsylvania, USA. *JAWRA Journal of the American Water Resources Association*, 41(5), 1177-1186.
- Bureau of Rural Sciences. (2009). *Australia's forest at a glance 2009*. Bureau of Rural Sciences, Canberra.
- Camargo, A. P., Marin, F. R., Sentelhas, P. C. and Picini, A. G. (1999). Adjust of the Thornthwaite's method to estimate the potential evapotranspiration for arid and superhumid climates, based on daily temperature amplitude. *Revista Brasileira Agrometeorology*, 7(2), 251-257.
- Campbell, G. S. and Norman, J. M. (1998). *Introduction to environmental biophysics*. Springer, New York.
- Campo, L., Caparrini, F. and Castelli, F. (2006). Use of multi-platform, multi-temporal remote-sensing data for calibration of a distributed hydrological model: an application in the Arno basin, Italy. *Hydrological Processes*, 20(13), 2693-2712.
- Chen, C., Yu, Z., Li, L. and Yang, C. (2011). Adaptability Evaluation of TRMM Satellite Rainfall and Its Application in the Dongjiang River Basin. *Procedia Environmental Sciences*, 10, Part A(0), 396-402.
- Chen, J. M., Chen, X., Ju, W. and Geng, X. (2005). Distributed hydrological model for mapping evapotranspiration using remote sensing inputs. *Journal of Hydrology*, 305(1-4), 15-39.
- Chow, V. T. (1959). *Open-Channel Hydraulics*. McGraw-Hill Companies
- Chow, V. T., Maidment, D. R. and Mays, L. W. (1988). *Applied Hydrology*. McGraw-Hill, Inc., New York.
- Cohen, J. (1960). A coefficient of agreement for nominal scales. *Educational and Psychological Measurement*, 20, 37-46.
- Colditz, R. R., Gessner, U., Conrad, C., Van Zyl, D., Malherbe, J., Nevvby, T., Landmann, T., Schmidt, M. and Dech, S. (2007). Dynamics of MODIS Time Series for Ecological Applications in Southern Africa. In: MultiTemp 2007. International Workshop on the Analysis of Multi-temporal Remote Sensing Images, 18-20 July 2007, Leuven, IEEE, 1-6.
- Collischonn, B., Collischonn, W. and Tucci, C. E. M. (2008). Daily hydrological modeling in the Amazon basin using TRMM rainfall estimates. *Journal of Hydrology*, 360(1-4), 207-216.
- Congalton, R. G. (1991). A review of assessing the accuracy of classifications of remotely sensed data. *Remote Sensing of Environment*, 37(1), 35-46.
- Coppola, E., Grimes, D. I. F., Verdecchia, M. and Visconti, G. (2006). Validation of Improved TAMANN Neural Network for Operational Satellite-Derived Rainfall Estimation in Africa. *Journal of Applied Meteorology and Climatology*, 45(11), 1157-1172.
- Cordery, I. (2007). Streamflow monitoring in Australia - Typical of worldwide neglect? In: IUGG General Assembly XXIV, 2-13 July 2007, Perugia, Italy, IAHS, 4843.
- Crawford, N. H. and Linsley, R. K. (1966). *Digital Simulation in Hydrology: Stanford Watershed Model IV*. Technical Report, Department of Civil Engineering, Stanford University, California.210.
- Dadhwal, V. K., Aggarwal, S. P. and Mishra, N. (2010). Hydrological simulation of Mahanadi River basin and impact of Landuse/landcover change on surface runoff

- using macroscale hydrological model. *In: Wagner, W. and Székely, B., eds. ISPRS TC VII Symposium – 100 Years ISPRS, July 5–7, 2010, Vienna, Austria, IAPRS.*
- Darbellay, G. A. (1999). An estimator of the mutual information based on a criterion for independence. *Computational Statistics & Data Analysis*, 32(1), 1-17.
- De Bruin, H. a. R. (1987). From Penman to Makkink. *In: Hooghart, C. (ed.) Evaporation and Weather.* Commission for Hydrological Research TNO. The Hague, The Netherlands. 5-30.
- De Bruin, H. a. R. and Stricker, J. N. M. (2000). Evaporation of grass under non-restricted soil moisture conditions. *Hydrological Science Journal*, 45(3), 391-406.
- De Fries, R., Hansen, M., Townsend, J. G. R. and Sohlberg, R. (1998). Global land cover classifications at 8 km resolution: The use of training data derived from Landsat imagery in decision tree classifiers. *International Journal of Remote Sensing*, 19(16), 3141– 3168.
- De Fries, R. S., Field, C. B., Fung, I., Justice, C. O., Los, S., Matson, P. A., Matthews, E., Mooney, H. A., Potter, C. S., Prentice, K., Sellers, P. J., Townshend, J. R. G., Tucker, C. J., Ustin, S. L. and Vitousek, P. M. (1995). Mapping the land surface for global atmosphere-biosphere models: Toward continuous distributions of vegetation's functional properties. *Journal of Geophysical Research*, 100(D10), 20867-20882.
- De Silveira, E. M., De Carvalho, L. M. T., Acerbi, F. W. and De Mello, J. M. (2007). The Assessment of Vegetation Seasonal Dynamics using Multitemporal NDVI and EVI images derived from MODIS. *In: MultiTemp 2007, International Workshop on the Analysis of Multi-temporal Remote Sensing Images 18-20 July 2007, Leuven, IEEE*, 1-5.
- Del Beato, R. (1981). The relationship between extratropical rainfall and satellite cloud-top temperatures. *Australian Meteorological Magazine*, 29(3), 125-131.
- Diop, M. and Grimes, D. I. F. (2003). Satellite-based rainfall estimation for river flow forecasting in Africa. II: African Easterly Waves, convection and rainfall. *Hydrological Sciences Journal*, 48(4), 585 - 599.
- Dittberner, G. J. and Vonder Haar, T. H. (1973). Large scale precipitation estimates using satellite data; application to the Indian Monsoon. *Archiv für Meteorologie, Geophysik und Bioklimatologie, Serie B*, 21(4), 317-334.
- Dorofki, M., Elshafie, A. H., Jaafar, O., Karim, O. A. and Mastura, S. (2012). Comparison of Artificial Neural Network Transfer Functions Abilities to Simulate Extreme Runoff Data *In: 2012 International Conference on Environment, Energy and Biotechnology*, 2012, Singapore IACSIT Press.
- Droogers, P. and Kite, G. (2002). Remotely sensed data used for modelling at different hydrological scales. *Hydrological Processes*, 16(8), 1543-1556.
- Eastman, J. R. and Fulk, M. (1993). Long sequence time series evaluation using standardized principal components. *Photogrammetric Engineering of Remote Sensing*, 59, 1307-1312.
- ENTRO. (2006). *Cooperative regional assessments for watershed management.* Trans-boundary analysis of the Abay–Blue–Nile sub-basin, Nile Basin Initiative, Addis Ababa, Ethiopia.
- Environment Canada (2011). *Water Survey of Canada* [Online].[Accessed 10/08/2011]. Available: <http://www.ec.gc.ca/rhc-wsc/default.asp?lang=En&n=4EED50F1-1>
- Estes, J. E. (2005). *Some Important Dates in the Chronological History of Aerial Photography and Remote Sensing* [Online]. University of California, Department of Geography. Santa Barbara:[Accessed Nov, 14th/2011]. Available: <http://www.geog.ucsb.edu/~jeff/115a/remotesensinghistory.html>

- Faust, N. L. (1989). *Image Enhancement*. Marcel Dekker Inc. Press.
- Fitch, D. T., Stow, D. A., Hope, A. S. and Rey, S. (2010). MODIS vegetation metrics as indicators of hydrological response in watersheds of California Mediterranean-type climate zones. *Remote Sensing of Environment*, 114(11), 2513-2523.
- Fleming, G. (1975). *Computer simulation techniques in hydrology*. Elsevier, New York.
- Foody, G. M. (2002). Status of land cover classification accuracy assessment. *Remote Sensing of Environment*, 80(1), 185-201.
- Foody, G. M. and Mathur, A. (2004). Toward intelligent training of supervised image classifications: directing training data acquisition for SVM classification. *Remote Sensing of Environment*, 93(1-2), 107-117.
- Fritsz, S. and Laszlo, I. (1993). Detection of water vapor in the stratosphere over very high clouds in the Tropics. *Journal of Geophysical Research*, 98(22), 953-967.
- Gamage, M. S. D. N., Ahmad, M. D. and Turrall, H. (2007). Semi-supervised technique to retrieve irrigated crops from Landsat ETM+ imagery for small fields and mixed cropping systems of South Asia. *International Journal of Geo informatics*, 3, 45-53.
- Gamage, N., Agrawal, R., Smakhtin, V. and Perera, B. J. C. (2011a). An Artificial Neural Network Model for Simulating Streamflow Using Remote Sensing Data. *In: 34th IAHR World Congress - Balance and Uncertainty*, 26 June - 1 July 2011a, Brisbane, IAHR & Engineers Australia, Brisbane, 1371 - 1378.
- Gamage, N., Ahmad, M. U. D. and Muthuwatta, L. (2009a). The use of medium resolution remote sensing data to compare spatio-temporal variation of irrigation performances and water consumption. *In: Anderssen, R. S., Braddock, R. D. and Newham, L. T. H., eds. 18th World IMACS Congress and MODSIM09 International Congress on Modelling and Simulation*, 13-17 July 2009a, Cairns, Australia, Modelling and Simulation Society of Australia and New Zealand; Canberra, Australia: International Association for Mathematics and Computers in Simulation., Canberra, Australia, 3697-3703.
- Gamage, N., Ahmad, M. U. D. and Turrall, H. (2009b). Mapping irrigated crops from Landsat ETM + imagery for heterogeneous cropping systems in Pakistan. *In: Thenkabail, P. S., Lyon, J. G., Turrall, H. and Biradar, C. M. (eds.) Remote sensing of global croplands for food security*. CRC Press Taylor & Francis Series in Remote Sensing Applications. Boca Raton, FL, USA. 421-437.
- Gamage, N. and Smakhtin, V. (2009). Do river deltas in east India retreat? A case of the Krishna Delta. *Geomorphology*, 103(4), 533-540.
- Gamage, N., Smakhtin, V. and Perera, C. (2011b). Estimation of Actual Evapotranspiration using Remote Sensing Data. *In: Chan, F., Marinova, D. and Anderssen, R. S., eds. 19th International Congress on Modelling and Simulation*, 12-16 December 2011b, Perth Conventional and Exhibition Centre, Modelling and Simulation Society of Australia and New Zealand, Perth, Australia, 3356-3362.
- Gao, B. C. (1996). NDWI - A normalized difference water index for remote sensing of vegetation liquid water from space. *Remote Sensing of Environment*, 58(3), 257-266.
- Giacomelli, A., Bacchiega, U., Troch, P. A. and Mancini, M. (1995). Evaluation of surface soil moisture distribution by means of SAR remote sensing techniques and conceptual hydrological modelling. *Journal of Hydrology*, 166(3-4), 445-459.
- Giglio, L. (2007). Characterization of the tropical diurnal fire cycle using VIRS and MODIS observations. *Remote Sensing of Environment*, 108(4), 407-421.
- Githui, F., Mutua, F. and Bauwens, W. (2009). Estimating the impacts of land-cover change on runoff using the soil and water assessment tool (SWAT): case study of

- Nzoia catchment, Kenya / Estimation des impacts du changement d'occupation du sol sur l'écoulement à l'aide de SWAT: étude du cas du bassin de Nzoia, Kenya. *Hydrological Sciences Journal*, 54(5), 899-908.
- Glenn, E. P., Huete, A. R., Nagler, P. L., Hirschboeck, K. K. and Paul, B. (2007). Integrating remote sensing and ground methods to estimate evapotranspiration. *Critical Reviews in Plant Sciences*, 26(3), 139-168.
- Goodman, M. (2011). *GHRC Dataset Catalog* [Online]. maintained by the NASA EOSDIS Global Hydrology Resource Center (GHRC) DAAC, Huntsville, AL. 2011.[Accessed 23/01/2011]. Available: http://ghrc.nsstc.nasa.gov/uso/ds_catalog/globalir.html
- Gourley, J. J. and Vieux, B. E. (2005). A Method for Evaluating the Accuracy of Quantitative Precipitation Estimates from a Hydrologic Modeling Perspective. *Journal of Hydrometeorology*, 6(2), 115-133.
- Govindaraju, R. S. and ASCE Task Committee on Application of Artificial Neural Networks in Hydrology (2000). Artificial Neural Networks in Hydrology. II: Hydrologic Applications. *Journal of Hydrologic Engineering*, 5(2), 124-137.
- Grimes, D. I. F., Coppola, E., Verdecchia, M. and Visconti, G. (2003). A Neural Network Approach to Real-Time Rainfall Estimation for Africa Using Satellite Data. *Journal of Hydrometeorology*, 4(6), 1119-1133.
- Grimes, D. I. F. and Diop, M. (2003). Satellite-based rainfall estimation for river flow forecasting in Africa. I: Rainfall estimates and hydrological forecasts. *Hydrological Sciences Journal*, 48(4), 576-584.
- Grimes, D. I. F., Pardo-Iguzquiza, E. and Bonifacio, R. (1999). Optimal aeral rainfall estimation using raingauges and satellite data. *Journal of Hydrology*, 222(1-4), 93-108.
- Guerschman, J. P., Van Dijk, A. I. J. M., Mattersdorf, G., Beringer, J., Hutley, L. B., Leuning, R., Pipunic, R. C. and Sherman, B. S. (2009). Scaling of potential evapotranspiration with MODIS data reproduces flux observations and catchment water balance observations across Australia. *Journal of Hydrology*, 369(1-2), 107-119.
- Gumindoga, W. (2010). *Hydrological impact of Landuse change in the Upper Gilgel Abay River Basin, Ethiopia; TOPMODEL Application*. M Sc Thesis, ITC, Enschede, The Netherlands.
- Hailelassie, A., Hagos, F., Mapedza, E., Sadoff, C., Awulachew, S. B., Gebreselassie, S. and Peden, D. (2008). *Institutional settings and livelihood strategies in the Blue Nile Basin: Implications for upstream/downstream linkages*. IWMI Working Paper 132, International Water Management Institute, Colombo, Sri Lanka.
- Hardy, S., Dugdale, G., Milford, J. R. and Sutcliffe, J. V. (1989). The use of satellite derived rainfall estimates as inputs to flow prediction in the River Senegal. *In: New directions for surface water modelling*, 1989, IAHS publications.
- Hargreaves, G. L., Hargreaves, G. H. and Riley, J. P. (1985). Agricultural Benefits for Senegal River Basin. *Journal of Irrigation and Drainage Engineering*, 111(2), 113-124.
- Harrington Jr, J. A., Schiebe, F. R. and Nix, J. F. (1992). Remote sensing of Lake Chicot, Arkansas: Monitoring suspended sediments, turbidity, and Secchi depth with Landsat MSS data. *Remote Sensing of Environment*, 39(1), 15-27.
- Hasmadi, M., Pakhriazad, H. Z. and Shahrin, M. F. (2009). Evaluating supervised and unsupervised techniques for land cover mapping using remote sensing data. *Malaysian Journal of Society and Space*, 5(1), 1-10.

- Haykin, S. (1999). *Neural Networks: A Comprehensive Foundation*. Macmillan, New York.
- He, H., Zhou, J. and Zhang, W. (2008). Modelling the impacts of environmental changes on hydrological regimes in the Hei River Watershed, China. *Global and Planetary Change*, 61(3-4), 175-193.
- Herschy, R. W. (1995). *Streamflow Measurement*. E. and F.N. Spon, an imprint of Chapman and Hall, London.
- Horton, R. E. (1933). The role of infiltration in the hydrologic cycle. *Transactions of American Geophysical Union* 14, 446-460.
- Huete, A., Didan, K., Miura, T., Rodriguez, E. P., Gao, X. and Ferreira, L. G. (2002). Overview of the radiometric and biophysical performance of the MODIS vegetation indices. *Remote Sensing of Environment*, 83(1-2), 195-213.
- Huete, A. R. (1988). A soil-adjusted vegetation index (SAVI). *Remote Sensing of Environment*, 25(3), 295– 309.
- Huete, A. R., Didan, K., Shimabukuro, Y. E., Ratana, P., Saleska, S. R., Hutyra, L. R., Yang, W., Nemani, R. R. and Myneni, R. (2006). Amazon rainforests green-up with sunlight in dry season. *Geophysical Research Letters*, 33(6), L06405.
- Huffman, G., Adler, R., F., Bolvin, D. T. and Nelkin, E. J. (2010). The TRMM Multi-satellite Precipitation Analysis (TMPA). In: Gebremichael, M. and Hossain, F. (eds.) *Satellite Rainfall Application for Surface Hydrology*. Springer Publishers. Netherlands. 3-22.
- Huffman, G. J., Adler, R. F., Arkin, P., Chang, A., Ferraro, R., Gruber, A., Janowiak, J., McNab, A., Rudolf, B. and Schneider, U. (1997). The Global Precipitation Climatology Project (GPCP) Combined Precipitation Dataset. *Bulletin of the American Meteorological Society*, 78(1), 5-20.
- Huffman, G. J., Adler, R. F., Bolvin, D. T., Gu, G., Nelkin, E. J., Bowman, K. P., Hong, Y., Stocker, E. F. and Wolff, D. B. (2007). The TRMM Multisatellite Precipitation Analysis (TMPA): Quasi-Global, Multiyear, Combined-Sensor Precipitation Estimates at Fine Scales. *Journal of Hydrometeorology*, 8(1), 38-55.
- Huffman, G. J., Adler, R. F., Morrissey, M. M., Bolvin, D. T., Curtis, S., Joyce, R., Mcgavock, B. and Susskind, J. (2001). Global Precipitation at One-Degree Daily Resolution from Multisatellite Observations. *Journal of Hydrometeorology*, 2(1), 36-50.
- Huffman, G. J., Adler, R. F., Rudolf, B., Schneider, U. and Keehn, P. R. (1995). Global Precipitation Estimates Based on a Technique for Combining Satellite-Based Estimates, Rain Gauge Analysis, and NWP Model Precipitation Information. *Journal of Climate*, 8(5), 1284-1295.
- Hursh, C. R. and Brater, E. F. (1944). Separating hydrographs into surface - and subsurface - flow. *Transactions of American Geophysical Union*, 22, 863-871.
- Hydrosult Inc, TecSult, DHV, Comatex Nilotica and T and A Consulting. (2006). *Trans-Boundary Analysis: Abay – Blue Nile Sub-basin*. NBI-ENTRO (Nile Basin Initiative-Eastern Nile Technical Regional Organization).
- ICEW. (1992). The Dublin statement and report of the conference. In: International conference on water and the environment: Development issues for the 21st century, 26 to 31 January 1992, Dublin, Ireland.
- Imbeau, M. E. (1892). La Durance: Regime. Crues et inundations. *Ann. Ponts Chaussées Mem. Doc. Ser.*, 3(1), 5-18 (in French).
- Immerzeel, W. W. and Droogers, P. (2008). Calibration of a distributed hydrological model based on satellite evapotranspiration. *Journal of Hydrology*, 349(3-4), 411-424.

- Immerzeel, W. W., Rutten, M. M. and Droogers, P. (2009). Spatial downscaling of TRMM precipitation using vegetative response on the Iberian Peninsula. *Remote Sensing of Environment*, 113(2), 362-370.
- Inoue, T. (1987). A cloud type classification with NOAA 7 split-window measurements. *Journal of Geophysical Research*, 92(D4), 3991-4000.
- Iqbal, M. (1983). *An introduction to solar radiation*. Academic Press, Toronto.
- Irons, J. R. (2011). *Landsat 1* [Online]. NASA.[Accessed 18/11/2011/18/11/2011]. Available: <http://landsat.gsfc.nasa.gov/about/landsat1.html>
- Isbell, R. F. and CSIRO. (1996). *The Australian soil classification*. CSIRO Australia, Collingwood, VIC, Australia.
- Isik, S., Kalin, L., Schoonover, J. E., Srivastava, P. and Graeme Lockaby, B. (2013). Modeling effects of changing land use/cover on daily streamflow: An Artificial Neural Network and curve number based hybrid approach. *Journal of Hydrology*, 485, 103-112.
- Islam, M. A., Thenkabail, P. S., Kulawardhana, R. W., Alankara, R., Gunasinghe, S., Edussriya, C. and Gunawardana, A. (2008). Semi-automated methods for mapping wetlands using Landsat ETM plus and SRTM data. *International Journal of Remote Sensing*, 29(24), 7077-7106.
- Jackson, R. D. (1983). Spectral indices in N-Space. *Remote Sensing of Environment*, 13(5), 409-421.
- Jackson, T. J., Chen, D., Cosh, M., Li, F., Anderson, M., Walthall, C., Doriaswamy, P. and Hunt, E. R. (2004). Vegetation water content mapping using Landsat data derived normalized difference water index for corn and soybeans. *Remote Sensing of Environment*, 92(4), 475-482.
- Jackson, T. J., Gasiewski, A. J., Oldak, A., Klein, M., Njoku, E. G., Yevgrafov, A., Christiani, S. and Bindlish, R. (2002). Soil moisture retrieval using the C-band polarimetric scanning radiometer during the Southern Great Plains 1999 experiment. *IEEE Transactions on Geoscience and Remote Sensing*, 40(10), 2151-2161.
- Jensen, J. R. (1996). *Introductory digital image processing: a remote sensing perspective*. Prentice Hall, Upper Saddle River, NJ.
- Jensen, J. R. (2000). *Remote Sensing of the Environment: an Earth Resource Perspective*. Prentice Hall, Saddle River, NJ.
- Jiang, S., Ren, L., Yong, B., Singh, V. P., Yang, X. and Yuan, F. (2011). Quantifying the effects of climate variability and human activities on runoff from the Laohahe basin in northern China using three different methods. *Hydrological Processes*, 25(16), 2492-2505.
- Joseph, G. (2005). *Fundamentals of Remote Sensing*. Universities Press (India) Private Limited, Hyderabad.
- Joyce, R. J., Janowiak, J. E., Arkin, P. A. and Xie, P. (2004). CMORPH: A Method that Produces Global Precipitation Estimates from Passive Microwave and Infrared Data at High Spatial and Temporal Resolution. *Journal of Hydrometeorology*, 5(3), 487-503.
- Justice, C. O., Townshend, J. R. G., Vermote, E. F., Masuoka, E., Wolfe, R. E., Saleous, N., Roy, D. P. and Morisette, J. T. (2002). An overview of MODIS Land data processing and product status. *Remote Sensing of Environment*, 83(1-2), 3-15.
- Kidd, C., Kniveton, D. R., Todd, M. C. and Bellerby, T. J. (2003). Satellite Rainfall Estimation Using Combined Passive Microwave and Infrared Algorithms. *Journal of Hydrometeorology*, 4(6), 1088-1104.

- Kim, T. and Valdés, J. (2003). Nonlinear Model for Drought Forecasting Based on a Conjunction of Wavelet Transforms and Neural Networks. *Journal of Hydrologic Engineering*, 8(6), 319-328.
- Kiptala, J. K., Mohamed, Y., Mul, M. L., Cheema, M. J. M. and Van Der Zaag, P. (2013). Land use and land cover classification using phenological variability from MODIS vegetation in the Upper Pangani River Basin, Eastern Africa. *Physics and Chemistry of the Earth, Parts A/B/C*, 66(0), 112-122.
- Kite, G. W. and Droogers, P. (2000). Comparing evapotranspiration estimates from satellites, hydrological models and field data. *Journal of Hydrology*, 229(1-2), 3-18.
- Kite, G. W. and Pietroniro, A. (1996). Remote sensing applications in hydrological modelling. *Hydrological Sciences Journal*, 41(4), 563-591.
- Krause, P., Boyle, D. P. and Base, F. (2005). Comparison of different efficiency criteria for hydrological model assessment. *Advances in Geoscience*, 5, 89-97.
- Krishnaswamy, J., Bonell, M., Venkatesh, B., Purandara, B. K., Lele, S., Kiran, M. C., Reddy, V., Badiger, S. and Rakesh, K. N. (2012). The rain-runoff response of tropical humid forest ecosystems to use and reforestation in the Western Ghats of India. *Journal of Hydrology*, 472-473(0), 216-237.
- Kuligowski, R. J. (2002). A self-calibrating real-time GOES rainfall algorithm for short-term rainfall estimates. *Journal of Hydrometeorology*, 3(2), 112-130.
- Kummerow, C., Hong, Y., Olson, W. S., Yang, S., Adler, R. F., Mccollum, J., Ferraro, R., Petty, G., Shin, D. B. and Wilheit, T. T. (2001). The evolution of the Goddard Profiling Algorithm (GPROF) for rainfall estimation from passive microwave sensors. *Journal of Applied Meteorology*, 40(11), 1801-1820.
- Kummerow, C. D., Barnes, W., Kozu, T., Shiue, J. and Simpson, J. (1988). Tropical Rainfall Measuring Mission (TRMM) sensor package. *Journal of Atmospheric and Oceanic Technology*, 15(3), 809-817.
- Kummerow, C. D., Masunaga, H. and Bauer, P. (2007). A next-generation microwave rainfall retrieval algorithm for use by TRMM and GPM. In: Levizzani, V., Bauer, P. and Turk, J. (eds.) *Measuring precipitation from space, EURAINSAT and the future*. Springer, Dordrecht, The Netherlands. 235-251.
- Kuo, C. M., Yu, O. S., Du, R. H. and Lin, C. Y. (2005). Using Penman-Monteith Method to Estimate Potential Evapotranspiration in Taiwan by Using AVHRR and MODIS Satellites Remote Sensing Data. In: 25th Asian Conference on Remote Sensing, 7 - 10 November 2005, Hanoi, Vietnam, ACRS, 345-354.
- Kupusovic, E. (2007). Hydrological services in Bosnia and Herzegovina. In: IUGG General Assembly XXIV, 2-13 July 2007, Parugia, Italy, IAHS, 4842.
- Lakshmi, V. (2004). The role of satellite remote sensing in the Prediction of Ungauged Basins. *Hydrological Processes*, 18(5), 1029-1034.
- Lee, J. H. W., Huang, Y., Dickman, M. and Jayawardena, A. W. (2003). Neural network modelling of coastal algal blooms. *Ecological Modelling*, 159(2-3), 179-201.
- Levick, L. R., Semmens, D. J., Guertin, D. P., Burns, I. S., Scott, S. N., Unkrich, C. L. and Goodrich, D. C. (2004). Adding Global Soils Data to the Automated Geospatial Watershed Assessment Tool (AGWA). In: 2nd International Symposium on Transboundary Waters Management, 16-19 November 2004, Tucson, Arizona.
- Levizzani, V., Bauer, P. and Turk, J. (eds.) (2007). *Measuring precipitation from space*. Springer, Dordrecht, The Netherlands.
- Li, X.-H., Zhang, Q. and Xu, C.-Y. (2012). Suitability of the TRMM satellite rainfalls in driving a distributed hydrological model for water balance computations in Xinjiang catchment, Poyang lake basin. *Journal of Hydrology*, 426-427(0), 28-38.

- Liang, H. and Song, W. X. (2009). Improved estimation in multiple linear regression models with measurement error and general constraint. *Journal of Multivariate Analysis*, 100(4), 726-741.
- Liang, S. (2001). Narrowband to broadband conversions of land surface albedo I Algorithms. *Remote Sensing of Environment*, 76(2), 213-238.
- Liang, S., Chad, J. S., Andrew, L. R., Hongliang, F., Mingzhen, C., Charles, L. W., Craig, S. T. D. and Raymond, H. J. (2002). Narrowband to broadband conversions of land surface albedo II Validation. *Remote Sensing of Environment* 84(1), 25-41.
- Lillesand, T. M. and Kiefer, R. W. (1999). *Remote Sensing and Image Interpretation*. John Wiley and Sons, Inc., Singapore.
- Lima, C. H. R. and Lall, U. (2010). Climate informed monthly streamflow forecasts for the Brazilian hydropower network using a periodic ridge regression model. *Journal of Hydrology*, 380(3-4), 438-449.
- Lovejoy, S. and Austin, G. L. (1980). The estimation of rain from satellite-borne microwave radiometers. *Quarterly Journal of the Royal Meteorological Society*, 106(448), 255-276.
- Loveland, T. R., Reed, B. C., Brown, J. F., Ohlen, D. O., Zhu, Z., Yang, L. and Merchant, J. W. (2000). Development of a global land cover characteristics database and IGBP DISCover from 1 km AVHRR data. *International Journal of Remote Sensing*, 21(6-7), 1303- 1330.
- Loveland, T. R., Zhu, Z., Ohlen, D. O., Brown, J. F., Redd, B. C. and Yang, L. (1999). An analysis of the IGBP global land-cover characterization process. *Photogrammetric Engineering and Remote Sensing*, 65(9), 1021– 1031.
- Lowdermilk, W. C. (1934). The role of vegetation in erosion control and water conservation. *Journal of Forestry* 32, 534.
- Madonna, L. A., Sciulli, C. M., Canjar, L. N. and Pound, G. M. (1961). Low Temperature Cloud Chamber Studies on Water Vapour *Proceedings of the Physical Society*, 78(6), 1218.
- Madugundu, R., Al-Gaadi, K. A., Patil, V. C. and Tola, E. (2014). Detection of land use and land cover changes in Dirab Region of Sudi Arabia using remotely sensed imageries. *American Journal of Environmental Science*, 10(1), 8-18.
- Maier, H. R. and Dandy, G. C. (1996). The Use of Artificial Neural Networks for the Prediction of Water Quality Parameters. *Water Resources Research*, 32(4), 1013-1022.
- Maier, H. R. and Dandy, G. C. (2000). Neural networks for the prediction and forecasting of water resources variables: a review of modelling issues and applications. *Environmental Modelling and Software*, 15(1), 101-124.
- Maier, H. R., Jain, A., Dandy, G. C. and Sudheer, K. P. (2010). Methods used for the development of neural networks for the prediction of water resource variables in river systems: Current status and future directions. *Environmental Modelling & Software*, 25(8), 891-909.
- Malek, E. (1987). Comparison of alternative methods for estimating ET_p and evaluation of advection in the Bajgah area, Iran. *Agricultural and Forest Meteorology*, 39(2-3), 185-192.
- Maling, D. H. (1989). *Measurements from maps*. Oxford: Pergamon.
- Mallick, K., Bhattacharya, B. K. and Patel, N. K. (2009). Estimating volumetric surface moisture content for cropped soils using a soil wetness index based on surface temperature and NDVI. *Agricultural and Forest Meteorology*, 149(8), 1327-1342.

- Mas, J. F. and Flores, J. J. (2007). The application of artificial neural networks to the analysis of remotely sensed data. *International Journal of Remote Sensing*, 29(3), 617-663.
- Matalas, N. C. (1967). Mathematical assessment of synthetic hydrology. *Water Resources Research*, 3(4), 937-945.
- May, R. J., Maier, H. R., Dandy, G. C. and Fernando, T. M. K. G. (2008). Non-linear variable selection for artificial neural networks using partial mutual information. *Environmental Modelling & Software*, 23(10–11), 1312-1326.
- Mc Cabe, M. F., Wood, E. F., Wójcik, R., Pan, M., Sheffield, J., Gao, H. and Sua, H. (2008). Hydrological consistency using multi-sensor remote sensing data for water and energy cycle studies. *Remote Sensing of Environment*, 112(2), 430-444.
- Mcculloch, W. and Pitts, W. (1943). A logical calculus of the ideas immanent in nervous activity. *Bulletin of Mathematical Biophysics*, 7(4), 115 - 133.
- McMichael, C. E., Hope, A. S. and Loaiciga, H. A. (2006). Distributed hydrological modelling in California semi-arid shrublands: MIKE SHE model calibration and uncertainty estimation. *Journal of Hydrology*, 317(3-4), 307-324.
- Melbourne Water. (2011). *Melbourne Water annual report 2010-2011*. Melbourne Water, Melbourne.
- Metcalf and Eddy Inc., University of Florida and Water Resources Engineers Inc. (1971). *Storm Water Management Model*. U.S. EPA, Washington, DC.
- Michaelides, S., Levizzani, V., Anagnostou, E., Bauer, P., Kasparis, T. and Lane, J. E. (2009). Precipitation: Measurement, remote sensing, climatology and modeling. *Atmospheric Research*, 94(4), 512-533.
- Milzow, C., Kgotlhang, L., Kinzelbach, W., Meier, P. and Bauer-Gottwein, P. (2009). The role of remote sensing in hydrological modelling of the Okavango Delta, Botswana. *Journal of Environmental Management*, 90(7), 2252-2260.
- Minnas, A. W. and Hall, M. J. (1996). Artificial neural networks as rainfall-runoff models. *Hydrological Sciences Journal*, 41(3), 399 - 417.
- Monteith, J. L. (1965). Evaporation and environment. In: Fogg, G. (Ed.), *The State and Movement of Water in Living Organisms*. In: *Proceedings of the XIXth Symposium on the Society of Experimental Biology*, 1965, Cambridge University Press, Cambridge, UK, 205 - 234.
- Moriasi, D. N., Arnold, J. G., Van Liew, M. W., Bingner, R. L., Harmel, R. D. and Veith, T. L. (2007). Model evaluation guidelines for systematic quantification of accuracy in watershed simulations. *Transactions Of The ASABE*, 50(3), 885-900.
- Morid, S., Smakhtin, V. and Bagherzadeh, K. (2007). Drought forecasting using artificial neural networks and time series of drought indices. *International Journal of Climatology*, 27(15), 2103-2111.
- MoWR. (2011). *RE: Quality of the streamflow data at Blue Nile River*.
- Mu, Q., Heinsch, F. A., Zhao, M. and Running, S. W. (2007). Development of a global evapotranspiration algorithm based on MODIS and global meteorology data. *Remote Sensing of Environment*, 111(4), 519-536.
- Mugnai, A., Smith, E. A. and Tripoli, G. J. (1993). Foundations for statistical-physical precipitation retrieval from passive microwave satellite measurements. Part II: Emission-source and generalized weighting-function properties of a time-dependent cloud-radiation model. *Journal of Applied Meteorology*, 32(1), 17-39.
- Mulvarny, T. J. (1850). On the use of self-registering rain and flood gauges. *Proceedings of the Institute of Civil Engineers*, 4(2), 1-8.

- Muthuwatta, L., Ahmad, M. D., Bos, M. and Rientjes, T. (2010). Assessment of Water Availability and Consumption in the Karkheh River Basin, Iran-Using Remote Sensing and Geo-statistics. *Water Resources Management*, 24(3), 459-484.
- Mwendera, E. J., Saleem, M. a. M. and Dibabe, A. (1997). The effect of livestock grazing on surface runoff and soil erosion from sloping pasture lands in the Ethiopian highlands. *Australian Journal of Experimental Agriculture* 37(4), 421 - 430.
- Nash, J. E. and Sutcliffe, J. V. (1970). River flow forecasting through conceptual models part I-A discussion of principles. *Journal of Hydrology*, 10(3), 282-290.
- Neitsch, S. L., Arnold, J. G., Kiniry, J. R., Srinivasan, R. and Williams, J. R. (2002). *Soil and Water Assessment Tool User's Manual*. Texas Water Resources Institute College Station, Texas.
- Neitsch, S. L., Arnold, J. G., Kiniry, J. R., Srinivasan, R. and Williams, J. R. (2010). *Soil and Water Assessment Tool Input/Output File Documentation Version 2009*. Texas A&M University System, Texas.
- Neitsch, S. L., Arnold, J. G., Kiniry, J. R. and Williams, J. R. (2005). *Soil and Water Assessment Tool Theoretical Documentaion*. Texas Water Resources Institute College Station, Texas.
- Nicks, A. D. (1971). Stochastic generation of the occurrence, pattern, and location of maximum amount of daily rainfall. *In: Statistical Hydrology*, Auguste 31-September 2 1974 1971, Tuscon, AZ, U.S. Department of Agriculture, 154-171.
- Nikolopoulos, E. I., Anagnostou, E. N., Hossain, F., Gebremichael, M. and Borga, M. (2010). Understanding the Scale Relationships of Uncertainty Propagation of Satellite Rainfall through a Distributed Hydrologic Model. *Journal of Hydrometeorology*, 11(2), 520-532.
- Oetter, D. R., Cohen, W. B., M., B., Maieresperger, T. K. and Kennedy, R. E. (2000). Land cover mapping in an agricultural setting using multiseasonal thematic mapper data. *Remote Sensing of Environment*, 76 (2), 139-155.
- Oguro, Y., Ito, S. and Tsuchiya, K. (2011). Comparisons of Brightness Temperatures of Landsat-7/ETM+ and Terra/MODIS around Hotien Oasis in the Taklimakan Desert. *Applied and Environmental Soil Science*, 2011(Part 1), 1-11.
- Oguro, Y., Tsuchiya, K. and Suga, Y. (1999). Comparison of land cover features observed with different satellite sensors over a semi-arid land in central Australia. *Advances in Space Research*, 23(8), 1401-1404.
- Ottlé, C., Vidal-Madjar, D. and Girard, G. (1989). Remote sensing applications to hydrological modeling. *Journal of Hydrology*, 105(3-4), 369-384.
- Oudin, L., Hervieu, F., Michel, C., Perrin, C., Andréassian, V., Anctil, F. and Loumagne, C. (2005a). Which potential evapotranspiration input for a lumped rainfall-runoff model?: Part 2-Towards a simple and efficient potential evapotranspiration model for rainfall-runoff modelling. *Journal of Hydrology*, 303(1-4), 290-306.
- Oudin, L., Michel, C. and Anctil, F. (2005b). Which potential evapotranspiration input for a lumped rainfall-runoff model?: Part 1-Can rainfall-runoff models effectively handle detailed potential evapotranspiration inputs? *Journal of Hydrology*, 303(1-4), 275-289.
- Pala, A. (2003). Runoff modelling of rural catchments in Turkey. *Journal of Arid Environments*, 54(3), 505-512.
- Panda, S. S., Hoogenboom, G. and Paz, J. (2009). Distinguishing blueberry bushes from mixed vegetation land use using high resolution satellite imagery and geospatial techniques. *Computers and Electronics in Agriculture*, 67(1-2), 51-58.

- Pax-Lenney, M., Woodcock, C. E., Macomber, S. A., Gopal, S. and Song, C. (2001). Forest mapping with a generalized classifier and Landsat TM data. *Remote Sensing of Environment*, 77(3), 241-250.
- Pearson, R. L. and Miller, L. D. (1972). Remote mapping of standing crop biomass for estimation of the productivity of the short grass Prairie, Pawnee National Grasslands, Colorado. *8th International Symposium on Remote Sensing on Environment*. Michigan, USA: Ann Arbor.
- Peel, I., Watson, F., Vertessy, R., Lau, A., Watson, I., Sutton, M. and Rhodes, B. (2000). *Predicting the water yield impacts of forest disturbance in the Maroondah and Thomson catchments using the Macaque model*. Technical report Cooperative Research Centre for Catchment Hydrology, Cooperative Research Centre for Catchment Hydrology.
- Penman, H. L. (1948). Natural evaporation from open water, bare soil, and grass. *In: Proceedings of the Royal Society*, 1948, London, 120-146.
- Pereira, A. R. and Pruitt, W. O. (2004). Adaptation of the Thornthwaite scheme for estimating daily reference evapotranspiration. *Agricultural Water Management*, 66(3), 251-257.
- Pierce, H. F. (2008). *Tropical Rainfall Measuring Mission* [Online]. NASA.[Accessed 11/01/2012]. Available: http://trmm.gsfc.nasa.gov/overview_dir/why-grad.html
- Pietroniro, A., Wishart, W. and Solomon, S. I. (1989). Use of remote sensing satellite data for investigate water resources in Africa. *In: Canadian Symposium of Remote Sensing*, 1989, Vancouver, 2169–2172.
- Pitman, W. (1976). *A mathematical model for generating daily river flows from meteorological data in South Africa*. Hydrological Research Unit, University of Witwatersrand.
- Pluhowski, E. J. (1977). *Application of remotely sensed land-use information to improve estimates of streamflow characteristics*. USGS.
- Priestley, C. H. B. and Taylor, R. J. (1972). On the assessment of surface heat flux and evaporation using large scale parameters. *Monthly Weather Review*, 100(2), 81-92.
- Raman, H. and Sunilkumar, N. (1995). Multivariate modelling of water resources time series using artificial neural networks *Hydrological Science Journal*, 40(2), 145-163.
- Refsgaard, J. C. (1996). Chapter 2: Terminology, modelling protocol and classification of hydrological model codes. *In: Abbott, M. B. and Refsgaard, J. C. (eds.) Distributed Hydrological Modeling*. Kluwer Academic. Dordrecht;Boston.
- Revenga, C., Brunner, J., Henninger, N., Kassem, K. and Payne, R. (2000). Pilot Analysis of Freshwater Ecosystems *Freshwater Systems*, (Pilot Analysis of Freshwater Ecosystems: Freshwater Systems), 83 pp.
- Rizzo, D. M., Besaw, L. E., Bierman, P. R. and Hackett, W. R. (2010). Advances in ungauged streamflow prediction using artificial neural networks. *Journal of Hydrology*, 386(1-4), 27-37.
- Rosenfeld, D. (2007). Cloud Top Microphysics as a Tool for Precipitation Measurements. *In: Levizzani, V., Bauer, P. and Turk, F. J. (eds.) Measuring Precipitation From Space*. Springer Netherlands. 61-77.
- Rosinski, J. and Lecinski, A. (1983). Temperature-supersaturation relation for natural sorption ice-forming nuclei. *Journal of Aerosol Science*, 14(1), 49-63.
- Roy, P. S., Ranganath, B. K., Diwakar, P. G., Vohra, T. P. S., Bhan, S. K., Singh, I. J. and Pandian, V. C. (1991). Tropical Forest Type Mapping and Monitoring Using Remote-Sensing. *International Journal of Remote Sensing*, 12(11), 2205-2225.

- Rüdiger, C., Davidson, R. E., Hemakumara, H. M., Walker, J. P., Kalma, J. D., Willgoose, G. R. and Houser, P. R. (2003). Catchment Monitoring for Scaling and Assimilation of Soil Moisture and Streamflow. *In: Proceedings of the International Congress on Modelling and Simulation (MODSIM)*, 14-17 July 2003, Townsville, Modelling and Simulation Society of Australia and New Zealand, Australia, 386-391.
- Running, S. W., Patterson, D. L., Spanner, M. A. and Teuber, K. B. (1986). Remote sensing of coniferous forest leaf area. *Ecology*, 67(1), 273-276.
- Sachindra, D. A., Huang, F., Barton, A. and Perera, B. J. C. (2013). Least square support vector and multi-linear regression for statistically downscaling general circulation model outputs to catchment streamflows. *International Journal of Climatology*, 33(5), 1087-1106.
- Sahoo, G. B. and Ray, C. (2006). Flow forecasting for a Hawaii stream using rating curves and neural networks. *Journal of Hydrology*, 317(1-2), 63-80.
- Samarasinghe, S. (2006). *Neural networks for applied sciences and engineering : from fundamentals to complex pattern recognition*. Boca Raton, Fla. : Auerbach ; London : Taylor & Francis.
- Samuel, J., Coulibaly, P. and Metcalfe, R. A. (2011). Estimation of Continuous Streamflow in Ontario Ungauged Basins: Comparison of Regionalization Methods. *Journal of Hydrologic Engineering*, 16(5), 447-459.
- Sánchez, J. M., Scavone, G., Caselles, V., Valor, E., Copertino, V. A. and Telesca, V. (2008). Monitoring daily evapotranspiration at a regional scale from Landsat-TM and ETM+ data: Application to the Basilicata region. *Journal of Hydrology*, 351(1-2), 58-70.
- Sarvestani, Z. T., Pirdashti, H., Sanavy, S. a. M. M. and Balouchi, H. (2008). Study of water stress effects in different growth stages on yield and yield components of different Rice (*Oryza sativa* L.) cultivars. *Pakistan Journal of Biological Science*, 11(10), 1303-1309.
- Schneider, D. J., Rose, W. I., Coke, L. R., Bluth, G. J. S., Sprod, I. E. and Krueger, A. J. (1999). Early evolution of a stratospheric volcanic eruption cloud as observed with TOMS and AVHRR. *Journal of Geophysical Research*, 104(D4), 4037-4050.
- Schnur, M. T., Xie, H. and Wang, X. (2010). Estimating root zone soil moisture at distant sites using MODIS NDVI and EVI in a semi-arid region of southwestern USA. *Ecological Informatics*, 5(5), 400-409.
- Schultz, G. A. (1996). Remote sensing applications to hydrology: runoff. *Hydrological Sciences Journal*, 41(4), 453-475.
- Scofield, R. A. and Oliver, V. J. (1977). *A Scheme for Estimating Convective Rainfall from Satellite Imagery*. Department of Commerce, Washington DC.
- Scott, C. A., Bastiaanssen, W. G. M. and Ahmad, M. D. (2003). Mapping root zone soil moisture using remotely sensed optical imagery. *Journal of Irrigation and Drainage Engineering*, 129(5), 326-335.
- Sefton, C. E. M. and Howarth, S. M. (1998). Relationships between dynamic response characteristics and physical descriptors of catchments in England and Wales. *Journal of Hydrology*, 211(1-4), 1-16.
- Senay, G., Budde, M., Verdin, J. and Melesse, A. (2007a). A Coupled Remote Sensing and Simplified Surface Energy Balance Approach to Estimate Actual Evapotranspiration from Irrigated Fields. *Sensors*, 7(6), 979-1000.
- Senay, G. B., Budde, M., Verdin, J. P. and Melesse, A. M. (2007b). A Coupled Remote Sensing and Simplified Surface Energy Balance Approach to Estimate Actual

- Evapotranspiration from Irrigated Fields. *Sensors (Basel, Switzerland)*, 7(6), 979-1000.
- Setegn, S. G. (2010). *Modeling Hydrological and Hydrodynamic Processes in Lake Tana Basin, Ethiopia*. Ph. D thesis, Royal Institute of Technology (KTH).
- Sharma, A. (2000). Seasonal to interannual rainfall probabilistic forecasts for improved water supply management: Part 1 — A strategy for system predictor identification. *Journal of Hydrology*, 239(1–4), 232-239.
- Sharma, S. K. and Tiwari, K. N. (2009). Bootstrap based artificial neural network (BANN) analysis for hierarchical prediction of monthly runoff in Upper Damodar Valley Catchment. *Journal of Hydrology*, 374(3–4), 209-222.
- Sharpley, A. N. and Williams, J. R. (1990). *EPIC-Erosion Productivity Impact Calculator, 1. model documentation*. U.S. Department of Agriculture, Agricultural Research Service.
- Sherman, L. K. (1932). Streamflow from Rainfall by the Unit Graph Method. *Engineering News-Record*, 108, 501-505.
- Shoichi, S., Yukari, N. T., Satoshi, K., Wei-Kuo, T., Xiping, Z., Chie, Y. and Tristan, L. (2009). Spectral Retrieval of Latent Heating Profiles from TRMM PR Data. Part IV: Comparisons of Lookup Tables from Two- and Three-Dimensional Cloud-Resolving Model Simulations. *Journal of Climate*, 22(20), 5577-5594.
- Shupe, S. M. and Marsh, S. E. (2004). Cover- and density-based vegetation classifications of the Sonoran Desert using Landsat TM and ERS-1 SAR imagery. *Remote Sensing of Environment*, 93(1–2), 131-149.
- Singh, J., Knapp, H. V., Arnold, J. G. and Demissie, M. (2005). Hydrologic modeling of the Iroquois River watershed using HSPF and SWAT. *Journal of the American Water Resources Association*, 41(2), 343-360.
- Singh, J., Knapp, H. V. and Demissie, M. (2004). *Hydrologic modeling of the Iroquois River watershed using HSPF and SWAT*.
- Singh, V. P. (1995). Chapter 1: Watershed modeling. In: Singh, V. P. (ed.) *Computer models of watershed hydrology*. Water Resources Publications. Littleton, Colorado. 1-22.
- Singh, V. P. and Woolhiser, D. A. (2002). Mathematical modeling of watershed hydrology. *Journal of Hydrologic Engineering*, 7(4), 270-292.
- Sivapalan, M. (2003). Prediction in ungauged basins: a grand challenge for theoretical hydrology. *Hydrological Processes*, 17(15), 3163-3170.
- Sivapalan, M., Takeuchi, K., Franks, S. W., Gupta, V. K., Karambiri, H., Lakshmi, V., Liang, X., McDonnell, J. J., Mendiondo, E. M., O'Connell, P. E., Oki, T., Pomeroy, J. W., Schertzer, D., Uhlenbrook, S. and Zehe, E. (2003). IAHS Decade on Predictions in Ungauged Basins (PUB), 2003–2012: Shaping an exciting future for the hydrological sciences *Hydrological Sciences*, 48(6), 857-880.
- Smakhtin, V. (2012). Solving the hydrology data dilemma. In: Clarke, J. (ed.). Colombo, Sri Lanka: IWMI.
- Smakhtin, V. and Wichelns, D. (2010). Hydrometeorological data collection and sharing: The global challenge. In: Improving the information base to better guide water resources management decision making, 4-7 May 2010, Zaragoza, Spain, The Organisation for Economic Co-operation and Development.
- Smakhtin, V. U. (2000). Estimating daily flow duration curves from monthly streamflow data. *Water South Africa*, 26(1), 13-18.
- Smith, M., Allen, R. G., Monteith, J. L., Perrier, A., Pereira, L. and Segeren, A. (1991). *Report on the expert consultation on procedures for revision of FAO guidelines for prediction of crop water requirements*. FAO, Rome, Italy.

- Smits, P. C., Dellepiane, S. G. and Schowengerdt, R. A. (1999). Quality assessment of image classification algorithms for land-cover mapping: a review and proposal for a cost-based approach. *International Journal of Remote Sensing*, 20(8), 1461–1486.
- Soofi, E. S. and Retzer, J. J. (2003). Information importance of explanatory variables. *IEE Conference in Honor of Arnold Zellner: Recent Developments in the Theory, Method and Application of Entropy Econometrics*. Washington (USA).
- Sorooshian, S., Hsu, K., Gao, X., Gupta, H. V., Imam, B. and Braithwaite, D. (2000). Evaluation of PERSIANN System Satellite-Based Estimates of Tropical Rainfall. *Bulletin of the American Meteorological Society*, 81(9), 2035-2046.
- Southern Rural Water (2011). *Macalister* [Online]. Southern Rural Water. Maffra:[Accessed 10/01/2012]. Available: http://www.srw.com.au/Page/Page.asp?Page_Id=155&h=0
- Sther, A., Debels, P., Romero, F. and Alcayaga, H. (2008). Hydrological modelling with SWAT under conditions of limited data availability: evaluation of results from a Chilean case study. *Hydrological Sciences*, 53(3), 588-601.
- Stisen, S., Jensen, K. H., Sandholt, I. and Grimes, D. I. F. (2008). A remote sensing driven distributed hydrological model of the Senegal River basin. *Journal of Hydrology*, 354(1-4), 131-148.
- Su, F., Gao, H., Huffman, G. J. and Lettenmaier, D. P. (2010). Potential Utility of the Real-Time TMPA-RT Precipitation Estimates in Streamflow Prediction. *Journal of Hydrometeorology*, 12(3), 444-455.
- Su, F., Hong, Y. and Lettenmaier, D. P. (2008). Evaluation of TRMM Multisatellite Precipitation Analysis (TMPA) and Its utility in hydrologic prediction in the La Plata basin. *Journal of Hydrometeorology*, 9(4), 622–640.
- Su, Z. (2002). The Surface Energy Balance System (SEBS) for estimation of turbulent heat fluxes. *Hydrology and Earth System Sciences*, 6(1), 85-99.
- Sudheer, K. P., Gosain, A. K. and Ramasastri, K. S. (2003). Estimating actual evapotranspiration from limited climatic data using neural network computing technique. *Journal of Irrigation and Drainage Engineering*, 129(3), 214-218.
- Sutcliffe, J. V. (2004). *Hydrology: A question of balance*. IAHS, Wallingford.
- Tang, Q., Gao, H., Lu, H. and Lettenmaier, D. P. (2009). Remote sensing: hydrology. *Progress in Physical Geography*, 33(4), 490-509.
- Taylor, M. P. (2014). *Landsat Science* [Online]. NASA.[Accessed November 13/2014]. Available: <http://landsat.gsfc.nasa.gov/>
- Teillet, P. M., Staenz, K. and William, D. J. (1997). Effects of spectral, spatial, and radiometric characteristics on remote sensing vegetation indices of forested regions. *Remote Sensing of Environment*, 61(1), 139-149.
- Thenkabail, P. S., Biradar, C. M., Noojipady, P., Dheeravath, V., Li, Y. J., Velpuri, M., Reddy, G. P. O., Cai, X. L., Gumma, M., Turrall, H., Vithanage, J., Schull, M. and Dutta, R. (2008). *A Global Irrigated Area Map (GIAM) Using Remote Sensing at the End of the Last Millennium*. International Water Management Institute, Colombo.
- Thenkabail, P. S., Gamage, M. S. D. N. and Smakhtin, V. U. (2004). *The use of remote sensing data for drought assessment and monitoring In South West Asia*. IWMI Research Report 85, International Water Management Institute, Colombo, Sri Lanka.
- Thenkabail, P. S., Schull, M. and Turrall, H. (2005). Ganges and Indus river basin land use/cover (LULC) and irrigated area mapping using continuous streams of MODIS data. *Remote Sensing of Environment*, 95(3), 317-341.

- Thirumalaiah, K. and Deo, M. C. (1998). River stage forecasting using artificial neural networks. *Journal of Hydrologic Engineering*, 3(1), 26-32.
- Thom, H. C. S. (1966). *Some Methods of Climatological Analysis*. WMO Technical Note, Secretariat of the World Meteorological Organization, Geneva, Switzerland.53
- Thomlinson, J. R., Bolstad, P. V. and Cohen, W. B. (1999). Coordinating methodologies for scaling landcover classifications from site-specific to global: steps toward validating global map products. *Remote Sensing of Environment*, 16(28), 70.
- Thornthwaite, C. W. (1948). An approach toward a rational classification of climate. *Geographical Review*, 38(1), 55-94.
- Tibebe, D. and Bewket, W. (2011). Surface runoff and soil erosion estimation using the SWAT model in the Keleta Watershed, Ethiopia. *Land Degradation & Development*, 22(6), 551-564.
- Tjemkes, S. A., Van De Berg, L. and Schmetz, J. (1997). Warm water vapor pixels over high clouds as observed by Meteosat. *Physical Atmosphere*, 70, 15-21.
- Tran, D. H., Perera, B. J. C. and Ng, A. W. M. (2009). Comparison of Structural Deterioration Models for Stormwater Drainage Pipes. *Computer-Aided Civil and Infrastructure Engineering*, 24(2), 145-156.
- Tran, L. T. and O'Neill, R. V. (2013). Detecting the effects of land use/land cover on mean annual streamflow in the Upper Mississippi River Basin, USA. *Journal of Hydrology*, 499(0), 82-90.
- Tucker, C. J. (1979). Red and photographic infrared linear combinations for monitoring vegetation. *Remote Sensing of Environment*, 8(2), 127-150.
- USCB (2011). *U.S. Census Bureau* [Online].[Accessed 08/11/2011]. Available: <http://www.census.gov/ipc/www/idb/worldpoptotal.php>
- USDA-Scs (1972). U.S. Department of Agriculture-Soil Conservation Service National Engineering Handbook - Hydrology Section. U. S. Department of Agriculture, Soil Conservation Service. Washington D.C.
- USDA. (1986). *Urban Hydrology for Small Watersheds*. USDA - Natural Resources Conservation Service, Conservation Engineering Division.
- Utset, A., Farré, I., Martínez-Cob, A. and Cavero, J. (2004). Comparing Penman-Monteith and Priestley-Taylor approaches as reference-evapotranspiration inputs for modeling maize water-use under Mediterranean conditions. *Agricultural Water Management*, 66(3), 205-219.
- Valor, E. and Caselles, V. (1996). Mapping land surface emissivity from NDVI: Application to European, African, and South American areas. *Remote Sensing of Environment*, 57(3), 167-184.
- Van Griensven, A., Meixner, T., Grunwald, S., Bishop, T., Diluzio, M. and Srinivasan, R. (2006). A global sensitivity analysis tool for the parameters of multi-variable catchment models. *Journal of Hydrology*, 324(1-4), 10-23.
- Vaze, J., Perraud, J. M., Teng, J., Chiew, F. and Wang, B. (2011). Estimating regional model parameters using spatial land cover information – implications for predictions in ungauged basins *In: 19th International Congress on Modelling and Simulation*, 12-16 December 2011, Perth, Australia.
- Velpuri, N. M., Senay, G. B. and Asante, K. O. (2012). A multi-source satellite data approach for modelling Lake Turkana water level: calibration and validation using satellite altimetry data. *Hydrology and Earth System Sciences*, 16(1), 1-18.
- Wagner, S., Kunstmann, H., Bárdossy, A., Conrad, C. and Colditz, R. R. (2009). Water balance estimation of a poorly gauged catchment in West Africa using dynamically downscaled meteorological fields and remote sensing information. *Physics and Chemistry of the Earth, Parts A/B/C*, 34(4-5), 225-235.

- Wang, H., Guan, H., Gutiérrez-Jurado, H. A. and Simmons, C. T. (2014). Examination of water budget using satellite products over Australia. *Journal of Hydrology*, 511(0), 546-554.
- Wang, W., Gelder, P. H. a. J. M. V., Vrijling, J. K. and Ma, J. (2006). Forecasting daily streamflow using hybrid ANN models. *Journal of Hydrology*, 324(1-4), 383-399.
- Wang, X., Xie, H., Guan, H. and Zhou, X. (2007). Different responses of MODIS-derived NDVI to root-zone soil moisture in semi-arid and humid regions. *Journal of Hydrology*, 340(1-2), 12-24.
- Water Resources Overview - Victoria (2009). *Australian Natural Resources Atlas* [Online]. Department of Sustainability, Environment, Water, Population and Communities Canberra ACT [Accessed 09/01/2012]. Available: <http://www.anra.gov.au/topics/water/overview/vic/swma-thomsonmacalister-rivers.html>
- Wegehenkel, M., Heinrich, U., Uhlemann, S., Dunger, V. and Matschullat, J. (2006). The impact of different spatial land cover data sets on the outputs of a hydrological model – a modelling exercise in the Ucker catchment, North-East Germany. *Physics and Chemistry of the Earth, Parts A/B/C*, 31(17), 1075-1088.
- Wegmuller, U. (1993). Signature research for crop classification by active and passive microwaves. *International Journal of Remote Sensing*, 14(5), 871-883.
- Weissling, B. P. and Xie, H. (2009). MODIS Biophysical States and NEXRAD Precipitation in a Statistical Evaluation of Antecedent Moisture Condition and Streamflow1. *JAWRA Journal of the American Water Resources Association*, 45(2), 419-433.
- Weng, F., Zhao, L., Poe, G., Ferraro, R. R., Li, X. and Grody, N. C. (2003). Advanced microwave sounding unit cloud and precipitation algorithms. *Radio Science*, 38(4), 8068-8079.
- Wesseling, J. G. and Feddes, R. A. (2006). Assessing crop water productivity from field to regional scale. *Agricultural Water Management*, 86(1-2), 30-39.
- West Gippsland Catchment Management Authority. (2005). *West Gippsland River health Strategy* West Gippsland Catchment Management Authority, Traralgon.
- West Gippsland Catchment Management Authority. (2008). *Soil Erosion Management Plan*. West Gippsland Catchment Management Authority, Traralgon.
- Williams, J. R. (1995). *The EPIC Model*. Water Resources Publications, Highlands Ranch, CO.
- Willmott, C. J., Rowe, C. M. and Mintz, Y. (1985). Climatology of the Terrestrial Seasonal Water Cycle. *Journal of Climatology*, 5(6), 589-606.
- Wine, M. L. and Zou, C. B. (2012). Long-term streamflow relations with riparian gallery forest expansion into tallgrass prairie in the Southern Great Plains, USA. *Forest Ecology and Management*, 266(0), 170-179.
- Woolhiser, D. A. (1973). Hydrologic and watershed modelling - State of the art. *Transactions of the ASAE*, 16, 533-559.
- World Water Assessment Programme. (2006). *The United Nations World Water Development Report 2: Water, a shared responsibility*. UNESCO, Paris, France.
- World Water Assessment Programme. (2009). *The United Nations World Water Development Report 3: Water in a Changing World*. UNESCO, Paris, France.
- Wu, C., Chen, J. M. and Huang, N. (2011). Predicting gross primary production from the enhanced vegetation index and photosynthetically active radiation: Evaluation and calibration. *Remote Sensing of Environment*, 115(12), 3424-3435.
- Xinping, Z., Tandong, Y., Jingmiao, L., Lide, T. and Nakawo, M. (2000). Simulations of stable isotopic fractionation in mixed cloud in middle latitudes-Taking the

- precipitation at Ürümqi as an example. *Advances in Atmospheric Sciences*, 20(2), 261-268.
- Yan, B., Fang, N. F., Zhang, P. C. and Shi, Z. H. (2013a). Impacts of land use change on watershed streamflow and sediment yield: An assessment using hydrologic modelling and partial least squares regression. *Journal of Hydrology*, 484(0), 26-37.
- Yan, Y., Yang, Z. and Liu, Q. (2013b). Nonlinear trend in streamflow and its response to climate change under complex ecohydrological patterns in the Yellow River Basin, China. *Ecological Modelling*, 252(0), 220-227.
- Yilma, D. A. and Awulachew, S. B. (2009). *Characterization and Atlas of the Blue Nile Basin and its Sub basins*. International Water Management Institute, Colombo.
- Yilmaz, A. G., Imteaz, M. A. and Jenkins, G. (2011). Catchment flow estimation using Artificial Neural Networks in the mountainous Euphrates Basin. *Journal of Hydrology*, 410(1-2), 134-140.
- Yong, B., Hong, Y., Ren, L. L., Gourley, J. J., Huffman, G. J., Chen, X., Wang, W. and Khan, S. I. (2012). Assessment of evolving TRMM-based multisatellite real-time precipitation estimation methods and their impacts on hydrologic prediction in a high latitude basin. *Journal of Geophysical Research-Atmospheres*, 117(D9), 1-21.
- Young, A. R. and Sabburg, J. (2006). Cloud effects on evaporation at a sub-tropical site. *Australian Institute of Physics 17th National Congress*. Brisbane.
- Zhang, X., Srinivasan, R. and Van Liew, M. (2009a). Approximating SWAT Model Using Artificial Neural Network and Support Vector Machine. *Journal of the American Water Resources Association*, 45(2), 460-474.
- Zhang, Y. Q., Chiew, F. H. S., Zhang, L. and Li, H. X. (2009b). Use of Remotely Sensed Actual Evapotranspiration to Improve Rainfall-Runoff Modeling in Southeast Australia. *Journal of Hydrometeorology*, 10(4), 969-980.
- Zhou, M. C., Ishidaira, H., Hapuarachchi, H. P., Magome, J., Kiem, A. S. and Takeuchi, K. (2006). Estimating potential evapotranspiration using Shuttleworth-Wallace model and NOAA-AVHRR NDVI data to feed a distributed hydrological model over the Mekong River basin. *Journal of Hydrology*, 327(1-2), 151-173.
- Zhu, Y. and Day, R. L. (2009). Regression modeling of streamflow, baseflow, and runoff using geographic information systems. *Journal of Environmental Management*, 90(2), 946-953.

APPENDICES

Appendix A

Table A.1 of Appendix A is tabled all the information used in first case study area selection process. These data were obtained from Department of Primary Industries – Victoria, and they are available on web with free of charge. Latest data available (senses on 1996/1997) were used in this process.

Table A.1 Relevant details of selecting the first case study area - All Victorian catchments*

	Total catchment area (ha)	Non-agricultural area (ha)	Agricultural area (ha)	Irrigated agricultural area (ha) in 1996/97	Dry land agricultural area (ha) in 1996/97	Percentage of Agriculture area	Percentage of regulated area	Non-agricultural area > 1500 km ²	Percentage of Agriculture area < 33.3
Avoca	1,420,274	125,682	1,294,592	46,287	1,248,305	91.2	3.3	0	0
Brown	381,527	64,458	317,069	3,213	313,856	83.1	0.8	0	0
Broken	709,505	133,877	575,628	108,314	467,313	81.1	15.3	0	0
Bunyip	407,605	134,721	272,884	10,306	262,578	66.9	2.5	0	0
Campaspe	405,815	55,020	350,796	32,269	318,526	86.4	8.0	0	0
East Gippsland	565,327	554,715	10,612	785	9,827	1.9	0.1	1	1
Glenelg	1,212,339	353,521	858,818	2,837	855,981	70.8	0.2	1	0
Goulburn	1,685,502	619,278	1,066,224	118,564	947,659	63.3	7.0	1	0
Hopkins	1,009,399	50,584	958,815	3,217	955,598	95.0	0.3	0	0
Kiewa	190,748	109,051	81,696	1,494	80,203	42.8	0.8	0	0
Lake Corangamite	407,996	65,865	342,132	3,698	338,434	83.9	0.9	0	0
Latrobe	467,132	236,445	230,687	11,869	218,818	49.4	2.5	1	0
Loddon	1,564,051	244,384	1,319,667	211,907	1,107,760	84.4	13.5	1	0
Mallee	4,148,063	1,479,394	2,668,668	39,239	2,629,429	64.3	0.9	1	0
Maribyrnong	144,735	36,395	108,340	295	108,045	74.9	0.2	0	0
Millicent	3,437,879	671,499	2,766,380	58,907	2,707,473	80.5	1.7	1	0
Mitchell	487,699	414,266	73,433	2,542	70,892	15.1	0.5	1	1

Table A.1 continuation....

Moorabool	223,272	47,191	176,081	1,760	174,322	78.9	0.8	0	0
Murray-Riverina	1,504,147	122,267	1,381,880	214,593	1,167,287	91.9	14.3	0	0
Otway Coast	388,764	179,336	209,428	3,193	206,235	53.9	0.8	1	0
Ovens River	797,588	434,102	363,486	8,851	354,636	45.6	1.1	1	0
Portland Coast	396,773	68,681	328,092	3,894	324,198	82.7	1.0	0	0
Snowy	1,578,416	1,009,280	569,137	1,180	567,957	36.1	0.1	1	0
South Gippsland	679,783	230,919	448,864	8,627	440,237	66.0	1.3	1	0
Tambo	420,117	330,811	89,306	782	88,523	21.3	0.2	1	1
Thomson	657,902	470,703	187,200	25,148	162,051	28.5	3.8	1	1
Upper Murray	521,020	309,908	211,112	601	210,511	40.5	0.1	1	0
Werribee	197,135	72,040	125,094	4,104	120,990	63.5	2.1	0	0
Wimmera	3,036,540	513,320	2,523,220	4,874	2,518,346	83.1	0.2	1	0
Yarra	410,577	263,160	147,416	5,673	141,743	35.9	1.4	1	0

Table A.2 and Table A.3 show information of the Blue Nile catchment subcatchments. Blue Nile originates from the mountains of Ethiopia, and covers a large extent of the country. It provides approximately 80% of flow to the Nile River, thus a vital blood line in regional livelihood.

Table A.2 Hydrometeorological information of the Blue Nile subcatchments*

No.	Subcatchment Name	Catchment Area (km ²)	Mean Annual Rainfall (mm)	Mean Annual Potential Evapotranspiration (mm)	Mean annual runoff (mm)	Mean annual flow (Mm ³)	Coefficient of runoff
1	Guder	7,011	910	1,307	312	2,187	0.34
2	Dabus	21,030	2,276	1,112	297	6,246	0.13
3	Finchaa	4,089	1,766	1,290	438	1,719	0.25
4	South Gojam	16,762	1,633	1,183	299	5,012	0.18
5	Anger	7,901	1,813	1,318	298	2,355	0.16
6	Beles	14,200	1,655	1,274	306	4,345	0.18
7	Didessa	19,630	1,816	1,308	289	5,673	0.16
8	Muger	8,188	1,347	1,210	298	2,440	0.22
9	North Gojam	14,389	1,336	1,242	305	4,389	0.23
10	Jemma	15,782	1,105	1,059	304	4,798	0.28
11	Lake Tana	15,054	1,313	1,136	253	3,809	0.19
12	Welaka	6,415	1,072	1,263	323	2,072	0.3
13	Beshilo	13,242	982	1,140	296	3,920	0.3
14	Wombera	12,957	1,660	N/A	299	3,874	0.18
15	Dinder	14,891	N/A	N/A	188	2,797	N/A
16	Rahad	8,269	N/A	N/A	133	1,102	N/A

*Source: IWMI working report 131

N/A means data are not available

Table A.3 Subcatchment information of the Blue Nile catchment*

Subcatchment Name	Area (km ²)	Elevation (m)	Annual rainfall (mm)	Min-max temperature (°C)	Annual PET (mm)	LULC
Didessa	19,943	630-3130	1200-2200	20-33	1340-1980	woodlands
South Gojam	17,029	725-300	800-2000	14-33	1100-2100	
Guder	7,123	950-3300	1000-1650	18-31	1300-2000	mostly cultivated
Anger	8,027	860-3200	1200-2030	20-31	1300-1900	woodlands and forest
Lake Tana	15,294	1800-3700	946-2000	14-27	1200-1900	cultivated
North Gojam	14,618	1000-4000	800-1800	13-31	1000-1900	cultivated
Dabus	21,367	485-3150	970-1900	20-35	1300-2100	uncultivated
Beshilo	13,453	1170-4160	825-1470	13-30	1060-1920	mostly cultivated
Fincha	4,154	880-3200	960-1900	20-30	1300-1900	cultivated
Muger	8,318	1000-3500	780-1200	16-31	1200-1700	mostly cultivated
Jemma	16,033	1100-3800	780-1200	15-31	1200-1900	mostly cultivated
Welaka	6,517	1700-4200	800-1300	18-31	1000-1900	mostly cultivated
Wombera	13,163	575-2590	1000-1965	22-34	1470-2000	wood and bush
Beles	14,426	529-2700	1000-2000	21-35	1400-2000	mixed
Rahad	8,401	crossing Sudan				
Dinder	15,128	crossing Sudan				

*Source: IWMI working report 131

Appendix B

This is an example sheet of the ground-truth data collection sheet which is used in the Macalister and Ribb catchments

Field Data Collection Sheet

GPS #		Date	
State		Irr. Scheme	
District		Level of canal	
Village		Agro-Eco Zone	
<u>Water Inflow</u>		<u>Soil Condition</u>	
Rainfall <input type="checkbox"/>		Flooded <input type="checkbox"/>	
Surface Irr. <input type="checkbox"/>		Wet <input type="checkbox"/>	
GW Irr. <input type="checkbox"/>		Moist <input type="checkbox"/>	
Other <input type="checkbox"/>		Dry <input type="checkbox"/>	
<u>Topography</u>			
Upland <input type="checkbox"/>		Plane <input type="checkbox"/>	
Valley <input type="checkbox"/>		Delta <input type="checkbox"/>	
<u>Crop</u>			
Rice <input type="checkbox"/>	Sugarcane <input type="checkbox"/>	Wheat <input type="checkbox"/>	Orchard <input type="checkbox"/>
Maize <input type="checkbox"/>	Vegetable <input type="checkbox"/>	Fodder <input type="checkbox"/>	Orchard +-----
Forest <input type="checkbox"/>	Pasture <input type="checkbox"/>	Grassland <input type="checkbox"/>	Other -----
<u>Growth Stage</u>			
Plough <input type="checkbox"/>	Sowing <input type="checkbox"/>	Early Veg. <input type="checkbox"/>	Mid Veg. <input type="checkbox"/>
Peak Veg. <input type="checkbox"/>	Flowering <input type="checkbox"/>	Stubble <input type="checkbox"/>	Other-----
<u>Health of the Crop</u>			
Wilted <input type="checkbox"/>	Stunted <input type="checkbox"/>	Average <input type="checkbox"/>	Healthy <input type="checkbox"/>
Very Healthy <input type="checkbox"/>	Other-----		
<u>Cropping Pattern</u>			
<u>Current</u>		<u>Previous</u>	
Winter		Summer	
		Winter	
Remarks:			

Appendix C

Table C.1 shows the calculated Pearson correlation coefficient between streamflow and potential input variables. In addition to that, this table also shows the level of significance in the calculation.

Table C.1 Pearson correlation coefficient of RS based potential variables with streamflow

Variable		Total Period	Autumn	Spring	Summer	Winter
NDVI	Pearson Correlation	-.134**	-.071	-.161*	-.024	-.071
	Sig. (2-tailed)	.000	.096	.000	.583	.098
lag_1_NDVI	Pearson Correlation	-.183**	-.099*	-.238**	-.077	-.151**
	Sig. (2-tailed)	.000	.020	.000	.080	.000
lag_2_NDVI	Pearson Correlation	-.205**	-.152**	-.273**	-.049	-.196**
	Sig. (2-tailed)	.000	.000	.000	.270	.000
lag_3_NDVI	Pearson Correlation	-.201**	-.143**	-.268**	-.066	-.185**
	Sig. (2-tailed)	.000	.001	.000	.137	.000
lag_4_NDVI	Pearson Correlation	-.194**	-.123**	-.279**	-.091*	-.143**
	Sig. (2-tailed)	.000	.004	.000	.039	.001
lag_5_NDVI	Pearson Correlation	-.170**	-.138**	-.247**	-.130**	-.068
	Sig. (2-tailed)	.000	.001	.000	.003	.112
lag_6_NDVI	Pearson Correlation	-.158**	-.167**	-.222**	-.106*	-.052
	Sig. (2-tailed)	.000	.000	.000	.016	.227
lag_7_NDVI	Pearson Correlation	-.149**	-.165**	-.182**	-.095*	-.055
	Sig. (2-tailed)	.000	.000	.000	.032	.200
8-day_avg_NDVI	Pearson Correlation	-.312**	-.245**	-.451**	-.137**	-.248**
	Sig. (2-tailed)	.000	.000	.000	.002	.000
NDWI	Pearson Correlation	.041	-.065	-.069	.062	.084*
	Sig. (2-tailed)	.056	.126	.109	.156	.049
lag_1_NDWI	Pearson Correlation	.074**	-.106*	-.003	.106*	.115**
	Sig. (2-tailed)	.001	.012	.940	.015	.007
lag_2_NDWI	Pearson Correlation	.092**	-.099*	.067	.130**	.107*
	Sig. (2-tailed)	.000	.021	.119	.003	.012
lag_3_NDWI	Pearson Correlation	.055*	-.088*	.005	.149**	.037
	Sig. (2-tailed)	.011	.038	.903	.001	.392
lag_4_NDWI	Pearson Correlation	.041	-.078	-.025	.160**	.015
	Sig. (2-tailed)	.055	.066	.561	.000	.730
lag_5_NDWI	Pearson Correlation	.064**	-.043	.002	.169**	.059
	Sig. (2-tailed)	.003	.310	.972	.000	.171
lag_6_NDWI	Pearson Correlation	.051*	-.063	-.038	.123**	.061
	Sig. (2-tailed)	.018	.139	.372	.005	.155
lag_7_NDWI	Pearson Correlation	.055*	-.096*	-.063	.151**	.087*
	Sig. (2-tailed)	.010	.024	.142	.001	.043
8-day_avg_NDWI	Pearson Correlation	.108**	-.155**	-.069	.178**	.156**
	Sig. (2-tailed)	.000	.000	.109	.000	.000
EVI	Pearson Correlation	-.098**	-.118**	-.251**	.205**	.166**
	Sig. (2-tailed)	.000	.005	.000	.000	.000
lag_1_EVI	Pearson Correlation	-.116**	-.128**	-.278**	.142**	.160**
	Sig. (2-tailed)	.000	.003	.000	.001	.000
lag_2_EVI	Pearson Correlation	-.133**	-.153**	-.297**	.155**	.125**

Table C.1 continuation....

	Sig. (2-tailed)	.000	.000	.000	.000	.003
lag_3_EVI	Pearson Correlation	-.135**	-.158**	-.283**	.151**	.124**
	Sig. (2-tailed)	.000	.000	.000	.001	.004
lag_4_EVI	Pearson Correlation	-.139**	-.152**	-.292**	.135**	.143**
	Sig. (2-tailed)	.000	.000	.000	.002	.001
lag_5_EVI	Pearson Correlation	-.143**	-.142**	-.297**	.099*	.172**
	Sig. (2-tailed)	.000	.001	.000	.025	.000
lag_6_EVI	Pearson Correlation	-.147**	-.161**	-.303**	.114*	.167**
	Sig. (2-tailed)	.000	.000	.000	.010	.000
lag_7_EVI	Pearson Correlation	-.151**	-.158**	-.299**	.123**	.181**
	Sig. (2-tailed)	.000	.000	.000	.006	.000
8-day_avg_EVI	Pearson Correlation	-.145**	-.188**	-.391**	.286**	.203**
	Sig. (2-tailed)	.000	.000	.000	.000	.000
BT31	Pearson Correlation	-.161**	-.057	-.108*	-.168**	-.007
	Sig. (2-tailed)	.000	.179	.013	.000	.872
lag_1_BT31	Pearson Correlation	-.217**	-.086*	-.155**	-.229**	-.138**
	Sig. (2-tailed)	.000	.044	.000	.000	.001
lag_2_BT31	Pearson Correlation	-.255**	-.146**	-.225**	-.216**	-.212**
	Sig. (2-tailed)	.000	.001	.000	.000	.000
lag_3_BT31	Pearson Correlation	-.242**	-.141**	-.189**	-.203**	-.204**
	Sig. (2-tailed)	.000	.001	.000	.000	.000
BT32	Pearson Correlation	-.154**	-.053	-.102*	-.164**	-.003
	Sig. (2-tailed)	.000	.213	.018	.000	.946
lag_1_BT32	Pearson Correlation	-.209**	-.082	-.150**	-.224**	-.133**
	Sig. (2-tailed)	.000	.056	.000	.000	.002
lag_2_BT32	Pearson Correlation	-.248**	-.144**	-.221**	-.211**	-.208**
	Sig. (2-tailed)	.000	.001	.000	.000	.000
lag_3_BT32	Pearson Correlation	-.237**	-.138**	-.187**	-.200**	-.202**
	Sig. (2-tailed)	.000	.001	.000	.000	.000
BT_Diff	Pearson Correlation	-.255**	-.134**	-.196**	-.162**	-.127**
	Sig. (2-tailed)	.000	.002	.000	.000	.003
lag_1_BT_Diff	Pearson Correlation	-.279**	-.153**	-.208**	-.224**	-.202**
	Sig. (2-tailed)	.000	.000	.000	.000	.000
lag_2_BT_Diff	Pearson Correlation	-.275**	-.111**	-.225**	-.219**	-.168**
	Sig. (2-tailed)	.000	.009	.000	.000	.000
lag_3_BT_Diff	Pearson Correlation	-.241**	-.129**	-.133**	-.191**	-.101*
	Sig. (2-tailed)	.000	.002	.002	.000	.019
BT_Grad	Pearson Correlation	-.014	-.044	-.060	.042	-.003
	Sig. (2-tailed)	.525	.305	.163	.339	.948
lag_1_BT_Grad	Pearson Correlation	.000	.008	-.049	.043	.032
	Sig. (2-tailed)	.999	.858	.261	.328	.460
lag_2_BT_Grad	Pearson Correlation	.005	.037	-.022	.019	.033
	Sig. (2-tailed)	.820	.385	.606	.669	.437
lag_3_BT_Grad	Pearson Correlation	.021	.042	-.007	.037	.074
	Sig. (2-tailed)	.323	.322	.866	.409	.084

*. Correlation is significant at the 0.05 level (2-tailed).

** . Correlation is significant at the 0.01 level (2-tailed).

Note: lag_1 means 1-day lag and lag_2 means 2-day lag and so on...